11-10-2016

Optimum Distribution System Architectures for Efficient Operation of Hybrid AC/DC Power Systems Involving Energy Storage and Pulsed Loads

Ahmed T. Elsayed
Florida International University, aghar002@fiu.edu

FLORIDA INTERNATIONAL UNIVERSITY

Miami, Florida

OPTIMUM DISTRIBUTION SYSTEM ARCHITECTURES FOR EFFICIENT

OPERATION OF HYBRID AC/DC POWER SYSTEMS INVOLVING ENERGY

STORAGE AND PULSED LOADS

A dissertation submitted in partial fulfillment of

the requirements for the degree of

DOCTOR OF PHILOSOPHY

in

ELECETRICAL ENGINEERING

by

Ahmed Elsayed

2016

To: Interim Dean Dr. Ranu Jung
    College of Engineering and Computing

This dissertation, written by Ahmed Elsayed, and entitled Optimum Distribution System Architectures for Efficient Operation of Hybrid AC/DC Power Systems Involving Energy Storage and Pulsed Loads, having been approved in respect to style and intellectual contents, is referred to you for judgment.

We have read this dissertation and recommend that is be approved.

_____
W. Kinzy Jones

_____
Sakhrat Khizroev

_____
Arif Sarwat

_____
Mark Roberts

_____
Osama A. Mohammed, Major Professor

Date of Defense: November 10, 2016

The dissertation of Ahmed Elsayed is approved.

_____
Interim Dean Ranu Jung
College of Engineering and Computing

_____
Andrés G. Gil
Vice President for Research and Economic Development
and Dean of the University Graduate School

Florida International University, 2016

DEDICATION

This dissertation is dedicated to my lovely and supportive wife, Eman Omar, my children, Omar and Maryam, my mother and my father, Mr. Taha Ghareeb. Without their patience, understanding, support, encouragement, and most of all love, the completion of this work would not have been possible.

ACKNOWLEDGMENTS

ABSTRACT OF THE DISSERTATION

OPTIMUM DISTRIBUTION SYSTEM ARCHITECTURES FOR EFFICIENT

OPERATION OF HYBRID AC/DC POWER SYSTEMS INVOLVING ENERGY

STORAGE AND PULSED LOADS

by

Ahmed Elsayed

Florida International University, 2016

Miami, Florida

Professor Osama A. Mohammed, Major Professor

After more than a century of the ultimate dominance of AC in distribution systems, DC distribution is being re-considered. However, the advantages of AC systems cannot be omitted. This is mainly due to the cheap and efficient means of generation provided by the synchronous AC machines and voltage stepping up/down allowed by the AC transformers. As an intermediate solution, hybrid AC/DC distribution systems or microgrids are proposed. This hybridization of distribution systems, incorporation of heterogeneous mix of energy sources, and introducing Pulsed Power Loads (PPL) together add more complications and challenges to the design problem of distribution systems. In this dissertation, a comprehensive multi-objective optimization approach is presented to determine the optimal design of the AC/DC distribution system architecture. The mathematical formulation of a multi-objective optimal power flow problem based on the sequential power flow method and the Pareto concept is developed and discussed. The outcome of this approach is to answer the following questions: 1) the optimal size and location of energy storage (ES) in the AC/DC distribution system, 2) optimal location of the PPLs, 3) optimal point of common coupling (PCC) between the AC and DC sides of the network, and 4) optimal network

connectivity. These parameters are to be optimized to design a distribution architecture that supplies the PPLs, while fulfilling the safe operation constraints and the related standard limitations. The optimization problem is NP-hard, mixed integer and combinatorial with nonlinear constraints. Four objectives are involved in the problem: minimizing the voltage deviation (ΔV), minimizing frequency deviation (Δf), minimizing the active power losses in the distribution system and minimizing the energy storage weight. The last objective is considered in the context of ship power systems, where the equipment's weight and size are restricted.

The utilization of Hybrid Energy Storage Systems (HESS) in PPL applications is investigated. The design, hardware implementation and performance evaluation of an advanced – low cost Modular Energy Storage regulator (MESR) to efficiently integrate ES to the DC bus are depicted. MESR provides a set of unique features: 1) It is capable of controlling each individual unit within a series/parallel array (i.e. each single unit can be treated, controlled and monitored separately from the others), 2) It is able to charge some units within an ES array while other units continue to serve the load, 3) Balance the SoC without the need for power electronic converters, and 4) It is able to electrically disconnect a unit and allow the operator to perform the required maintenance or replacement without affecting the performance of the whole array. A low speed flywheel Energy Storage System (FESS) is designed and implemented to be used as an energy reservoir in PPL applications. The system was based on a separately excited DC machine and a bi-directional Buck-Boost converter as the driver to control the charging/discharging of the flywheel. Stable control loops were designed to charge the FESS off the pulse and discharge on the pulse. All the developments in this dissertation were experimentally verified at the Smart Grid Testbed.

TABLE OF CONTENTS

CHAPTER   PAGE

xi

LIST OF TABLES

LIST OF FIGURES

LIST OF ACRONYMS

BMS	Battery Management System
ES	Energy Storage
FESS	Flywheel Energy Storage System
HESS	Hybrid Energy Storage System
MESR	Modular Energy Storage Regulator
NSGA	Non-dominated Sorting Genetic Algorithm
PMSM	Permanent Magnet Synchronous Machine
VSI	Voltage Source Inverter
CSI	Current Source Inverter
PCC	Point of Common Coupling
PV	Photo-Voltaic
PPL	Pulsed Power Load
GA	Genetic algorithm

Chapter 1   Introduction and Literature Survey

The turn of the 20th century witnessed a fierce battle over how electricity would be generated, transmitted and utilized. This battle, famously known as the "War of currents," was waged by G. Westinghouse and N. Tesla, supporting AC on one side, and T. Edison leading proponents of DC on the opponent side. Obviously, the debate ended by predominant implementation of AC distribution in the vast majority of our power systems, due to reasons that made much sense at that time. One of these reasons was the invention of the transformers that offered a great and simple means to step up the voltage. Consequently, the area covered by a distribution system widened, but changing DC voltage levels was an impediment. Moreover, the invention of poly-phase AC machines helped people find an alternative to DC machines, which had remained the only option for some time back then. However, DC systems did not completely disappear from the distribution scene. For instance, there is an old system used by Pacific Gas and Electric (PG&E) in San Francisco to feed variable speed DC-motored elevators in several historic buildings [1].

The advances achieved in power electronics, which made DC voltage regulation a simple task, in addition to the increasing penetration of DC loads and sources encouraged researchers to reconsider DC distribution for at least portions of today's power system to increase its overall efficiency. In this chapter, the author will present an exhaustive literature survey and overview of the research efforts conducted on several issues such as the design, control, operation, stability and protection of DC systems. The objective is to give an integrated background about what has already been achieved in these areas by giving details about the topics and/or guidance on where to find further information about them. The author also attempts to develop a simplified

conceptual path to the new researchers in the field of DC power systems on what the challenges of DC systems are and how their peers tackled them.

1.1 Motivation for DC Systems Reconsideration

Recently, dealing with DC power systems became significantly easier due to the stunning advent of semi-conductor technology and the continuous developments of power electronic converters. In addition, there are several other valid reasons for the rethinking of DC deployment. These reasons can be classified as reasons related to the loads, sources and storage elements.

1.1.1 DC Loads

Many of today's consumer loads are DC supplied. Electronic based office and home appliances, such as computers, laptops, tablets, phones, printers, TVs [2], microwave ovens [3] and lighting, consume electricity in DC form [4]-[7]. Newer, more-efficient lighting technologies such as compact fluorescent fixtures and solid-state lighting involve a DC stage and, hence, it is more efficient to utilize them in a DC distribution system [8], [9]. DC power is used in Variable Speed Drives (VSD) for pumps, HVAC systems, fans, elevators, mills and traction systems. In addition, for industrial applications, steel industry is employing more DC electric arc furnaces since they consume less energy than their corresponding AC ones and cause less light flicker [10]. The electrochemical industry is almost pure DC application [11], [12]. Supplying these loads through the predominant AC distribution systems adds conversion stages and, consequently, adds inefficiencies to the delivery chain. According to [13], nearly 30% of the generated AC power passes through a power electronic converter before it is utilized. The amount of lost energy varies, but, generally, it lies within the range of 10-25% [14]. In another study [15], the authors mentioned that the power conversion

efficiency can be increased by about 8% if a DC-bus system is used and further savings of around 25% can be achieved as a result of removing one rectifier and one PFC stage.

1.1.2 Renewable Energy Sources

Current power systems encounter changes on the source side. These changes can be milestones in the history of power systems. Motivated by environmental and economic conditions, there is a global trend towards more utilization of renewable energy sources (RES). Some of the RES are natively DC, such as Photovoltaic (PV) and Fuel Cells (FC), or AC with variable frequency, such as wind which is integrated to the AC grid through a DC link [16], [17]. Hence, wind farms can be integrated to a DC distribution system with more efficiency. Micro-turbines are also considered as a distributed generation resource. Micro-turbines generating high-frequency AC are also easier to connect to a DC system than to an AC system, where inversion and generating a synchronized sinusoidal AC current is required. The integration of micro-turbines to DC distribution networks is discussed in [18] as the authors proposed a local DC distribution network to interface a variety of AC and DC sources. The AC sources included in this study were micro-turbines, variable speed wind generators and flywheels. The included DC sources were PV arrays, fuel cells and ES.

1.1.3 Energy Storage

One of the great benefits of DC microgrids is their inherent capability of facilitating static storage integration. Most of storage elements are purely DC, such as batteries and ultra-capacitors. Moreover, flywheels, even though they are mechanical energy storage systems, are mostly coupled to a permanent magnet synchronous machine (PMSM) that is integrated to the distribution system through a DC link [19], [20]. A study carried out by NTT facility, Japan, to compare between an AC uninterruptible power supply (UPS)

3

and a DC one, from an availability perspective, shows that the reliability of DC supply is higher [21].

1.1.4 Data Centers

Data centers store and transfer huge amounts of digital information such as internet, cellular communications, and credit card transactions. The main feature that must be maintained in a data center power system is high reliability [21]-[23]. Therefore, data centers are typically equipped with Uninterruptable Power Supplies (UPS) that require multiple conversion stages to connect the batteries to a DC bus. These conversion stages create losses that can be avoided if the power is distributed in DC form [24], leading to increased overall system efficiency. As a result, energy cost, which contributes to around 20% of the total operating cost of a data center, is decreased. Therefore, DC distribution is a more economical and efficient option for data centers [25], [26].

Firstly, in 2006, the idea of utilizing DC based power distribution systems in data centers was opposed in [27], the conclusion was based on comparing the efficiencies of 5 distribution architectures (two AC- and three DC-based). In 2008, a more recent and accurate study prepared by Lawrence Berkeley National Laboratory (LBNL) revealed that converting the typical AC distribution systems in data centers to DC based systems can achieve up to 28% energy saving [28]. LBNL prepared a research roadmap towards high performance data centers [29], they emphasized the importance of the conversion of the main power infeed to DC as a step to improve the reliability and efficiency of data center power supplies. In [21], the authors implicitly promoted the idea of utilizing DC distribution for data centers: they proposed a grounding scheme and recommendations for a 380V DC distribution system for data centers.

1.1.5 Plug-In Electric Vehicles

It is highly anticipated to see a significant increase in number of EV in the near future for a variety of reasons; 1) the global call for reduced CO_2 emissions. 2) The investments that pioneer automotive companies have been making to advance plug-in all electric, and hybrid electric vehicle (HEV) technologies. 3) The problems inherently associated with fuel availability and price stability. 4) The stunning advancements in power electronics and energy storage devices that contribute to a noticeable reduction in their prices. The problem of coordinating the charging process of a large number of EVs has lately acquired the attention of many researchers, and is still under study [30]. A tool for assessing the impacts of the EV charging and its coordination with the electricity tariff is presented in [31].

It is not yet determined whether EVs will be charged casually at home like any other home appliance, at a fast charging station, similar to a gas-fueling station for conventional vehicles, at a place where a discharged EV battery is replaced with a completely charged one, or at a smart charging park where EVs are coordinated centrally at a smart garage that enable vehicle-to-vehicle (V2V) and vehicle-to-grid (V2G) services [32]-[35]. Each of these different techniques has supporters and opponents for reasons that are outside the scope of this review. However, the last model relates to DC distribution since some of the researchers who work on the concept of smart charging parks believe that they should operate as DC microgrids, with a common DC bus at which the EV batteries and any Distributed Generation (DG) units should be integrated [36]-[39].

1.1.6 DC Microgrids

Microgrids are local energy networks that involve renewable energy sources and storage systems. They have the capability to be locally controlled. Therefore, they can

disconnect from the grid when there is a blackout, or a fault at the microgrid, and continue to supply a portion of their local loads in a so called "islanded mode." Several states in the USA invested millions to promote high penetration of microgrids as a part of their climate resiliency plans against natural disasters, especially after hurricane Sandy. Since microgrids typically include renewable sources and batteries, DC microgrids [40]-[49] will have the capability to increase the overall system efficiency [50]-[58].

Various papers have shown that DC microgrids can play an effective role in solving the operational issues on the main grid [59]. In [60], a DC microgrid involving PV generation and hybrid energy storage (super capacitors and Li-ion batteries) was used for mitigation of heavy non-linear Loads. It was shown experimentally in [61] that a DC microgrid can be used for voltage support by making use of its capability of injecting reactive power as an ancillary service.

In conclusion, the aforementioned factors motivated many researchers to raise a fundamental, yet essential, question: is AC distribution still the most efficient means to distribute electrical power or it is time to reconsider deploying DC distribution systems? Researchers realized that DC power systems would be more efficient because they are more aligned with today's needs than they were 100 years ago.

1.2 Feasibility of DC distribution systems

The feasibility of using DC for power distribution has been studied by several researchers in recent years. One of the major factors that were used to judge the superiority of DC over AC is efficiency. Therefore, comparing AC to DC in terms of efficiency, losses and economic merits received special attention.

D. J. Hammerstrom presented in [62] a model to compare the overall conversion efficiencies of AC and DC distribution topologies for residential applications. Based on

the author's assertion, each power conversion stage loses about 2.5% of the energy it converts. It was shown that DC systems incorporating fuel cells, or other local DC generations, encounter less conversion losses. This conclusion was supported by the results presented in [63] by G. Seo et al. They presented a mathematical model to analyze the losses of the components of DC distribution systems. It was also shown that the converter efficiency increases as the power capacity and load increase.

A loss comparison between AC and DC distribution systems was conducted by the authors of [64]. The authors created two models, AC and DC, for a large distribution system consisting of 714 buses and 235 loads. The comparison results showed that for the same conductor cross sectional area, the DC current can be 1.22 times larger than the AC current so that the distribution system encounters the same conduction losses. Nevertheless, the comparison was oversimplified by assuming that the resistance of the cable will remain the same in the AC and DC cases, neglecting the skin effect. The same assumption was used in the study presented in [65], in addition to some other overestimated assumptions quoted from [66], such as considering the wire resistance as 0.069 Ω/m, which is impractically large. To give an idea about the real values, references [67]-[69] provide some cable catalogues from different manufacturers. Furthermore, the reader can refer to tables 8 and 9 of the National Electric Code [127]. This led to a conclusion that delivering power to residential premises in DC form is not recommended. Latter studies showed different conclusions. According to the study presented in [70], the relation between AC and DC cable resistances can be given as:

$$R_{ac} = \frac{\pi.r^2}{\pi.r^2 - \pi.(r-\delta)^2}.R_{dc} \qquad (1\text{-}1)$$

Where R_{ac}, R_{dc} are the cable AC and DC resistances, respectively, r is the conductor radius and δ is the conductor skin depth, which is dependent on the frequency. From

this formula, it can be concluded that the cable AC resistance will always be higher than its corresponding DC resistance and the difference cannot be ignored, especially at higher frequencies, e.g. 60 Hz or 400 Hz systems. In order to test the practicality of this conclusion, the AC and DC values of cable resistances listed in one of the large manufacturers' catalogue [69] were compared. It was found that the AC resistance is more than the DC resistance by approximately 19% for cables with a cross sectional area (CSA) ranging from 4mm^2 to 95mm^2. Moreover, for larger CSAs, the difference is in the range of 21%-37%. This difference was considered in [71] when the authors compared AC and DC systems for off-shore distribution applications. It was emphasized that the resistance increase due to skin and proximity effects has to be considered while comparing DC to AC systems in order to derive accurate conclusions. This comparative analysis showed that, by utilizing double pole DC system, the cable loss can be reduced to 40%-50% of that of an AC system. It was also concluded that DC systems have lower losses over a wide range of operating voltages, load currents and transmission distances. Larruskain et al proposed converting existing AC lines to DC lines to increase the current carrying capacity of these lines [72].

In [73], it was shown that DC distribution systems are feasible for commercial buildings with sensitive electronic loads. In [74], the same conclusion was seconded. Moreover, it was shown that DC distribution leads to more advantages than those related to reduced losses, such as safety, reduction of electromagnetic fields, and power quality improvement.

In [75], the authors studied the applicability of DC distribution in industrial applications. It was shown that DC distribution is feasible for industrial applications, and the challenges associated with DC distribution can be addressed by proper system design. The feasibility of connecting multiple AC microgrids through a DC link is

8

investigated in [76]. The results show that systems' reliability and sustainability improved.

1.3 Design of DC distribution systems

The design of DC distribution systems has been lately investigated in several publications. Various factors should be taken into consideration while designing a DC distribution system, especially if the used equipment is originally designed for AC applications. One of the basic requirements of a reliable design is to obtain simplified models that express the load behavior under DC operation. In [4], the authors developed steady state and transient models for a large number of loads (63 loads). It was found that heating loads can be modeled (in steady state) as pure resistance and lighting loads can be modeled as temperature-dependent resistance. The steady state model of a universal machine is a variable current source, $I = Y_o U + I_o$, while it was found that electronic loads that use switch mode power supply behave as constant power loads. This means that the load consumes the same amount of power regardless of its supply voltage changes.

D. Salomonsson *et al*. discussed in [73] the general design issues associated with DC power systems. They held a comparison among different cable configurations. It was shown that a DC five wire installation is slightly better than that of an AC, while for three wire installations, DC is superior to AC in terms of power transferring capacity. The authors tested the performance of some typical loads when operated with DC power. It was demonstrated that supplying the loads with a DC supply can prevent voltage disturbance from affecting the loads.

In [77], the authors proposed an adaptive control system for DC microgrids installed in data centers. They compared two configurations for the data center power system (shown in Figure 1.1). According to the authors, configuration (a) is better than (b) to

9

avoid generator synchronization and achieve better power flow control; while, (b) can be better than (a) in terms of power losses and converter size. It is worth mentioning that other advantages may be added to (b) over (a), such as: 1) connecting HVAC to the same DC bus not only increases the converter size, but also increases the energy storage capacity and, consequently, increases the cost and the complexity of protection, operation and transition modes; 2) it is not practical to connect high power machine loads to the same bus where sensitive loads are connected to minimize voltage fluctuations. It is worth mentioning that the main focus of the mentioned study was on system operation and control. The study outlined the operation of a DC data center, eight possible operation modes and twenty-three transitions were defined. Among these possible operation modes and transitions, the ones of interest were discussed. Simulation results showed that continuous supply for sensitive DC load was guaranteed by coordinating the main two converters. The authors emphasized the importance of having fast detection of AC-grid outage and fast switches [77]. Another study of
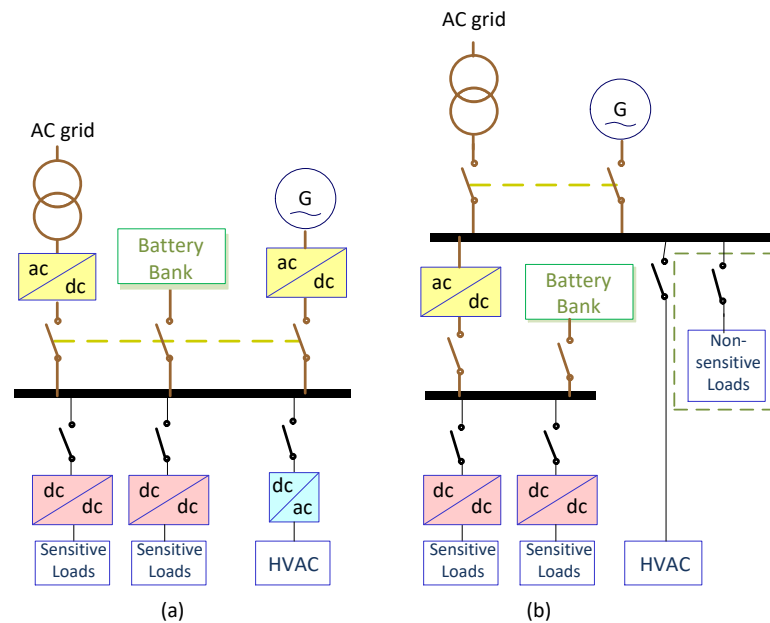
Figure 1.1 Configurations of data center power system discussed in [77].

different operation situations and transitions between interconnected and islanded modes of DC microgrids was presented in [78], but with more simplifications and limitations.

In [74], A. Sannino et al. proposed a simplified scheme for DC distribution system, in which a lower number of converters is needed in order to increase the overall efficiency. They studied the feasibility of the proposed system by simulating its implementation on their own research facility using actual parameters and conditions and with four different DC voltage levels: 48V, 120V, 230V and 326V. Voltage drops and power losses were calculated and compared to those of the existing AC system. In addition, the system was economically evaluated by calculating installation and operation costs. The final conclusions were: 1) DC supply can lead to major advantages if a proper voltage level is chosen (results showed that 326V is the most suitable). It should be noticed that this conclusion was based on the European system and cannot be generalized to systems that use other voltage levels, such as the U. S. power system; 2) By adding a battery bank, they guaranteed emergency backup power for their critical loads for a much longer time than that guaranteed by commercial UPS, with less costs; 3) It was shown that the commercially available circuit breakers can be adopted to provide adequate DC protection, even at a relatively high current rating and short circuit capacity.

M. Amin et al. compared, in [5], low voltage DC distribution systems with different voltage levels (24V and 48V) to a 230V AC distribution system when feeding different household appliances. Conductor losses and device losses were calculated and considered for each system. They presented a principle for cable cross section optimization based on comparing the investment cost of the cable and the cable losses. The results showed that the 48V DC systems with optimized cable area have the lowest

total energy consumption, and the 24V DC system has high losses. This conclusion was expected since the total distributed power was assumed to be around 8 kW, which is too high for such a low voltage.

In [6], K. Techakittiroj et al. carried out an experiment to demonstrate the possibility of using the appliances available in market in DC distribution systems without modifications. They supplied a compact fluorescent lamp, LED lamp, television, computer and small motor drive with DC power. Successful results and improved power quality confirmed the possibility and plausibility of supplying appliances directly with DC voltage. The authors emphasized the idea of co-existence of AC and DC distribution systems for easier migration towards DC.

H. kakigano *et al.* presented in [79] a DC microgrid for residential applications. The system consisted of cogeneration systems connected to a DC distribution line (3 wire, ± 170V). Electric double layer capacitors (EDLC) were used as the main energy storage. System operation under interconnected mode and intentional islanding mode were demonstrated. They constructed a laboratory scale experimental system. The system operation was tested under voltage sag on the utility grid point of common coupling (PCC), disconnection from, and reconnection to the grid. Experimental results showed that the system can supply high-quality power continuously to the loads under those conditions.

M. E. Baran *et al.* investigated in [75] the neutral voltage shift phenomenon that is associated with DC/AC power systems by simulating a small scale shipboard power system. As a solution for this phenomenon, they proposed using a DC/DC buck converter with an isolation transformer, and grounding the transformer through high resistance (250 p.u was used in this case).

The concept of power buffer was adopted in [80]. The authors integrated power buffer and load shedding to enhance the transient performance of DC distribution systems. The power buffer was achieved by a boost converter with a DC bus capacitor. It was shown that power buffer is suitable for short term transients; while, for long term transients, load shedding is mandatory. Load shedding was based on load classifications according to their priorities. In [81], Logue *et al.* utilized power buffering to prevent voltage violations in DC systems by controlling the input resistance directly.

As a part of the Future Renewable Electric Energy Delivery and Management Systems Center (FREEDM), a USA National Science Foundation (NSF)-sponsored project , an arc free DC plug for 380V DC systems was developed [82]. In another study within the same project, a solid state transformer based on Silicon Carbide (SiC) MOSFET was developed to replace the traditional electromagnetic transformer [83]. Solid state transformers [46] inherently involve a DC intermediate stage, which increases the possibility of integrating some of the DC loads at the DC bus to avoid unnecessary conversion losses.

1.4   Stability of DC distribution systems

Stability has always been one of the main concerns of power system engineers. The stability criteria for AC systems are well established and investigated. On the contrary, the stability of DC power systems is still under investigation.

One of the sources of instability in DC power systems was highlighted by Sokal and Middlebrook in the 1970's. In [84], it was shown that DC converters can yield a negative input resistance. If this negative resistance exceeds the positive resistance of the input LC filter of the converter, the whole system can oscillate, leading to instability. In [85], [86], Middlebrook investigated the problem of negative input resistance at low frequencies. To eliminate the oscillations, the design of a switch-mode converter and

its input filter was provided, in which the output impedance of the filter is kept smaller than the input impedance of the converter to preserve the system stability.

Based on the same impedance analysis, Feng *et al.* [87] defined a forbidden region for the impedance ratio. If the ratio of the output impedance to the input impedance is kept outside this region, Nyquist stability criterion is not violated and the system remains stable. Based on the defined forbidden region, the impedance specifications for subsystems utilized in DC distributed power systems were proposed. It is worth noting that the proposed forbidden region and impedance specifications were for each individual load, not for the aggregated load [88]. These impedance requirements were for voltage source systems. An extended study for current source systems showed that the stability requirements are actually the opposite [89]. The stability analysis for a DC-DC converter with its input filter using Routh-Hurwitz criterion was presented in [90]. In summary, for voltage source converters, the system is stable if the ratio of the load impedance to source impedance is more than unity, while for current source converters the system is stable if the same ratio is less than unity.

In [91], an active stabilization technique was proposed to maintain the stability of isolated microgrids in the presence of direct online induction motors (IMs) as loads. After carrying out a detailed small signal admittance modelling and analysis, the authors verified the previous findings. It was shown that there is a source-load admittance mismatch between the Voltage Source Inverters (VSIs) on one side and the IMs on another side. This mismatch led to medium frequency instabilities due to violation of Nyquist stability criterion. The stabilization technique was based on the addition of a compensation transfer function to re-map the low damped modes in the open loop system to higher damping locations in the closed-loop system. The efficiency of the stabilization technique was verified by simulation and experimental results. This

study was concerned with isolated AC microgrids dominated by IMs fed from DC sources or DGs through VSIs. Therefore, it is of interest for this survey. Using a similar procedure, the same authors of [91] presented a comprehensive assessment and active mitigation strategy for the interactions in hybrid AC/DC distribution systems [92] and DC microgrids [93]. It was shown that in converter-dominated distribution systems, even if each individual converter is stable by itself, the stability of the whole system is not guaranteed because of the tight regulation of controllers. The problem was investigated for a MV multi-MW droop controlled microgrid system [94]. The stability analysis of DC loads fed through Voltage Source Rectifier (VSR) was presented in [95].

Instabilities due to negative incremental input admittance in DC systems feeding Permanent Magnet Synchronous Motors (PMSM) through VSI speed drives were investigated by Mohamed *et al* in [96]. An active compensation method based on reference voltage was proposed to stabilize the DC link. More active stabilization algorithms for speed drives with a DC link can be found in [97] and [98]. A method based on modifying the control structure to emulate the effect of a capacitor was presented in [99]. Another solution based on a passive damping circuit was proposed in [100].

In [101], Davari et al proposed a variable structure nonlinear controller for a master Voltage Sources Converter (VSC) regulating the DC link voltage in DC distribution systems. The distribution system is based on multi-terminal energy pool architecture. The controller employs a sigma-delta modulation scheme. The results showed that global stabilization of all system states was achieved.

Small signal stability analysis of low voltage DC microgrids was presented in [102]. Sources and loads were modeled by first order differential equations. The distribution cables were included in the model as well. The impacts of changing the inductance and

resistance of the cable on the stability were investigated. It was proved that the poles move further inside the negative half of the S plane as cable resistances increase or inductances decrease. An important note should be considered here: any increase in the cable resistance will increase the transmission losses. Hence, a tradeoff must be considered between the system stability and transmission losses. This study modeled all the loads as constant power loads (CPLs), which partially contradicts the findings of [4], as it was shown that significant portion of DC loads can be represented by constant impedance models.

Instabilities of current controlled DC based distributed generation units interfaced to the grid through VSIs were investigated in [103], the main focus is on the instabilities due to grid parameters variation, grid distortions and the instabilities associated with the current control loop parameters. A solution based on a combination of high bandwidth predictive current controller, an adaptive internal model for the capacitor voltage and grid current dynamics, was proposed.

A small signal stability analysis of MVAC and MVDC architectures of a zonal shipboard power system showed that MVDC has higher damping, and tends to be more stable for different exciter types [104]. Another detailed model and small signal stability analysis for an electric aircraft is presented in [105]. The parameters affecting system's stability were scrutinized.

Wide deployment of DC systems has some negative impacts on the utility grid. Various research efforts have been made to mitigate such impacts. It was found that DG-based DC microgrids have a disturbing impact on utility grids, which may lead to instability because of due to the absence of mechanical inertia or very low inertia dynamics [106]. A solution to this problem could be the utilization of synchronverters, which were proposed by Zhong et al [107]. A synchronverter is an inverter with

modified control to emulate the characteristics of a traditional synchronous generator. Later, the control of the Synchronverter was improved by adding two major changes to make it able to synchronize itself to the grid without PLL [108]. The idea of emulating virtual rotor characteristics was adopted in [109] to design a nonlinear stabilizer for microgrids.

A recent literature review on control strategies for DC networks is presented in [110]. The control strategies were categorized into two main categories: 1) active load sharing, which includes the master-slave control and 2) the droop based control methods. It was noticed that droop control methods are gaining increased interest. A new decentralized control scheme for islanded DC microgrids is proposed in [111]. The philosophy of this control scheme is based on enforcing each local controller to regulate the voltage at the PCC of the corresponding distributed generation unit. It was shown that it is possible to add/remove a distributed generation unit and the stability of the system is still maintained. Also, the control scheme is scalable (i.e. when a distributed generation unit is installed or uninstalled, the control system can still function).

1.5   Protection of DC distribution systems

Since DC current does not have natural zero crossing, protection of DC systems is a challenging task. In [73], it was suggested to use three-phase AC circuit breakers connecting the three contact pairs in series to eliminate the spark. Several publications investigated the problem of DC short circuit current calculation [112].

D. Salomonsson *et al.* proposed in [113] a protection scheme for a LV DC microgrid. This scheme was studied during different fault events located at different points on the grid. The results showed that it is possible to use commercial AC protection devices, such as fuses and CBs, to protect batteries and loads. However, converters using IGBT modules are very sensitive to over-currents. Therefore, they require faster protection,

which can be provided by an ultra-fast hybrid DC-CB. In addition, a method for coordination of protection devices was discussed. It was shown that problems can arise with high-impedance ground faults. Two grounding architectures for DC systems were presented: TN-S & IT. In TN-S systems, the S letter indicates that the neutral and the protection conductor are separated. The separation of the neutral and the protection conductor, provides a clean PE (protective Earthing). IT systems involve the interconnection and earthing of exposed conductive parts.

In [114], Tang *et al.* presented an economic handshaking method to locate and isolate the faults on a multi-terminal DC network using fast DC switches instead of DC circuit breakers. This resulted in significant savings. The method is based on extinguishing the DC fault current by opening all the AC-circuit breakers, which the VSCs are already equipped with on the AC-sides. According to the authors, through extensive testing, they concluded that their proposed method is reliable.

In [115], a fault detection and isolation scheme for low-voltage DC microgrid systems was presented. The proposed protection scheme divided the microgrid into segment controllers that can detect and isolate the faulted segment. Their proposed scheme was verified by simulations and hardware experiments.

In [116], a self-healing protection approach was proposed for shipboard MVDC applications. The authors focused not only on protection system's response to faults, but also on its response to failures in the measurement system and sensor delays. They developed an integrated validation and protection approach that proved to be sensitive to communication delays.

In [117], J. Jeon *et al.* proposed a solution for the problem of arcing during plugging/unplugging of home appliances when supplied with DC current. Their solution was based on adding a shunt diode/capacitor branch to the plug.

In [118], the utilization of the power electronic converters already included in the system to interrupt fault currents was discussed. It was shown that, by associating relays with the different converters and by adopting overcurrent-based protection schemes for these relays, the faults on DC systems can be quickly detected and localized. Moreover, a study to investigate the means to achieve fast and effective protection system operation at a minimum installation cost was presented in [119].

In [120], Mehl *et al.* held a comparison between electronic and mechanical breakers for 400 V DC systems. They found that electronic breakers outperform mechanical ones in terms of current limitation, rated current controllability, trip time curve adjustment, wire break indication, remote controllability and monitoring functions for current and voltage. However, due to the leakage current at the OFF state of electronic breakers, they do not provide complete physical isolation, which makes the process of protecting them against line induced voltage spikes challenging. In [121], the authors developed a DC hybrid circuit breaker with ultra-fast contact opening and Integrated Gate-Commutated Thyristors (IGCTs). Its hybrid structure comprises a high speed mechanical switch and bi-directional IGCT. The authors verified experimentally (on a 4 kA, 1.5 kV prototype) that their proposed hybrid breaker can significantly decrease the current interruption time.

A comprehensive overview on microgrids in general is presented in [122], the authors discussed recent trends in protection of DC microgrids. It was emphasized that commercially available protection devices can be used in the DC microgrid protection. This overcomes one of the major difficulties in DC microgrid deployment. The authors highlighted that there are some problems that may arise with the converter protection. They recommended a reliable protection scheme based on using the converter fault current and the DC-link voltage to solve the problem.

1.6   Standardization efforts

AC has been utilized for more than a century; therefore, AC standards are much more mature than those of DC systems. One of the impediments against global adoption of DC systems is the lack of the required standards, as we do not yet have a comprehensive standard for how to generate, transmit, distribute and use DC power. We do not even have a standard for DC voltage levels [11]. Such standards are quite essential to convey the beneficial experiences of experts of DC systems to help improve the reliability and efficiency of such systems. In addition, DC standards will put unified outlines for the design and installation methods; thereby, DC systems will become easier to install, and more trustworthy for entrepreneurs.

However, there are some related standards, which will be highlighted in this section. Reviewing those existing standards shows that, in 2004, IEEE power engineering society issued a revised version of IEEE standard 946 [123], which was first issued in 1992. This standard provides recommended practice for the design of lead acid batteries based DC auxiliary power systems for generating stations. It provides guidelines for the selection of the number of batteries, battery duty cycle, battery capacity and voltage level, as well as the battery charger. The output ripples level for the charger was restricted to 2% of the operating voltage without additional filtering and 30mV with extra filters. The standard briefly discusses the effect of grounding on the operation of DC auxiliary systems. It shows that the incautious grounding design can initiate operation of de-energized DC loads or prevent disconnecting energized loads. Important guidance for design, types, minimum attributes and protection of uninterruptable power supply (UPS) systems can be found in [124]. It covers UPS systems associated with lead acid or nickel cadmium batteries. Methods for short circuit analysis and models of DC system components are provided in [125]. The IEEE

1547 [126] standard provides a set of technical specifications for, and testing of, the DG interconnection to utility Electric Power Systems (EPS). For instance, the rules for islanding from the grid when there is a fault or reclosing when the fault is cleared, and the guidelines for power quality, such as the permissible harmonic distortion limits, are included.

Some standardization efforts in the subject of DC distribution power systems and standard key points are listed in [21]. National Electrical Code (NEC), or known as NFPA70 issued by National Fire Protection Association (NFPA), contains articles that regulate the utilization and installation of DC technologies. Outlines of the related articles are selected to be summarized here. More information and detailed provisions can be found in [127]. Regarding grounding of DC systems, which can be a challenging task, important guidelines and limitations were provided in NEC article 250, clauses160 through 169. Article 393 is a new article added in the 2014 edition [128] for low-voltage suspended ceiling power distribution systems. The growing interest in alternative energy sources and the proliferation of low-voltage, low-power devices (sensors, LED lighting, etc.), created a significant need for adequate language supporting the practical safeguarding of circuits and electrical equipment operating at 30 volts AC, or 60 volts DC. Although this new article is covering AC and DC installations, in terms of practicality, most of these systems are DC-based.

Article 625 covers the charging system of electric vehicles (EV). For the purpose of rating the EV charging equipment, three charging methods were defined as level 1, level 2 and level 3. For level 1, the maximum load is rated 1.4 kVA and the minimum overcurrent rating is 15 or 20 amp. In level 2, the maximum load is limited to 32 Amps and the minimum overcurrent rating is 40 Amps. Level 3 is a high speed method that

requires high power to charge the vehicle in a short period. Specifications for charging equipment are left to be specified by the equipment manufacturer.

Article 690 was added to the code in the 1984 edition and since then it has been subject to improvements and additions. This article covers photovoltaic (PV) systems, either standalone, interactive, with or without energy storage. Simplified guiding circuit schematics for different configurations of PV systems are provided. According to the code, bipolar PV systems are permitted, but monopole sub-arrays should be separated physically. It is required that the PV circuit conductor is selected to withstand- at least- 125 percent of the sum of parallel module rated short circuit currents and the overcurrent protection device (which is mandatory) should be rated at 156 percent of the same sum. Regarding the sizing of the inverter in a standalone system, the code doesn't require the inverter to be sized for the multiple loads to be simultaneously loaded to it. For grounding of PV systems involving both AC and DC systems, both grounding systems should be bonded together. The clauses of this article provide provisions and important guide lines for installation, arrangement, circuit requirements, wiring, protection and grounding of PV system.

Article 692, which covers on-premises fuel cell systems, was added to the code in the 2002 revision. This article requires providing suitable means to de-energize all current carrying conductors of a fuel cell based power source. In addition, bonding the DC grounding system to the AC grounding system (in case of using an AC/DC inverter) to a single common grounding electrode is also required.

Emerge Alliance [129], a group of over 100 companies, research labs and universities, works on promoting DC distribution, and developing DC standards. Up to the present, they have completed two standards; the standards confirm the importance of converting the existing AC power sources to DC power at a local distribution level

rather than at individual devices. The first one is the Occupied Space standard, which is a guide for the hybrid use of DC power in commercial buildings [130]. The standard defines a multifunctional low voltage DC power distribution infrastructure layer that interconnects sources of power to devices in the space, which draw the power. Moreover, the Standard defines the control systems necessary to monitor and control such devices and power sources. The second standard [131] focuses on the data and telecom centers domain; it defines low voltage DC power distribution requirements for use in such spaces. Specifically, the standard defines nominal 380VDC infrastructure requirements. It is mandatory to note that this standard is not intended to be a replacement of NEC.

MIL-STD-1399 is a military standard, section 390 defines the electrical interface requirements and constraints of DC equipment utilized in shipboard power systems [132]. For instance, it limits the permitted frequency tolerance to ±3% in 60 Hz system, while permitted frequency modulation (periodic frequency fluctuations) is limited to ±0.5%.

Current standardization efforts done by the International Telecom Union (ITU-T) and the European Telecom Standard Institute (ESTI) to accelerate the deployment of DC power systems with voltage less than 400 VDC in telecom and data centers are summarized in [133]. Various DC architectures used in data centers are discussed as well.

1.7 Existing DC distribution systems

There are several power systems that typically employ DC distribution. Some of these systems include the following:

1.7.1 Spacecraft

Spacecraft systems involve a large number of solar panels, DC-DC converters, batteries, battery chargers and DC loads [134], [135]. Hence, DC distribution is employed. A good example is the NASA International Space Station (ISS), requiring over 100 kW. The ISS is composed of two relatively independent DC systems with different voltage levels. The American system runs at 120 V and has solar power modules with a capacity of 76 kW. On the other hand, the Russian system is divided into two voltage levels: 120 V and 28 V components, and it has 29 kW solar power modules. The two systems are linked with bi-directional DC-DC converters to enable power transfer [136]-[137].

1.7.2 Data centers

Even though most of the existing data centers use AC distribution, some of them use DC. Duke Energy data center in Charlotte, NC, is employing a 380 VDC distribution system. Duke Energy and the Electric Power Research Institute (EPRI) prepared a study showing that the system uses 15 percent less energy than a typical AC system with double conversion UPS [138]. Data center of the University of California, San Diego is a 2.8 MW DC-based data center, which is powered through a large fuel cell stack. The data center was brought into service in August 2010 [24]. Green, which is one of the top ICT services providers in Switzerland, announced the opening of their 1MW DC-based data center in May, 2012. HP provided the IT equipment supporting DC input, commercial availability of DC enabled IT equipment is a stunning and encouraging step towards a wide deployment of DC data centers. Although DC distribution is not utilized in Google data centers, they managed to save $30/yr/server by optimizing the power path by eliminating two AC/DC conversion stages and bringing the batteries on the server rack.

1.7.3 Telecommunication

Telecommunication power systems, similar to data center power systems, are designed to transfer tremendous amounts of data. They also require high reliability and efficiency at a low cost. Therefore, 48 VDC distribution power system is widely used in telecommunication central offices. The reliability of that system is 99.999 percent [139]-[143].

1.7.4 Traction

DC distribution is used in traction power systems, such as trolleybuses, trams, and underground railways, mainly because DC motors are typically used in this application [144]-[147]. Even for traction systems that use induction motors (IM) [148], interfacing with DC supply is much easier and reduces conversion stages. Consequently, the system efficiency and controllability increase. Moreover, using DC distribution helps designers use a single conductor since the rails can be used as the return path for the current. DC distribution in traction power systems supplies the vehicles and other auxiliary loads on them. Their supply voltage ranges from 600 V to 1 kV [149], [150]. The load flow problem and description of DC traction system are discussed in [151].

1.7.5 Shipboard power systems

Normally, shipboard power systems involve a mechanical system for propulsion along with an electrical system for weapons, communication, navigation, hotel and auxiliary loads. However, in integrated power systems (IPS), these two energy systems are combined seeking an increased reliability during normal sailing and battle conditions. Adopting DC in ship power systems offers a set of attracting advantages as follows [152]: 1) elimination of large-heavy low frequency transformers, 2) simplified connection and disconnection of different types and sizes of generators, in other words,

eliminating the synchronization process, 3) elimination of reactive power flow, 4) reduction of fuel consumption because of the improvement in overall efficiency and reduction of unnecessary conversion stages. Another factor largely contributing to the fuel consumption reduction is the utilization of Variable Speed Drives (VSD), which operate the propulsion systems at their optimal efficiency point.

One of the architectures that are likely to be commonly used in IPS is the DC zonal distribution system [153]-[155], which assures several advantages other than the increased reliability, such as the facilitation of protection since the sources and loads are distributed into different zones each with its own converters. Medium voltage DC distribution is another architecture that is also extensively investigated to be implemented on future shipboard power systems [156], [157].

1.7.6 Experimental Setups

Initiated by the imperative need for more research and development of DC microgrids (or DC systems), a wide variety of studies have been carried out during the last couple of decades. Most of these studies were simulation-based. However, the recent interest of some of the funding agencies in DC systems elevated a portion of these studies towards hardware experimentation. A DC testing grid is presented by M. Albu *et al.* in [158]. The established grid is a laboratory scale microgrid to examine the operation of low-voltage (230 V) DC grids. Extended details about the system construction, hardware implementation and the developed LabVIEW monitoring application are provided.

A 15 kW Naval Combat Survivability (NCS) zonal DC distribution testbed setup was developed at Purdue University and the University of Missouri-Rolla with grants from the US Navy to examine the various aspects related to that system [159], [160].

Another example of practical experimental setups is the hybrid AC/DC smart grid power system established in Energy Systems Research Laboratory (ESRL) at Florida International University. The AC side is comprised of four generators and several bus and transmission line models. There are two DC microgrids interfaced to the AC network through bi-directional VSIs. The voltages of DC buses are 380 VDC and 325 VDC. Both microgrids contain PV emulators, fuel cell emulators, wind emulators and battery storage [161], [162].

In order to study the power quality issues associated with DC pulsed loads, an established microgrid testbed in University of Texas at Arlington (UTA) was presented in [163], the microgrid has a single phase 120V AC-60Hz AC bus and a 24 V DC bus with a total power of around 3-4 kW. The microgrid is considered low voltage-low power, but it involves various renewable energy sources, and it has the capability of performing AC studies as well. In the same work, power quality indicators are introduced to characterize the behavior of DC networks.

A test bed of 380V DC distribution system was presented in [7]. The system consists of a single phase bi-directional CLLC resonant converter for DC bus voltage control, dual active bridge converter for controlling the charging and discharging of the battery, and LLC resonant converter for interfacing a renewable energy simulator. Normal home appliances, such as TV, LED, washing machine, refrigerator, air conditioner and laptop, were used as loads. Some of these appliances were modified by removing the AC-DC rectifier and the power factor correction circuits to be operable with DC power. However, these modifications and implementation steps were not included in detail.

1.8 Problem statement

As an intermediate solution, hybrid AC/DC distribution systems or microgrids are proposed, which seems to be a viable solution in the foreseeable future [164],

[165], [166]. The migration from the traditional AC distribution systems to the modern AC/DC distribution systems impose new challenges to the system designer/ planner. In addition, the fierce competition among the electric utilities and service providers and the tight regulations applied by regulatory authorities, mandate operating the system with high efficiency, reliability and stability under different events and dynamic scenarios. In order to adequately address these challenges, new design methodologies are needed.

In the context of smart grids, it is proposed to cluster the distribution systems into microgrids (i.e. a hybrid AC/DC distribution system can be seen as two microgrids, one is AC and the other is DC, interlinked through a power electronic device). Therefore, the developed methods in this dissertation can be applied to hybrid AC/DC microgrids as well as hybrid distribution systems. Also, both terminologies are used interchangeably in the rest of this dissertation.

Due to the recent technological advancements in the different realms, new loads with harsh requirements are introduced to the power system. The loads of interest in this dissertation are the high demand loads and Pulsed Power Loads (PPL). PPL is defined as a load that demands frequent or regular repeated power input. A PPL is measured as the average power during the pulse interval minus the average power during the same interval immediately preceding the pulse. Examples of a PPL are sonar, radar, EM rail gun and Aircraft Launching System (ALS). Some studies showed that the amplitude of these pulsed loads are 120 MW and last for a duration of two seconds [167]. Furthermore, a large electric vehicle park with several cars requesting fast charging at the same time or an industrial facility are good examples of the high demand or pulsed loads. Since the PPLs require intermittent power with high rise/drop rates, a large departure in the system voltage and frequency from their nominal values can occur.

These fluctuations can cause violation of safe operation limits and disconnection of sensitive loads. If not mitigated, the consequences can be catastrophic from technical and financial points of views. Therefore, it is of high importance to consider the PPLs in the design stage and optimize the distribution architecture to safely accommodate them.

In order to mitigate the effects of the PLL and prevent the power oscillations from propagating either between the AC and DC sides of the network or to the mechanical parts of the generators, ES are used. Utilizing the ES gives rise to more questions: what is the optimal size of ES to be used? what is the best ES technology? where to allocate ES arrays in the network?. One of the goals of the research effort presented in this dissertation is to develop a design methodology to find answers to these questions and, hence, achieve the optimal design.

During the system operation, there's an imperative need to develop adequate management and control schemes for the ES to efficiently handle their charging/discharging under PPL. One of the goals of these schemes should be to preserve the health of the ES and prevent their fast degradation. Another goal is to expand the in-service time of the ES with a given size. In other words, increase the number of PPL cycles that can be served with the same size of ES. This can be done through flexible charging/discharging schemes.

One of the salient characteristics of Pulsed Power Loads is the high power to time ratio (i.e. they require high power in short time duration). This entails using an ES type with high power-to-energy ratio. This significantly limits the types of ES that can be used. For example, Lead-acid batteries are known with their high energy and low power densities; thus, they are not appropriate candidates for the PPL applications. Moreover, the high weight of Lead-acid batteries limits their adoption in weight sensitive

environments, such as ship power systems. Therefore, other alternatives should be explored and exploited, if possible. These alternatives can be flywheel, ultra-capacitors, Lithium-ion or Hybrid Energy Storage Systems (HESS), which are composed of a mixture of several ES technologies.

1.9   Research objectives

Hybridization of distribution systems, incorporation of heterogeneous mix of energy sources, and introducing Pulsed Power loads altogether add more complications and challenges to the design problem of distribution systems. In this dissertation, new ideas and solutions related to the design of hybrid AC/DC with PPLs and ES are provided. Furthermore, management schemes for ES are developed. The objectives of this dissertation can be summarized as the following:

−   Mathematically formulate and solve a multi-objective optimization problem based on Pareto concept to determine the following: 1) the optimal size and location of energy storage (ES) in the AC/DC distribution system, 2) optimal location of the PPLs 3) optimal point of common coupling (PCC) between the AC and DC sides of the network, and 4) optimal network connectivity. These parameters are to be optimized to design a distribution architecture that supply the PPLs, while fulfilling the safe operation constraints and the related standard limitations.

−   Achieve the optimal management of ES to serve a heavy PPL and mitigate its negative effects. It is aimed to extend the in-service time of the ES to serve as many PPL cycles as possible without SoH degradation. In other words, the Depth of Discharge (DoD) should be constrained to prevent irreversible damage in the ES.

−   Investigate the utilization of Hybrid Energy Storage Systems (HESS) in PPL applications. Then, develop the required control and management algorithms to handle the different charging/discharing requirements for the HESS elements.

- Investigate the performance and design a low speed Flywheel Energy Storage System (FESS) to be utilized in smoothing the PPL. Develop the required control and charging/discharging mechanisms for the FESS, it should be noticed that the charging of the FESS should be done seamlessly to avoid causing any disturbances in the network. Furthermore, the performance of the systems is anticipated to be stable while rapidly responding to the high di/dt demand of the PPL.

1.10 Original contribution and significance

In the past few years, the idea of utilizing the DC in distribution systems re-surfaced again. This is called by the research community "second war of currents", as the first war of currents took place early in the past century between Thomas Edison and Nikola Tesla. Unlike their AC counterparts, DC distribution systems suffer from lack of standards, solid and mature research and immature technology. Moreover, the recent technological advancements and modern life styles of most of the customers introduce new loads to the power distribution system, including, but not limited to, electric vehicles, LED lighting, IT equipment, even smart refrigerators, etc. Adding to these factors, the fierce competition among the electric utilities and the open market concepts obligate them to provide service with high power quality levels and reliability. Altogether, the aforementioned considerations, open the gate to a lot of questions about the optimal design of the DC distribution systems and their implementations, for example, what is the optimal DC bus voltage level? What is the optimal location of interfacing point between the DC system and the main AC grid? How to accommodate the newly introduced loads while still obligated to fulfill the standards? In order to answer these question, a comprehensive optimal design procedure is needed. Furthermore, applying smart grid concepts (e.g. Demand Side Management DSM) and

the ever increasing deployment of intermittent Renewable Energy Sources (RES) give rise for wider deployment of ES. Consequently, the placement and sizing of ES systems should be considered in the design process. Some of the researchers are tackling only certain aspects of the design process while the overarching approach for designing a hybrid AC/DC distribution system is still missing. In order to fill this gap, one of the contributions of this dissertation is to provide a systematic approach to optimally design the hybrid AC/DC distribution system.

The topic of hybrid distribution system is quite recent and not many research works can be found in the literature covering this topic comprehensively. Throughout this dissertation, advances and novel ideas are presented on different scales, from the component level to the system scale.

At the component level, the design, hardware implementation and performance evaluation of an advanced – low cost Modular Energy Storage regulator (MESR) to efficiently integrate ES to the DC bus are depicted. MESR provides a set of unique features: 1) It is capable of controlling each individual unit within a series/parallel array (i.e. each single unit can be treated, controlled and monitored separately from the others), 2) It is able to charge some units within an ES array while other units continue to serve the load, 3) Balance the SoC without the need for power electronic converters, and 4) It is able to electrically disconnect a unit and allow the operator to perform the required maintenance or replacement without affecting the performance of the whole array.

At the same level, a flywheel Energy Storage System (FESS) is designed and implemented to be used as an energy reservoir in PPL applications. The system was based on a separately excited DC machine and a bi-directional Buck-Boost converter as the driver to control the charging/discharging of the flywheel. Stable control loops

were designed to charge the FESS off the pulse and discharge on the pulse.

At the system level, a systematic approach to select the optimal design for hybrid AC/DC distribution architecture is presented. The approach is based on Pareto Optimality (PO) where multiple objectives are considered simultaneously. Variety of objectives (minimizing voltage and frequency deviations, minimizing the active power losses) are included in the multi-objective optimization problem. Several formulations of the problem are presented while considering two or three objectives at each time. The resultant optimal solutions are discussed and analyzed. The developed approach is generic and can be applied to most of the hybrid distribution systems using VSC. The approach is modified and applied to maritime power distribution systems. Since the weight is crucial in these systems, the weight of energy storage is considered as an additional objective function in the problem.

The original contribution and studies of this dissertation can be summarized as following:

- Mathematically formulate and solve a multi-objective optimization problem based on Pareto concept to achieve the optimal design of hybrid AC/DC distribution systems.

- The outcomes of the optimization problem are to determine the following: 1) the optimal size and location of energy storage (ES) in the AC/DC distribution system, 2) optimal location of the PPLs 3) optimal point of common coupling (PCC) between the AC and DC sides of the network, and 4) optimal network connectivity. These parameters are to be optimized to design a distribution architecture that supply the PPLs, while fulfilling the safe operation constraints and the related standard limitations.

- Different formulations of the problem are considered, the problem is solved while

considering four objectives, minimizing ΔV, Δf, power losses and ES weight.

- A trade-off analysis among the design elements was performed to achieve the balance between the weight and reliability the power system requirements.

- Design and experimentally investigate the performance of a low speed Flywheel Energy Storage System (FESS) to be utilized in smoothing the PPL. Develop the required control and charging/discharging mechanisms for the FESS.

- Achieve the optimal management of ES to serve heavy PPLs and mitigate its negative effects. It is aimed to extend the in-service time of the ES to serve as many PPL cycles as possible without SoH degradation.

- Investigate the utilization of Hybrid Energy Storage Systems (HESS) in PPL applications. Then, develop the required control and management algorithms to handle the different charging/discharing requirements for the HESS elements. "Rolling charging" algorithm is proposed and tested.

1.11 Dissertation organization

The dissertation is organized as follows:

A comparative study on the optimal allocation and combination of hybrid energy storage systems (HESSs) is presented in chapter 2. Based on the studies developed in chapter 2, an empirical study is conducted in chapter 3. This study is targeting the investigation of the effects of different pulsed load profiles and energy storage sizing change of the system's performance. Chapter 4 presents the design, development and hardware implementation of the Modular Energy Storage Regulator (MESR). The initial goal of developing the MESR is to achieve the optimal management of ES arrays under different operation conditions, especial attention was paid to pulsed power loads. Chapter 5 discusses the management of hybrid energy storage arrays with considering multiple pulsed loads. Moreover, in the same chapter, the concept of "rolling charging"

is introduced. In chapter 6, the formulation of a multi-objective optimization problem to determine the optimal size and type of energy storage in ship power systems is presented. A detailed analysis of the results is provided. Chapter 7 presents a more generalized multi-objective optimization problem to determine the optimal DC distribution architecture to accommodate pulsed power loads. The design and implementation of a low speed flywheel is presented in chapter 8. The experimental results of using the developed Flywheel Energy Storage System (FESS) in mitigating the pulsed loads are discussed as well. The hierarchical control of a cluster of DC microgrids is presented in chapter 9. Finally, the conclusions and recommendation for the future research are presented in chapter 10.

Chapter 2   A Comparative Study on the Optimal Combination and Allocation of Energy Storage Systems for Ship Power Systems

2.1   Introduction

Serious unique challenges are associated with the design and operation of Shipboard Power Systems (SPS). Since the system is not supported with a relatively stronger grid, it encounters faster dynamics due to the finite generation inertia and is more susceptible to disturbances. The system is physically confined, and hence the connecting cables have negligible impedance, which may cause instability issues among the different components of the system. Moreover, some particular loads draw very high currents for short periods of time in an intermittent fashion, such as Aircraft Launch Systems (ALS), Electromagnetic weapons and free electron lasers [168], [169]. On the other hand, the U.S. Navy is calling to develop more advanced technologies to improve productivity, maximize survivability and reduce the manning, overall cost and the weight. The latter is of high importance in these systems to allow shrinking the size and signature of the ship or elevating the platforms' capabilities by adding more logistics [153].

Around a decade before the writing of this dissertation, the flywheel was investigated to be introduced in future naval platforms [169]. This is due to the latest developments of relevant technologies, such as magnetic levitation, composite materials, frictionless, vacuum-encased machinery and power electronic switching. It is found that the flywheel performs as a reliable energy storage solution for short-term applications, ranging from a few tens of milli-seconds to a few minutes. This property makes it suitable for utilization with pulsed loads in SPS. Unlike batteries and ultra-capacitors, the flywheel has less fire hazards because it is completely chemical free and its state-of charge is always easy to be known by measuring its rotational velocity [170].

Moreover, the flywheel offers, with the adequate maintenance, unlimited charging/discharging cycles, since its performance doesn't degrade over time. Another key advantage of the flywheel is that it has the capability to work under a wide range of temperatures. This advantage is shared with the ultra-capacitors while most of the batteries - especially Lithium-Ion - are preferred to work within a narrow temperature range [171].

The aforementioned reasons have made it attractive and feasible to utilize flywheels in a harsh environment like that of the shipboards. However, it can't be said that the flywheel can be an explicit replacement for other energy storage types. Major advantages offered by the ultra-capacitor make it a viable energy storage solution. The ultra-capacitor offers very high power density, relatively high energy density and low losses. Batteries with their reliable performance, long history in the market, significantly mature technology and lower cost are an effective and trustworthy solution.

This chapter is mainly divided in two parts. In the first one, the utilization of two or more energy storage technologies in Ship Power Systems (SPS) to mitigate the Pulsed Power Load (PPL), is investigated. In the second part, the allocation and performance of dispersed flywheels in the SPS is optimized.

When dealing with Energy Storage Systems (ESSs) in SPS, an inevitable question arises to be answered: what's the optimal combination/ size of this system? This research work presents a serious trial to answer such a crucial question through performing a comparative study. This comparative study is comprehensive in a sense that it is covering all the practically feasible combinations. The used criterion to determine the optimal combination is minimizing the voltage and frequency fluctuations (ΔV and ΔF) consequent to the occurrence of the pulsed load. This study

is prepared in compliance with MIL-STD-1399 sections 300B and 390 regarding the allowed frequency and voltage tolerances. MIL-STD-1399 is a military interface standard for shipboard systems establishing and defining electrical interface characteristics for shipboard equipment utilizing AC power (section 300B) and DC power (Section 390) [172], [132]. It should be highlighted, that this study serves as an introductory for the rigorous multi-objective optimization problem formulated in chapter 6 and 7. It gives an accurate indication to select the constrained variables and their limitations. Additionally, it shows the parameters that effectively gauge the system's performance and stability. Therefore, these parameters are included as objective functions.

2.2   System Understudy

In order to determine the optimal combination of the hybrid energy storage system to minimize the impacts of the pulsed loads, a notional model for a ship power system is prepared using the DIgSILENT PowerFactory software package. Figure 2.1 shows the system under study. The system is simulated with a reduced scale for the purpose of simplification of comparisons and future implementation on the laboratory-based power system test-bed. Once the concept is verified, it can be extended easily to larger systems. The system consists of 4 synchronous generator units; two are main generators (MTG) with rated power of 13.8 kVA for each and two are auxiliary ones (ATG) with 10.4 kVA for each. Two Permanent Magnet motors controlled by Pulse Width Modulated (PWM) drives are representing the propulsion of the ship. A 0.318 kV DC bus is connected to the system through a controlled PWM converter and an uncontrolled rectifier [60]. There's a continuous, normal, resistive load of 10 kW connected to the DC bus to represent the hotel loads. In addition, there's a pulsed load of an amplitude of 30 kW connected to the same DC bus. The train of pulses is considered to be

consisting of four pulses with a cycle time period of 5 seconds and the duty ratio is 10%. Another pulsed load is connected to the AC side on Bus 1, the same bus of the main generator (MTG1). The amplitude of the three-phase AC pulsed load is 15 kW and it has the same frequency and duty cycle of the DC pulsed load. A flywheel, ultra-capacitor and battery are provided on the DC side to support the pulsed load. The capacity and connection status of each element is altered depending on the studied case, as will be explained later.
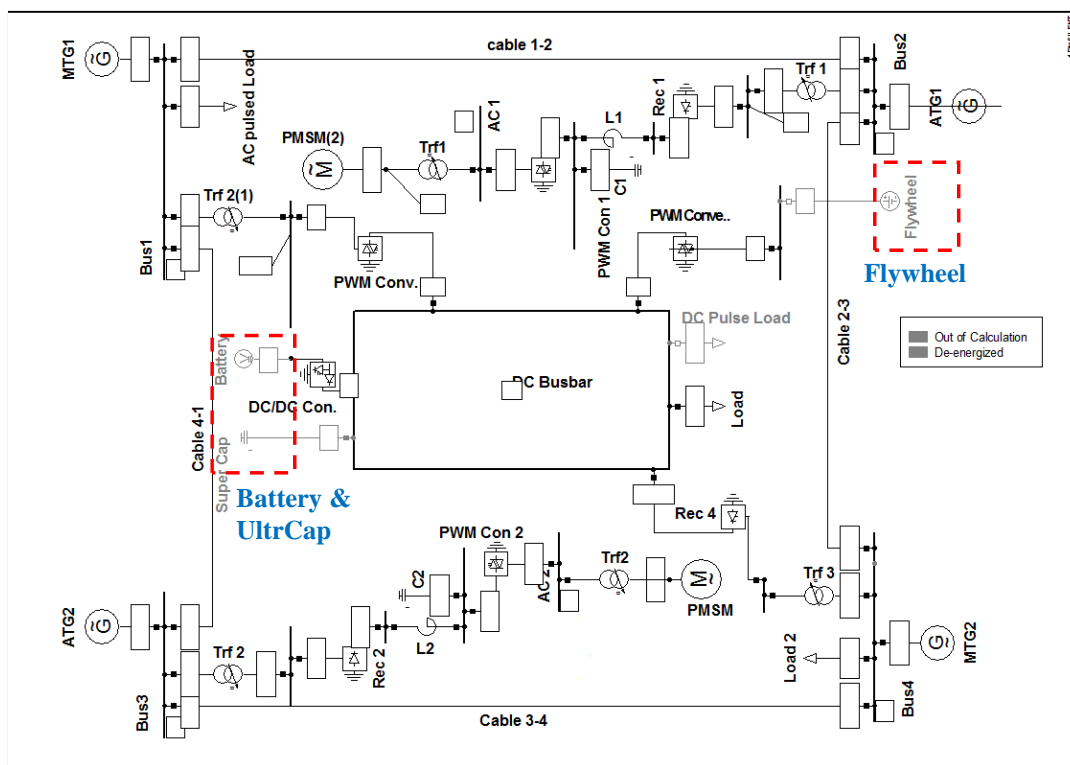
Figure 2.1 Configuration of system understudy.
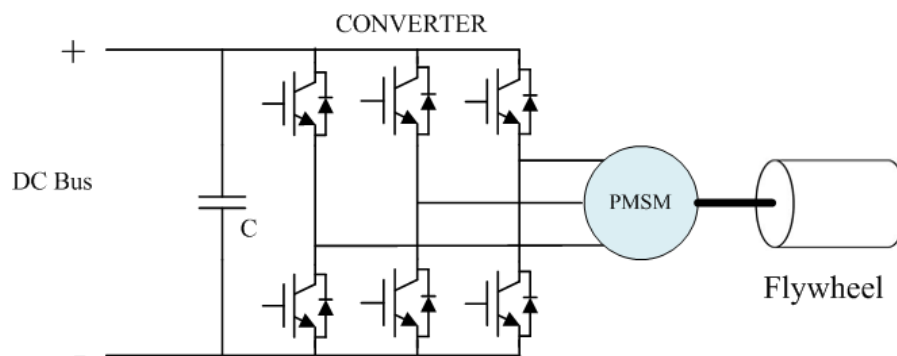
Figure 2.2 Integration of the flywheel to DC bus.

Permanent Magnet Synchronous Machine (PMSM) is selected in this work to be coupled to the flywheel, as it meets the major requirements for flywheel machine. These requirements are: high power-to-mass ratio, high efficiency, simple mechanical construction and absence of moving contacts, which make it suitable for high-speed operation [173]. As shown in Figure 2.2, a single stage three-phase, six step, IGBT-based converter is used to interface the flywheel machine to the DC bus. The battery is interfaced to the DC bus through a Buck-Boost DC/DC converter, as shown in Figure 2.1. The battery type is Lithium-ion and the nominal bank terminal voltage is 120 V. The ultra-capacitor is connected directly to the DC bus [174].

2.3   CASE STUDIES AND DISCUSSION

2.3.1   With DC pulsed load

In this case, the DC pulsed load is connected while the AC one is not. Several case studies are performed. For the sake of space, only the major five cases with the best results are shown. These five cases comprise five different combinations:

1) Ultra-capacitor, battery and 20 kWh flywheel.

2) Ultra-capacitor and 20 kWh flywheel (no battery).

3) Ultra-capacitor and battery (no flywheel).

4) Battery and 20 kWh flywheel (no ultra-capacitor).

5) Battery and 25 kWh flywheel (no ultra-capacitor).

For all cases, the capacitance of the ultra-capacitor is fixed at 0.8 F and the capacity of the battery array is 10 kWh. These sizes are determined through several other cases that aren't included here due to the space limitations. It is worthy to mention that the sizes of all elements are minimized to reduce the weight, cost and size. The objective during the sizing was to keep voltage and frequency within the envelopes defined by

40

the corresponding MIL-Stds.

Simulation results are shown in Figure 2.3, Figure 2.4 and Figure 2.5 (a) through (f). Letter A is used to identify the cases of this section (with DC pulsed load only). The figures are comparing all the cases. The systems' parameters used for comparison are: the AC voltage waveforms for the four main AC buses, the DC bus voltage and frequency. In Figure 2.3, the system performance in each case is compared. Figures (a) and (b) are showing the AC voltages. It can be seen that the system in case A.1 experiences less voltage oscillations on the AC buses. These voltage fluctuations propagated to the DC bus, as shown in figures (c) and (d). Therefore, the system in case A.1 (with an ultra-capacitor, battery and 20 kWh flywheel) suffers from less fluctuations if compared to case A.2. From Figure 2.3 (c), the minimum and maximum DC voltages are 0.963 p.u and 1.024 p.u., respectively, which are still within the allowed limits by the standards. High-frequency oscillations are shown in Figure 2.3 (f). These oscillations remain after the end of the pulse train. These high-frequency oscillations violate the restrictions stated in MIL-Std 1399 section 300B [172], as the allowed frequency modulation is ±0.5% which corresponds ±0.3 Hz in 60Hz systems. In this case, the installed energy storage systems are an ultra-capacitor and a 20 kWh flywheel. This shows the de-stabilization effect of the absence of the battery. On the other hand, less frequency oscillations are detected in case A.1, as in Figure 2.3 (e).

The least voltage and frequency oscillations are provided through integrating the battery with the flywheel, which are cases A.4 and A.5. As shown in Figure 2.4 (b), the AC voltage departure from the nominal value is within the safe limits. Upon the energization of the PPL, the voltage drops to 0.961 p.u. then rises to 1.034 upon the de-energization of the PPL. The voltage drop/rise on the DC side are around similar values to that of the AC side. Generally, it can be seen that the voltage and frequency

41

fluctuations are minimized and within the specified safe limits.

(a)

(b)

42
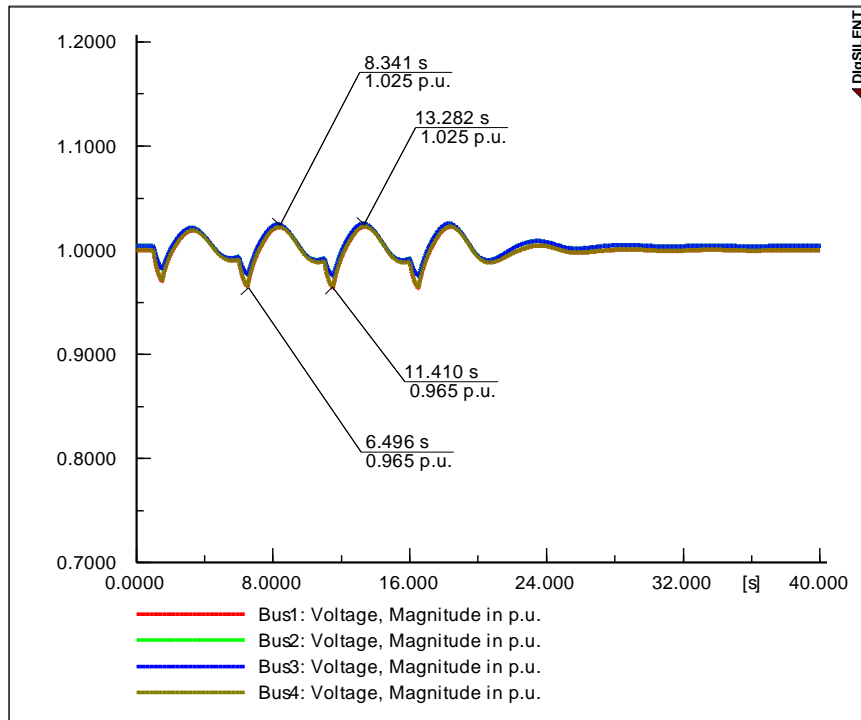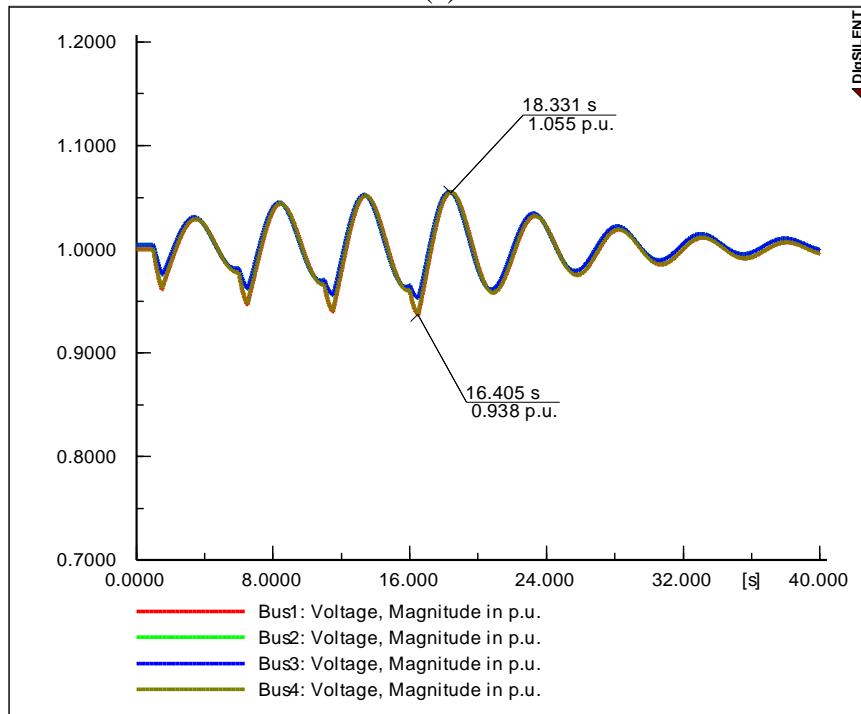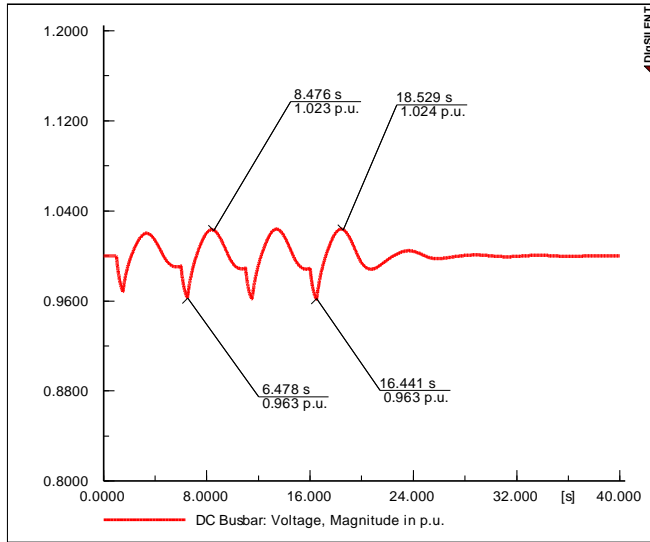
(c)
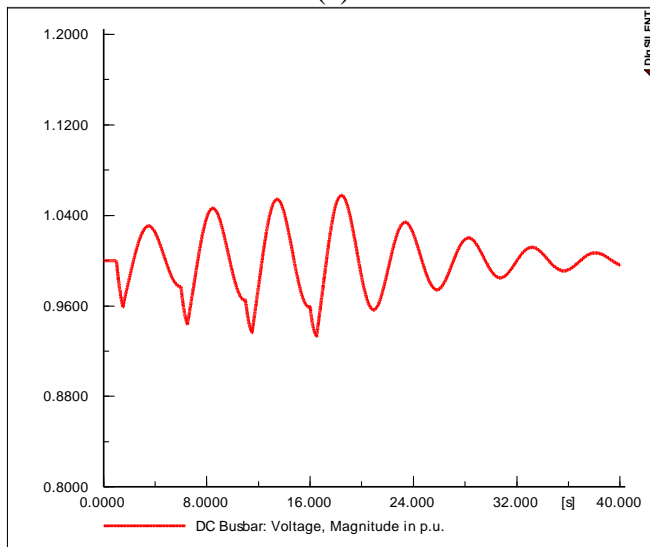
(d)
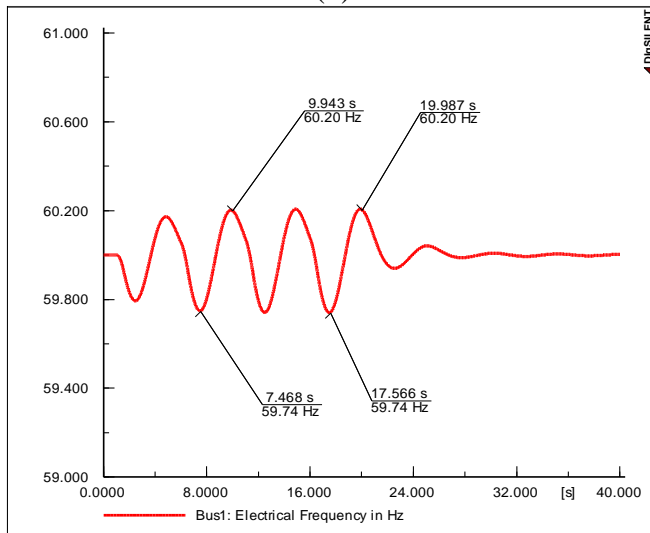
(e)
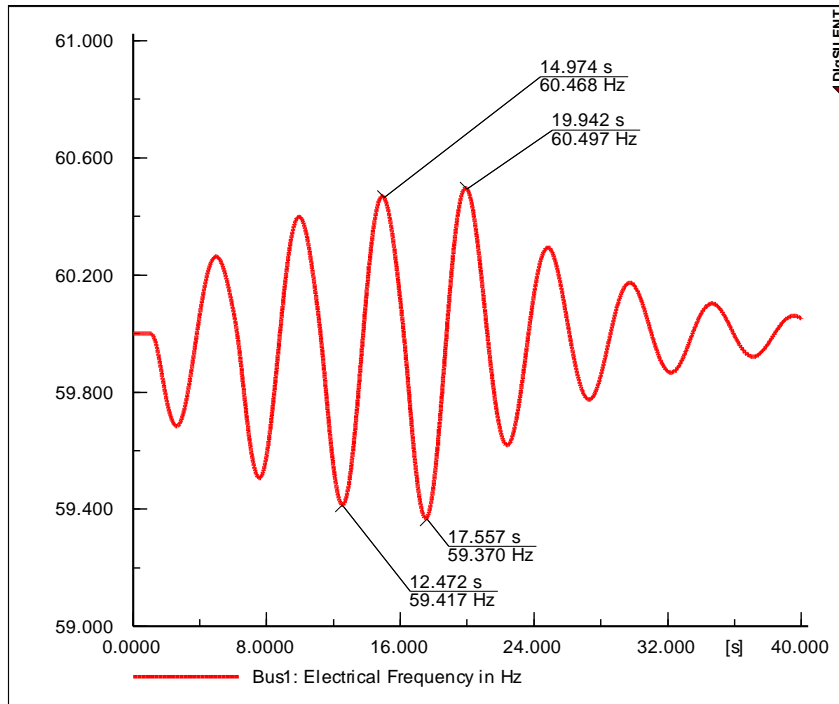
(f)

Figure 2.3 Performance analysis for cases A.1 and A.2.
(a) AC voltages of case A.1, (b) AC voltages of case A.2, (c) DC bus voltage of case A.1, (d) DC bus voltage of case A.2, (e) Frequency of case A.1, and (f) Frequency of case A.2.

(a)

(b)

(c)

(d)

45
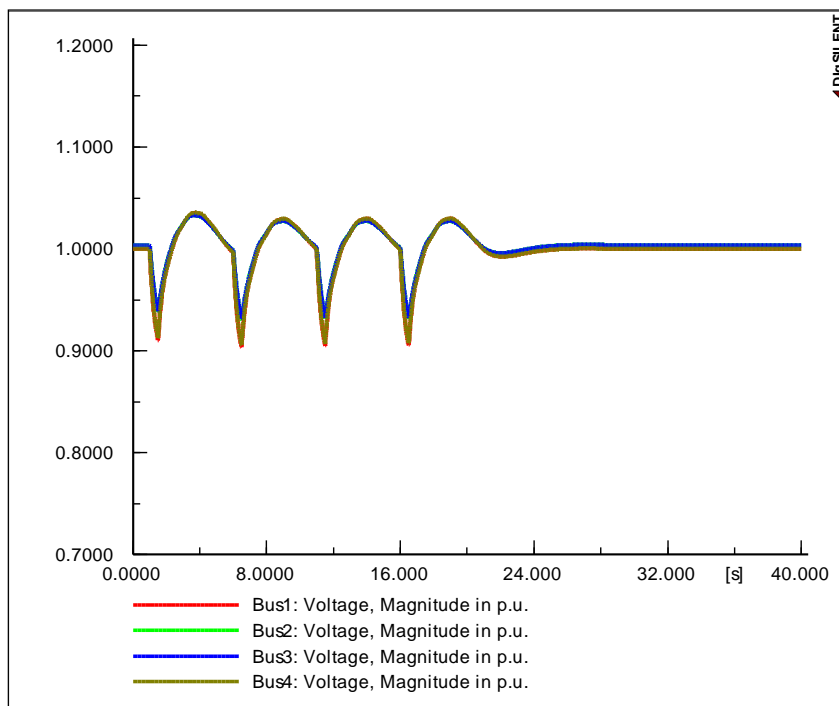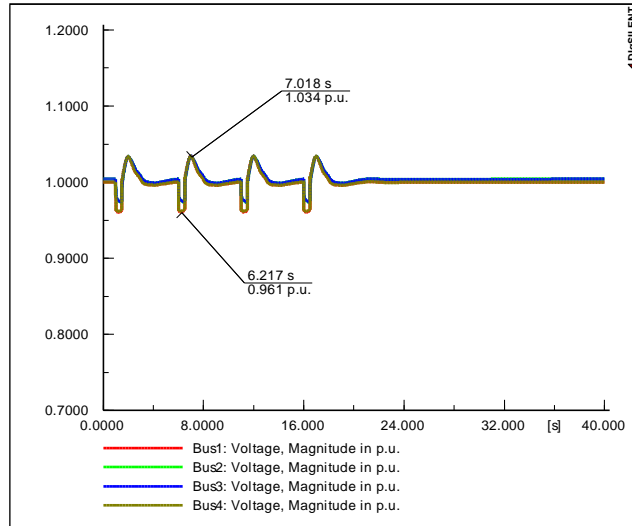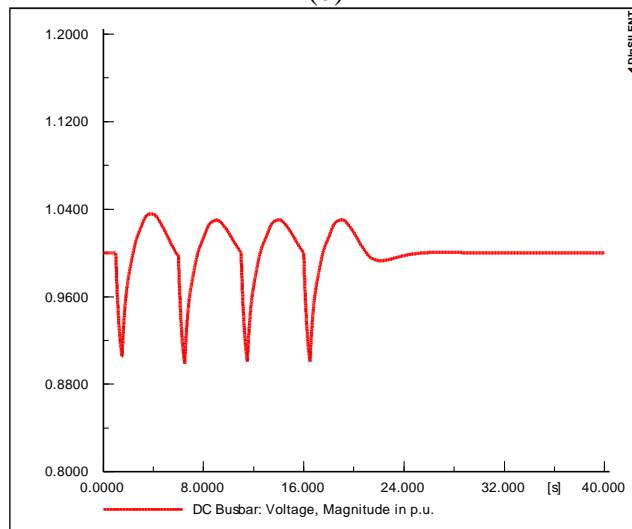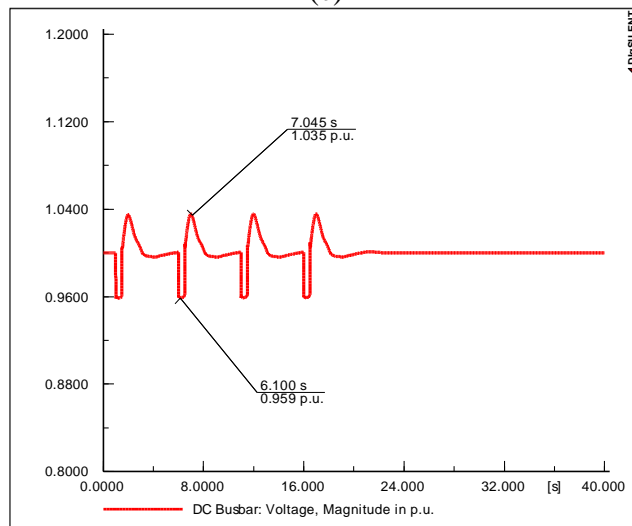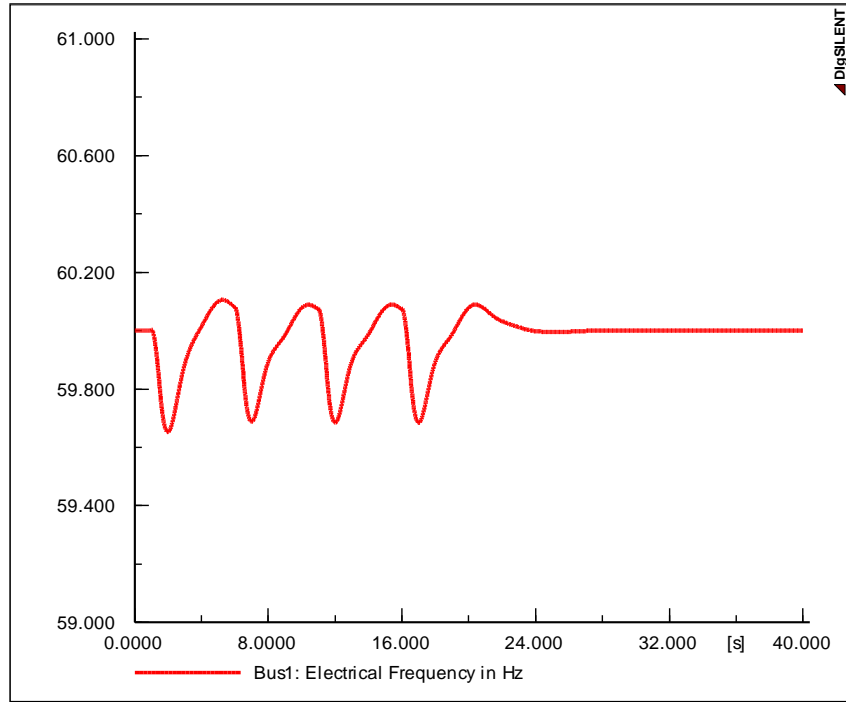
(e)
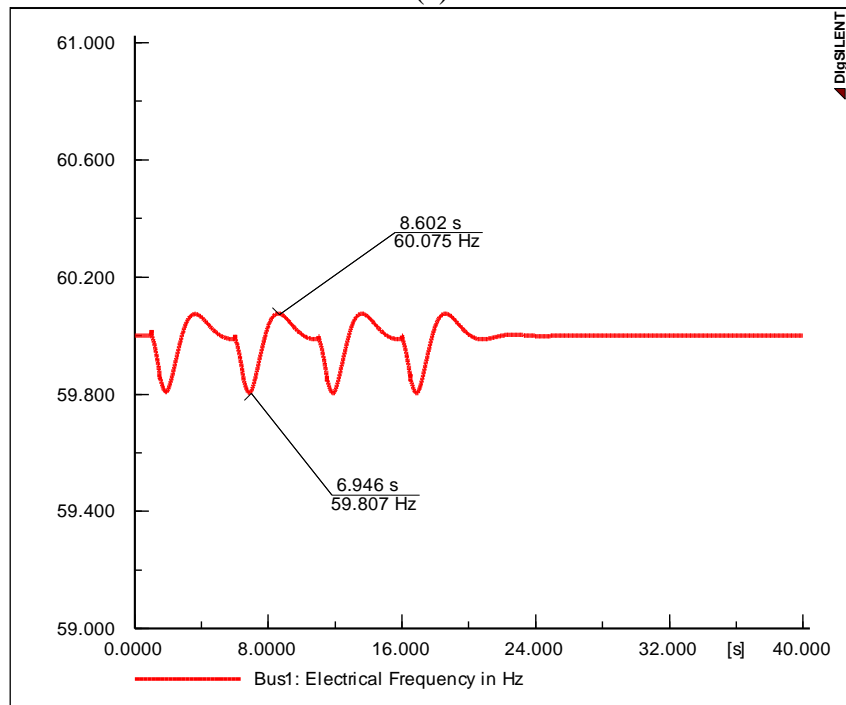
(f)

Figure 2.4 Performance analysis for cases A.3 and A.4.
(a) AC voltages of case A.3, (b) AC voltages of case A.4, (c) DC bus voltage of
case A.3, (d) DC bus voltage of case A.4, (e) Frequency of case A.3, and (f)
Frequency of case A.4.
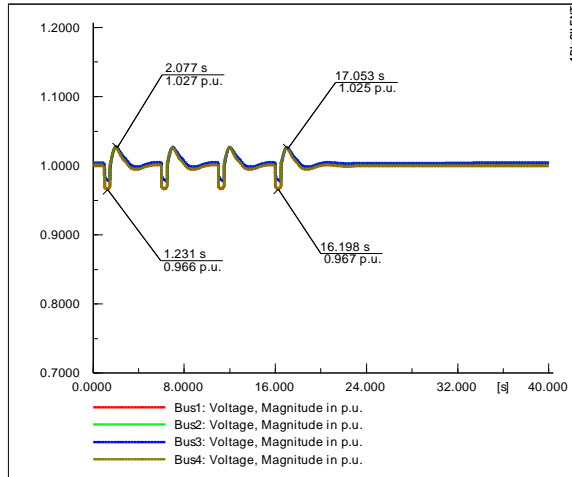
(a)
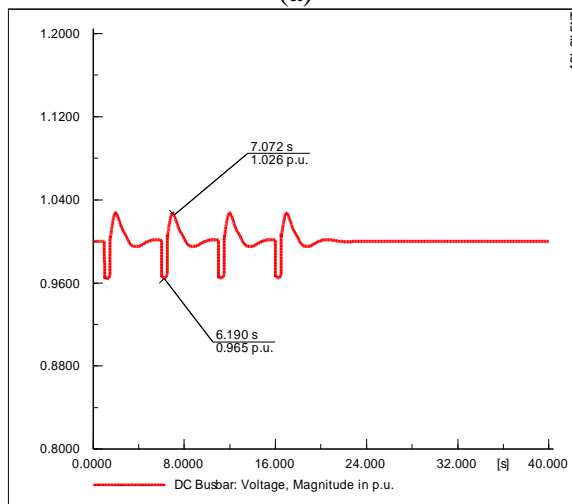
(b)
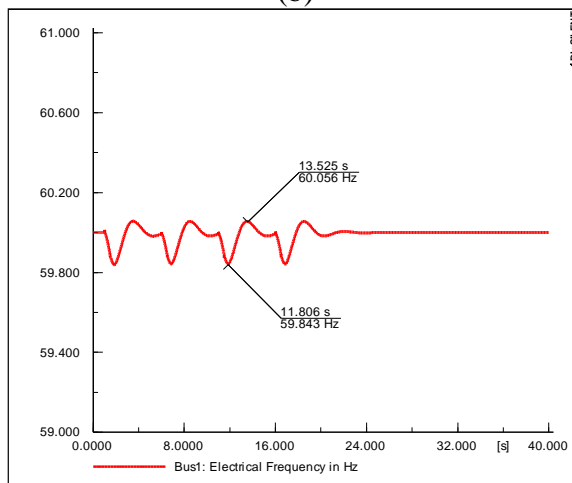
(c)

Figure 2.5 Performance analysis for case A.5 (a) AC voltages, (b) DC bus voltage, and (c) Frequency.

47

When comparing cases A.4 and A.5, it is noticed in case A.5, where the energy capacity of the flywheel is increased from 20 kWh to 25 kWh, that no noticeable improvement is achieved. This is due to the fact that the capacity of the flywheel is enough to supply the energy demanded by the load, therefore any further over-sizing will not be utilized. The detailed sizing of the flywheel by an analytical method is conducted in one of the following chapters.

2.3.2 With AC and DC Pulsed Loads

In this case, an AC pulsed load with 15 kW amplitude is connected to Bus 1. The AC and DC pulsed load profile is shown in Figure 2.6. Among the previous five cases, the three combinations with the best results are selected to be simulated with the AC pulsed load added. These combinations are:

1) Ultra-capacitor, battery and 20 kWh flywheel.

2) Battery and 20 kWh flywheel (no ultra-capacitor).

3) Battery and 25 kWh flywheel (no ultra-capacitor).
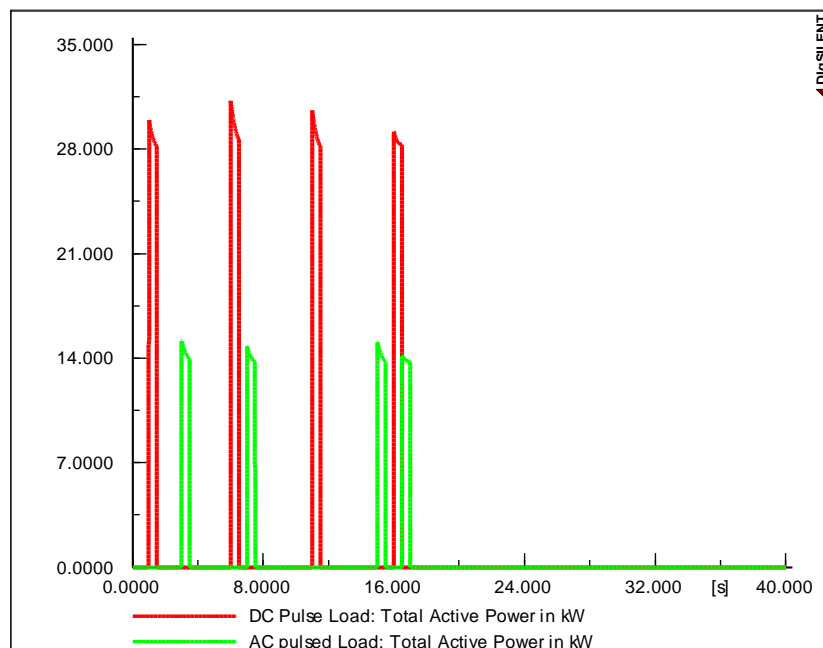
Figure 2.6 Pulsed loads profile.

The simulation results are shown in Figure 2.7 and Figure 2.8; Figure 2.7 (a) through (f) are presenting a comparison between the system performance in case B.1 and B.2. By comparing the results, it can be seen that the first combination (ultra-capacitor+ battery+ flywheel) is giving the least voltage and frequency fluctuations. The minimum frequency is 59.682 Hz, the minimum and maximum DC voltage points are 0.956 p.u. and 1.04 p.u., respectively. On the other hand, the second case is experiencing a wider range of fluctuations; it can be realized from Figure 2.7 (d) that the voltage is dropping to 0.94 p.u. then rises drastically to 1.075 p.u at second 16. Moreover, looking at Figure 2.7 (f) reveals that the frequency drops sharply to 59.622 Hz. This behavior can be explained by looking at Figure 2.6. It is noted that there are three consequent pulses that occurred around second 16 (AC-DC-AC), which introduces a very tough situation to the system. This kind of situation requires a reliable energy storage system to supply the required energy and maintain the system's operation. The energy stored in combination 3.B (battery + flywheel) is not enough to maintain the system's operation points within the required boundaries. Hence, more energy has to be supplied by the generators, causing more frequency and voltage fluctuations.

Accordingly, the size of the flywheel is increased from 20 kWh to 25 kWh to accommodate more energy, while the size of the battery is kept fixed. Results are shown in Figure 2.8. This case yields a response similar to that of the previous case (B.2), however they are shifted as the voltage and frequency are fluctuating in a narrower range. The minimum frequency is 59.69 Hz, the minimum DC voltage is 0.945 p.u. and the maximum is 1.056 p.u. Although the voltage and frequency are slightly out of the required range, the net weight and size reduction of the hybrid system resulting from removing the ultra-capacitor bank and increasing the flywheel size would make it an

acceptable and feasible solution. It is clear that the increase in weight due to increasing the size of the flywheel will be less than the weight of the 0.8 F ultra-capacitor that is removed. Figure 2.9 shows the power flow between the DC and AC sides through the power electronic converters. It can be seen that during the ON period of the AC pulsed load, the amount of energy transferred from the energy storage installed on the DC side to the AC side is very high. This can be resolved by installing energy storage on the AC side to supply the energy demand of the pulsed load locally, which is investigated in the following sections of this chapter.

(a)

(b)

(c)

(d)

(e)

51
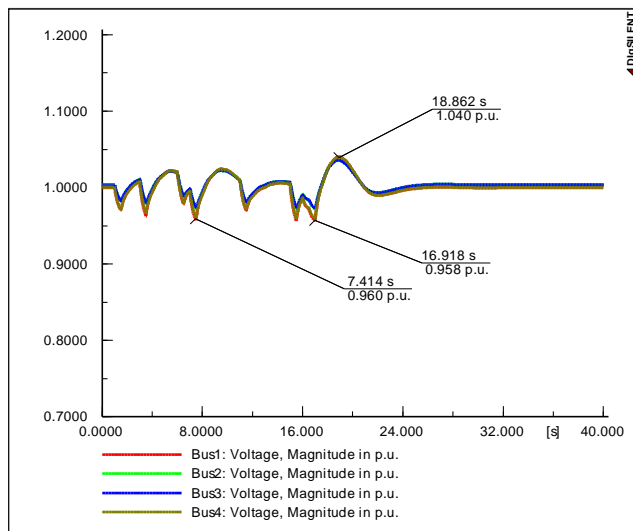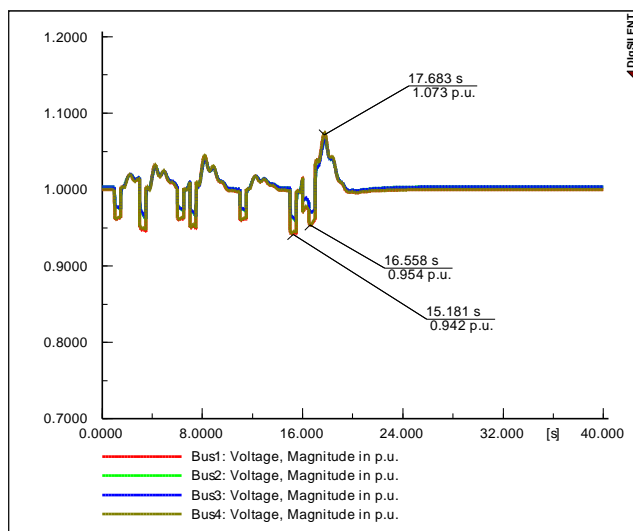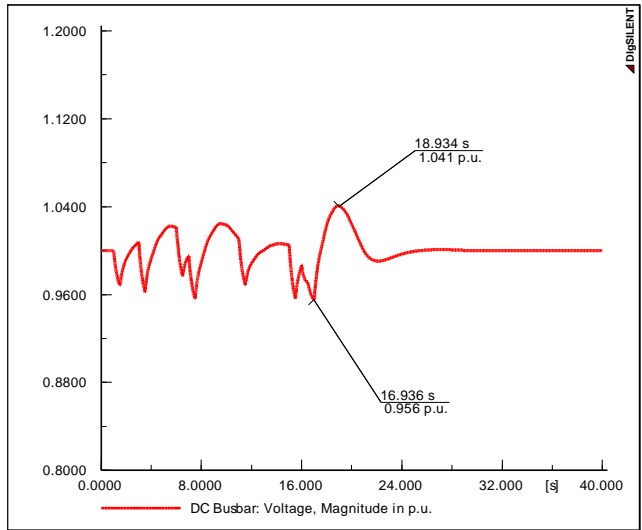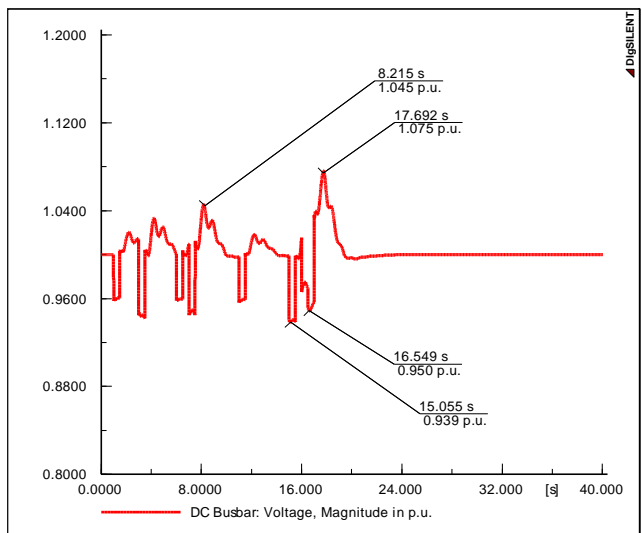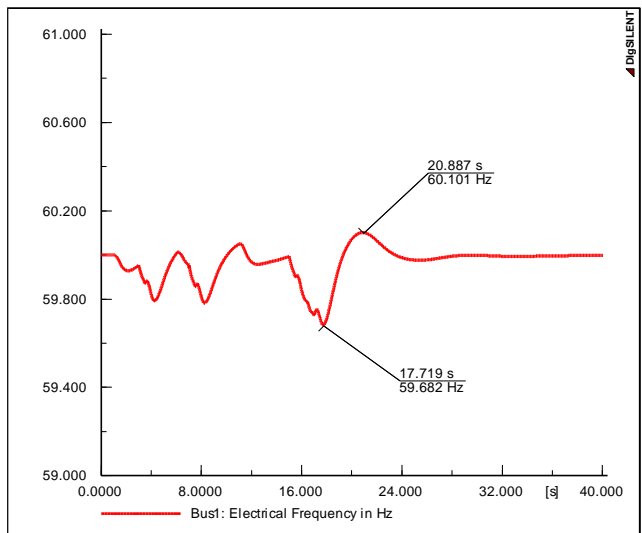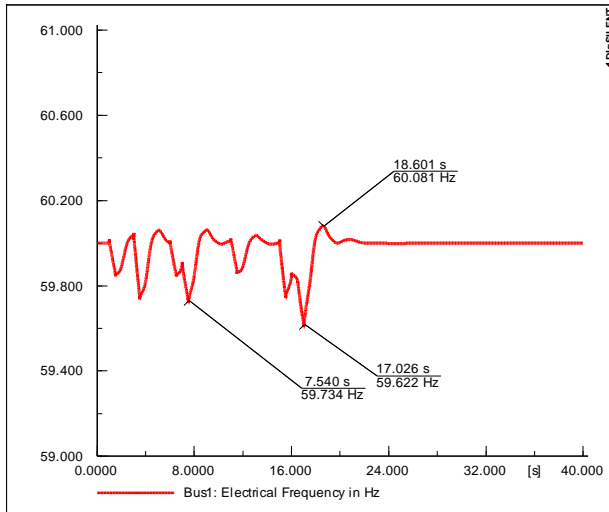
(f)

Figure 2.7 Performance analysis for cases B.1 and B.2.
(a) AC voltages of case B.1, (b) AC voltages of case B.2, (c) DC bus voltage of
case B.1, (d) DC bus voltage of case B.2, (e) Frequency of case B.1, and (f)
Frequency of case B.2.
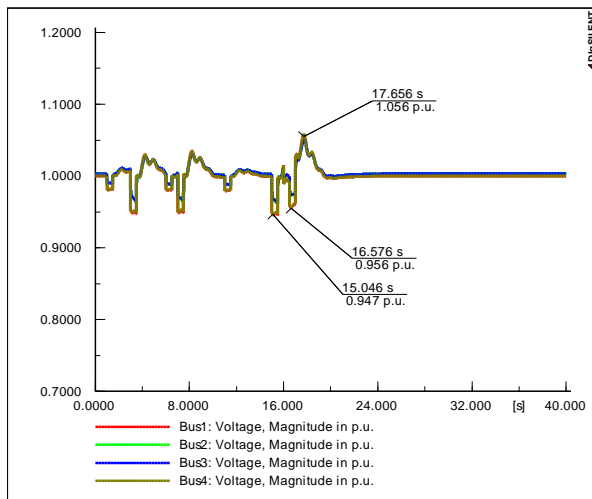
(a)
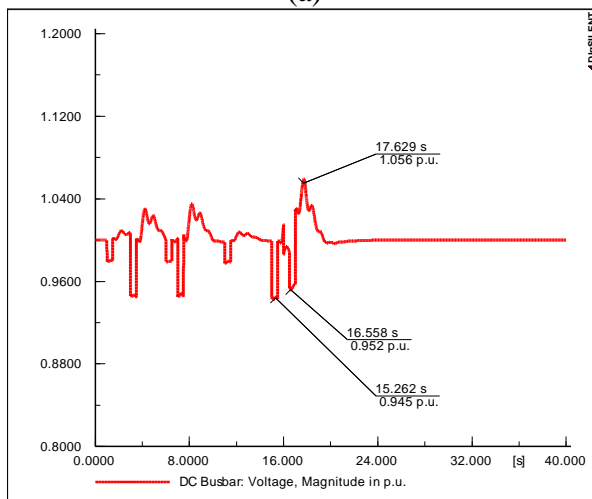
(b)
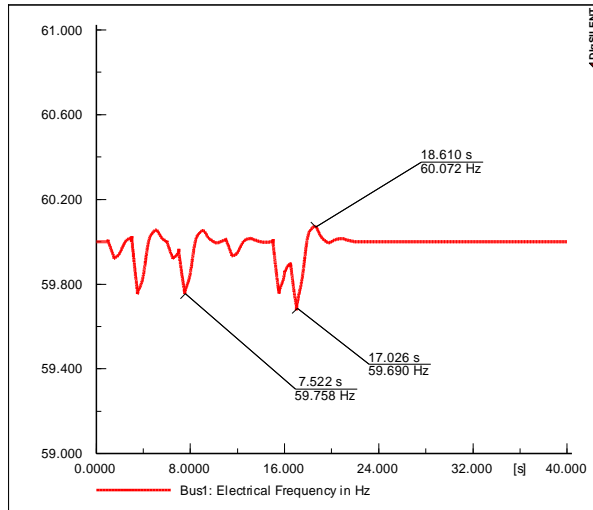
(c)

Figure 2.8 Performance analysis for case B.3 (a) AC voltages, (b) DC bus voltage, and (c) Frequency.
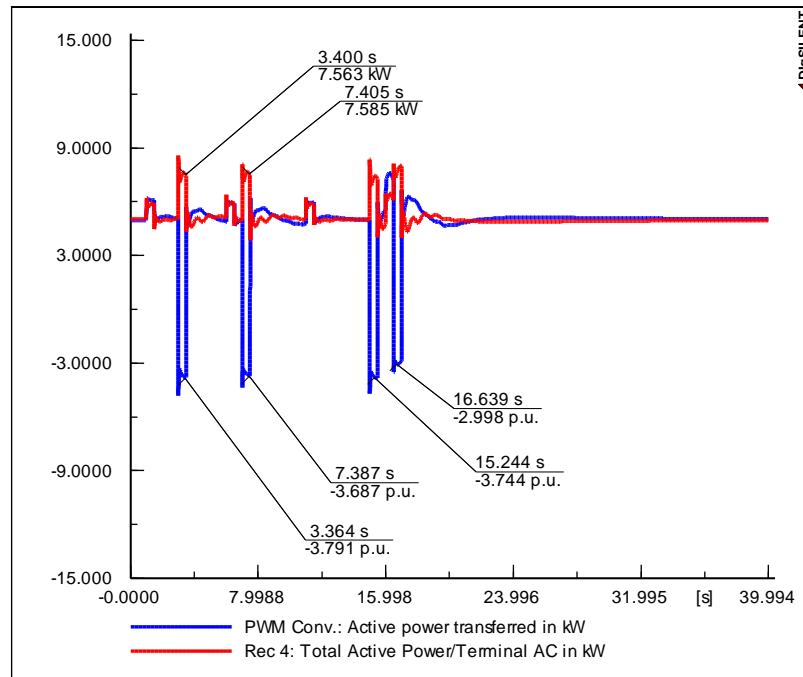
Figure 2.9 Power exchange between DC and AC sides.

2.4   Distributed Flywheel Energy Storage Systems (FESS)

As mentioned earlier in this chapter, Flywheel Energy Storage System (FESS) has attracted recent research attention in several applications. The reason for this recent research interest is due to the latest developments of relevant technology, such as magnetic levitation, composite materials, low-loss machinery and power electronic

switch, particularly in high-power insulated-gate bipolar transistors (IGBTs) and field-effect transistors (FETs) [175]. It was found that the flywheel is a very reliable solution for short-term energy storage. It can provide high power for short periods, which makes it an ideal candidate to be used in PPL applications.

Many practical examples prove that it is possible and feasible to construct flywheels strong enough to operate reliably at high speed with achieving higher efficiency. The University of Texas at Austin has subjected a composite flywheel spinning at about 48,000 r/min to more than 90,000 charge-discharge cycles with no loss of functionality (which is very high if compared to batteries). Another example is the FESS installed in an AMD semiconductor fabrication facility in Dresden, Germany. The system can supply or absorb 5 MW for 5 seconds—that is, it can store 25 MJ. In addition, FESS is very promising to be used on the International Space Station as NASA estimates that more than US $200 million will be saved if flywheels replace the first generation of space station batteries [176][177].

One of the points that should be taken into consideration is the selection of the motor/generator combined with the flywheel. High-speed operation and high reliability requirements limit the available selections to brushless and permanent magnet (PM) machines. PM machines offer higher efficiency, smaller size for the same rating, lower rotor losses and lower winding inductances, which make them more suitable for rapid energy transfer in flywheel applications [168], [173][178], [179].

FESS operates in three operating conditions: charge, stand-by and discharge. In the charging mode, the power grid injects energy into the flywheel through a bi-directional converter (given that it is integrated to a DC bus). When the flywheel reaches to the maximum stored kinetic energy limit, the FESS moves into the standby mode, in which the charging current is kept small to maintain its charge and spinning at the rated speed.

If a power outage occurs, the FESS switches into the discharge mode and the Permanent Magnet Synchronous Machine (PMSM) acts as a generator to provide energy to loads through a bi-directional power converter. When the power grid recovers from failure, the FESS re-enters the charge mode and is ready to handle the next event.

2.5 Case Studies and Discussion on FESS Allocation

The same model of the hybrid AC/DC SPS shown in Figure 2.1 is re-used for these case studies, but with some modifications. A schematic diagram for the modified system is depicted in Figure 2.10. The amplitude of the PPL is increased to be 35 kW. A 0.75 F ultra-capacitor is provided on the DC side to support the pulsed load. Three flywheels are added to the AC side of the system at the highlighted locations in Figure 2.10. Extended studies were carried out to investigate the optimum distribution and locations of flywheels over the system. The 3 locations of the 3 flywheels are selected as follows:

- Flywheel 1: is installed on the low-voltage side of the transformer connected to the main generator 2 (MTG2).

- Flywheel 2: is installed on the low-voltage side of the transformer connected to the main generator (MTG1). Flywheels 1 and 2 are responsible for supporting the power flow for the pulsed load on the DC bus.

- Flywheel 3: is installed on an intermediate location between generators 1 and 2, which is the bus of the auxiliary generator 2.

The capacity of each flywheel is varied and the connection status of the ultra-capacitor is altered depending on the studied case, as will be explained later.

Different power electronics topologies are adopted in the literature to integrate the FESS to the system. One of the most widely and successfully used is the back-to-back three-phase, six step, IGBT-based converter, shown in Figure 2.11. In this study, the

same interfacing scheme will be used. In this topology, during the motor mode when the flywheel is charging, the grid-side converter operates as a rectifier and the machine-side one operates as an inverter. During a power outage (generator mode), the machine-side converter acts as a controlled rectifier and the grid-side one works as an inverter [180].
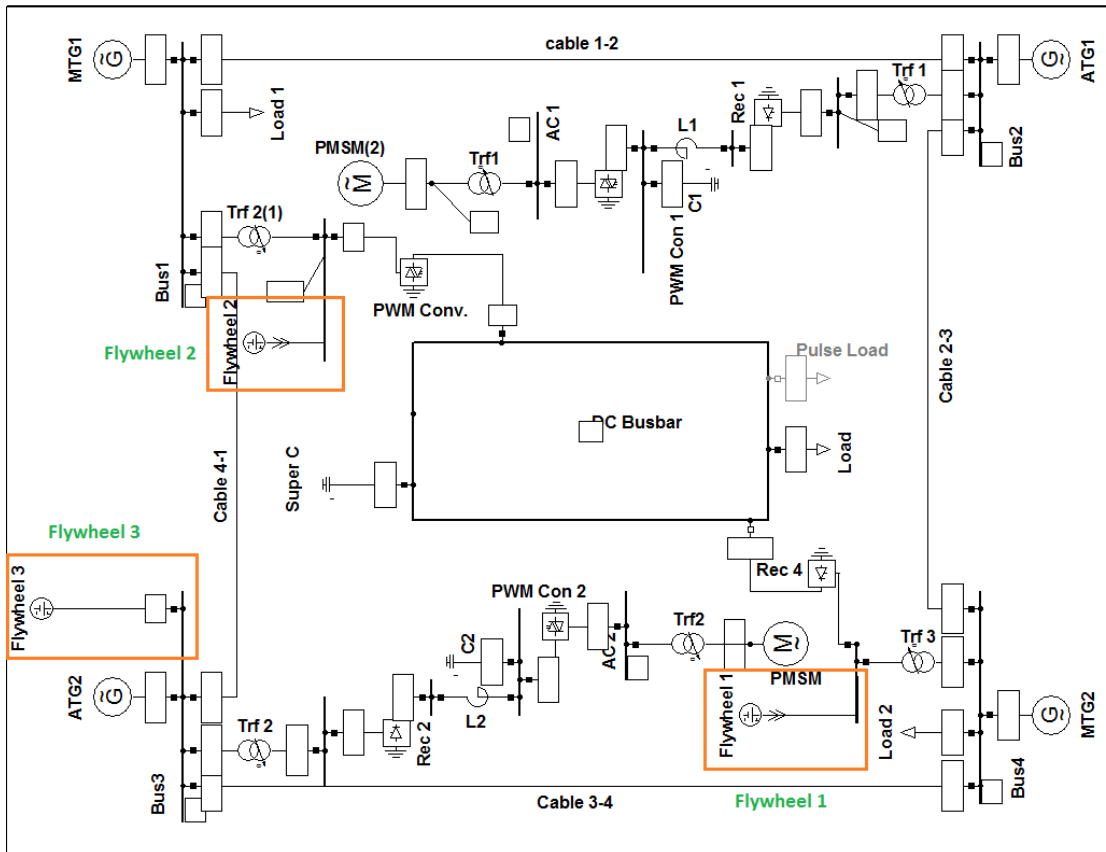
Figure 2.10 Configuration of system understudy.
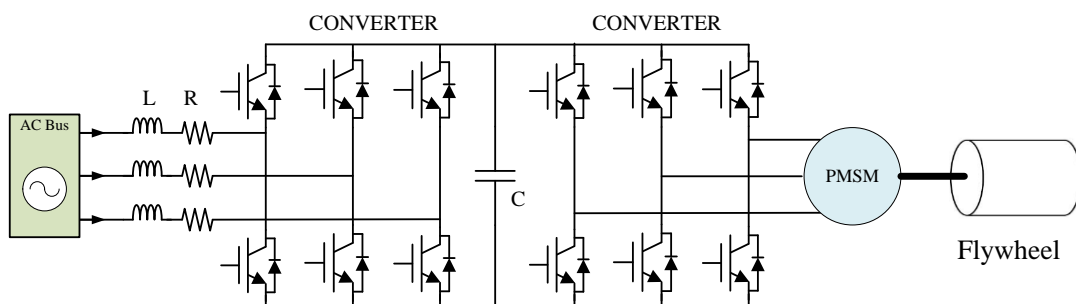
Figure 2.11 Integration of flywheel through back to back six step converter.

56

2.5.1   Case 1 (with Ultra capacitor on the DC side)

To make the study more realistic, clear and to compare the performance of the system with and without adding FESS, the system was simulated without the FESS first. It was found that with the first pulse of the load, the system is overloaded up to the maximum limits, at which the protection operate and tripped the generators. The super-capacitor (SC) discharged very rapidly, however it didn't provide enough energy support to sustain the system operation. Figure 2.12 shows tripping of the 4 generators representing a failure of the whole system.
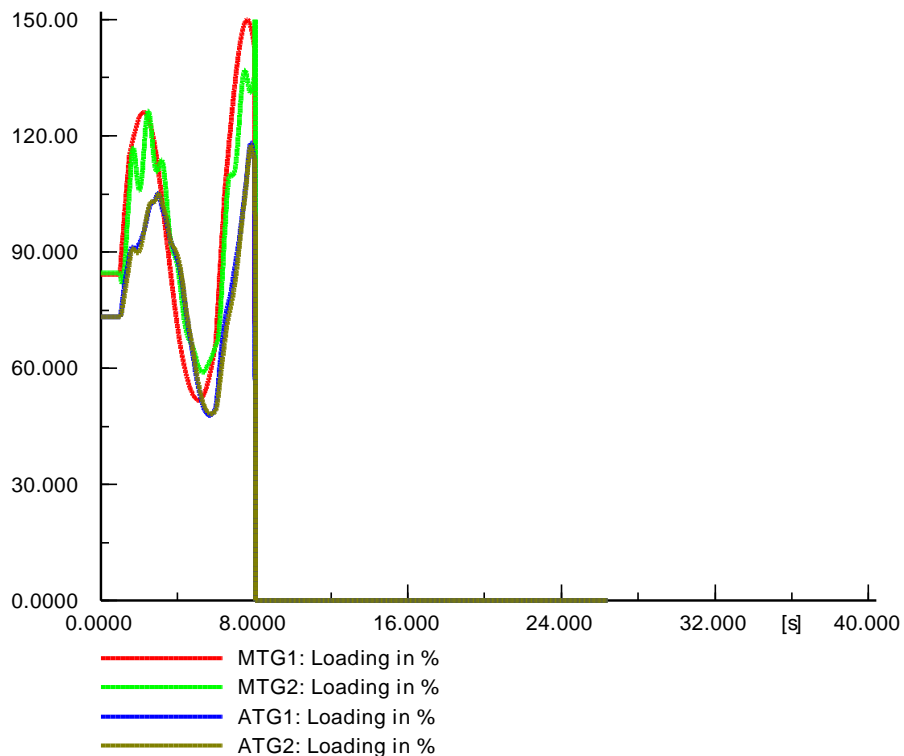
Figure 2.12 System collapse due to energy insufficiency during the first pulse.

The FESSs are connected at the aforementioned locations. Each flywheel is capable of delivering a net energy of 1 kWh and maximum power capability of 3 kW.

57

Figure 2.13, Figure 2.14 and Figure 2.15 show the performance of the system under the heavy pulsed load condition and with the FESS. It can be seen from Figure 2.13 that the main generators are periodically overloaded, but auxiliary generators are within the acceptable loading conditions. Figure 2.14 shows active power of the pulsed load and active power of the ultra-capacitor. The power of the ultra-capacitor is plotted, as seen from the bus-bar side. The positive power denotes discharging and the negative power denotes charging. It is shown that the capacitor discharges during the pulse and starts to recharge again. Herein, the time span between any two consecutive pulses is enough for the capacitor to recharge.
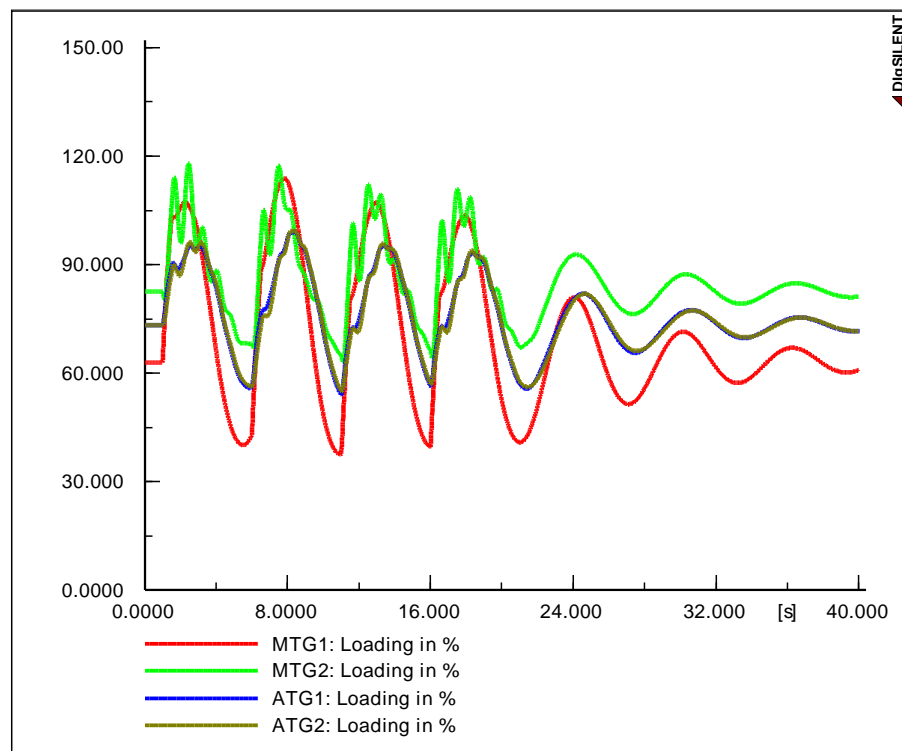
Figure 2.13 Generators percentage loading.
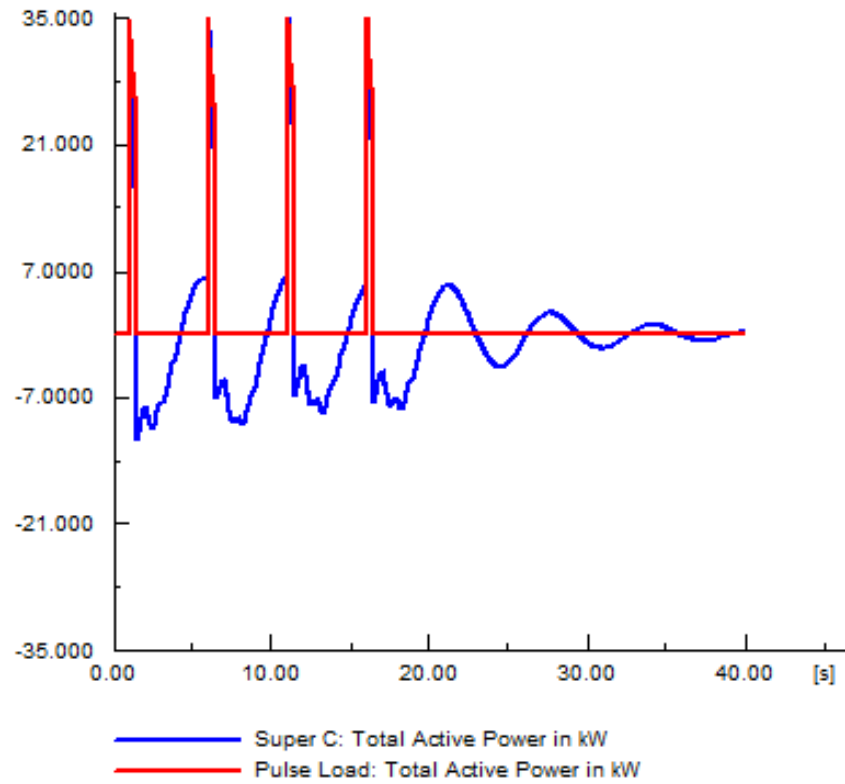
Figure 2.14 Active power of the pulsed load and the ultra-capacitor.
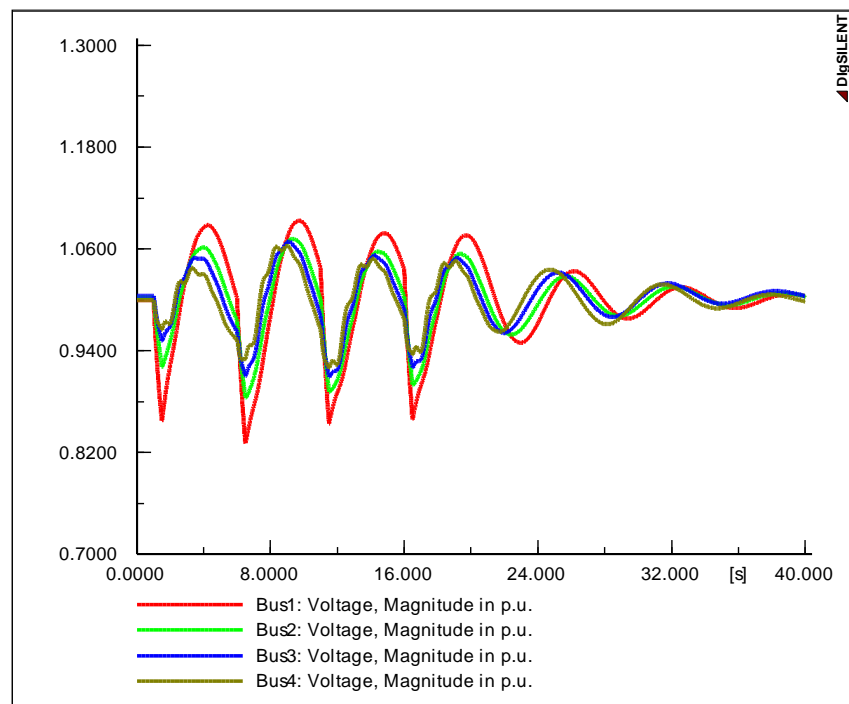
Figure 2.15 Voltages of AC buses.

Narrowing the time span between two pulses can have a negative effect, as the next pulse will occur while the capacitor is still charging. This situation can lead to major instability issues if it is not considered in sizing the flywheel, as the flywheel should be capable of handling very high-power demand rapidly. Figure 2.15 shows voltages of AC buses; voltage fluctuations can be seen. These fluctuations can be reduced by increasing the injected reactive power into the system by controlling i_q of the inverter. Overall, the distributed FESS supports the system to survive and prevents a blackout. Another solution that can be suggested here is to increase the energy stored in the ultra-capacitor, which is given by:

$$E = \frac{1}{2}CV^2$$

(2-1)

Where E, C and V are the energy stored, capacitance of the capacitor and bus voltage, respectively. Increasing the energy stored can be done either by increasing the capacitance or increasing the voltage. Both ways are associated with an exponential increase in costs and fire hazards due to increasing the amount of chemicals. Also, the weight of the equipment will increase which is problematic. Increasing the DC voltage adds more complexity to the design of the converters. If this solution is compared to adding FESS, the result is that FESS provides a simpler and more feasible solution, especially with considering the special and sensitive nature of SPS.

2.5.2   Case 2 (without Ultra capacitor on the DC side)

In this case, the ultra-capacitor on the DC side is disconnected and the amplitude of the pulsed load is reduced to be 16 kW. The size of each flywheel is increased to be capable of delivering a net energy of 1.5 kWh and maximum power capability of 4 kW. The system is simulated twice with and without the flywheel. The system's state and security can be evaluated by monitoring the frequency.

The system frequency with and without FESS is shown in Figure 2.16 and Figure 2.17, respectively. Figure 2.16 shows high-frequency oscillations; the frequency drops to 59.4 Hz and rises to 60.237 Hz, which exceed the acceptable limits for frequency oscillations specified by IEEE standards and by MIL-STD. MIL-STD-1399 limits the acceptable frequency modulation to ±0.5 % of the nominal frequency, which means ± 0.3 Hz in 60 Hz systems [172]. These oscillations can represent a serious threat to the system's stability, as they may cause cascaded outages of generators. The effect of these fluctuations can be more significant in SPS, as sensitive equipment may go into self-protection mode and then shut down [181]. Figure 2.17 shows the frequency oscillations after connecting the three distributed FESSs. The frequency oscillations are significantly reduced and within ± 0.1 Hz, which is acceptable. The speedy response of the FESS smooths the frequency fluctuations and increases the stability margin for the system.
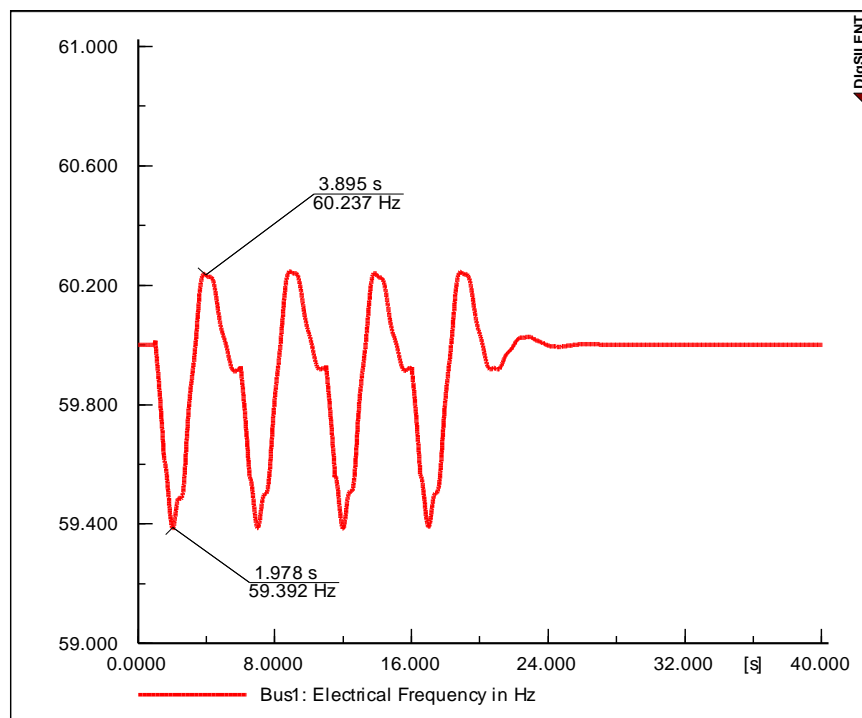
Figure 2.16 System frequency without FESS.
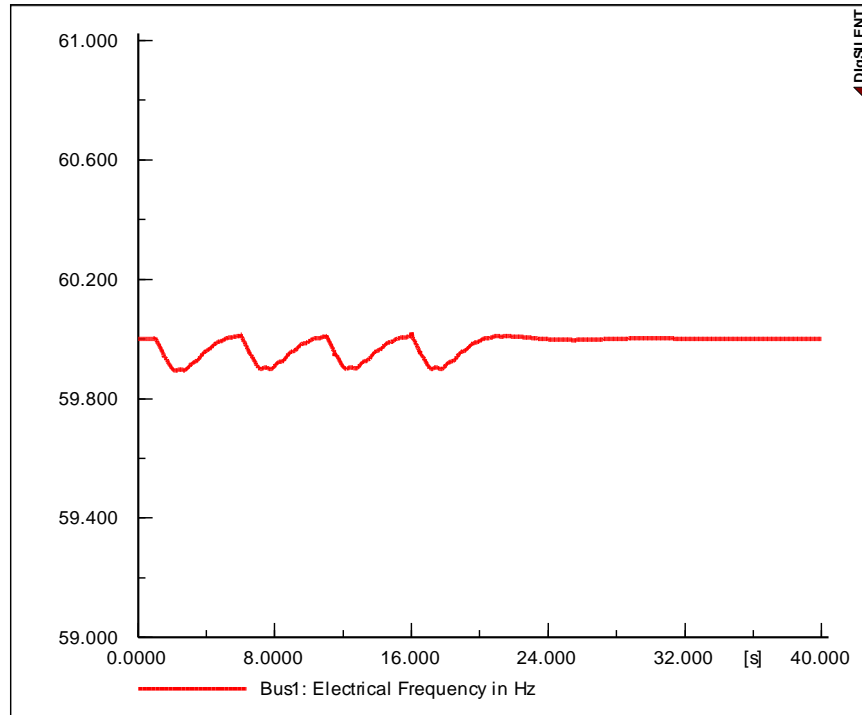
Figure 2.17 System frequency with FESS.

2.5.3 Case 3 (Centralized FESS with Ultra capacitor on the DC side):

In this case, one large centralized FESS will be used to compare the system performance to that in case one where the distributed FESS is used. The pulsed load amplitude is increased again to 35 kW and the ultra-capacitor is connected. Flywheels 1 and 2 are disconnected, while the size of flywheel 3 is increased to be capable of delivering a maximum power of 9 kW (triple the size of each one used in case one). Figure 2.18 shows the percentage loading of the four generators. It can be seen that generator 1 suffers from high power fluctuations and it is overloaded up to 128%. Generator 2 is not overloaded but suffers from power fluctuations with higher frequency. It can be said from comparing this figure to Figure 2.13 that centralizing the FESS results in overloading the generators due to increasing the losses in the transmission system. This problem can be more obvious if the transmission system is more complex or if longer transmission lines are involved. Another revealed problem

62

from this comparison is the inter-area oscillations, which are clear on generator two. The impact of allocation of energy storage on the system performance depends on the distribution architecture. The zonal distribution system is one of the options that is very likely to be commonly used in SPS. The system understudy is zonal distribution system, as it consists of four zones tied to each other using four cables. Therefore, distributed energy storage systems fit more to this type of distribution architectures, which are mostly used in SPS. Figure 2.19 shows the active power of the pulsed load and the ultra-capacitor. The behavior of the ultra-capacitor is almost the same if compared to what is shown in Figure 2.14 but with reduced oscillations after the end of the train of pulses. The voltages of the four AC buses are shown in Figure 2.20. High voltage dips are noted on the voltage of bus 1. These dips are associated with the energization of the pulsed load. This indicated that the generators are injecting high power that cannot be compensated (please relate to Figure 2.18). Furthermore, the voltage rises to approximately 1.08 p.u. after de-energizing the pulsed load. The output power of the other three generators (MTG2, ATG1 and ATG2) are exhibiting less fluctuations.
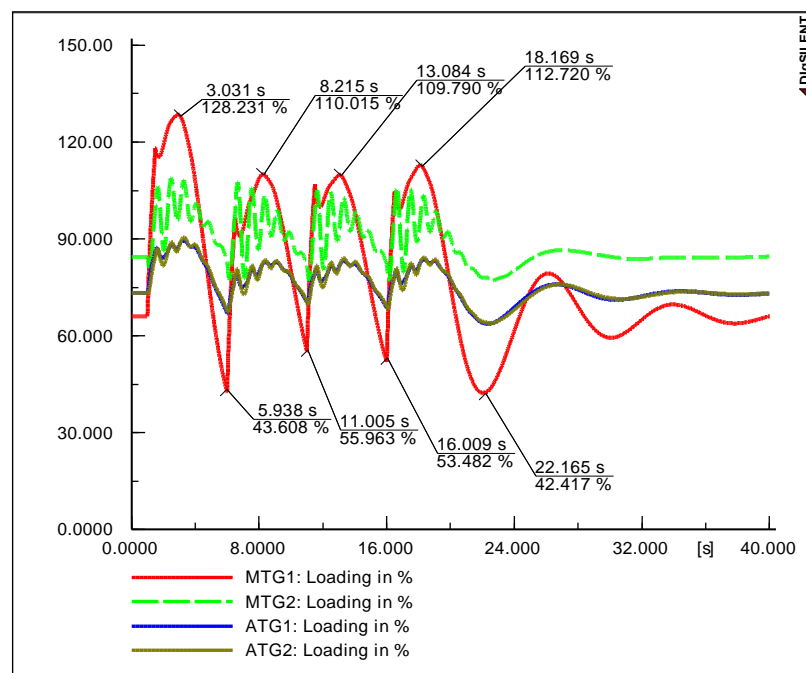
Figure 2.18 Generators percentage loading.
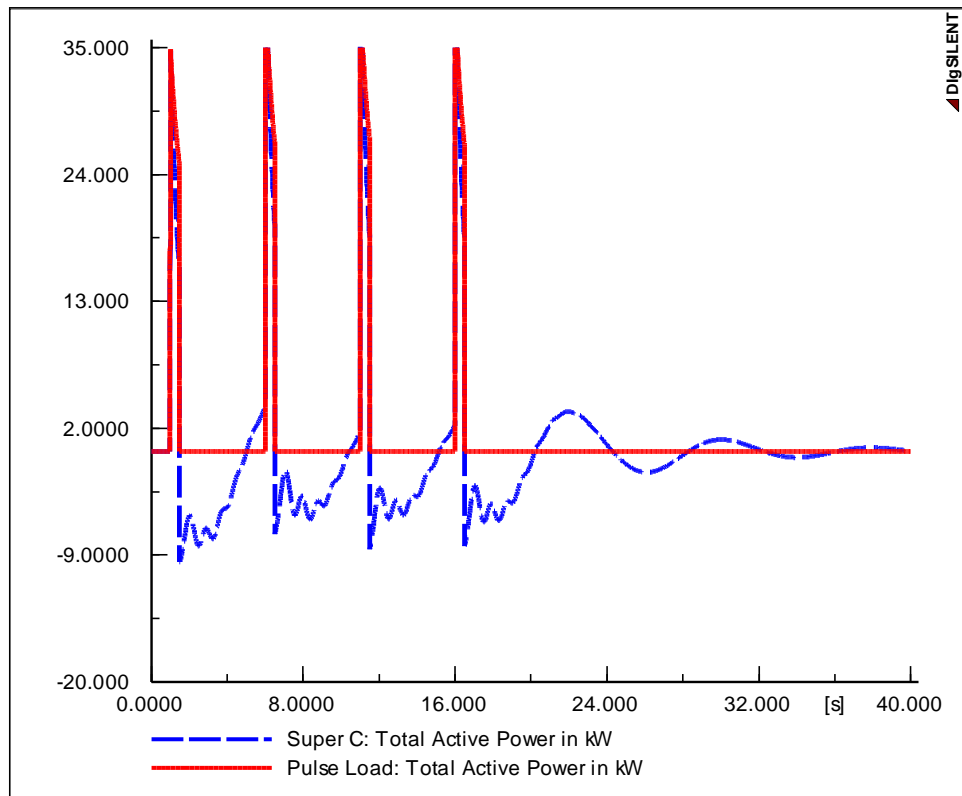
Figure 2.19 Active power of the pulsed load and the ultra-capacitor.
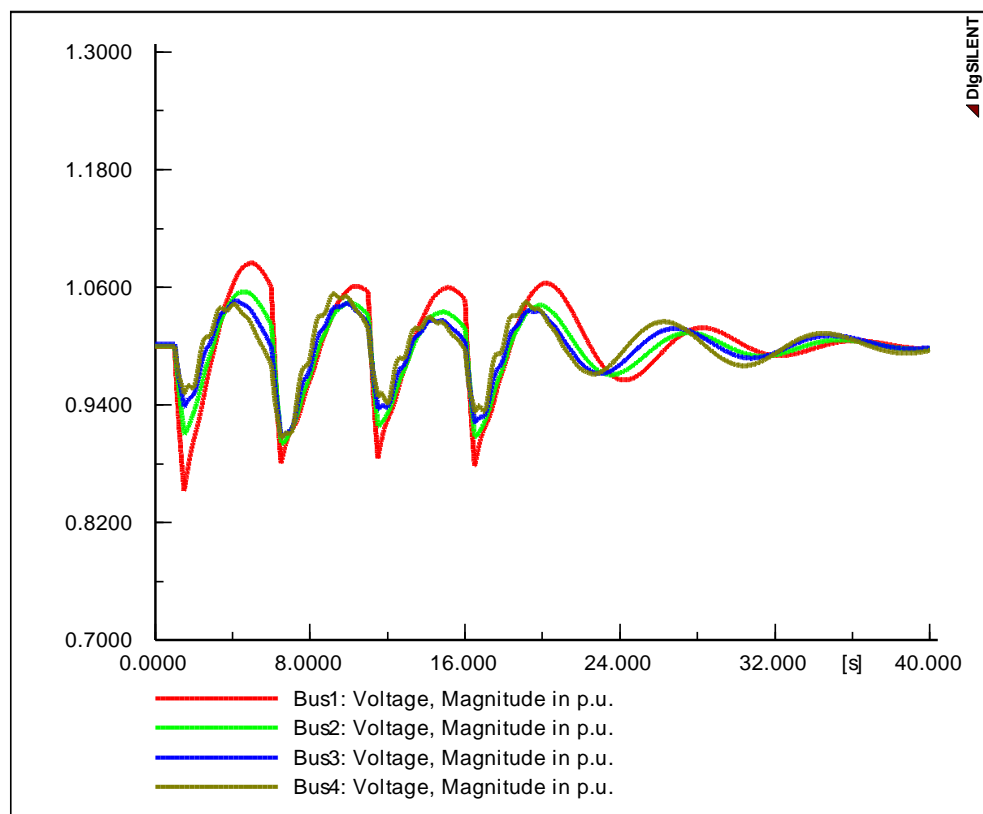
Figure 2.20 Voltages of AC buses.

64

2.6   Summary

This chapter presents a comparative study to determine the optimal combination for a hybrid energy storage system to mitigate the negative effects of pulsed power loads on a ship power system. A model for a hybrid AC/DC distribution system is built in the DIgSILENT PowerFactory software package and several case studies are conducted with all the possible combinations. The results are analyzed and discussed in detail. This study showed that the battery and flywheel combination deserves a merit and can achieve better performance over the other combinations. It is shown that a combination comprises a flywheel, and ultra-capacitor can cause frequency oscillations. Another conclusion drawn from this work is that the combination of the three elements (ultra-capacitor, flywheel and battery) yields a performance close to that of the battery and flywheel combination. However, this solution is less preferred due to weight and size limitations in the SPS environment.

Further studies are performed to investigate the performance of the flywheel and ultra-capacitor combination. The idea of allocating small flywheels in a distributed manner is proposed to reduce the frequency oscillations. Three different cases are conducted to investigate the effectiveness of the proposed idea. The results of each case are analyzed and discussed. It is proven that flywheels can play an effective role in maintaining the system's stability and reduce the frequency oscillations. Furthermore, a comparison between the distributed and centralized FESS is conducted. It is shown that three small flywheels can provide better results than one large flywheel. The distributed flywheel solution reduced the frequency oscillations significantly.

In conclusion, this chapter presents a top-level study on three different energy storage systems. Deeper details and further investigations on each system are presented in the following chapters. For example, the design of a controller for hybrid energy

storage systems will be detailed in chapter 4. Furthermore, the design and control of the FESS will be presented in chapter 7. The required design modifications and issues associated with interfacing flywheels to DC systems are discussed in the same chapter.

The outcomes of this study cannot overlook the importance of formulating a comprehensive optimization problem, where multiple objectives have to be considered. Also, in the problem, broader search space should be considered to take into account more architectures that may seem to be not feasible if evaluated using in-accurate metrics. Rather, this study draws the necessary guidelines to formulate a formal optimization problem. This problem uses multiple criteria to evaluate each architecture. The detailed formulation, discussion and results of this problem are provided in chapters 6 and 7.

Chapter 3   An Empirical Study on the Effects of Different Pulsed load Profiles and Energy Storage Sizing on the Performance of Ship Power Systems

3.1   Introduction

Since there are tight constraints on the size and weight of the equipment to be installed onboard, sizing the energy storage (ES) systems is a very crucial task in Ship Power Systems (SPS). Therefore, oversizing the ES will add unnecessary load to the system. Since the total weight capacity of the ship is limited, the additional equipment will be loaded at the expense of logistics and manning. This may affect the length of the mission and the capabilities of the ship. On the other hand, under-sizing the ES may cause overloading of the generators, and consequently, the voltage and frequency drop. In some heavy loading conditions, the impacts may be severe, reaching the point of tripping the generation units. Thus, the lack of enough energy storage may jeopardize the security of the system and violate the safe operation limits. Accordingly, the optimal size of ES should be determined, while fulfilling the dynamic security constraints.

In this chapter, an empirical study is conducted to investigate the impacts of the ES sizing on the performance of the SPS under heavy loading conditions. In addition, the impacts of changing the Pulsed Power Load (PPL) profile on the required size of the ES is investigated. The presented study dedicate more focus on the non-uniform PPL profiles. Non-uniform profile means that the duty cycle of the power pulses and the span between any two consecutive pulses are different. The non-uniform PPL profile used in this study is shown in Figure 3.1. Three issues are investigated in this study:

- The impact of non-uniform PPL profile on a single DC bus on the SPS.

- The impact of two PPLs on two DC buses with different voltages in the SPS. One of the loads is with uniform profile while the other is non-uniform.

- The impact of two PPLs on two DC buses with different voltages in the SPS. Both PPLs are with non-uniform profile.

These three issues are investigated as three case studies. Where the size of the ES is changed, the results are obtained and then analyzed for each case. These simulation studies are performed using the DIgSILENT PowerFactory software package. The performance of the SPS is judged by monitoring the system's frequency, the loading of the four generators, the DC bus voltage and the voltages on the main four AC buses.
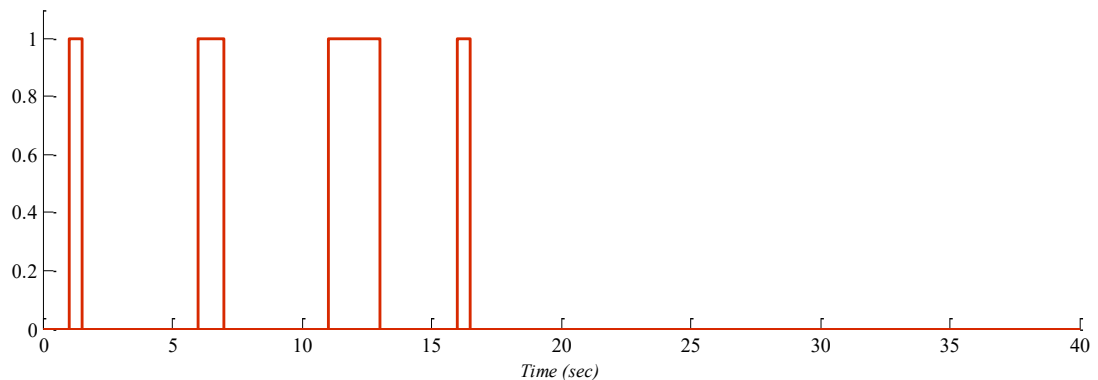
Figure 3.1 Non-uniform PPL profile used in this study.

3.2 A single non-uniform PPL on the DC bus:

In this case, the impact of a single PPL with non-uniform profile is investigated. The PPL is connected to the DC bus. The system under study is similar to the system shown in Figure 2.1. Two energy storage devices are connected to the DC bus: Super-Capacitor (SC) and battery. In the following cases, the effect of changing the size of the supercapacitor is studied, while the battery size is kept fixed with a constant amount.

3.2.1 Case I: Base case:

In the base case, the PPL with the profile shown in Figure 3.1 is applied to the notional four-shaft SPS depicted in Figure 2.1. The size of the SC is set to 0.8 F. The

results are shown in Figure 3.2. From Figure 3.2(a), it can be seen that the AC voltage

on bus 1 dropped to 0.88 p.u. This value is beyond the minimum voltage limit allowed

by the standards. By looking at Figure 3.2(b), it can be said that the situation on the DC

side is not better. The DC bus voltage dropped below the allowed minimum limit. This

situation is very critical as it may activate the under voltage protection devices, and

consequently, trip the sensitive loads. The generator loading and system frequency are

shown in Figure 3.2(c) and Figure 3.2(d), respectively. It is seen that the generators are

overloaded to un-safe limits. This implies that the stored energy in the SC is not enough

to cover the energy deficiency caused by the PPL.
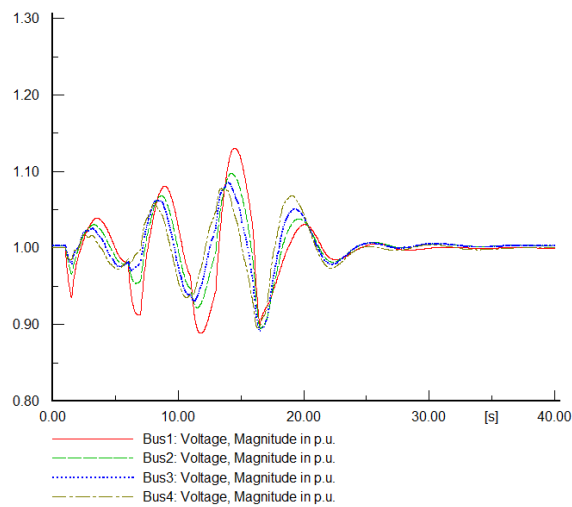
(a)
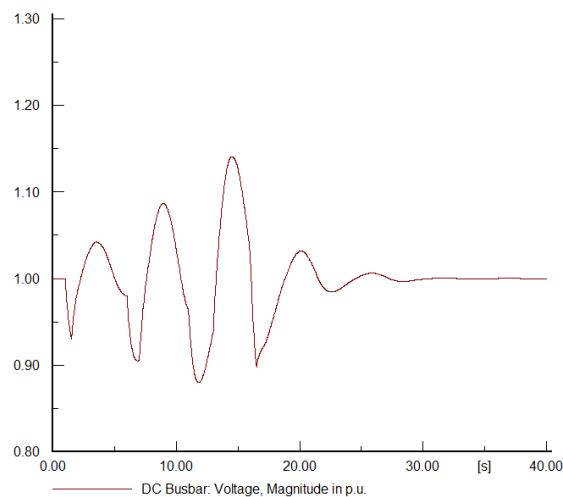
(b)
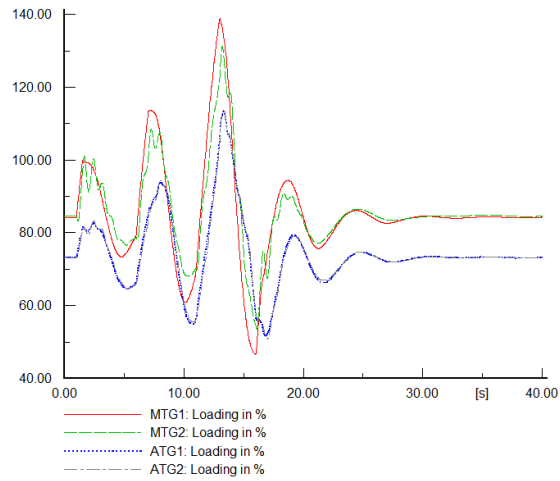
(c)
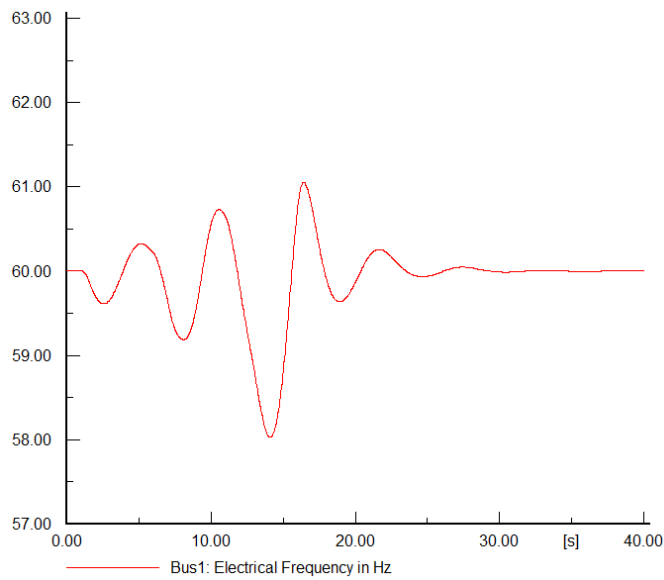
(d)

Figure 3.2 Ship power systems response in the base case.
(a) Voltages on the main four AC buses, (b) DC bus voltage, (c) Generator
loading, (d) System's frequency.

3.2.2 Case II: SC 200%:

In this case, the size of the SC is doubled to be 200% of the base case. The results

are shown in Figure 3.3. Although, there is some improvement due to increasing the

size of the SC, there are some high oscillations. From Figure 3.3(c) and Figure 3.3(d),

it can be seen that the highest generator loading point and the lowest frequency are

70

associated with the wide pulse of the profile (please refer to Figure 3.1). In order to mitigate these unwanted effects, further increases of the battery and the SC are needed. The accurate sizing of the ES is carried out using a comprehensive multi-objective optimization problem presented in Chapter 5.
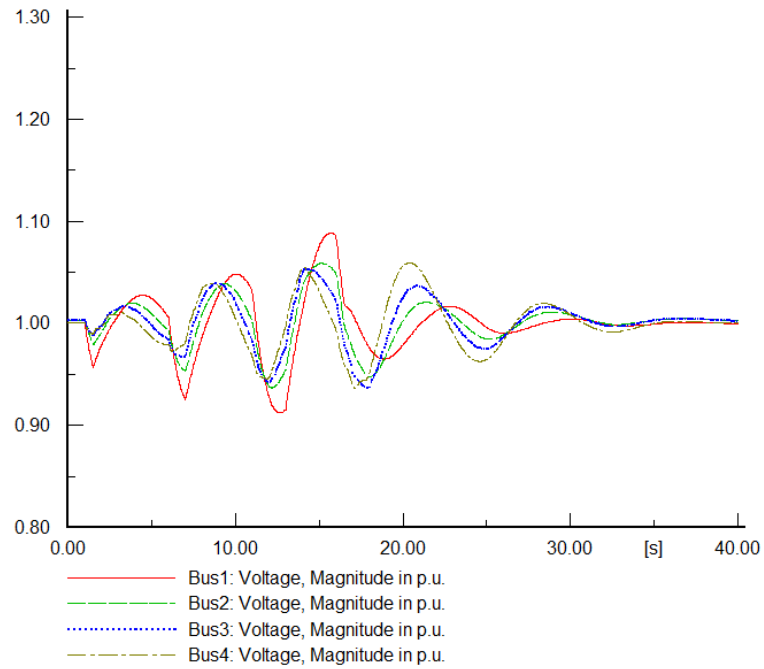
(a)
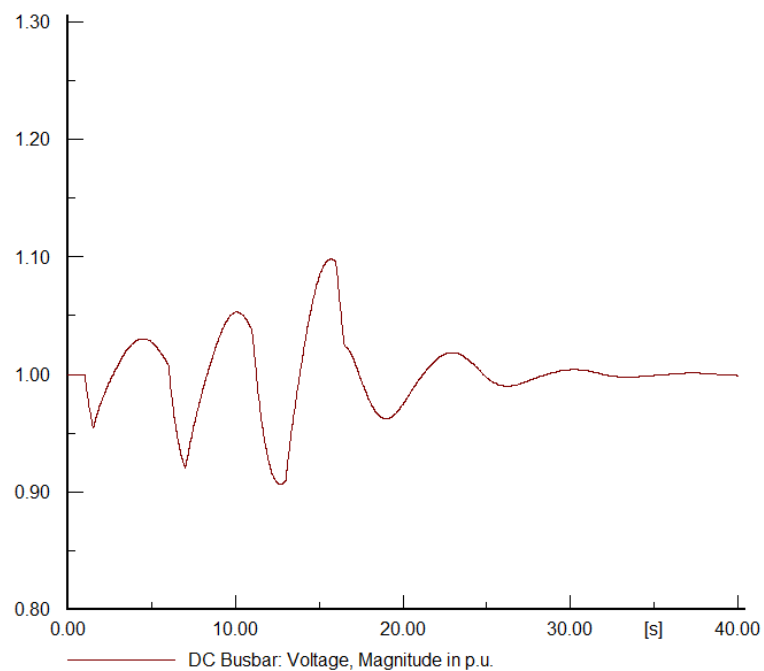
(b)
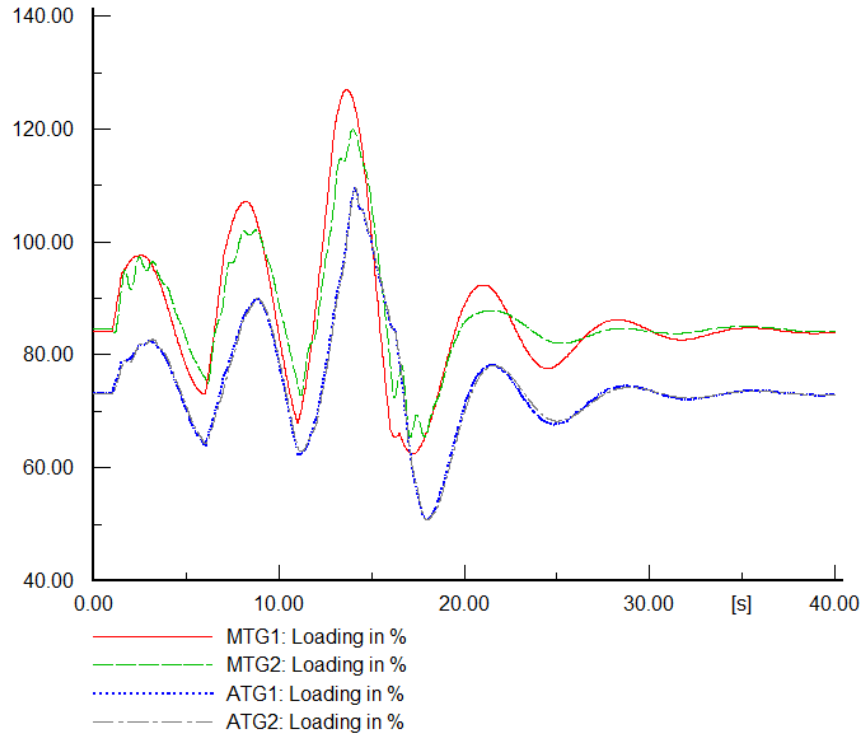
(c)
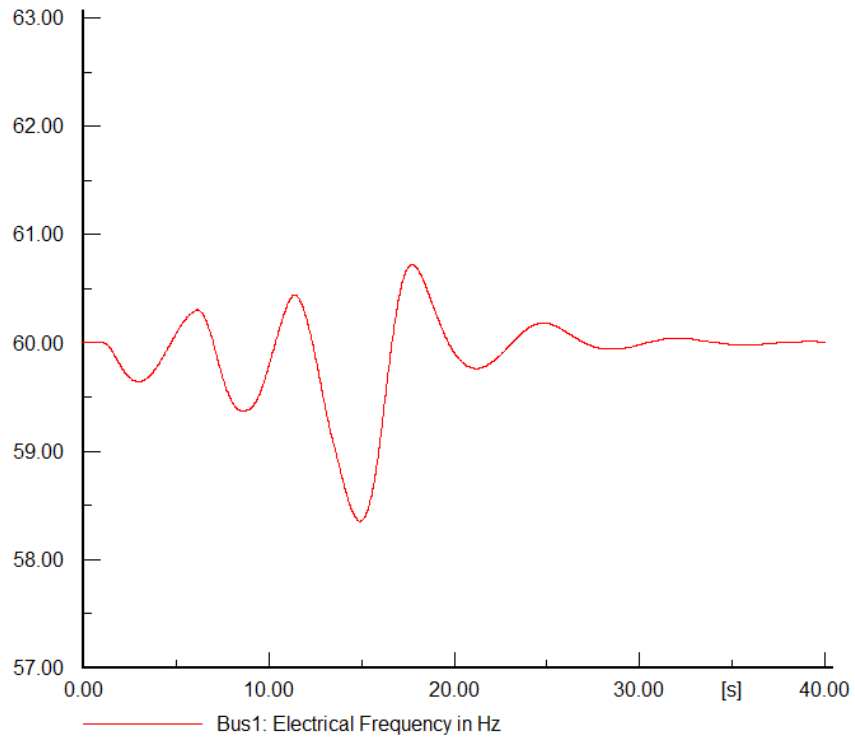
(d)

Figure 3.3 Ship power systems response after doubling the size of the SC.
Voltages on the main four AC buses, (b) DC bus voltage, (c) Generator loading,
(d) System's frequency.
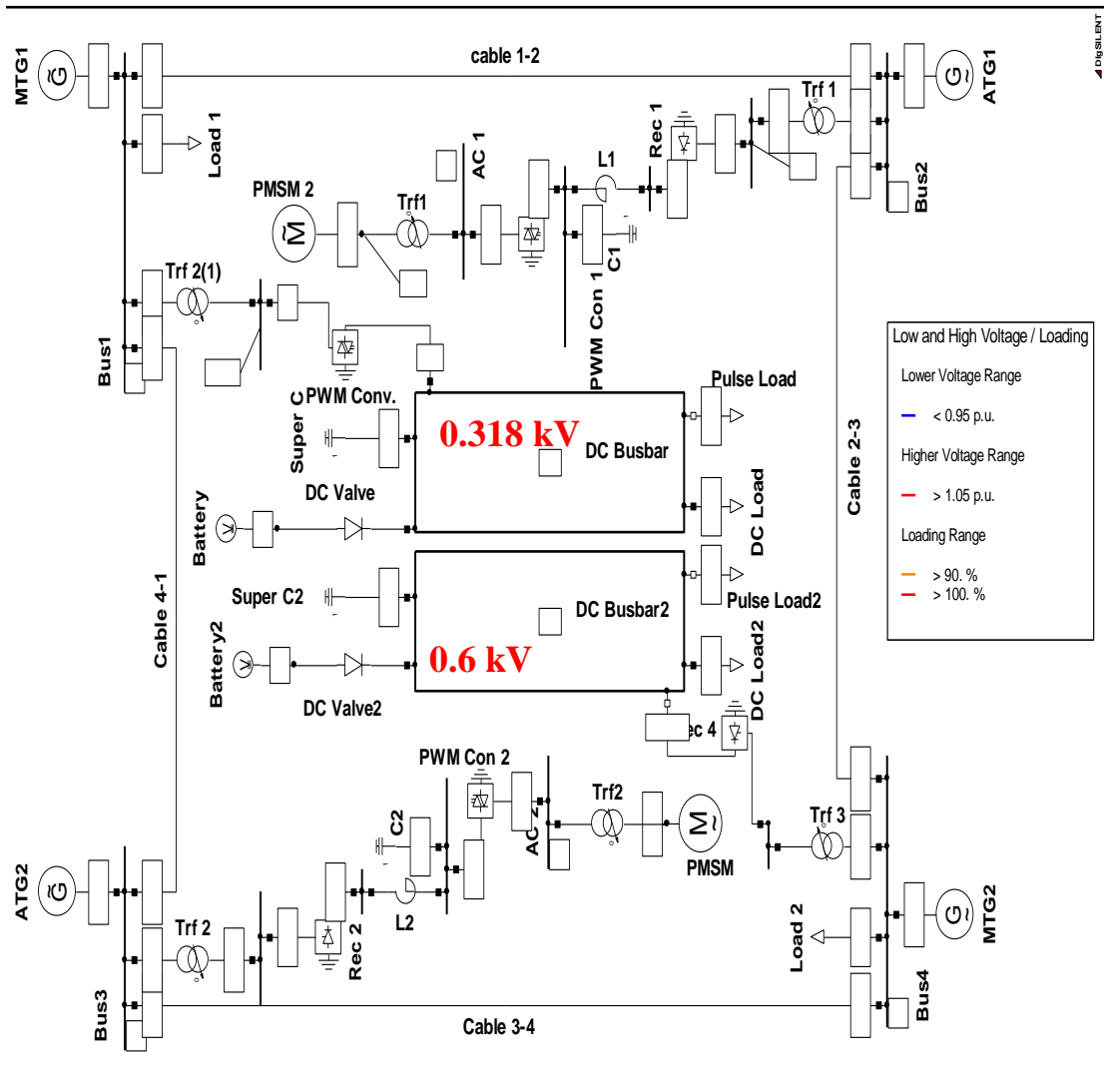
Figure 3.4 Notional four shaft ship power system with two DC buses.

3.3   Two PPLs (uniform and non-uniform profiles):

3.3.1   Case I:Base case

It is very likely that two different PPLs will be existing in the modern designs of SPS. One of them is with lower amplitude and uniform pulsing profile. Examples of this type of loads are the radar and sonar. The other load is of higher amplitude and non-uniform operating profile. This load can resemble an EM rail gun or Air Launching System (ALS). In this case, the effect of the presence of these two PPLs with different profiles (uniform and non-uniform) in the SPS is investigated.
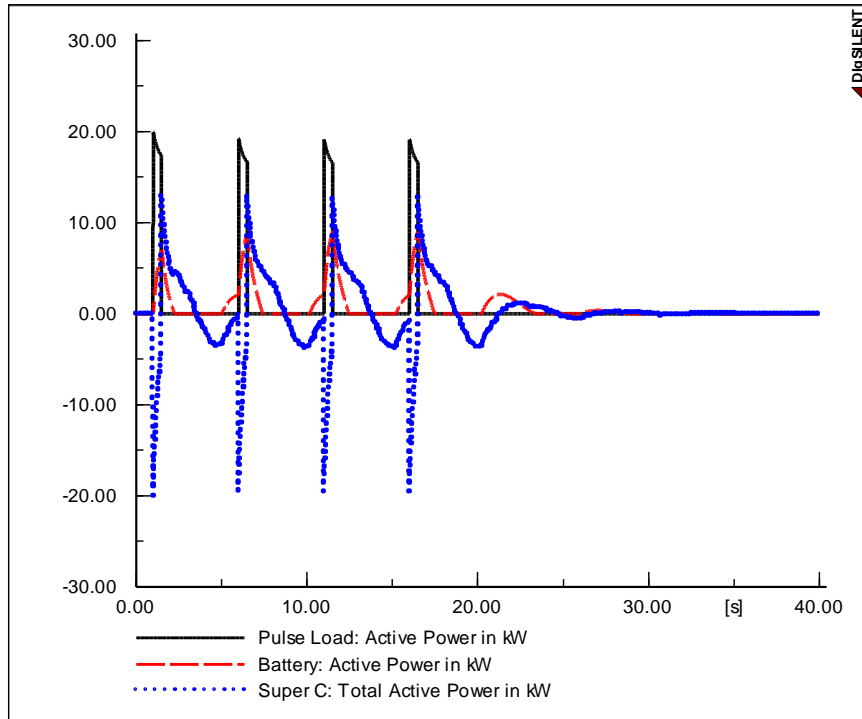
(a)
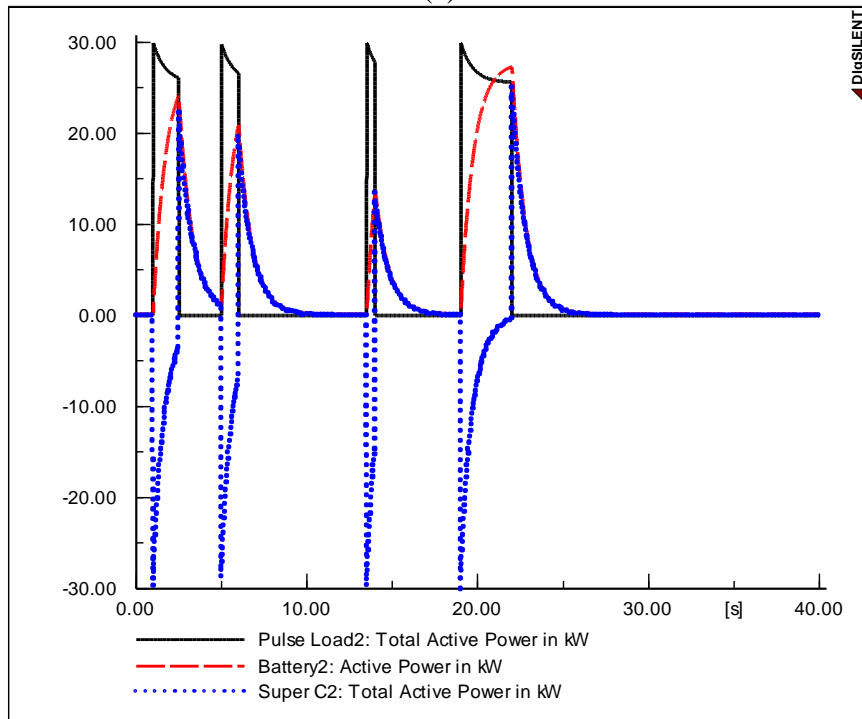
(b)

Figure 3.5 PPL profiles under study and ES output power.
(a) 20 kW uniform PPL, (b) 30 kW non-uniform PPL.
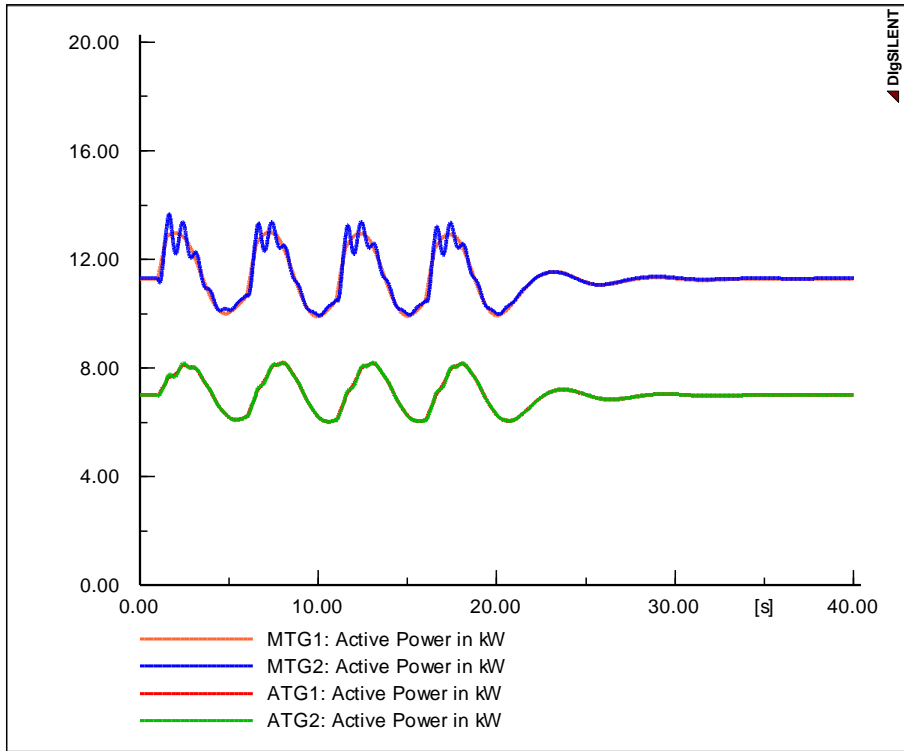
(a)
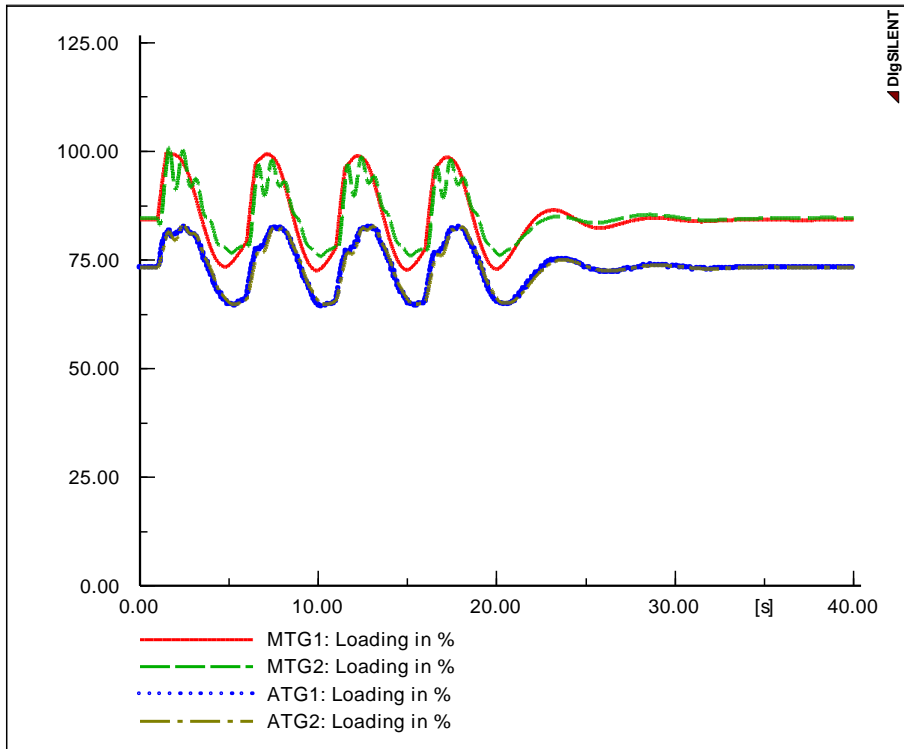
(b)
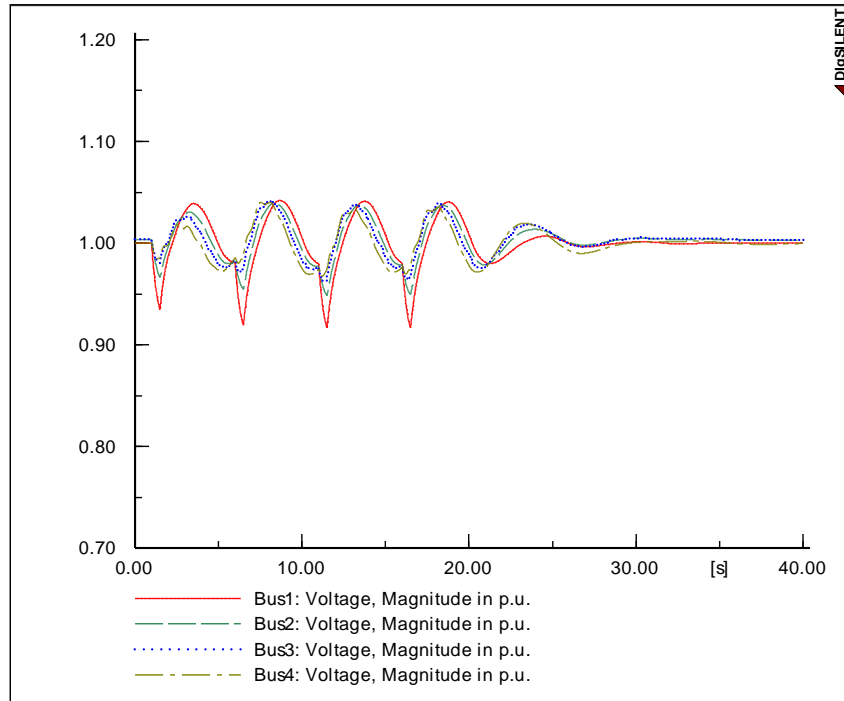
(c)
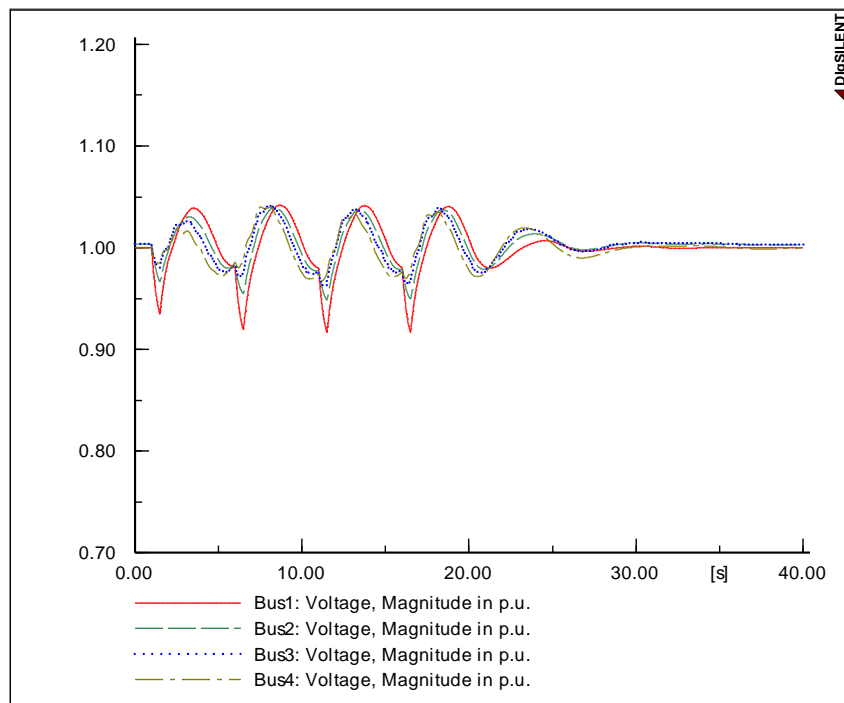
(d)

Figure 3.6 Ship power systems performance-two PLLs, base case.
(a) Generators active power output, (b) Generators percentage loading,
(c) AC bus voltages, (d) DC bus voltages.

In order to accommodate the two PPLs, a modification of the architecture shown in Figure 2.1 is introduced. Another DC bus with higher voltage is added to the system. The PPL with higher power amplitude is connected to the DC bus with higher voltage. This is done to reduce the pulsed current and the cable Cross Sectional Area (CSA). The modified architecture is shown in Figure 3.4. The voltages of DC bus 1 and DC bus 2 are 0.318kV and 0.6kV, respectively.

The amplitude of PPL1 is 20 kW and its profile is as depicted in Figure 3.5(a) in black solid line. The duty cycle is 10%, its active time period is 0.5 sec, while the entire cycle time is 5 sec. This load is connected to DC bus 1, which voltage is 0.318 kV. The amplitude of PPL2 is 30 kW and its profile is as depicted in Figure 3.5(b) in black solid line. The pulse train is composed of four pulses with active durations of 1.5 sec, 1 sec, 0.5 sec and 2 sec. Furthermore, the span between any two consecutive pulses is widely different. This load is connected to DC bus 2, which voltage is 0.6 kV. Please note that the total generation in the system is around 50 kVA; therefore, the pulsed loads are representing a significant load in the system with respect to the available total generation power. Without the support of ES, the system failure in inevitable as the generators cannot support these loads.

After running the simulation and solving the power flow of the system, the output power of the SC and battery are shown in Figure 3.5, overlapping the pulsed load profile. It can be seen from Figure 3.5(b), that the SC has enough stored energy to cover the energy deficit in the short duration pulses, whereas, for the long duration pulse (fourth pulse), the SC is discharged prematurely. On the same figure, the difference in the time response of the battery and SC is clear. The SC response is much faster than the battery, the battery takes few tens of mili-seconds to inject energy. This may create

77

an energy gap at the front of the pulse. This shows the role played by the SC and its importance.

The rest of the simulation results are shown in Figure 3.6. It can be seen from Figure 3.6(b) that MTG1 and MTG2 are highly loaded. The output power is reaching the rated values during the active period of the PPL. However, the generation units are not overloaded as the loading is not exceeding the safe limits. Nevertheless, it can be seen that the load on the main units is varying between 75% to 100%. These power fluctuations can cause mechanical stresses on the shaft, and consequently, reduce the unit's lifetime. Figure 3.6(c) shows the AC voltages on the four main AC busses, the voltage on bus 1, where MTG1 is connected, dropped below the allowed 0.95 p.u. limit. The voltages on the other buses are within the allowed limits. The DC bus voltages are depicted in Figure 3.6(d). The voltage of DC bus 1, where the lighter PPL is connected, is within the limits. The voltage of the DC bus 2 (shown with dashed blue line) is dropping below the allowed safe limits. As anticipated, the largest drop is corresponding to the widest pulse. This indicates that there is not enough energy to cover the energy deficiency.

3.3.2   Case II: 300% SC

In this case, the size of the SC is increased to 300% of that of the base case. The results are shown in Figure 3.7 and Figure 3.8. It can be seen from Figure 3.7(b), that the energy stored in the SC became enough to supply the PPL. This is noticed by giving a closer look to the SC output power (shown in dotted-blue line) during the two sec pulse. It can be seen that the SC injects a high power spike to cover the deficit caused by the slowness of the battery response. The battery output power is shown on the same figure with the dashed-red line. It is clear that the battery output takes time to rise. This

is explained by the high capacitance used to model the battery, which affects its time response.
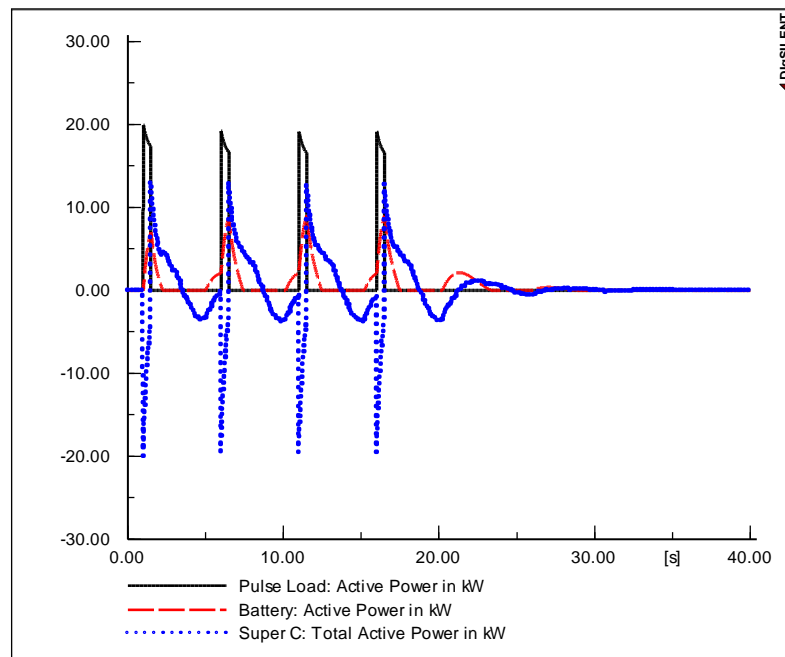
(a)
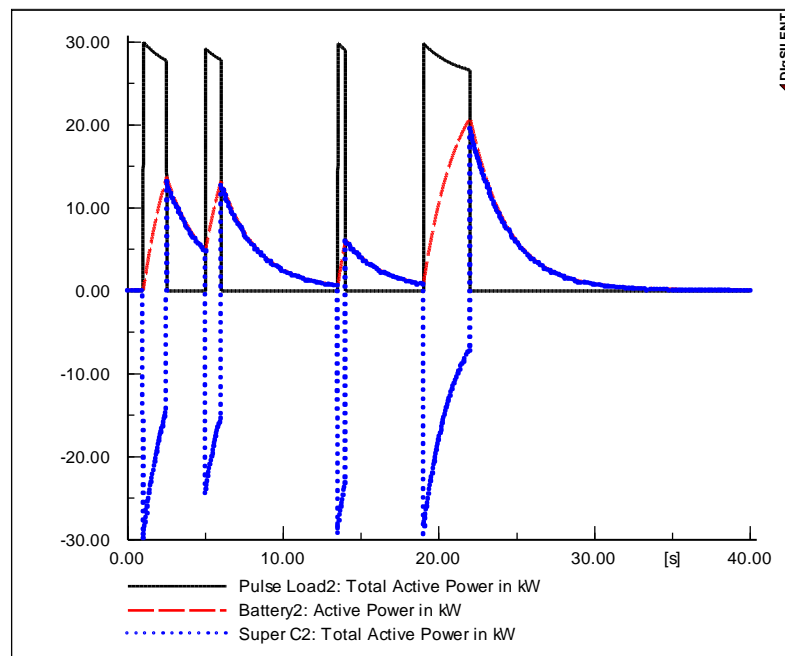
(b)

Figure 3.7 ES output and load powers: Case II
(a) 20 kW uniform PPL, (b) 30 kW non-uniform PPL.
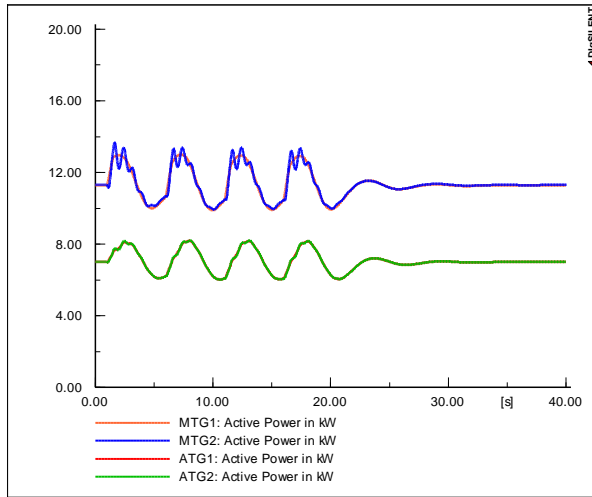
(a)
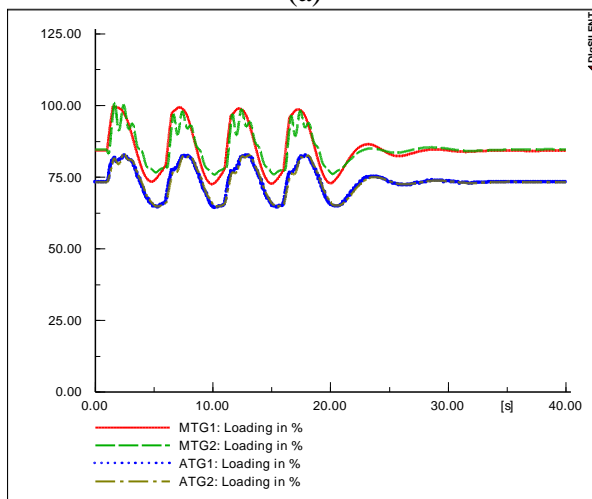
(b)
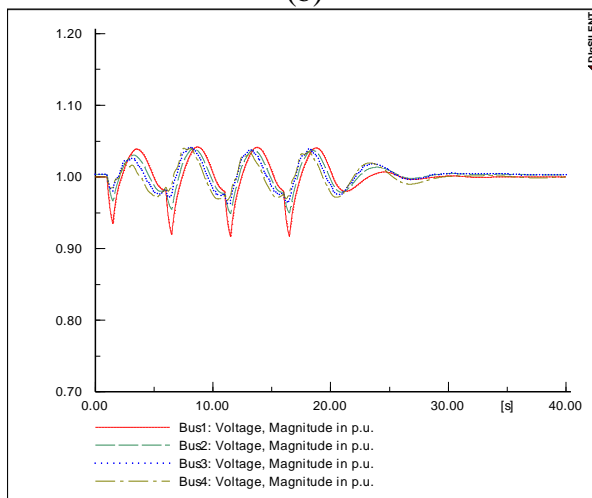
(c)
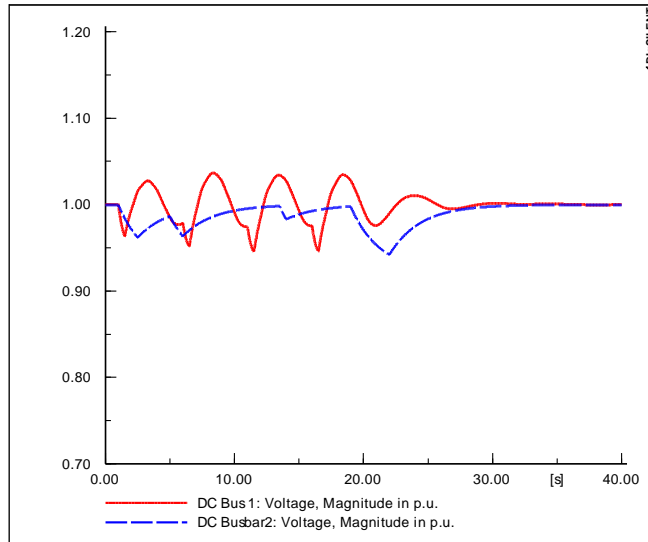
(d)

Figure 3.8 Ship power systems performance-two PLLs-Case II.
(a) Generators active power output, (b) Generators percentage loading,
(c) AC bus voltages, (d) DC bus voltages.

It can be noticed from Figure 3.8(b) that there is no noticeable reduction in the generator output power if compared to the previous case. This is due to the fast dynamics of the SC; it means that the SC changes its state from discharging to charging rapidly. Also, the larger the size of the SC, the higher the charging energy required to be transferred from the AC side, which is loaded on the generators. Therefore, increasing the size of the SC increases its charging current, and then increases the stresses on the generators during charging. The effect of increasing the size of the SC on the DC bus voltage is noticed by looking at Figure 3.8(d), where the voltage fluctuations are smoother. The voltage of DC bus 2 is supported without significant drop.

3.4 Two PPLs with non-uniform profiles:

In this case, the uniform profile PPL connected to DC bus 1 is replaced with another one with a non-uniform profile. However, the power amplitude is kept the same. This

case represents a very tough situation because the existence of two PPLs with non-uniform profiles can cause significant oscillations, especially if they are not coordinated (i.e. overlapping is possible).
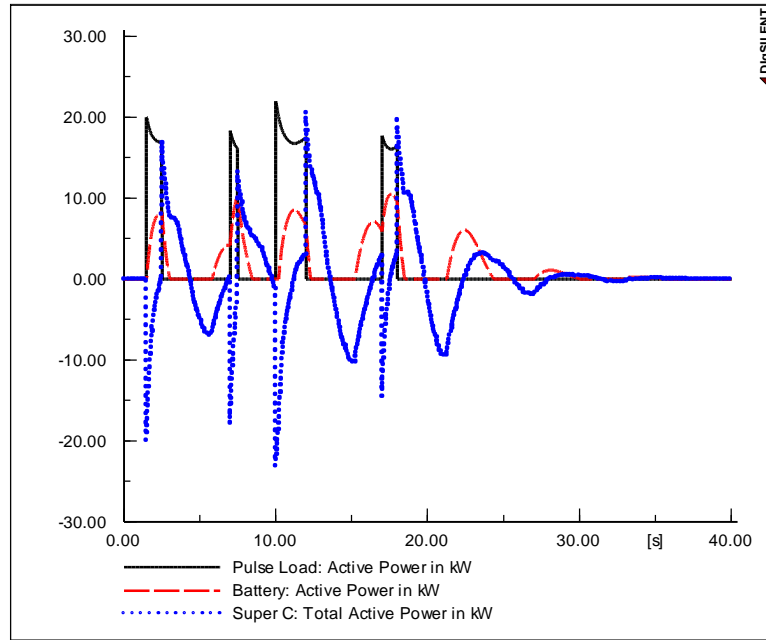
(a)
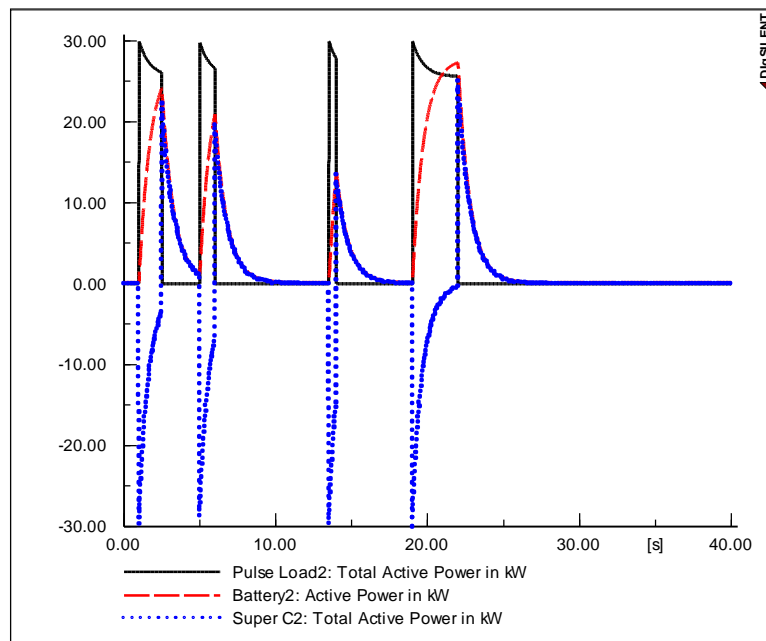
(b)

Figure 3.9 ES output and load powers: Case I
(a) 20 kW non-uniform PPL, (b) 30 kW non-uniform PPL.
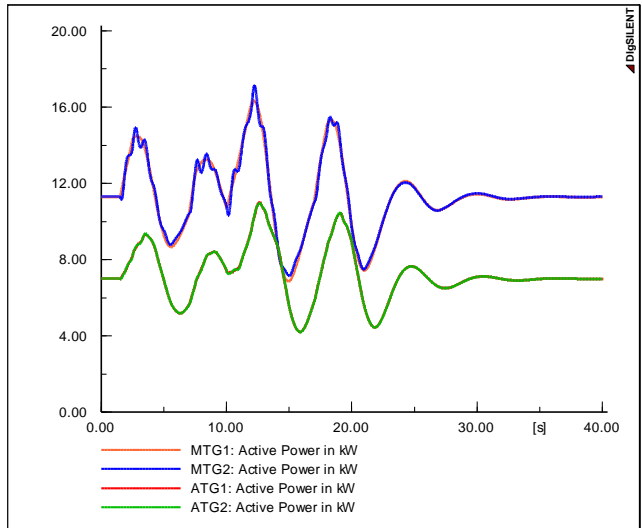
(a)
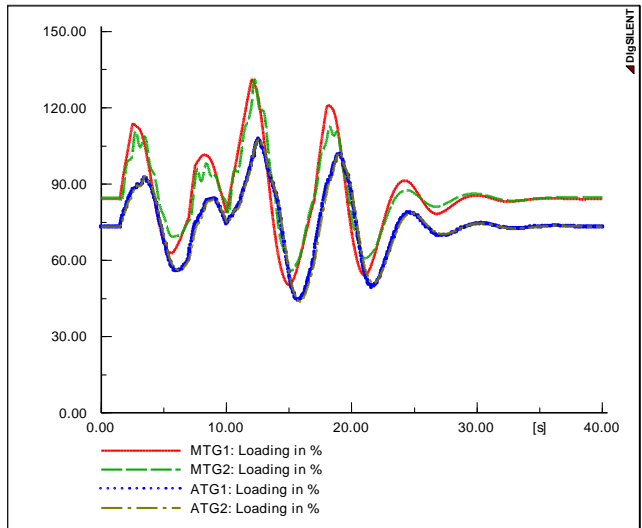
(b)
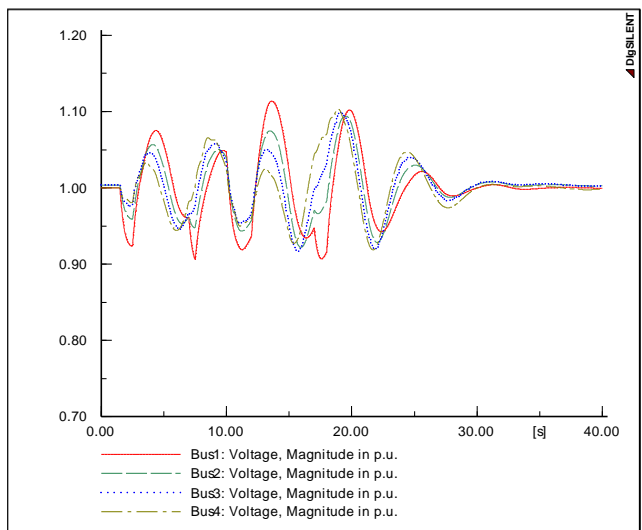
(c)
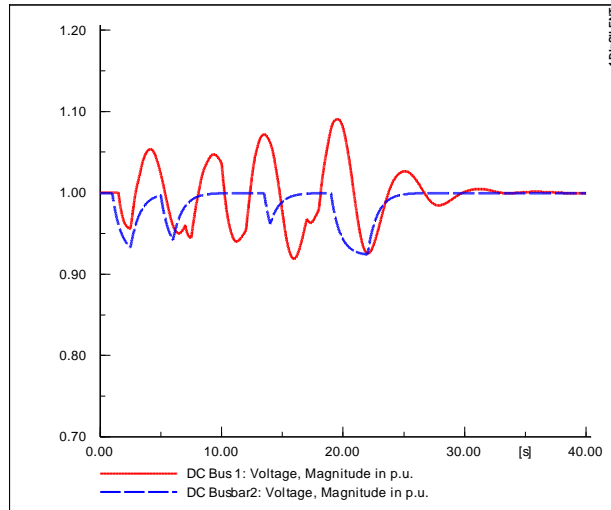
(d)

Figure 3.10 Ship power systems performance, two non-uniform PLLs- Base case.
(a) Generators active power output, (b) Generators percentage loading,
(c) AC bus voltages, (d) DC bus voltages.

3.4.1 Case I: Base case

The battery, SC and load powers are depicted in Figure 3.9. It is clear that the SC is discharged prematurely because of its small capacity. This caused higher fluctuations in the battery output power. Figure 3.10(a) shows the output active power of the four generators in kW. The percentage loading of the four generators is depicted in Figure 3.10(b), it can be seen that because of the high power oscillations on the DC side, the generator output power is oscillating significantly. For example, MTG1 is overloaded at 135% at some points and reaches 50% at other points on the load profile. Furthermore, due to the non-uniformity of the load profile, the generator power is fluctuating rapidly. This is obvious around second 10. The output power of the auxiliary units are fluctuating, as well, in a wide range from 50% to 110%. These high power fluctuations are not safe because they cause high mechanical stresses and torsions on the generator shaft. As a result, it is highly anticipated that the generator's lifetime will be significantly shortened. These power oscillations are reflected on the voltage as shown in Figure 3.10(c) and (d). This mandates the re-sizing of the ES units.

84

3.4.2 Case II: 300% SC

In this case, the size of the SC is increased to be triple that of the base case. It is found that increasing the SC size with this amount did not noticeably improve the performance since both PPLs overlap at certain points, causing a very heavy load on the system. It is obvious from Figure 3.11 that, the power oscillations are still significant. This case is presented as an intermediate case to show the steps of the empirical approach and the sizing progress. Several other cases are conducted; however, their results are omitted and not presented because of the unsatisfactory performance.

(a)

(b)

85
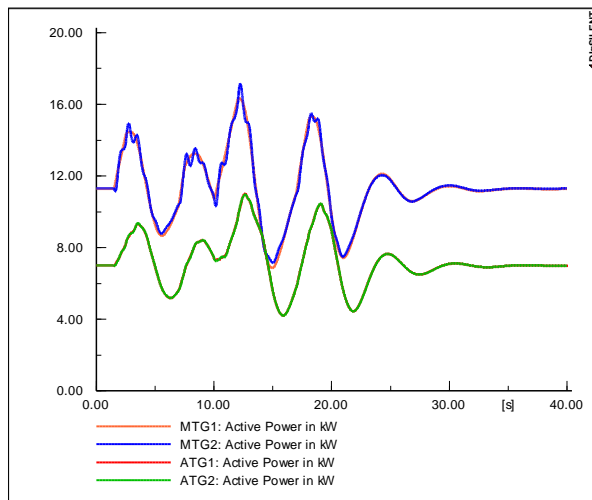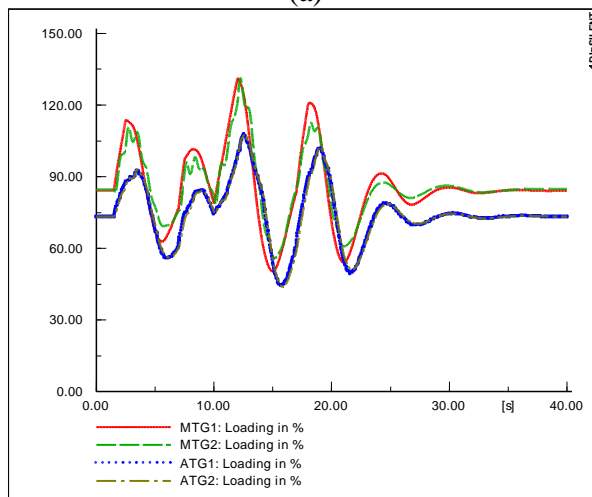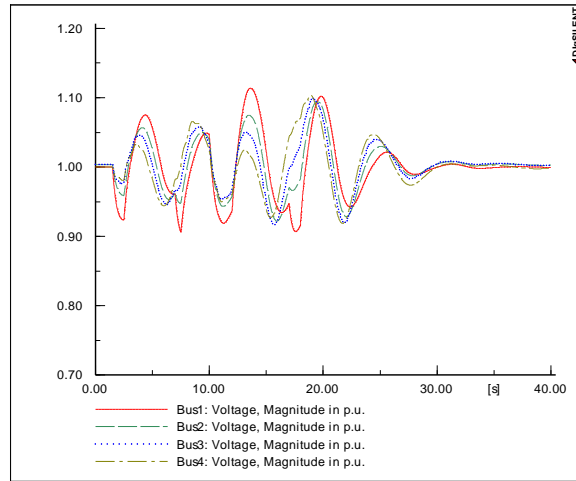
(c)
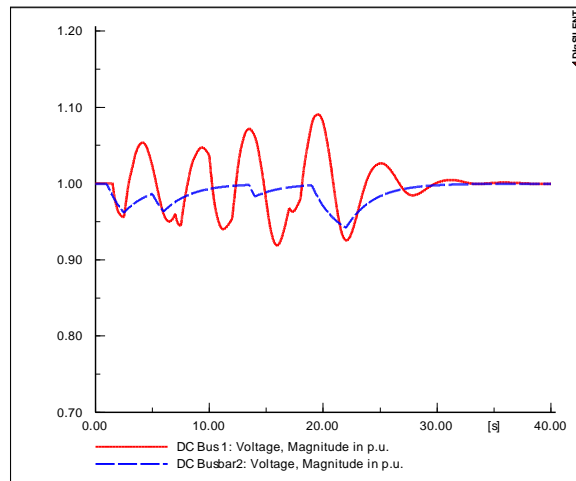
(d)

Figure 3.11 Ship power systems performance, two non-uniform PLLs- Base case.
(a) Generators active power output, (b) Generators percentage loading,
(c) AC bus voltages, (d) DC bus voltages.

3.4.3 Case III: 800% SC

In the third case, the SC is re-sized to be eight times that of the first case. From the results, it is clear that increasing the SC size with this amount improves the performance and mitigates the undesirable effects of the two irregular pulsed loads. Figure 3.12 shows the profiles of the two PPLs and the output power of the SC and battery. As shown in Figure 3.12(b), the SC output lasts to the end of the pulse even for the wide

one (highlighted with the dashed-green oval). This indicates that the energy stored in

the SC became enough to cover the energy deficit on the DC side.
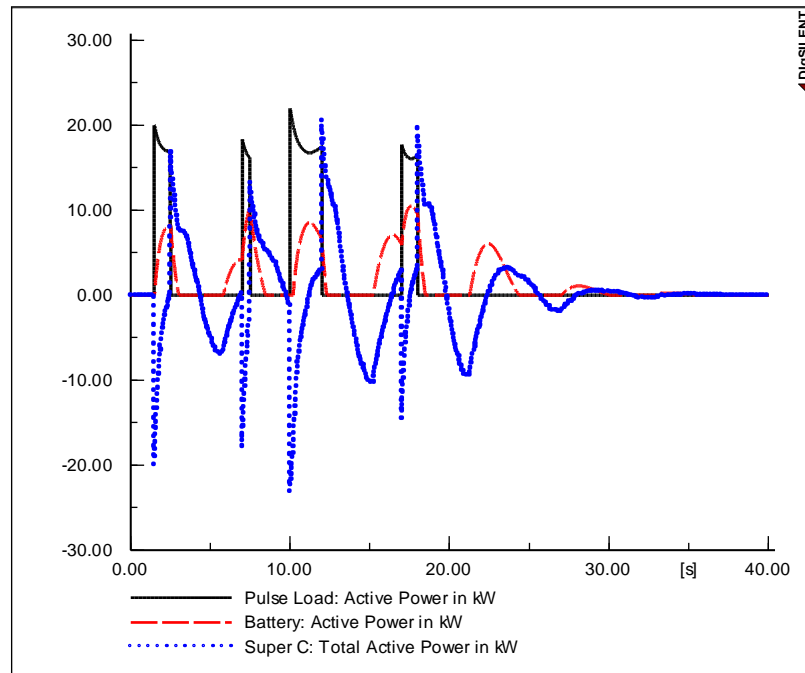
(a)
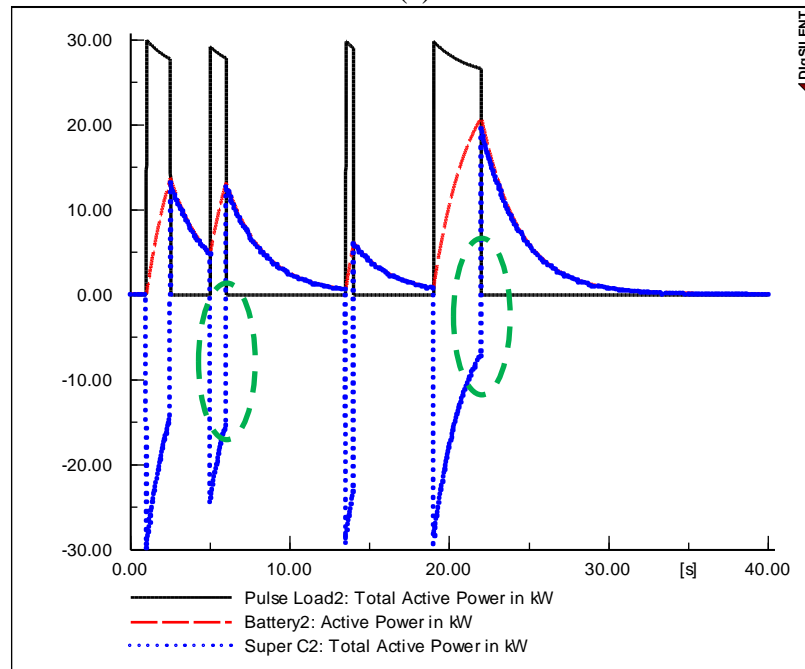
(b)

Figure 3.12 ES output and load powers: Case III
20 kW non-uniform PPL, (b) 30 kW non-uniform PPL.

20.00
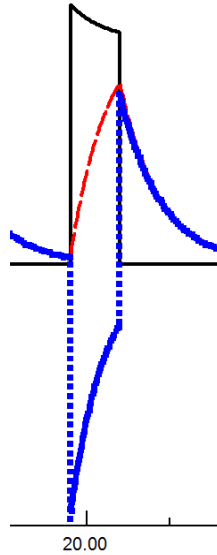
Figure 3.13 A close-up of the wide pulse to show the ES dynamics.

In order to get a better understanding of the ES dynamics and inter-dynamics between the SC and the battery, a close-up of the wide pulse (fourth) of PPL2 profile, is shown in Figure 3.13. At the beginning of the pulse, the SC starts injecting high power rapidly. Then, the injected power by the SC decreases as the output power of the battery rises. This is explained by the vast differences between the time constants of these ES technologies. At the end of the pulse, the SC output is cut while it has some energy to supply. This emphasizes the fact mentioned earlier that the SC energy is enough to supply the deficit. The SC state changes from discharging to charging in a very short time, where discharging is indicated by the negative power and charging is indicated by the positive power. The output power of the battery decays and coincides with the charging power of the SC. This leads to recognizing the fact that, in this configuration, the excess decaying power of the battery goes to charge the SC.

The output powers of the generators in kW are depicted in Figure 3.14(a). It can be seen that the fluctuations are smoother than the base case. The generator overloading is significantly reduced as shown in Figure 3.14(b). MTG1 and MTG2 are overloaded at

a single point on the profile to approximately 110%. ATG1 and ATG2 are overloaded to approximately 105%. These overloading levels are acceptable as it is occurring for a short time period and not frequently. The minimum loading point is around 55% for ATG1 and ATG2.

AC and DC voltages are shown in Figure 3.14(c) and (d), respectively. From both figures, one can realize that the voltage fluctuations are within the range of ±0.04 p.u., which is allowed by the standards. The active powers transferred through the two PWM converters interfacing the DC buses are depicted in Figure 3.14(e). The power transfer is negative during the entire simulation period, this indicates that the power is transferred from the AC side to the DC side all the time. The power is transferred from the AC side during on-the-pulse to contribute to the PPL and during off-the-pulse to charge the ES units and compensate the lost energy. The fluctuations in the transferred power between the AC and DC sides can be reduced by using tight regulators for the charging of the ES units. Regulating the charging of the different ES units is covered in the following chapters in this dissertation.
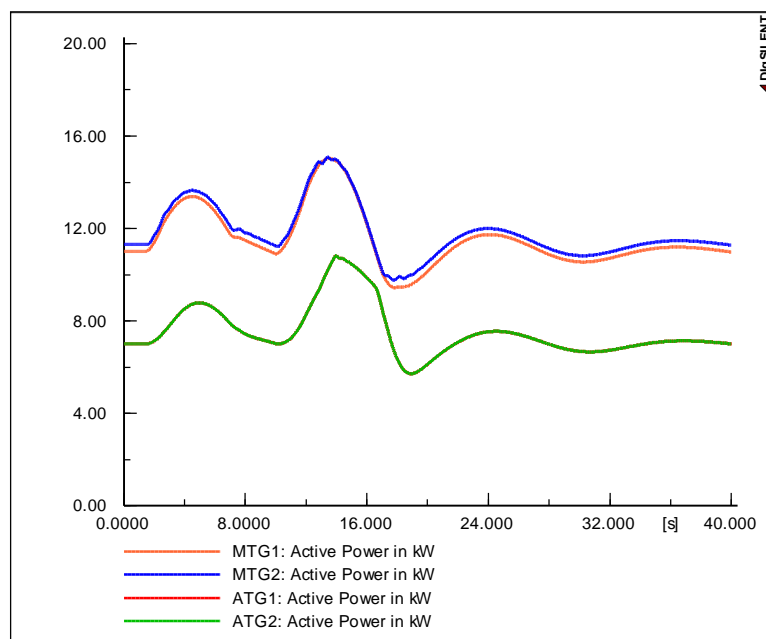
(a)
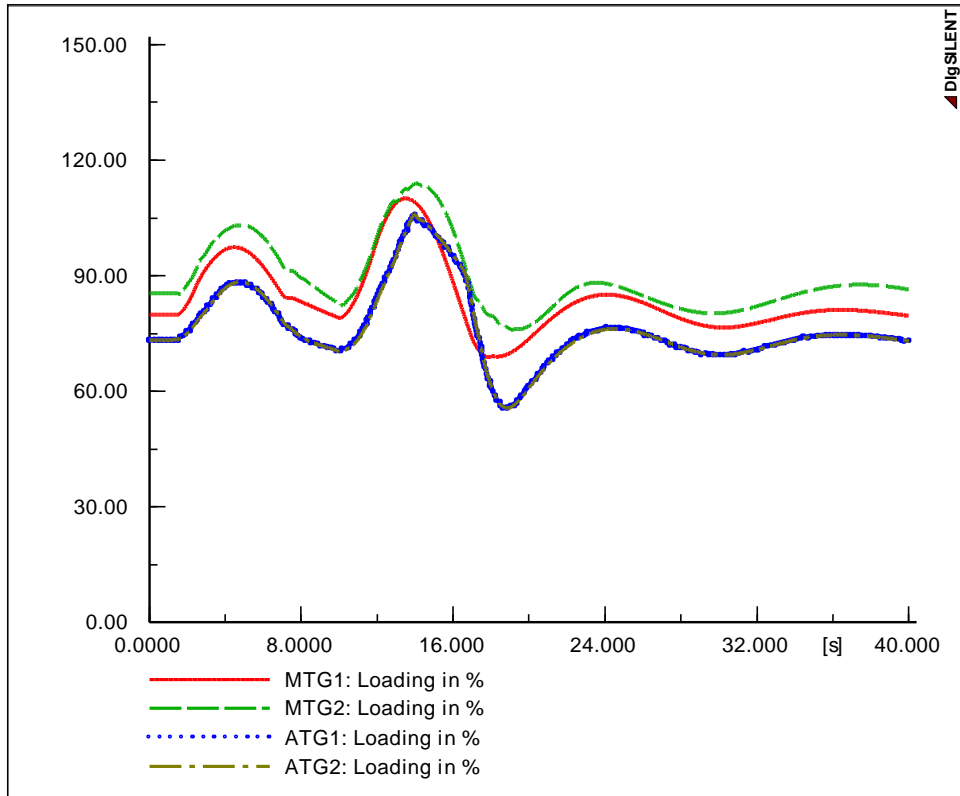
(b)
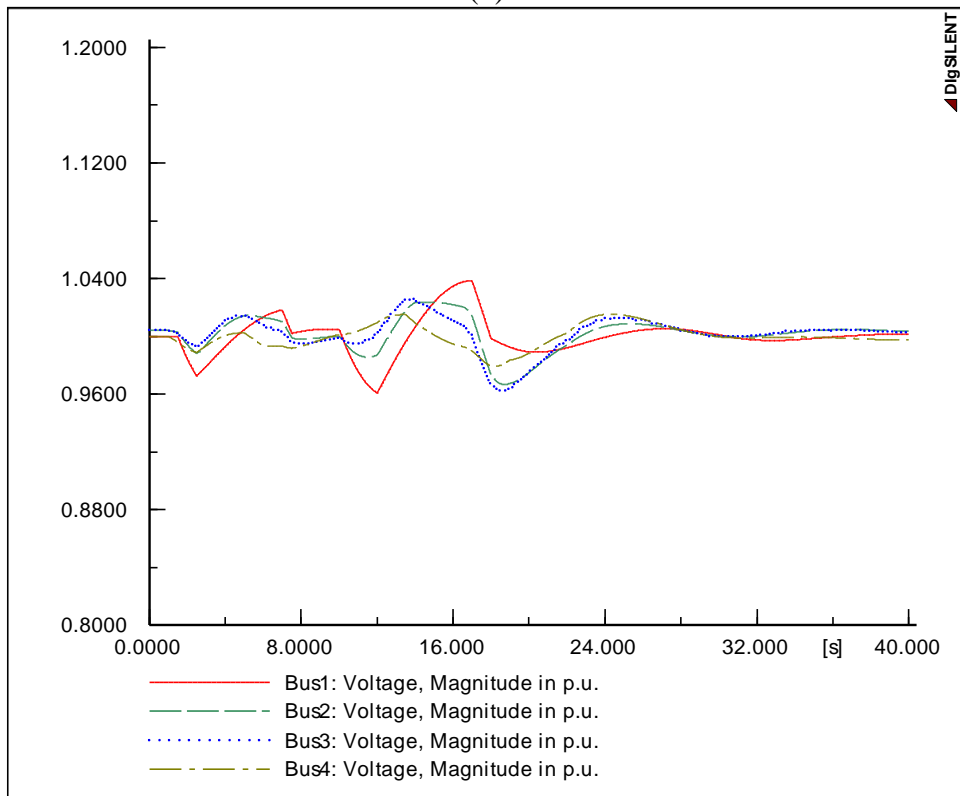
(c)
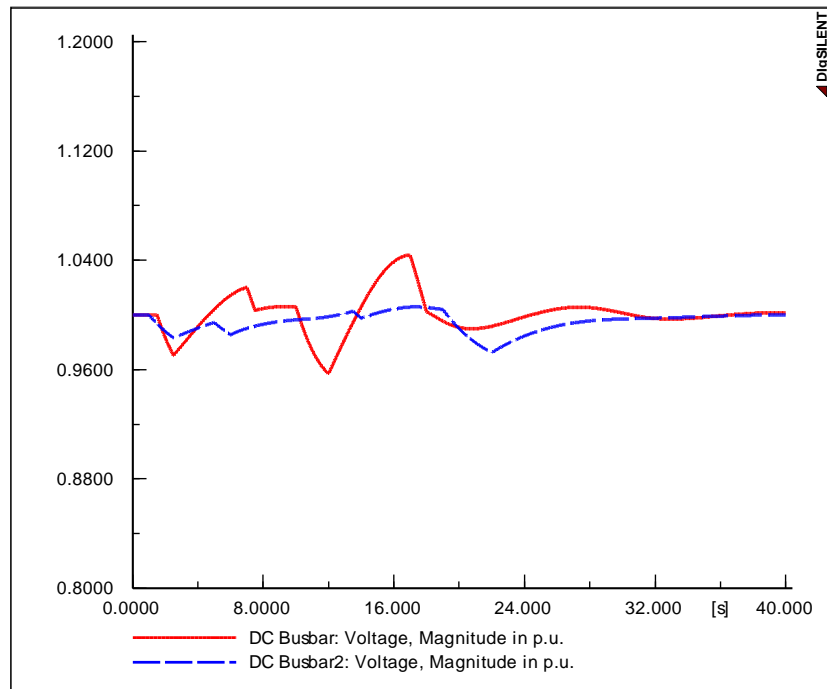
(d)
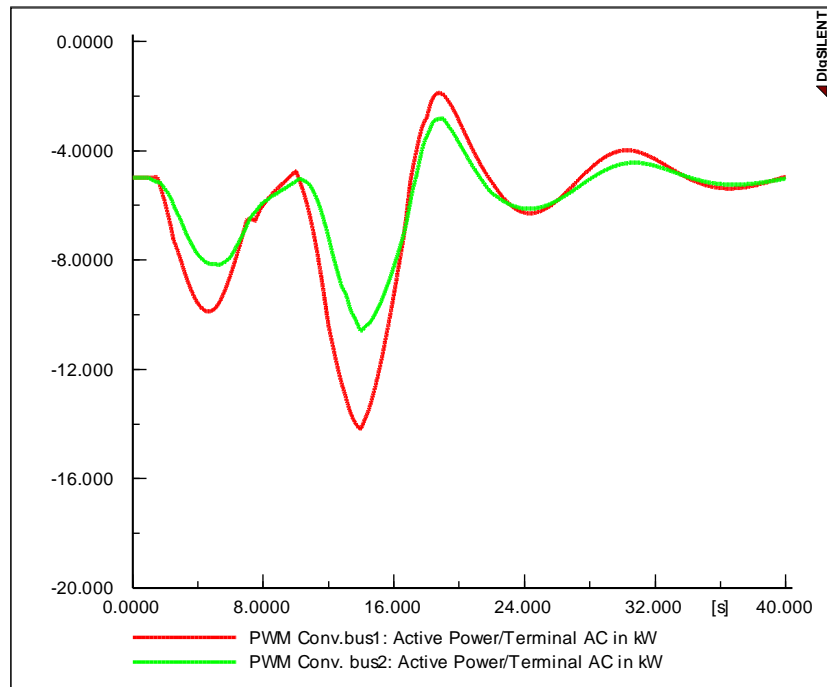
(e)

Figure 3.14 Ship power systems performance, two non-uniform PPLs- Base case.
(a) Generators active power output, (b) Generators percentage loading,
(c) AC bus voltages, (d) DC bus voltages,
(e) Active power transfer between the AC and DC sides.

3.5   Summary

In this chapter, a study based on an empirical approach is presented to investigate the effects of the ES sizing on the performance of the SPS under heavy loading conditions. This study is intended to provide guide lines for the formulation of a comprehensive multi-objective optimization problem. It gives the designer an estimate for the constraints and the limits of the decision variables. More importantly, it helps in determining the initial conditions for the decision variables. This can significantly improve the convergence of the meta-heuristic technique provided in later chapters of this work.

In this study, a Super-Capacitor and battery are used as energy storage systems to mitigate the effects of the pulsed load and prevent the power fluctuations. Three case studies are presented: a single PPL with a non-uniform profile; two PPLs on two different DC busses, one of them is with a non-uniform profile and the other's profile is uniform; and two PPLs, both profiles are non-uniform. The load with a uniform pulsing profile is representing a radar or a sonar. The other load is of higher amplitude and non-uniform operating profile. This load can resemble an EM rail gun or Air Launching System (ALS). Several simulation runs are performed using DIgSILENT PowerFactory, which is a commercial software package. The results are presented and analyzed in detail.

The study starts by investigating the performance of the system with a small ES size, then increases the size gradually. At each size step, the system's performance is investigated. It was shown that the existence of two Pulsed Power Loads can cause severe oscillations in the system, especially if these two loads are not coordinated. It was shown that high power oscillations are occurring repeatedly, which can cause

mechanical failure of the generators. Therefore, the accurate sizing of ES to mitigate these effects is very important to maintain the system's security.

The ES dynamics and inter-dynamics between the SC and the battery during the pulse are investigated. It was shown that, the SC is playing an important rule to supply the energy at the front of the pulse due to its fast response. It was shown that it covers the energy gap caused by the slow response of the battery.

Chapter 4   Battery Management System for Improved Battery Integration to DC distribution Architecture

4.1   Motivations

The structure and resiliency of the emerging smart grid will rely heavily on storage facilities in cooperation with renewable energy to provide uninterrupted service to the customer [182]. The usage of battery arrays continues to grow due to their capability in restoring system voltage and frequency following an outage [183]-[184]. Moreover, promoting smart grid concepts, along with the high penetration of renewable energy sources and distributed generation in modern grid architecture, drives the deployment of new energy storage systems (ESS) [185]. It is well known that the output of the renewable energy sources is intermittent and uncontrollable, therefore ES are used in conjunction with the renewable energy sources in order to make them more usable and achieve the maximum benefits. Wee *et al* proposed a design for a battery-supercapacitor energy storage system to be used with a wind power plant. The goal is to realize a dispatch-able wind power plant, i.e. its output can be controlled based on the operator or system requirements [186].

Since 2009, renewable energy generation has increased at an unprecedented rate, while costs have decreased dramatically. Motivated by the global call for enhancing transparency and preserving nature, fear of environmental changes, wider deployment of renewable energy resources and introduction of demand side management, the installation of energy storage has been accelerated and gained significant momentum. As evidence, in 2015 alone, the United States doubled the installed capacity of advanced energy storage to 500 MW, and deployment of this key resource is projected to continue to expand [187].

Success of large scale practical projects involving energy storage requires the development of intelligent control and monitoring techniques for energy storage, especially when deployed in a large scale applications. In these applications, any minor inefficiency in a single energy storage unit may result in significant losses on the global scale. Furthermore, when talking about mission-critical applications, the reliability requirements are very high. Therefore, monitoring energy storage arrays to predict any fault in a single energy storage unit and isolate it before propagation is mandatory. Another highly interesting subject is the battery second use (B2U) or sometimes known as second life battery. Simply, it implies reusing the degraded batteries after they are decommissioned from mission-critical applications in a less sensitive application. It is well known that the capacity of chemical batteries fades as they are being cycled (charging/discharging). Experimental studies showed that after applying 3000 full charge-discharge cycles to high-power Lithium Iron Phosphate (LiFePO4) battery cells, the capacity and Open Circuit Voltage (OCV) profile are changed from their original values when the battery was at full State of Health (SOH) [188]. Therefore, implementing the B2U concept is not an easy task. The reason for this claim is that it requires accommodating different used batteries with different capacities and OCV in the same array. Consequently, this requires specialized control and coordinated charging/discharging to avoid further rapid capacity degradation.

The US energy storage market has witnessed a significant growth during the past few years. A jointly report published by Energy Storage Association (ESA) and GTMResearch [189] outlined that 18.3 MW of energy storage were deployed in the first quarter of 2016. This amount represents an increase of 127% from the first quarter of 2015. The deployment of energy storage in the US in the first quarter of each of the four years (2013-2016) is depicted in Figure 4.1. A significant increase in the deployed

energy storage from Q1 2015 to Q1 2016 can be noticed. Furthermore, in this report, which monitors the energy storage in the US, it is anticipated that the energy storage market in the US will be worth $2.9 billion by 2021 [189]. Figure 4.2 shows a bar chart illustrating the historical and expected growth for the US energy storage market expressed in monetary value. It is expected by the reporters that the US energy storage market will be worth $528 million at the end of year 2016 and continue to grow exponentially. Also, the share of the market is divided into three categories: residential, non-residential and utility.
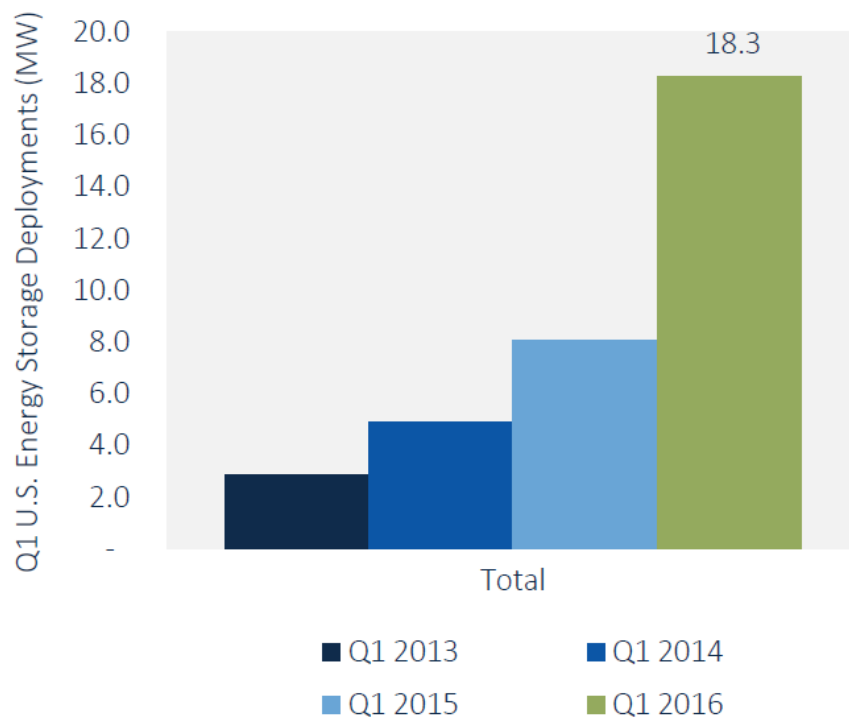
Figure 4.1 Energy storage deployment in USA in the first quarter of four years in MW [189]

Based on the aforementioned discussion, overview and statistical facts, it can be emphasized that the energy storage deployment has been accelerated and will continue with the same trend. It should be highlighted that in modern systems, the energy storage cannot be operated without a controller. This controller is responsible for controlling

the charging rates to be within the allowed limits by the manufacturer and preventing the State of Charge (SoC) from going below certain limits and performing several other functions. This created a serious motivation for creating a Modular Energy Storage regulator (MESR). The detailed control, design, implementation and experimental testing are presented in the following sections.
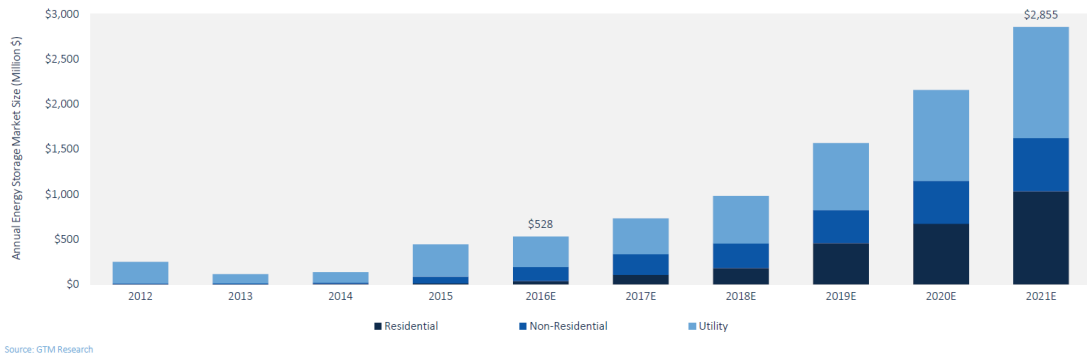
Figure 4.2 Historical and expected US energy storage market growth.

4.2 Battery Management Systems: Current State of the Art

Currently, batteries are being widely deployed for usage in grid energy storage due to their versatility and low cost. Their share in energy storage deployment is higher than that of other ES technologies (supercapacitors, flywheels, Compressed Air Systems (CAS), Superconducting Magnetic Energy Storage (SMES), etc.). However, since they are chemical based, batteries are burdened by a number of factors, which result in a declination of their performance without the proper management system. As a battery ages, the series resistance will begin to increase as it is susceptible to many factors that impact its lifespan [190]. Most notably, the number of cycles that it has charged and discharged, effects of temperature, and the types or levels of discharge currents it has been exposed to [191]. These factors lead to electrochemical changes inside a battery, which result in decreased usable capacity and inefficient charging. A number of studies have been presented in literature on Battery Management System (BMS) architectures,

97

but most have only looked at case studies under smaller configurations. In [192], a management system solution is presented to highlight the importance of including battery State of Health (SoH) in measurements for grid applications. Focusing on a range of discharge rates and the Depth of Discharge (DoD) for two parallel-configured lead-acid batteries, the Life Consumption Rate (LCR) is modeled for each of the two batteries independently. The total SoC of a battery stack can be provided through the means of the current integration method, or in some simplified cases, voltage-based measurements [193]. In [194], an advanced method to depict the SoC of a lithium-ion utility array is tested in grid-connected and islanded modes of microgrid operations. Three modes of operation are proposed to indirectly measure the SoC of the battery array. The system in [194] was able to demonstrate the effectiveness of its control strategy, but was still unable to access individual battery modules within the array.

Although individual modules have been difficult to access or be independently controlled in series configurations, research has been conducted with SoC balancing for parallel connections. In [195], a supervisory energy management algorithm is designed to regulate charge flow to a bank of three batteries. A constant current is used to charge each battery independently with respect to the load profile and individual SoC measurements. Balancing of the array was accomplished simply through switching and was unable to adjust the charging current. Different methods of cell equalization for lithium ion batteries, including the flying capacitor charge shuttling method, shared single and multiple transformer methods, are discussed in [196]. Reference [197] identifies a common battery management and cell-balancing technique employing a topology, which has been developed specifically for lithium ion cell balancing systems when they are interfaced with power electronic converters. In this topology, the charging voltage is pulsed through a control signal and passed through a transformer.

The current from the cell stack induces currents in each of the secondary coil windings where each one (connected to each battery) with the least reactance will have the highest induced current. This ensures that each cell has a charge current proportional to its SoC. This method is effective in balancing, but still lacks the capability of extracting and isolating each battery from the configuration. Switching is only provided from the charging circuit, where the loading side is not given the option of using an alternate path around the battery. Figure 4.3 shows the circuit diagram for this charging scheme.
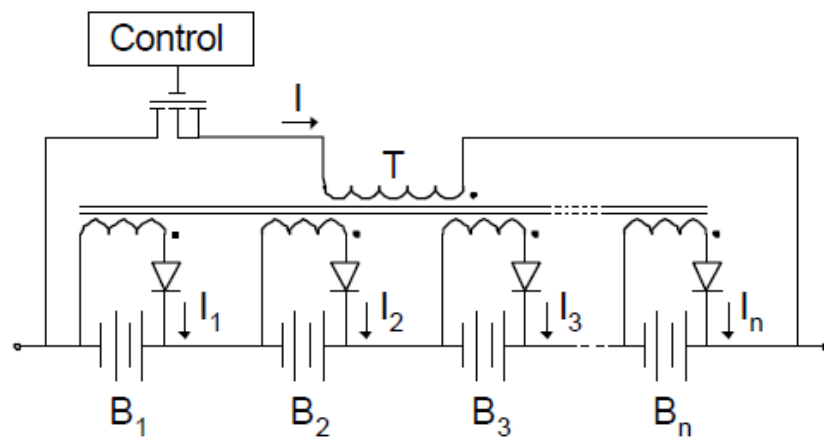
Figure 4.3 Single primary multiple secondary transformer Li-ion charging scheme.

In [198], a comprehensive review of the existing BMSs for grid-scale applications is provided. A notional model for implementing a BMS into a battery energy storage system (BESS) is presented. In this model, a number of objectives are identified, including source peak power demand, cell balancing, and thermal control, but it still lacks the capability of extracting individual cells from a stack or even parallel configuration. In this case, SoH and SoC methods are identified for lithium ion and redox flow batteries only. Although the lead acid is identified as a medium of technological maturity and is low cost, it is not presented for use in this survey. Two simplified battery management schemes are presented in [199] and [200]. The latter

emphasized the importance of not neglecting the differences in a battery's internal resistance during charging.

In [201], an energy management system is developed with respect to extending the lifetime and efficiency of an ESS. Using the Peukert Lifetime Energy Throughput (PLET) model, energy efficiency of the ESS is improved. An optimization algorithm is presented in [202], where a discrete-time model of an electrochemical storage device is developed to introduce a battery system but is limited to simply a wind turbine and sodium nickel chloride battery combination.

Pulsed charging has introduced revolutionary control over battery charging behaviors, accelerating charging rates and providing battery charge balancing [203]. In [204], a battery equalization method is proposed utilizing a positive/negative pulsed charge to balance cells for an electric vehicle (EV). Pulsed charging is not only used as a method to regulate charging current. In the case of a damaged battery, charging current pulses can be used in an attempt to characterize or improve the battery SoH by neutralizing the internal electrolyte [205]-[207]. Introducing this capability to each battery in a stack configuration would not only provide controlled current charging, but also a tool to potentially revive batteries in the event of a failure.

Based on the presented literature survey, most of these energy storage management systems focus on either cell equalization, SoC and SoH estimation or pulsed charging. Moreover, some of these schemes involve transformers or large complicated power electronic devices. To the best of the author's knowledge, no system has all the aforementioned capabilities and features like the one proposed in this dissertation.

This chapter presents the development of a Battery Management System (BMS) to monitor individual batteries inside a series configuration and identify independent voltages, current contributions, and SoC levels for each battery. A method to balance

SoC and diagnose SoH is established where a BMS can fully decouple a single unit (a unit refers to a battery or a stack within an array) from the system and apply it to a charging and diagnostics bus while still maintaining a connection to the load. The system bypasses the decoupled battery to guarantee continuity of supply and normal operation of the entire array. The proposed system offers the capability of charging more than one battery at the same time with different charging levels by applying pulsed charging currents with different duty cycles and frequencies to control the charging energies. The voltage fluctuations, accompanied by the coupling/decoupling of batteries, are mitigated by a simple DC-DC boost converter with the well-known conventional topology to maintain bus voltages, preventing the propagation of problems from the BMS to the utility side.

This work is motivated by the imperative need for individual and independent control of each unit (battery or stack) in the array to achieve efficient operation. Another objective is to prevent failure of a single battery from impacting the operation of the whole array. The system presented can be suitable in applications ranging from microgrid to utility scale and is tested with heavy pulsed loads to be suitable in shipboard power systems. The proposed topology offers a variety of features and capabilities, which can be summarized as follows:

- It is capable of controlling each individual unit within a series/parallel array, i.e. each single unit can be treated, controlled and monitored separately from the others.

- The capability to charge some units within a battery array while other units continue to serve the load. By applying a pulsed charging profile at different frequencies and duty cycles, the BMS can regulate the charging energy to each unit. Hence, SoC balancing can be accomplished without the need for power

electronic converters.

- It is able to electrically disconnect a unit and allow the operator to perform the required maintenance or replacement without affecting the performance of the whole array.

- Considering the appropriate design, selection of relays and other components, the system can be expanded for controlling other types of energy storage.

- The system can be designed and implemented at low cost.

It is worth mentioning that the presented BMS has gone through various developmental phases in which several modifications, either in the control or the hardware, have been done. In the first stage, the scope was to control and manage a series array of lead acid batteries; this stage is covered in this chapter. Thus, all the discussions in this chapter are focused on lead acid batteries. However, in later developmental stages, the BMS was expanded to be utilized with arrays including Lithium-ion and/or supercapacitors. Also, major modifications have been introduced to the system to be used with parallel configured ES arrays. Further, more control functions have been added. For space and time limitations, some phases and unsuccessful prototypes are omitted and not presented in this dissertation.

4.3 Theory and Background

The system under test involves the connection of a battery bank divided into an extendable number of stacks where each stack contains N_{batt} batteries. A common misconception is that each battery in the array introduces identical aging and current distributions when their in-service dates are identical. Nevertheless, without the measurement of voltage and current from each battery, there is no guaranteed method to determine the SoC.

Consider a simple 4 - 12V battery series array with nominal array terminal voltage

of 48 VDC with a 110 Ah capacity. When charging the array, it is found that only one battery achieves the true full charge level, where the remaining batteries are cutoff prematurely to different SoC levels from 90% to 98%. Equation (4-1) presents an averaging function to obtain the SoC of the entire array:

$$SOC_{tot} = \frac{1}{N_{batt}} \sum_{i=1}^{N_{batt}} SOC_i \qquad (4\text{-}1)$$

where SOC_i represents the SoC of each battery connected in series. It can be shown that the actual SoC of this configuration would be reduced by 5% until individual battery charging levels are corrected. A 5% miscalculation of SoC appears to be minimal, except when compared to the capacity of the array where 5.5 Ah of energy is left unutilized. Furthermore, the continued undercharging of batteries 2-4 would eventually result in the permanent inability to charge the battery to its full capacity [208]. This performance shift is driven by differences in the SoH of each battery. Varying material impurities, thermal stresses and minute offsets in manufacturing processes can produce a wide range of results. These metrics are further complicated when a pulsed load or charging current is introduced. To mathematically model the shift, the operation of lead acid battery is discussed. The electro-chemical formula describing the battery operation is defined in Equation (4-2), where lead and lead dioxide electrodes are placed in an electrolyte of sulfuric acid and water to precipitate the storage and removal of electrons.

$$Pb + PbO_2 + 2H_2SO_4 + 2e^- \rightleftharpoons 2PbSO_4 + 2H_2O + 2e^- \qquad (4\text{-}2)$$

A fully charged battery has an electrolyte composed of approximately 60% sulfuric acid and a discharged battery is primarily composed of water. Discharging results in precipitation and the removal of electrons from the sulfuric acid, thereby resulting in spent solid sulfate at the plates. The charging process removes the solid sulfate and

places it back into the electrolyte, but the process is not 100% efficient and some solid remains. Over many cycles, the sulfate mass increases and this phenomenon, known as sulfation, is one of the largest culprits impacting reduction of SoH and capacity-loss. Some works have been published to find an electrochemical method to essentially break down the collection of sulfate at the battery plates [205]-[207]. If breaking down solid sulfate is successful, it can be introduced back into the electrolyte. The pulsing of electrical current is analogous to repetitively pressing against the sulfate layer at the pulse frequency. The material stress associated with this can result in cracking of the sulfate layer.
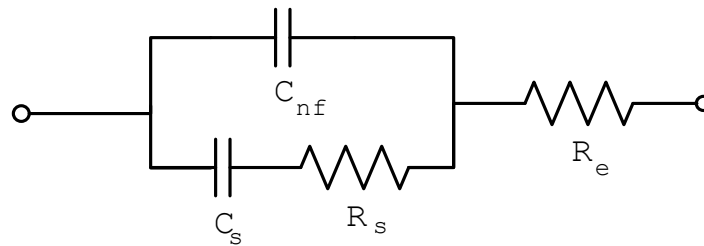
Figure 4.4 Equivalent circuit model for a Lead acid cell based on EIS.

Analyzing battery behavior with varying SoH with respect to a current pulse requires an extension from the common battery equivalent circuit to account for an impedance variance present at the interface between the electrode and electrolyte. Electrochemical Impedance Spectroscopy (EIS) introduces kinetics to solve for three new parameters governing Lead acid cell behavior [209]. As shown in Figure 4.4, a modified RC circuit is added in series with the resistance of the electrolyte (R_e), where C_s and R_s represent faradic capacitive and resistive elements in parallel with non-faradic capacitance (C_{nf}) value to explain the reduced absorption and extraction of electrons from the electrodes into the electrolyte. The transfer function depicting the overall impedance is:

$$Z(s) = \frac{R_s C_s s + 1}{R_s C_{nf} C_s s^2 + (C_{nf} + C_s)s} + R_e \tag{4-3}$$

The voltage $V(t)$ response on the battery cell V_c is:

$$V(t) = V_c - \left[\frac{C_s e^{-\frac{t(C_s + C_{nf})}{C_s C_{nf} R_s}}}{C_{nf}(C_{nf} + C_s)} + \frac{1}{C_{nf} + C_s} + R_e \delta(t) \right] i(t) \tag{4-4}$$

where C_s and C_{nf} are chosen to model the capacitive response on the battery during and after a pulse, R_s controls the voltage drop following a pulse train, and R_e controls the steepness of the voltage drop ΔV in each pulse.

A comparison is shown in Figure 4.5 where the solid and dashed lines depict pulsed load responses for a healthy versus damaged battery. Minor adjustments are made to C_s and C_{nf} to depict a reduced response and recovery time following a pulse on the damaged battery, but R_e and R_s represent the most salient characteristics. The voltage drop after applying a pulse to a healthy battery ΔV_{eh} increases significantly as the battery ages, where a damaged battery voltage drop is much sharper ΔV_{ed}. In addition, impacts of the pulse train on a healthy battery $V_{sh}{}'$ present a much gentler voltage slope than that of a damaged battery $V_{sd}{}'$. The steeper downward trend is directly correlated to an SoC impact. Without accurate measurements for each battery, one would be unable to identify these characteristics and detect possible damage.
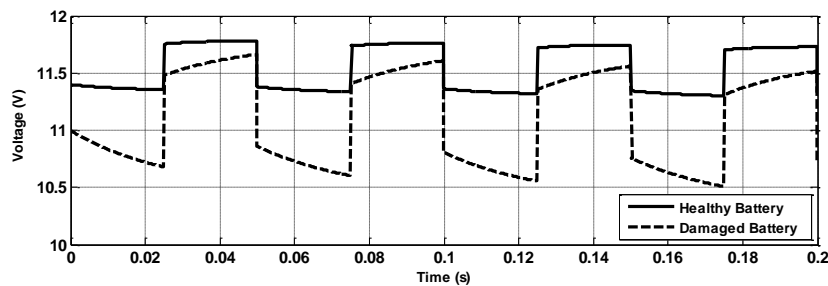
Figure 4.5 Pulsed load response on healthy & damaged batteries.

4.4 BMS Design and Hardware Implementation

This section discusses the philosophy of the BMS design and its hardware implementation. As mentioned earlier, in section 4.2, over the period of the preparation of this dissertation, the proposed BMS has gone through a wide variety of changes and development phases. The phase presented in this section was focused on Lead acid batteries. The other developments and expansions are discussed further in the following chapters of this dissertation. It is worthy to mention that this design is generic and the developed BMS can be connected across an individual battery or stack of batteries in large-scale implementations. In this context, the design process and implementation is explained for 12 V batteries, however, it should be kept in consideration that the system can be scaled up to utility scale with adequately considering the current and voltage ratings. The overall topology for connecting BMS units for N_{batt} batteries is shown in Figure 4.6. The low voltage charging and diagnostic bus is connected in parallel to all BMS links. The voltage of this bus is selected to be 14.7V to fulfill the charging constraints of Lead acid batteries. However, the voltage of this bus can be changed based on the type and requirement of the installed ES type. The terminals of the battery bank are connected to a DC-DC boost converter to stabilize the bus DC voltage. This converter is unidirectional, as the charging of the batteries is accomplished through another bus. This can be considered as an advantage, as it reduces the system's complexity and cost and increases its reliability.

The schematic for a single BMS unit is shown in Figure 4.7. The battery is placed in-between a network of relays in order to provide complete coupling and decoupling.

- *DC Bus Connectivity:* In order to achieve full isolation, two normally-closed (NC) relays connect the positive and negative terminals of the battery to the DC bus. A normally-open (NO) relay is connecting the positive terminal of the BMS to its

106

negative side to offer a battery bypass circuit decoupling it from the array while still providing an alternative path to maintain continuity of supply. An interlock is provided between the three relays to avoid simultaneous connection. This would fully isolate the battery in the case of performing maintenance or coupling the charging circuit.
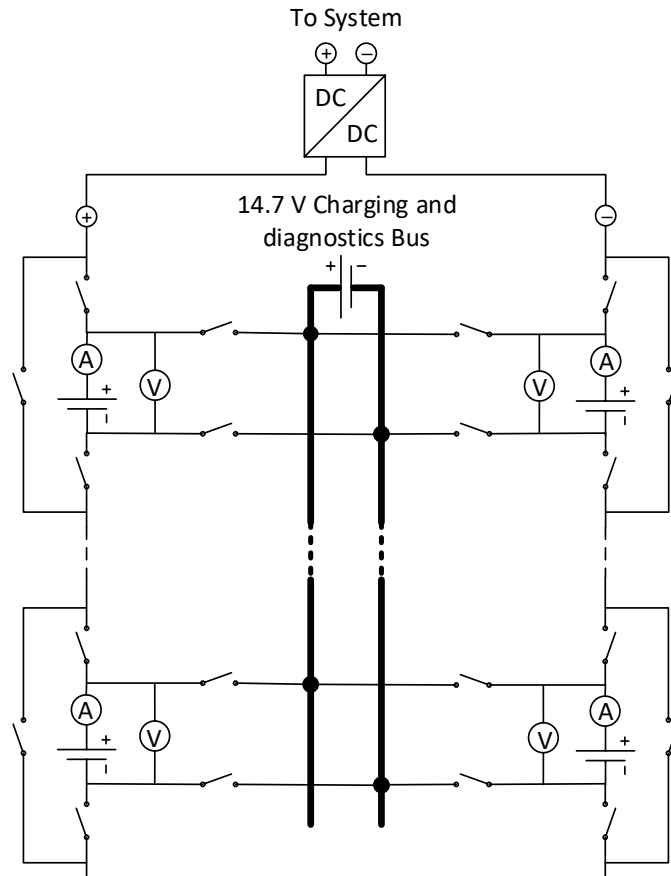
Figure 4.6 Battery Management System for Array of N_{batt}.

- *Current Measurement:* Current measurement is provided directly at the battery terminals. This specific point is selected to enable measuring the charging/discharging current of each battery independently from the current passing through the array. In hardware implementation, a current transducer LA 25-NP is installed in series in the current path from the positive terminal. The LA 25-NP can measure currents up to 36 A. The battery used for testing is rated 110 Ah, thus the

nominal C20 current is rated 5.5 A. A constant current of up to 7x the nominal (~C3 rate) can be passed and measured accurately through this transducer.
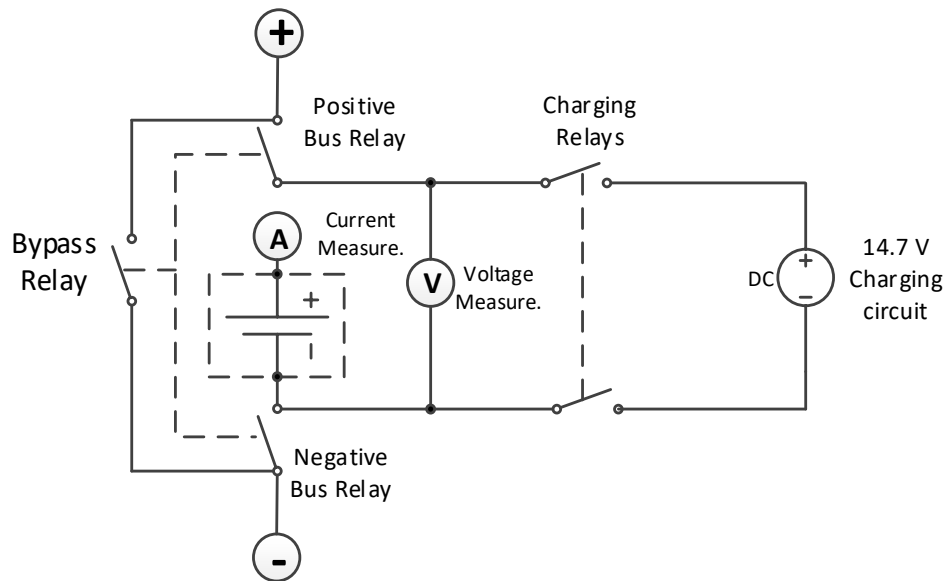
Figure 4.7 A schematic diagram for individual battery management unit.

- *Voltage Measurement:* Due to limitations of the most data acquisition equipment available in the market, a voltage range of ±10 VDC must be adhered to. Since stack voltages will range from 10.5 VDC to 14.7 VDC, this had to be stepped down with a voltage transducer LV25-P. Using a simple voltage divider circuit would not be possible because of lacking the required isolation. With respect to keeping the BMS universal for usage with other battery chemistries and cell configurations, it was decided to set the maximum voltage to handle up to an 8-cell lithium ion series battery configuration (≤29.6 VDC). Similar to the current measurement, the voltage transducer is placed directly at the terminals of the battery. It is connected after the charging relays to measure the Open Circuit Voltage (OCV) of the battery when it is disconnected form the array.

- Charging and Diagnostic Bus Connectivity: The BMS is connected to this bus via two switches to fully couple/decouple the DC bus. Figure 4.7 identified the bus

operating voltage at the typical charging voltage for a lead acid battery (14.7 VDC), but it has the versatility to operate at a very wide range of voltages to accommodate different types of batteries. This is one of the major flexibilities added by the proposed system. Two (Normally Open) NO relays offer a connection or total isolation from this bus depending on the operating scenarios. This bus can provide the charging current for multiple batteries in parallel, or the isolation of a single battery where diagnostics can be performed. Battery diagnostic signals can be sent directly to the battery to evaluate its performance or individual SoH. This useful feature can allow an operator to initiate test procedures and identify a consistently failing battery while the system is running. These relays are interlocked with the other relays to prevent simultaneous charging or discharging of the battery.
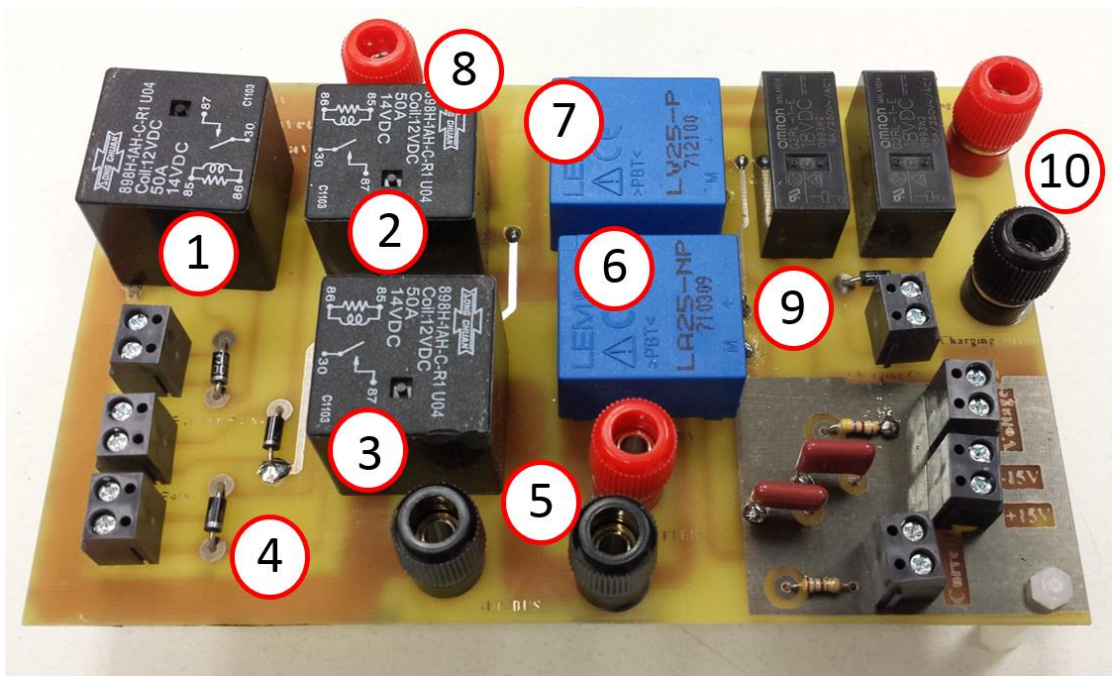
Figure 4.8 A prototype of Battery Management System.

Figure 4.8 shows the laboratory prototype for the BMS unit implemented on a 10 x 16 cm Printed Circuit Board (PCB), which reflects the compactness and simplicity of the proposed design. The components on the board are: 1) bypass relay, 2&3) positive

and negative DC bus relays, respectively. 4) freewheeling diode for DAQ device protection as per manufacture recommendation [210], 5) battery terminals, 6) current transducer, 7) voltage transducer, 8) DC bus terminals, 9) charging bus relays, 10) charging bus terminals. A unified color coding is followed for all terminals; red for positive and black for negative.
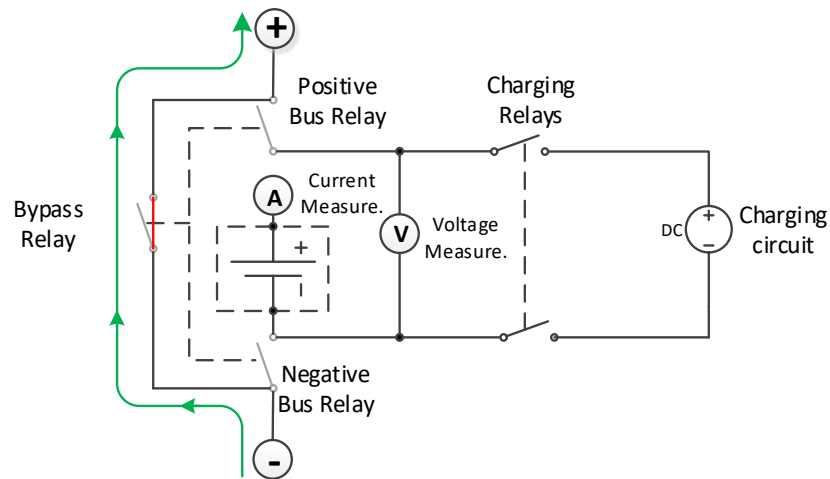
Figure 4.9 BMS configuration in idle mode.

4.5 BMS Modes of Operation

The BMS can be operated in 3 modes:

4.5.1 Idle mode

In this mode, all relays are open except the bypass relay. In this case, the voltage measured at the battery terminals is its Open Circuit Voltage (OCV). The whole energy storage bank can continue operation. This mode is useful for maintenance because the battery is completely isolated from the electric system and can be safely accessed by a maintenance person safely. The BMS configuration and current flow in the idle mode is shown in Figure 4.9.

4.5.2 Charging Mode

In this mode, the charging relays and the bypass relay are closed while the negative

and positive bus relays are open. In this case, the battery is connected to the low voltage charging and diagnostics bus to be charged. The operator can use either constant or pulsed charging. The circuit configuration is depicted in Figure 4.10, it can be seen that the bypass relay provides an alternative path for the current while the battery is being re-charged to restore some of the lost energy.
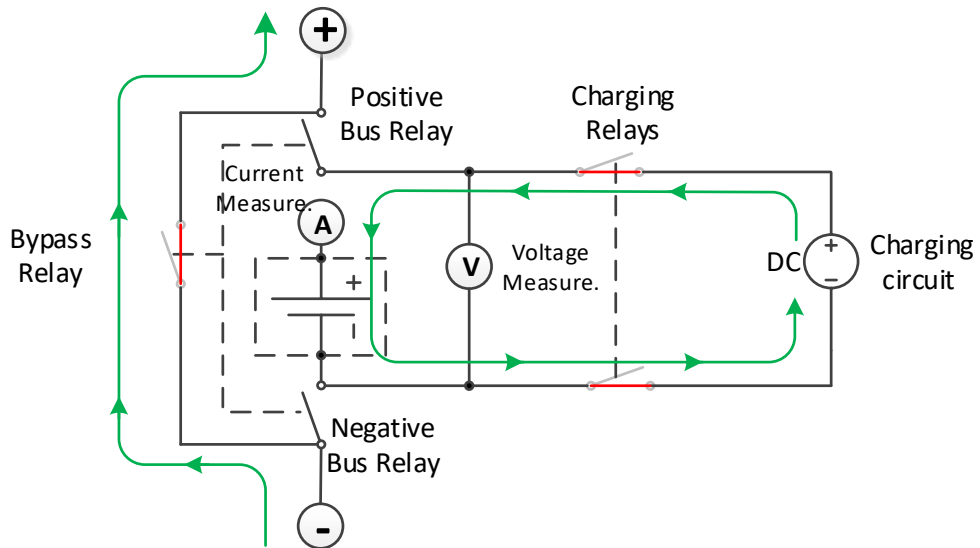
Figure 4.10 BMS configuration in charging mode.
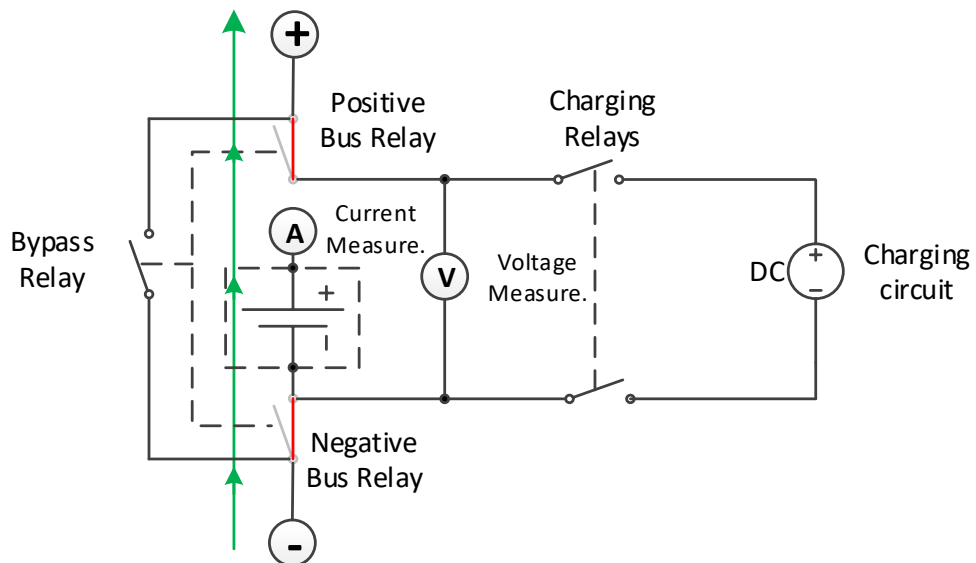
Figure 4.11 BMS configuration in normal (load connected) mode

4.5.3 Load connected mode

This is the normal operation mode. In this mode, the bypass and charging relays are open while the positive and negative bus relays are closed. In this case, the battery is connected to the stack and contributes to supply the load. The BMS configuration in the normal operation is as depicted in Figure 4.11. Table 4-1summarizes the statuses of each BMS relay in the three operation modes.

Table 4-1 BMS relay status in the three operation modes.

	Positive bus relay	Negative bus relay	Positive charging relay	Negative charging relay	Bypass relay
Ideal Mode	OFF	OFF	OFF	OFF	ON
Charging Mode	OFF	OFF	ON	ON	ON
Load Connected Mode	ON	ON	OFF	OFF	OFF

4.6 Control and Monitoring Platform

Voltage and current measurements are collected from each BMS and hardwired to a NI-9206 DAQ module manufactured by National Instrument. This module is a 32-channel single-ended/16-channel differential analogue input module. The voltage and current on the low voltage and the high-voltage sides of the boost converter are measured as well. Control commands are passed to the switching relays from a NI 16 Digital Input/16 Digital Output channel module. The two modules are connected to the supervisory computer through the NI 9174 4-slot USB chassis. The implemented control and monitoring platform is as shown in Figure 4.12. Real-time measurements are provided to the operator scaled back to the real values. This is done by multiplying the raw measured data by the reciprocal of the voltage and current transducer gains.

Since Hall-effect sensors are used in this prototype and they are known to exhibit bias to the measurements in some cases, bias adjustments had to be done from the LabVIEW to assure the accuracy of the measurements.
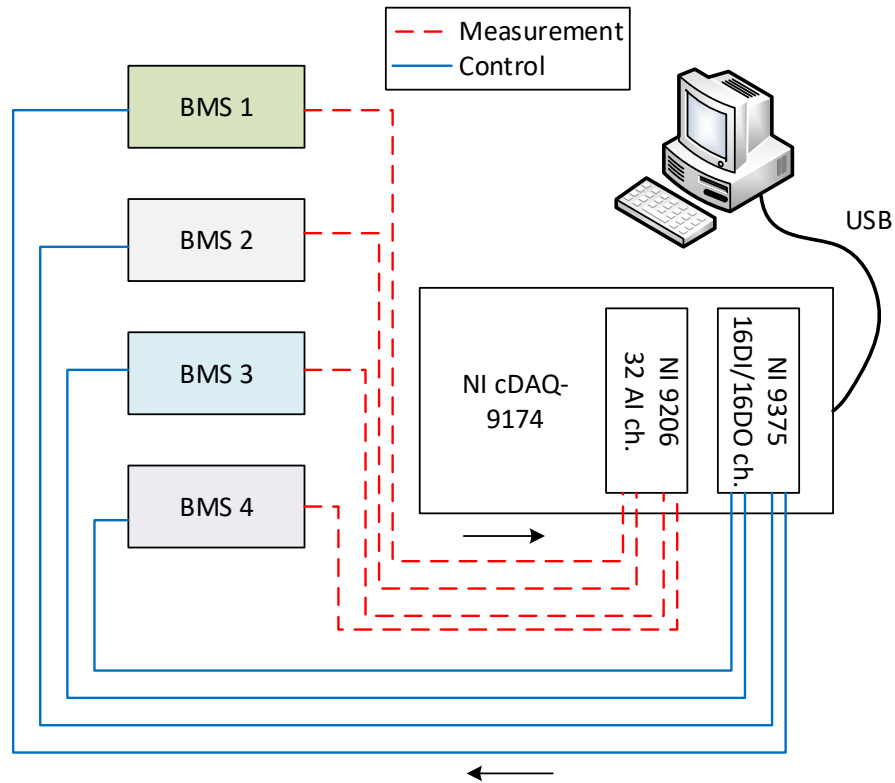
Figure 4.12 Integrating the developed software to the hardware platform.

A Graphical User Interface (GUI) has been designed using LabVIEW in a way to be clear and user-friendly. The design of GUI is as shown in Figure 4.13, which is captured directly from the screen. Please note, the GUI design was optimized to fit in two monitors or an ultra-wide screen. DC Bus parameters and a graph depicting the input and output voltages from the DC/DC converter, as well as the load current, is shown. Several controls are provided to operate the load in constant or pulsed conditions, where the frequency and duty cycle of the pulsed load can be controlled. Voltage, current, power, charge rate (C-rate), SoC and Ampere-hour (Ah) energy indicators are provided for each battery. Each BMS has its own control section and measurements provided in a separate tab. C-rate measures the current into or out of the

battery with respect to its capacity and can be used as a metric to analyze each battery's performance. The C20, or 20-hour discharge rate, provides the standard operating condition when estimating capacity output for the SoH. As the C-rate increases, the available usable capacity will be decreasing at a high rate. This value is most useful in the discharge phase, as it will influence run-times, operation voltage ranges, and SoH progression. The user has the ability to designate an independent charging method for each BMS. In charging mode, the battery is fully decoupled from the series stack, where the bypass relay is activated to continue normal system operation. Three modes are provided: Off, Constant Charging, and Pulsed Charging. A section for data logging control is provided, where there is a button to start data logging. The collected real-time measurements are saved in either an .xlsx or .csv files based on the user preference.
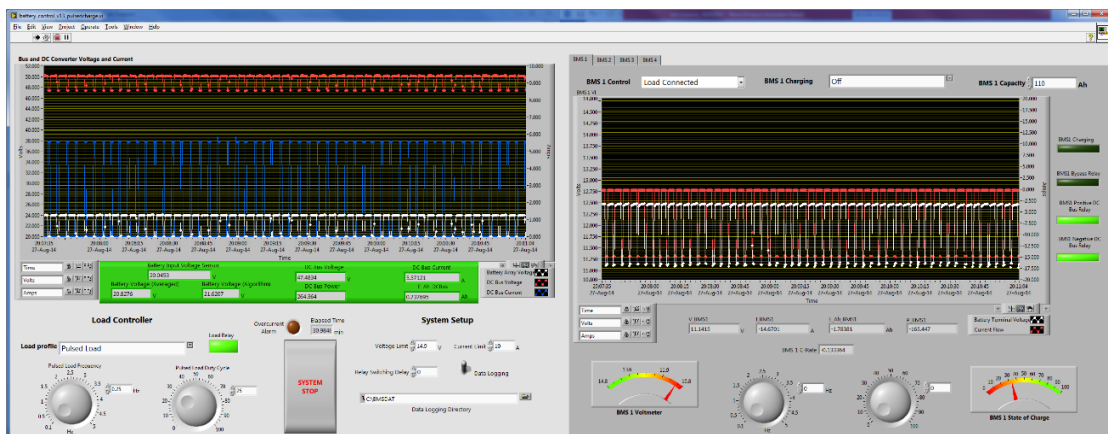
Figure 4.13 Designed user friendly Graphical User Interface (GUI).

4.7 Experimental Results and Discussion

In order to test and verify the applicability of the developed design, a testing platform is established at the FIU smart grid test-bed, which is a part of the Energy Systems Research Laboratory (ESRL) facility. Four complete BMS units have been built and the hardware setup is shown in Figure 4.14. The system features 4 BMS units connected in series to support a 48 VDC bus, which is widely used in

telecommunication applications. The input and output voltages to the DC-DC converter are shown on two Fluke 289 multimeters, from left to right, respectively. The current bus voltage is 49 V. Three commercially available DC-DC boost converters are connected in parallel to permit an output current up to 30 A. Four 12 V, 110 Ah sealed lead-acid batteries (model: UB121100) are used for the experiments. More information about the battery can be found in [211]. Only two batteries are being connected to the low voltage side of the DC-DC converters to serve the bus. The input battery bus voltage is only 20.1 VDC. The reason for this is that one of the batteries has very low SoH; its Open Circuit Voltage (OCV) is as low as 8 V. This battery was selected intentionally for experimental purposes. Each battery has a different SoC, where some are deeply discharged and others are highly charged. In order to validate the plausibility and prove the capabilities of the developed BMS, the BMS units are tested experimentally under realistic conditions similar to real-world conditions. The four BMS units are connected to four batteries with different SoC and SoH levels. Different scenarios are created with different events and load profiles.
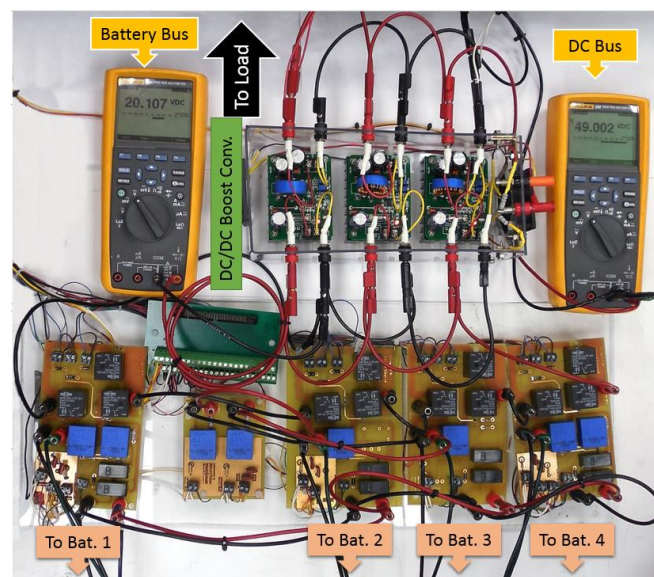
Figure 4.14 Hardware setup with 4 BMS units.
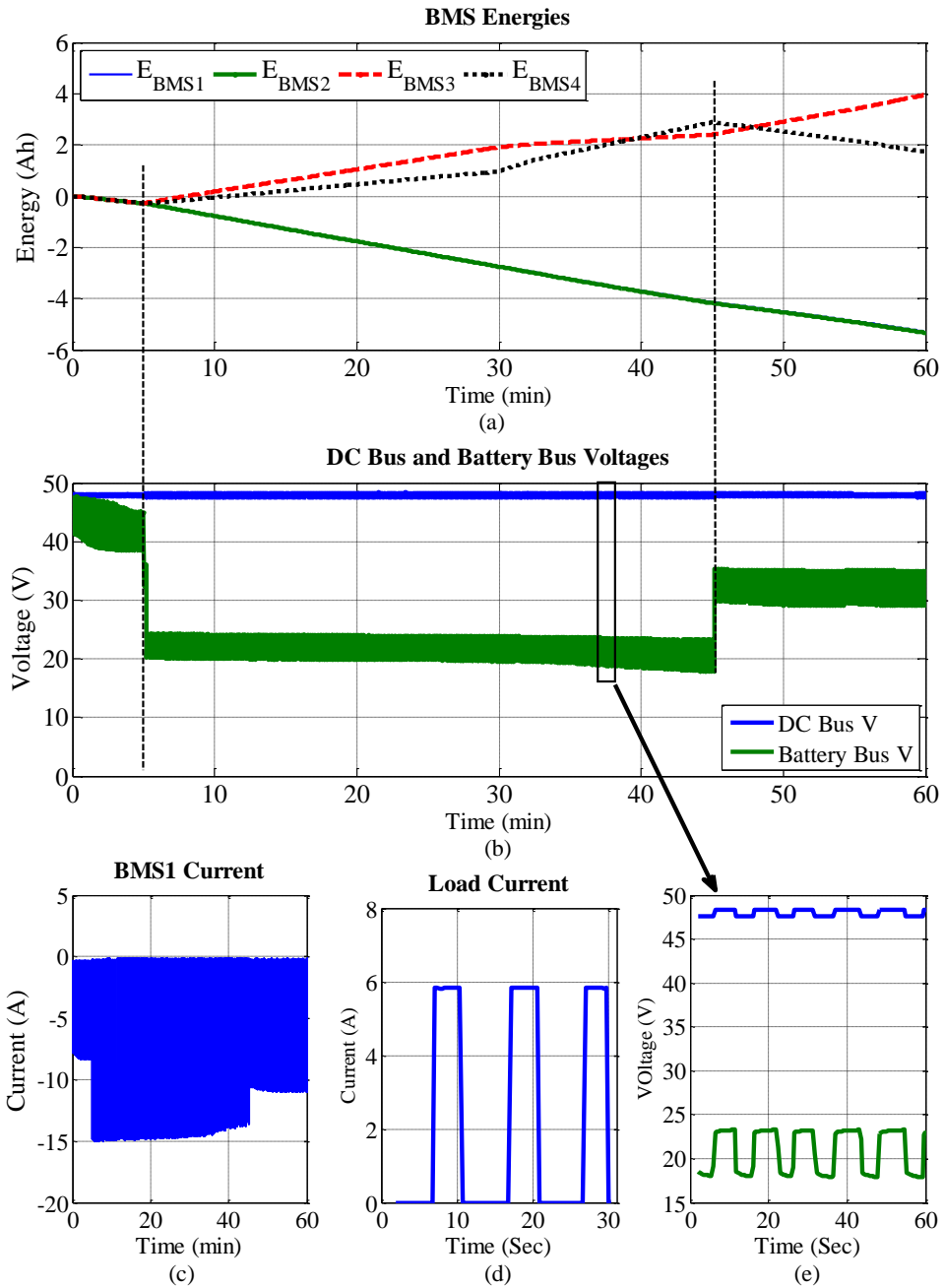
Figure 4.15 SoC balancing scenario.

(a) Energies injected to/withdrawn from each battery (b) DC bus and battery bus
voltages (c) current of the first battery (d) Pulsed load current (e) DC bus and battery
bus voltages (close up window).

4.7.1 SOC Balancing

When more than one battery is placed on charge, current regulation is not possible

and the magnitude of the current absorbed by each battery will vary based on many

characteristics. These range from a simple deviation in SoC to a mismatch in their internal impedance. With the individual charging control capability introduced by the BMS, the operator can control the energy injected into each battery regardless of its individual characteristics.

Consider a scenario as the one depicted in Figure 4.15. Initially, 4 batteries are connected in series and serve a load. At minute 5, the SoC of two batteries (3 & 4) is decreased falling below a certain pre-specified threshold. Keeping a battery running with low SoC increases its Depth of Discharge (DoD) and can permanently damage it. To solve this, these two batteries are changed from the load connected mode to the charging mode. Figure 4.15(a) shows the energy withdrawn from each battery (negative sign) and the charging energy (positive sign) over a 1-hour operation cycle. Both batteries are connected to regular constant charging at minute 30 due to the aforementioned reasons, where both batteries were not withdrawing the same energy: battery 3 withdrew more energy than 4 because of the drift in their internal impedances. Battery 3 has lower SoH and higher internal impedance because of the aging and accumulation of the sulfur layer. Hence, in order to regulate the energy injected into each battery, a pulsed charging profile is applied to both batteries. The pulsed charging currents were under the same frequency (0.25 Hz) but with different duty cycles to control the average injected energy to the battery. The duty cycles were 25% and 75% for battery 3 and 4, respectively. It can be seen that the slopes of the curves have changed, indicating variation in the amount of the charging energy. At minute 45, the injected energy to battery 4 exceeded the energy of battery 3, so battery 4 is selected to be returned to the stack to share the load with 1 and 2. Consequently, the slope of the energy curve changes to be negative, which indicates it is losing energy. The energies of batteries 1 and 2 are shown in Figure 4.15(a), with the negative slope over the entire

operation cycle. It should be noted that connection, disconnection and transition of each battery from state to another are occurring seamlessly, while the other two batteries continue to supply the pulsed load. The load pattern is depicted in Figure 4.15(d). The DC bus voltage and terminal voltage of the battery bank (battery bus) are shown in Figure 4.15(b). It can be seen that the voltage of the battery bank dropped from 48 V to 24 V when 2 batteries were disconnected. Returning the third battery to the stack brings the battery bank back to around 35 V. High-voltage fluctuations are associated with the pulsed load, as shown in Figure 4.15(e). The DC-DC boost converter regulated the DC bus voltage, isolating any voltage variations from propagating from the battery to the load side. The current withdrawn from battery 1 is shown in Figure 4.15(c), where it changed from 7 A in the first 5 min to 15 A between minutes 5 and 45, reducing to 11 A when the third battery was connected. It is worth mentioning that this added functionality not only allows balancing the SoC, but also distributes the stresses on the batteries, as those serving the load for longer periods can be put to charge while the charged ones can be connected to the load, and so on.

4.7.2   Fault Event

A protection scheme is designed as an additional functionality to the BMS. This scheme is designed in a way to protect the system and reduce interruptions. If a fault occurs in the charging circuit, the system disconnects the charging relays to isolate the batteries from the chargers. The system is able to detect the fault location by checking the current sign where a positive sign denotes a current injected into the battery. As shown in Figure 4.16, three batteries are connected to the charger, while only one battery (battery 1) is supplying a 0.9 A load. As shown in Figure 4.16(c), an event is created to increase the charging current in BMS 4 where the current rises rapidly to 13.5 A, hitting the pre-specified threshold. The system is able to identify this situation

and send an "off" command to the charging relays. The current of all the charging batteries fall to zero, while the current of the battery supplying the load remains unaffected. The charging relays for battery 1 are opened as well, but do not affect its operation in "load connected" mode. Figure 4.16(b) shows that the DC bus voltage remained constant; the battery bus voltage is constant at 11.4 V, which is equal to the voltage of battery 1.
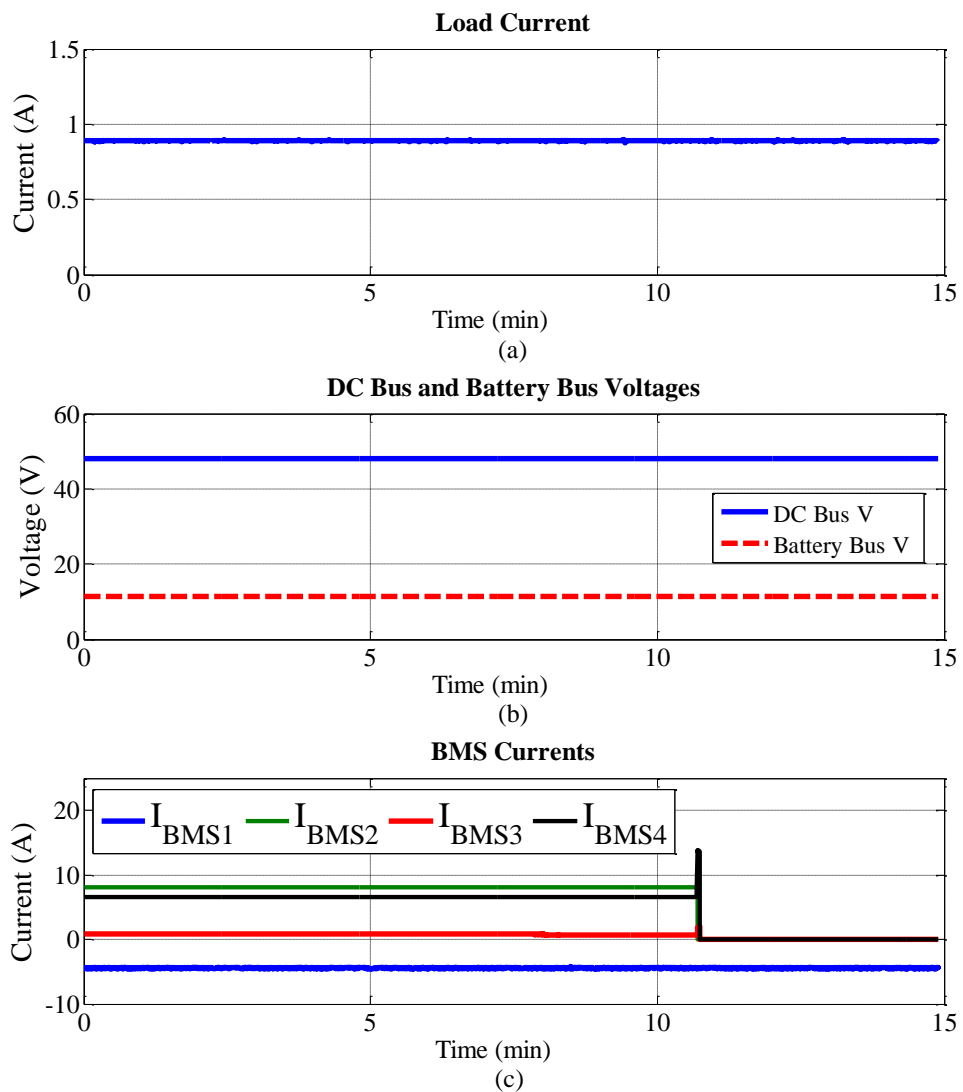
Figure 4.16 Protection against fault events in the charging circuit.

(a) Load current (b) DC bus and battery bus voltages (c) Current of the four BMS units.

This scenario demonstrates the effectiveness and reliability of the designed protection scheme. It should be noted that if the fault occurred on the load side, all BMS units and the load would be disconnected. When the three batteries are connected to charging, each battery withdrew a different current. The charging currents were 8.1 A, 0.8 A and 6.5 A for batteries 2, 3 and 4, respectively. The lowest charging current on battery 3 indicates high internal impedance and very low SoH. This emphasizes the previously mentioned points and the importance of individual pulsed charging. In case of a single battery supplying the load, the current withdrawn from battery 1 is almost four times the load current (considering the converter's efficiency), as the voltage on the battery side is one quarter that on the load side.

4.7.3 Discharging under Heavy Pulsed Load

The performance of the developed BMS is investigated under a heavy pulsed load condition. The pulsed load amplitude is 9 A at a frequency of 0.1 Hz and 50% duty cycle for approximately 30 minutes. The load is maintained for 2 minutes and the complete load profile is shown in Figure 4.17(a). It can be seen that the operation cycle is divided into 3 sections, where each section is approximately 15 minutes long. In the first section, it was found that battery 3 had a low voltage due to excessive aging, as opposed to the other batteries, which reflects on its SoH and SoC. Hence, battery 3 was placed in charging mode to improve the SoC, where a constant charging current of approximately 6 A is applied for the first 15 minutes. The other three batteries remained connected to serve the pulsed load. The terminal voltage of the stack is 36 V under no load and drops to 30 V during the high period of the pulsed load. The voltages of the DC bus and the battery stack are shown in Figure 4.17(b).

Figure 4.17(c) depicts a compilation of the currents measured from each of the 4 BMS modules. The first 15-minute segment shows the pulse being supported by only

3 batteries, or a 36 VDC bus. The levels of currents contributed from BMS 1, BMS 2, and BMS 4 are somewhat balanced at a high pulse current of 16.5 A at the battery side. This current is corresponding to a discharge C-rate of C-6.67. Looking at the envelope formed by the amplitude of the pulsating battery currents, the current drawn from the remaining battery stack is stable for the first 15 minutes.

Load Current

(a)

DC Bus and Battery Bus Voltages

(b)

BMS Currents

(c)

BMS Voltages

(d)
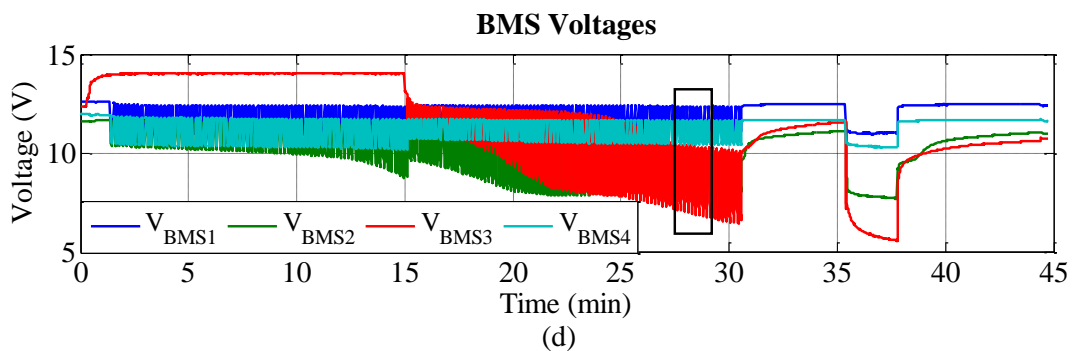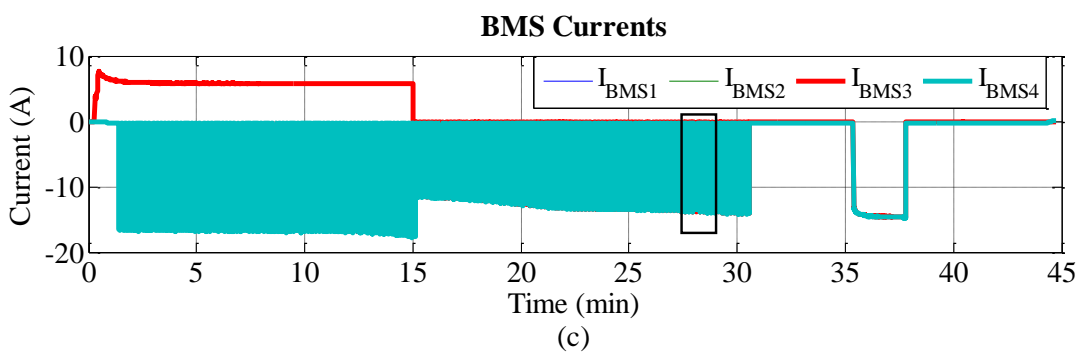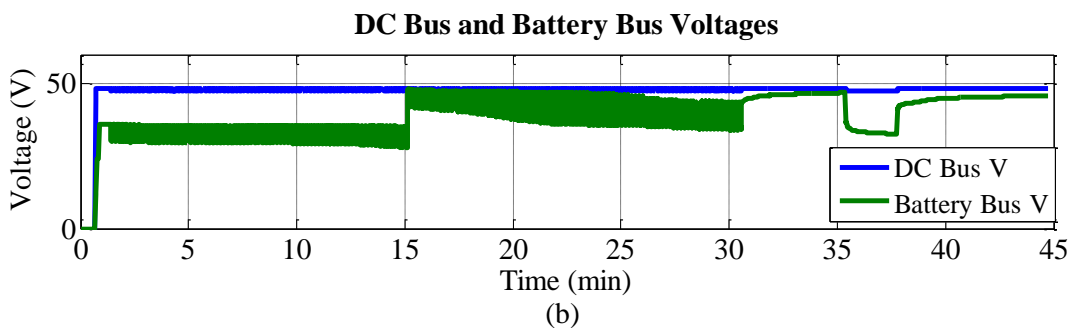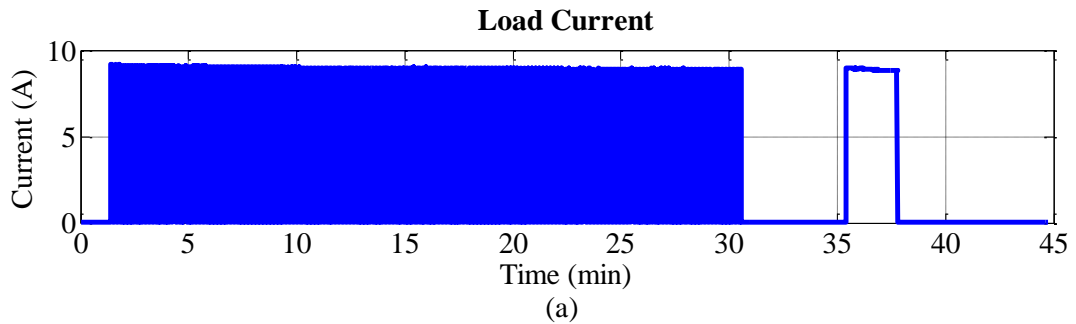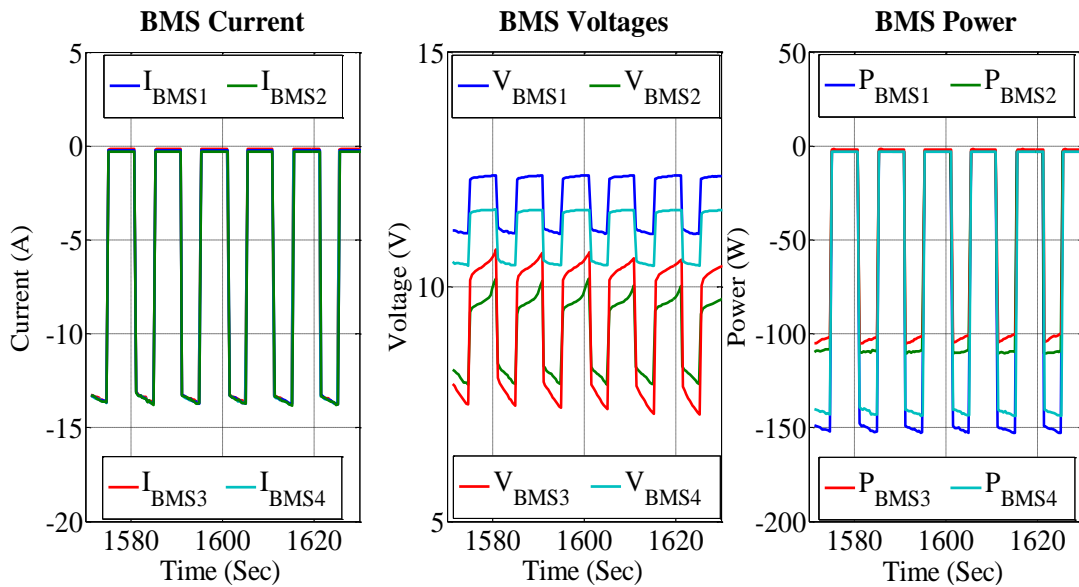
Figure 4.17 Discharging under heavy pulsed load.

(a) Pulsed load current (b) DC bus and battery bus voltages (c) BMS currents (d) BMS voltages (e) BMS currents (close up window-one minute from (c)). (f) BMS voltages (close up window-one minute from (d)). (g) BMS power.

Following the charging of BMS 3, at minute 15, the battery is placed back in to serve the load, reducing each battery current to approximately 13 A. Initially, this reduces the burden and C-rates on the batteries, but as the system continues, the currents' amplitudes begin to expand, as shown in Figure 4.17(c), demonstrating that a weak battery is still present in the series array. To compensate for the continuously dropping voltage on BMS 3, the remaining batteries are forced to increase their currents to supply the required energy and fill the pulse. This is explained by looking at Figure 4.17(d). It can be seen that the voltage of battery 3 is decaying drastically. A close up of the voltage waveform is provided in Figure 4.17(f), where a steep decay of the voltage during the pulse is present, indicating that the battery cannot sustain the high load current for a longer period. This rate of change can be used to determine the exact parasitic parameters of the battery using the equations provided in section 4.3 and EIS methods. A close look into these figures reveals a wide range of information about

122

the characteristics of the batteries and their expected life. The voltage profile of battery 3 (red) compared to that of battery 1 (blue) can give a realistic indication for the relative differences in their characteristics. The voltage of battery 1 is consistent and steady. This can be used to easily identify an unhealthy or low-performing battery inside a large stack. The current and power injected by each battery are depicted in Figure 4.17(e) and (g), respectively.

During a short rest period, it is shown that the voltages of batteries are recovering to their initial values. The slowest recovery rates were yielded by batteries 3 and 4. A final test is conducted, where a constant current of 9 A is applied for 2 minutes. Using the current sourced during the constant current stage in Figure 4.17(a), the load is essentially stable, but should be lower with 4 batteries contributing. A load current of 15 A reveals that one battery is faulty. By analyzing the bus voltages in Figure 4.17(d), one can identify a weaker battery input voltage, as the slope of the voltage drop during the pulse is substantial. The voltages of batteries 3 and 4 drop to 6 and 8 V, respectively, whereas batteries 1 and 2 are relatively healthy.

The output DC bus voltage is shown in Figure 4.17(b) in green, and the input battery array voltage is in blue. A closer look at Figure 4.17(b) in the pulsed load region is shown, demonstrating the stability of the DC bus and voltage variation present on the battery array input while the terminal voltage of the battery array transitions from 45 V to 33 V. The input voltage depicts the voltage stabilization and number of batteries connected to the stack. In addition, though the DC bus voltage is impacted by the magnitude of the pulse, the voltage variation remains relatively small and within standard limits. Thus, a change in the battery array size and input voltage only introduces a small deviation to the output DC bus voltage.

BMS Voltage

(a)

BMS Current

(b)

BMS Voltage

(c)
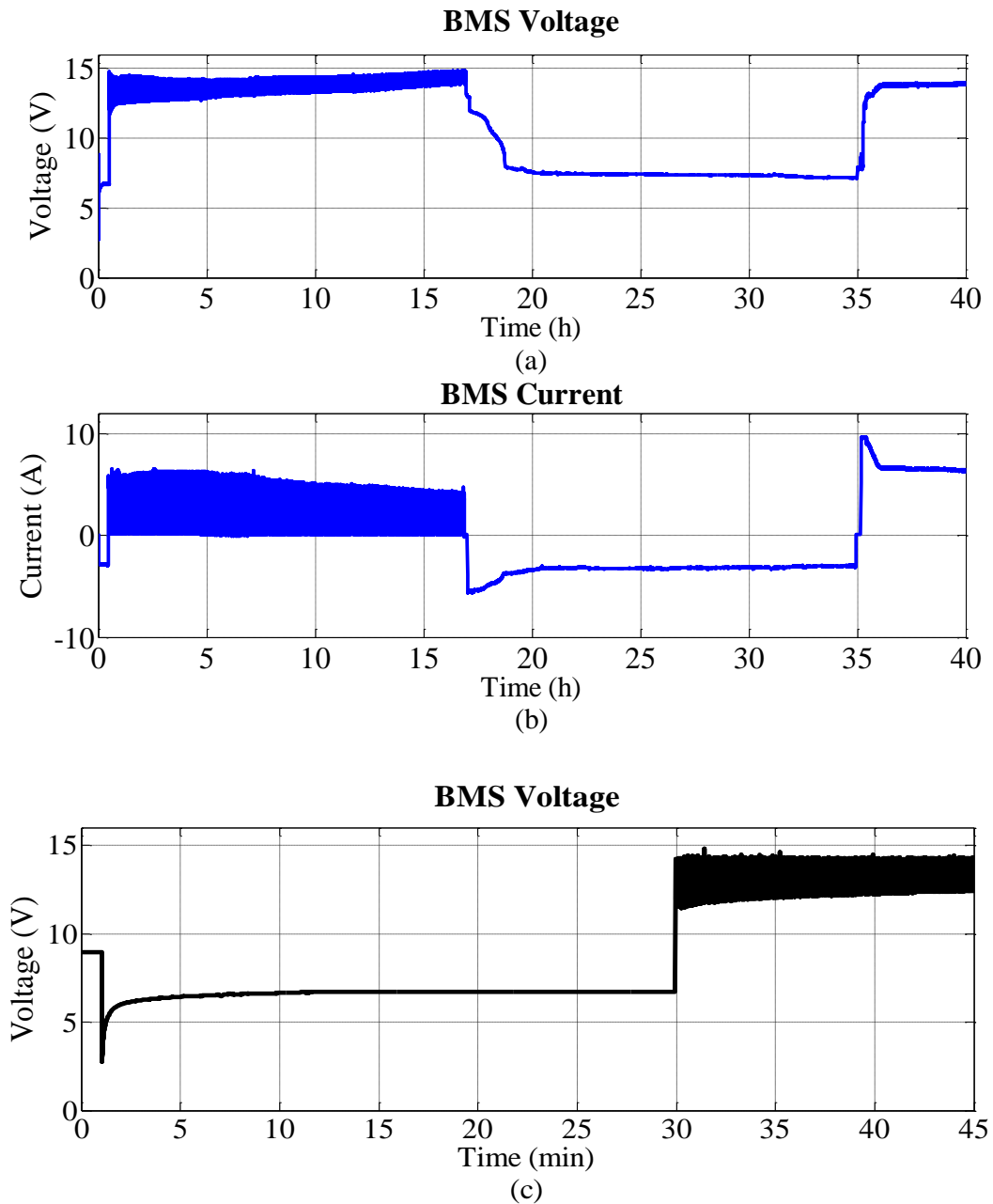
Figure 4.18 Endurance and robustness test.
(a) BMS voltage (b) BMS current (c) BMS voltage (first 45 min).

4.7.4 Endurance and Robustness test

In order to examine the endurance and robustness of the developed prototype, it was put in operation for a continuous 40-hour test. The measurements were collected through LabVIEW and saved through data logging function. During this test, the system performed the different functions (supplying a load, pulsed charging, then supplying a

load again and constant charging) without recording any issues or failures. The voltage and current data are shown in Figure 4.18(a) & (b), respectively.

Figure 4.18(c) shows a close-up of the voltage in the first 45 minutes of the test. The test was performed using a battery with very low SoH. A secondary purpose of this test was to investigate the effectiveness of pulsed charging. It can be seen from

Figure 4.18(c) that initially, the open circuit terminal voltage of the battery was 8.5 V. When a load was applied to the battery, the voltage dropped significantly reaching around 6.75 V. Pulsed charging was applied to the battery injecting maximum current at a 14.7 V charging voltage under a pulse frequency and duty cycle of 1 Hz and 75%, respectively. After charging, the same load was applied again where the voltage dropped drastically in the beginning reaching around 7.1 V. This test shows improvement in the battery voltage (around 0.35 V) due to the partial cracking of the accumulated sulfate layer.

4.8   Summary

In this chapter, the design of an advanced BMS is proposed. A laboratory prototype is built and tested under different loading conditions. The developed BMS is capable of monitoring the voltage, current, power, energy and SoC for each battery in the array. Furthermore, it can independently control individual batteries. By isolating individual batteries, the operator can charge one or more batteries in a series stack while the system continues to supply the load. This includes the impacts associated with heavy pulsed loads. This topology significantly increases the reliability of the system. In this work, it was proven that the load can be supplied normally even when a four battery stack has been significantly reduced to only one or two batteries (depending on load current). In addition, this system is lower in cost as no bi-directional converter is needed as the batteries are charged from another low voltage DC source and can be suitable for wide

range of applications. It can be used in utility scale energy storage systems, as the large battery array can be divided into sub-sections or stacks and each stack is monitored and controlled using a BMS unit. The system can also be suitable for shipboard power systems, where batteries are deployed to not only serve a base load, but also mitigate the effects of pulsed loads.

Chapter 5   Modular Energy Storage Regulator (MESR) for Optimal Management of Hybrid Energy Storage Systems (HESS)

5.1   Introduction

As various types of energy storage (ES) continue to penetrate the grid, electric vehicles, and Naval applications, more management techniques have to be investigated. Each ES type has its own distinct characteristics that outline its advantages and disadvantages. For example, Lead acid batteries are known for their low power density, higher susceptibility for SoH degradation with frequent cycling, and heavy weight. On the other hand they provide a reliable mean of energy storage at low cost. Ultra-capacitors are known for their very high power density and long life time in terms of number of cycles (~ 500,000 cycles) [212]. However, they are criticized for their very low energy density. Recently, ES hybridization was proposed in the literature, this means combining two or more ES technologies to overcome the shortcomings of a single technology [213]. In this case, the produced Hybrid Energy Storage System (HESS) exhibits enhanced characteristics (i.e. improved energy/power density or faster response) over the traditional single technology based ES systems. Examples of HESSs are provided in [214] and [215]. In the first reference, the authors presented a supervisory energy management strategy for optimal power sharing between a battery and a supercapacitor. In the second reference, an HESS composed of the zinc bromide flow battery and lithium-ion capacitors is proposed.

With this recent emergence of HESS, a need arises in extending the traditional analysis methods to cover the revised performance metrics associated with them. More important, there's a need for flexible control and power splitting strategies. Considering the fact that each ES technology has its own charging limitations and manufacturer

recommendations for optimal capacity utilization, any adopted controller should be capable of handling the individual charging requirements for each ES element independently.

In the previous chapter, the design of a BMS is presented; the control and protection functions were developed specifically for Lead-acid batteries connected in series. As a continuation, this chapter builds on the work presented earlier. The BMS is expanded to be adequately used with other ES types. Also, more functionalities are added and the controller has been adjusted to be able to flexibly handle different types of ES. In addition, some changes have been made to the unit topology to be used in parallel arrays. Therefore, with the new manipulations, features and scope, the name has been changed from Battery Management Systems (BMS) to Modular Energy Storage Regulator (MESR). Hence, MESR is an expansion or a second phase of BMS.

The term "modular" is based on the fact that the system is divided into modules and each module is controlling either a single ES unit in small scale systems or a stack of ES units (sub-array) in large scale implementations. Using MESR, the charging of mixed ES technologies is then accomplished using a special controller to handle the unique charging constraints of each ES module. Moreover, this same controller was used to apply a "rolling charging" algorithm to extend the in-service time of the HESS. The effectiveness of the developed MESR is validated experimentally through a hardware setup simulating different loading events.

5.2 Energy Storage Management in Ship Power Systems

Research into ES systems continues to flourish to support the future microgrid infrastructure and proceed towards smarter power systems. To serve an ever-changing fluctuation in the consumer demand, the grid must rely on the inclusion of a variety of ES sources. The most common solution, an electrochemical battery, is utilized for a

wide range of different tasks including restoring system voltage and frequency following an outage. In islanded microgrids, following a major disturbance or a variance in load/generation, system stability will rely solely on the support of ES when MTGs and ATGs reach their generation capacities. In [216], a battery management system scheme is demonstrated to control the power flow in a lithium ion based battery array. The system is tested under both grid-connected and islanded modes of operation. In islanded mode, a battery with an inverter acts as a synchronous generator providing voltage and frequency support. A number of other control strategies have been demonstrated, but they have only focused on one type of ES [217]-[220].

In a utility grid, a wide range of ES can be deployed due to the absence of any concerns over weight and space. On the contrary, mobile applications do not have this luxury. The localized microgrid present on a ship, aircraft, or electric vehicle (EV) is susceptible to major operational and logistic challenges. Heavy and frequently fluctuating loads, which may present a minimal disturbance to the utility-connected system, can prove to be catastrophic when generation resources are limited. Without the aid of carefully selected ES, the energy must either be available from generators on-demand, or the ES units must be prepared and deployed effectively in anticipation of the disturbance.

A Naval ship power system (SPS) can be seen and electrically treated similar to an islanded microgrid, which is physically confined. The SPS is composed of a complex isolated power system, typically consisting of two main turbine generators (MTG) and two auxiliary turbine generators (ATG) [152]. For example, the upcoming all electric DDG1000 Destroyer contains 74.8 MW of onboard total shaft power [221]. Critical loads reserve approximately 15% of the available energy, but the next generation of equipment will introduce loads several magnitudes greater than this figure [222].

Energy and power requirements can vary from 100 kW to 10 GW over microseconds to seconds [223]. Without proper management, ES units may experience high depth of discharge (DoD), which would reduce their capability of responding quickly to fluctuating demands while significantly reducing their lifespans, or state of health (SoH) [224].

Since they are inherently islanded systems, SPSs present unique challenges in terms of ES deployment. Pulsed load management and mitigation is an emerging topic in the future, all-electric SPS. In [225], a 0.25 Hz 36 MW pulsed load is tested on a notional SPS model where case studies were conducted over the use of a dynamic reactive compensator to maintain bus voltages. However, power demands of multiple pulsed loads present a major challenge in terms of design and implementation. The electromagnetic (EM) railgun and EM catapult were investigated in [226] where short-term pulsed loads were tested, both significantly exceeding the available energy from the MTGs when tested independently. ES was proposed as a solution to support both, but was not demonstrated. A comprehensive discussion on the impact of multiple pulsed loads on the electric SPS was provided in [227]. EM railgun and free electron laser firing profiles were tested as connected pulsed loads without electrochemical ES, but employed the railgun launcher rotor as flywheel ES. The system proved that the current infrastructure could support one important pulsed load, but not both.

In [228], a supercapacitor (SC) was tested independently with an EM railgun to fill an 800 kA firing pulse. The topology was capable of supplying the pulse, but required an enormous 500 F SC. Combinations of ES have offered more realistic solutions [229] -[231]. In [231], Lead acid and sodium sulfide battery banks are simulated in parallel on a SPS to fill a single pulsed load. Each ES bank was installed on a different zonal bus where it was noted that the ES units were able to respond quicker than the MTG to

deliver energy. However, HESS support has not yet been evaluated on the same bus. A control topology for a SPS is proposed in [232], where a parallel-configured battery-SC HESS was simulated with respect to a constant and pulsed load. Four operation modes were tested to meet critical and pulsed load demands, but only the voltage recovery period following the pulse was discussed and no investigation was provided into the SC or battery performance. Furthermore, the battery type was not identified.

Typical battery and SC HESS have utilized parallel topologies; however, control of these systems is challenging as a result of the wide voltage operating range of the SC. Without a specialized interfacing converter, the SC terminal voltage would follow that of the battery leaving a significant amount of unutilized energy due to a narrowed operating range [233]. Moreover, a mismatch in the equivalent series resistance of each ES would result in unequal, uncontrolled charging or induce internally circulating currents.

Although the literature has demonstrated the impacts of pulsed loads on SPS, it has been limited to testing of each pulsed load independently. In practicality, a robust system should have the capability to handle multiple pulsed loads under the same period. Multiple pulsed loads can be seen under a multitude of applications, but for this focus, this will be realized under a SPS. To the best of the author's knowledge, serving multiple pulsed loads on the SPS has not yet been tested and analyzed.

In order to overcome this challenge, two novel concepts have been established as a part of the significant contributions of this dissertation. First, several series-configured HESS combinations are proposed and tested through utilizing lead acid and lithium ion batteries as well as a SC bank. The performance of each combination is analyzed. Second, a specialized dispatch control scheme is demonstrated in an effort to replenish some of the energy required to serve one of the pulsed loads considering the SoH trade-

offs. This scheme is given a name "rolling charging," a coordination scheme between the load and charging is applied to the heaviest pulsed load in an effort to recover a portion of the discharged energy. The dynamics of each ES is optimized with respect to their operational constraints as well as best practices to preserve their SoH.

5.3 Coordinated Control of HESS

In order to handle the diverse charging characteristics for the different ES types within the hybrid stack, a management system is utilized to provide a safe interconnection to each ES. The following subsections describe the features of the MESR utilized in this research, as well as how the dynamic rolling charging algorithm functions. Following a discussion over the rolling charging concept, the charging constraints for each ES and how they are fulfilled will be explained in-detail.

5.3.1 Energy Storage Management System Controllers

As discussed earlier, MESR is a second phase of the BMS presented in 2.3.2, expanded to be utilized to manage each battery and SC module in the HESS. This tool provides individual monitoring and protection for each ES module as well as a number of unique control features. Through a certain topology of relays and measurements interfaced to a LabVIEW-NI DAQ based control platform, the MESR is able to electrically couple and decouple an ES module in a series configuration while maintaining a current path to operate the load. In series configuration, the same relay and measurement topology will be used. Therefore, since the topology is already explained in section 4.4, it will not be covered in this chapter. However, more focus will be dedicated to the added control features.

5.3.2 Rolling Charging

A new concept of rolling charging has been developed to extend the operation time of a certain HESS supplying heavy PPLs. This concept utilizes capabilities of the

MESR to extract a weak or low SoC ES module from the HESS and place it on charge while maintaining system operation. As an example, in real SPS systems, the EM railgun pulsed power requirement would present a challenge in terms of available energy on the HESS and may drop the SoC of an ES module to dangerously low levels. If the firing frequency and number of shots for the railgun were known, then one could anticipate when the energy requirement was needed. Using this information, an ES module could then be extracted to charge when the pulse is off and reconnected again only when the pulse is active. Through control and timing, this could be synchronized with the pulsed load. To balance the impact on all ES modules while providing each applicable ES module an opportunity to charge, each ES module is dispatched for a period of time and then "rolled" to the next ES module with the lowest SoC. This strategy can allow the system to be sustained for extended operation periods while, at the same time, permitting the maintenance of some ES units while the stack is still under operation. This could be very beneficial for critical loads. Figure 5.1 illustrates the proposed concept of rolling charging; for simplification, an ES array composed of four modules is used for illustration. During the on-pulse period of the high amplitude pulse (EM railgun), the four modules are in service. During the off-pulse duration, ES1 is extracted by the MESR to be recharged while the other three modules are still in-service to serve the low amplitude pulsed load (e.g. radar or sonar) and the hotel loads if needed. Then, in the next cycle, the next ES module will be extracted. This cycle is repeated until the end of the array is reached. After recharging the last module in the array (ES4 in this particular case) the controller goes back to extract ES1 again. Without MESR and its features, this process would be impossible.

To get an understanding of the significance of the developed controller, it will be compared to the existing ones. With the conventional controllers, the whole ES array

133

has to be disconnected from the load and charged during the off-pulse period. This situation adds several complications to the system because the other pulsed load and hotel loads will be left unsupported. This may create fatal issues in case of emergency or battle conditions. Furthermore, the reliability of the system is drastically reduced because a problem in any module can affect the operation of the whole array. These issues are overcome using the MESR, as will be shown experimentally.
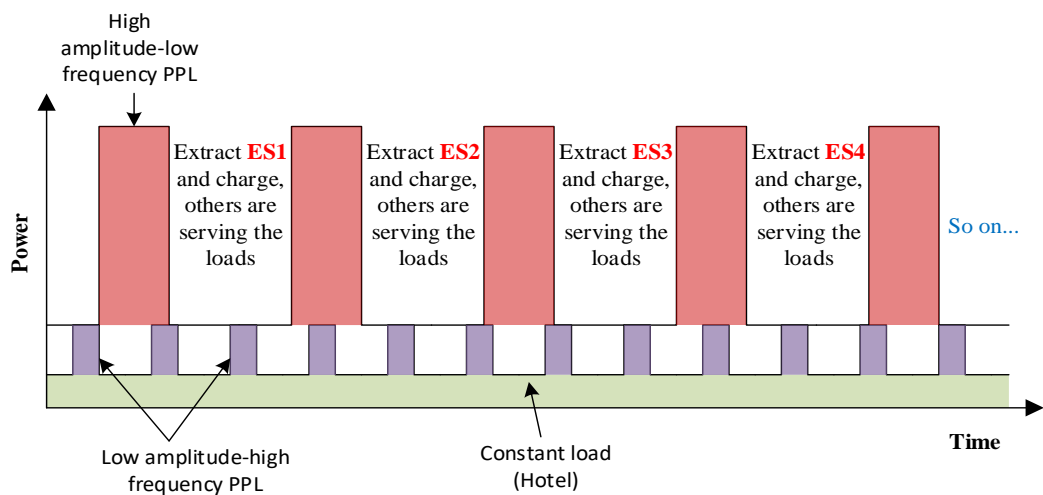
Figure 5.1 Rolling charging algorithm for ES array composed of four modules with multiple pulsed loads.

5.3.3   Charging Constraints

Charging currents and voltage levels vary based on each type of ES module. Since the utilized topology employs two isolated busses, namely load and charging bus, another major advantage of the developed MESR is that it is capable of handling different charging constraints for different types of ES. Consequently, the voltage and current limits of the charging bus can be adjusted dynamically based on the type of ES connected. In more complicated or larger systems, with the aid of the utilized topology, multiple low voltage busses can be provided. Moreover, the controller sets the current limits to pre-specified values to maintain safe charging currents which will limit SoH degradation.

For the 6-cell lead acid battery employed in this research, particular care has been taken to regulate the charging current to prolong its SoH. The manufacturer established an absolute maximum charging current at C/4, but to limit thermodynamic and material stress, this has been reduced to a conservative C/6 current under a charging bus voltage of 14.8 V. Lithium ion batteries, however, have much less susceptibility to higher charging currents as long as the charging voltage levels are carefully controlled. For the lithium ion cells deployed in this experiment, a voltage tolerance of 4.20±0.03 V/cell or 12.60±0.09 V is regulated for the 3-cell series module where the maximum charging current can be increased to C/2 safely [234].

The SC module is an exception as the charging current is not referred to its storage capacity. Theoretically, charging to its full voltage level $V_{max_{SC}}$ is only limited by the equivalent series resistance R_{ESR}, but the IEC 62576 has established a safety limit I_{max} for practical applications based on 2.6% of this current [235]. For the SC modules employed in this study [236], $I_{max} \cong 19$ A.

$$I_{max} = 0.026 \left(\frac{V_{max_{SC}}}{R_{ESR}} \right) \tag{5-1}$$

5.4   Hardware Implementation & Experimental Results

In order to investigate the feasibility of the proposed control technique, a hardware setup has been established as depicted in Figure 5.2. Three types of ES are used: Lead acid batteries, lithium ion batteries and Supercapacitors. Each lead acid battery is 6 cell type which has a nominal voltage and capacity of 12 V and 21 Ah, respectively. The lithium ion battery module is composed of 3 individual cells connected in series where the nominal voltage of each is 3.7 V, delivering a similar module voltage to the lead acid at 11.1 V under a matching capacity of 21 Ah [234]. The SC used is manufactured by Maxwell and composed of two 58 F modules in parallel, each rated at 16.2

VDC [236]. The voltage of the load bus is set to 48 V while the voltage of the charging bus is controlled dynamically based on each ES charging requirement. Therefore, a programmable DC power supply was needed. The used programmable DC power supply is manufactured by Magna-Power. This supply is a member of XR series with rated output power 6 kW, maximum current 15.9 A and maximum DC voltage 375 V.
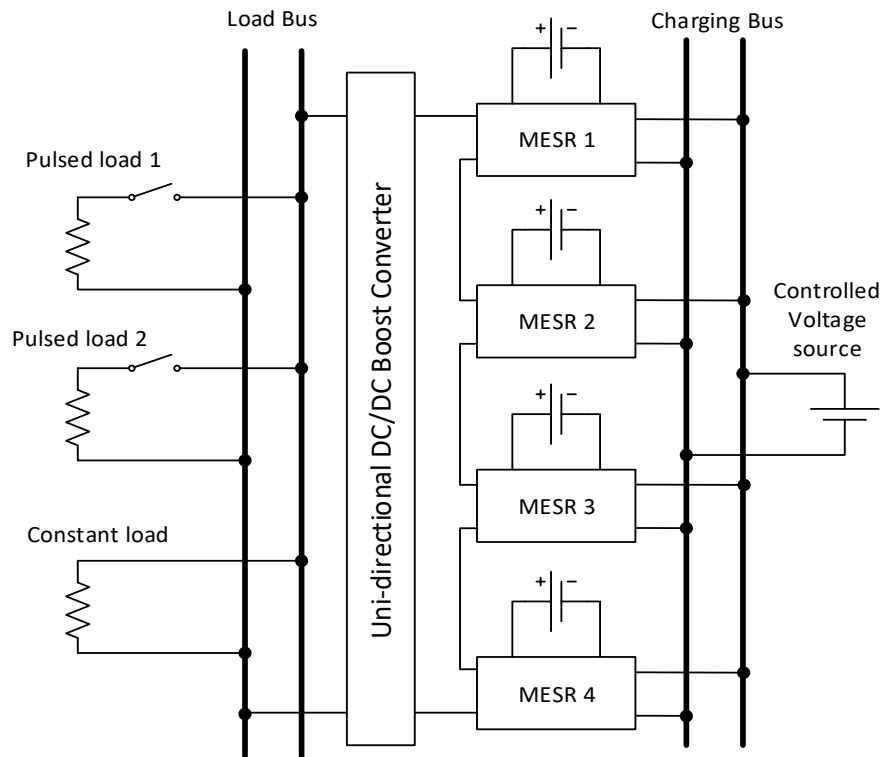
(a)
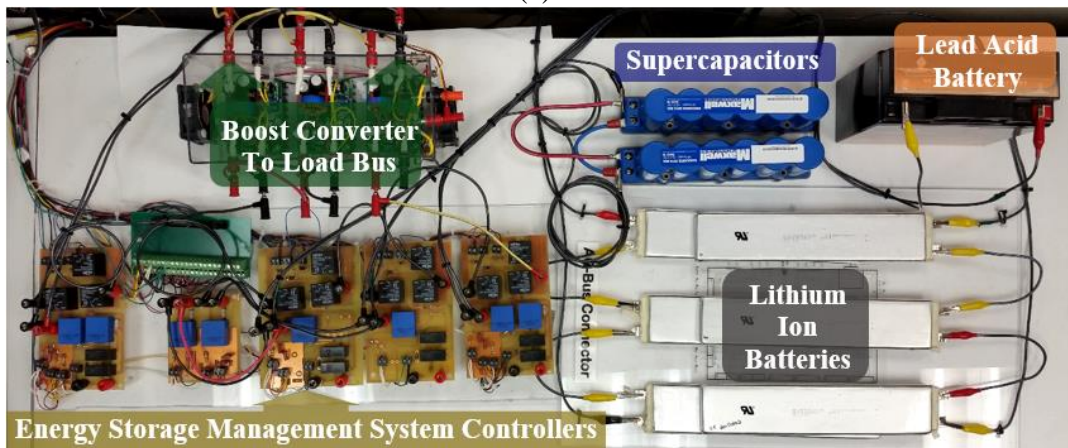
(b)

Figure 5.2 Configuration of 4 MESR in series with two pulsed loads.
a) Schematic, b) Experimental setup.

The load values have been selected closely based on the information gathered from one of the new naval platforms (DDG-1000) [221] where its parameters were scaled down. In this experimental platform, the constant load represents hotel load in a generic SPS with scaled down power of 105 W. PPL 1 is modeled after a radar system presenting the lighter of two considerable pulsed loads installed on the SPS, operating at a scanning frequency of 0.5 Hz, under a 50% duty cycle, with an amplitude of 60 W. PPL 2 emulates the EM railgun, a load that is a major disruption to the SPS. The EM railgun is modeled with a 5-second active duration (0.05 Hz frequency) under a duty cycle of 25%, with an amplitude of 385 W. Five different tests are examined on this system.

5.4.1   Test I: 2 Lithium Ion and 2 Lead Acid Batteries

In this test, the HESS was composed of two lithium ion batteries connected to MESR 1 and MESR 2 and two lead acid batteries connected to MESR 3 and MESR 4. The test results are shown in Figure 5.3 where the test duration was around 20 minutes (0.33 h), divided into 5 intervals. Looking at Figure 5.3(a), it can be seen that in the first interval, all four batteries served the load whereas in the second interval, lithium ion battery (MESR 1) was extracted during the light loading periods (when the large pulsed load was off) and connected to the charging bus. This can be further illustrated by looking at Figure 5.3(b), where a close up over a period of 72 seconds (0.02 h) is shown. The effect of the fast pulsed load (of lower amplitude) is clear, and both pulsed loads are overlapped over some periods. It should be noted that the negative current indicates discharging the battery while positive current indicates charging. Then, in the third interval, the second lithium ion battery is extracted to be charged, and so on. This technique helps to replenish some of the lost energy during the high amplitude pulsed load, consequently extending the operation time of the array.
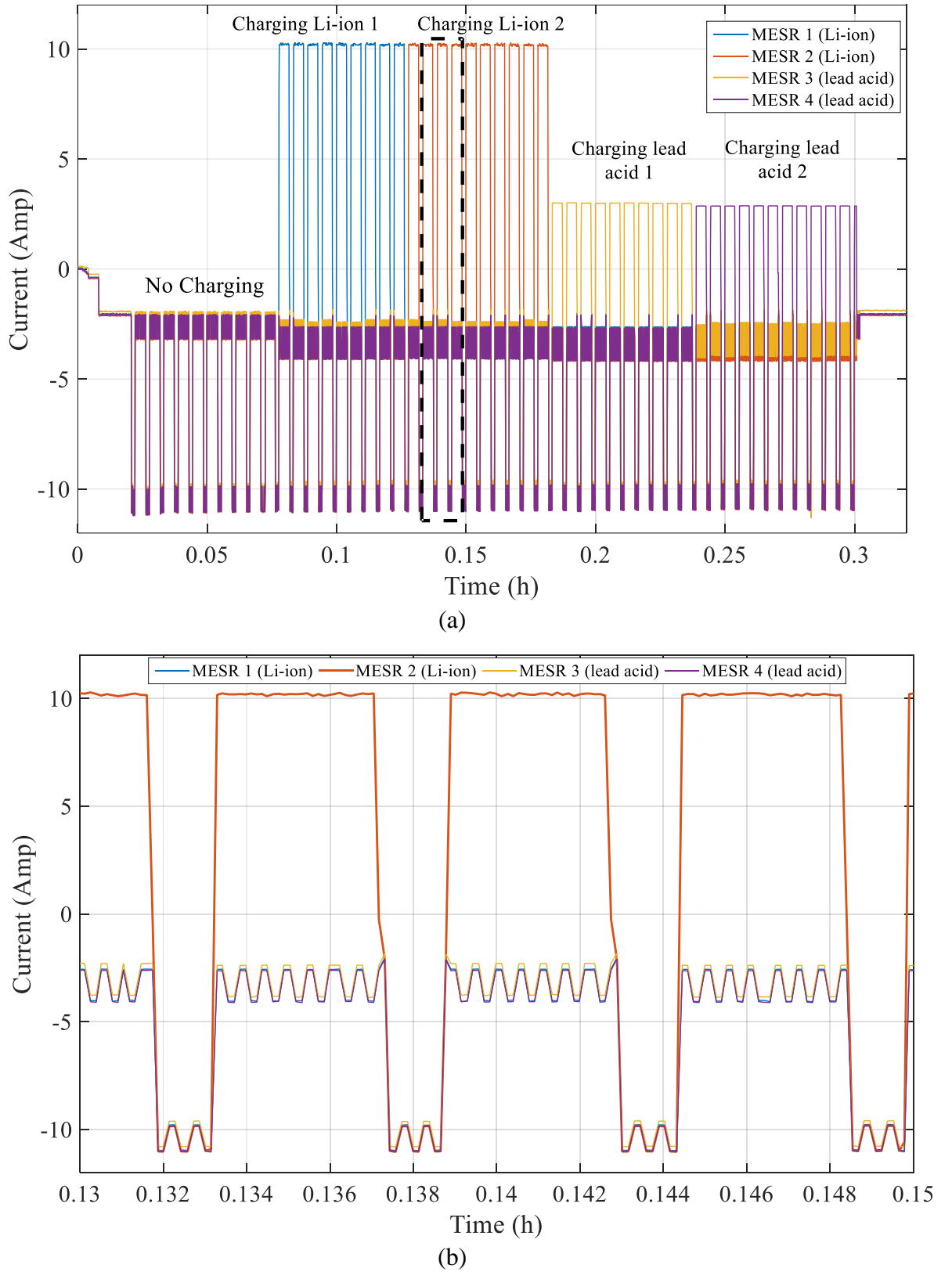
Figure 5.3 Test I: 2 Lead acid and 2 Lithium ion ES array under multiple PPLs.
(a) Currents of Individual ES modules and (b) 72-second Close-up.

5.4.2 Test II: Endurance Test

To investigate the effectiveness of the proposed rolling charging technique in expanding the "in operation" time of the HESS, an endurance test was performed utilizing the full potential of the ES modules. Figure 5.4 (a) and (b) show the test results without and with the MESR, respectively. It can be seen from Figure 5.4 (a) that the HESS was discharged reaching a full discharge voltage cutoff (collapsing point) after 164 minutes (2.73 hours), while Figure 5.4 (b) shows that with the utilization of the developed controller, the operation time was extended to 207 minutes (3.45 hours). This system achieved a 26% increase in HESS service time through replenishing some of the lost energy online (while the stack was operating), which would not have been possible in the legacy system. This system could be of significant importance for SPS in critical operating scenarios where it is not possible to shed vital loads [152].

(a)

(b)
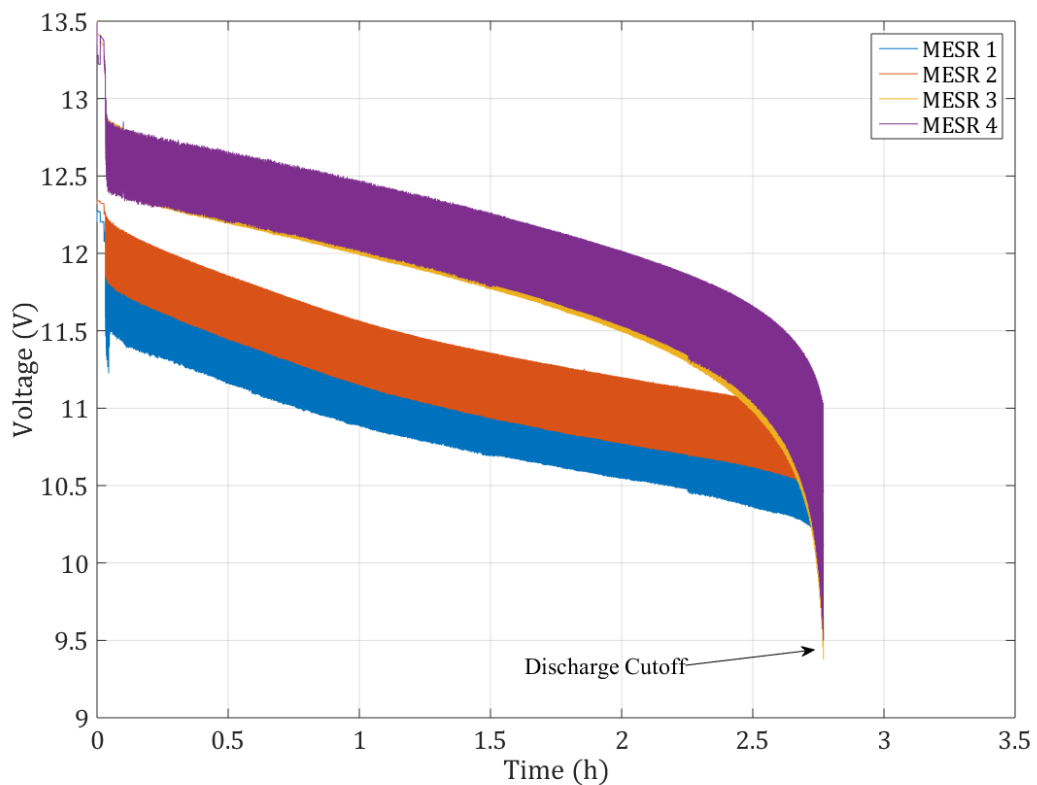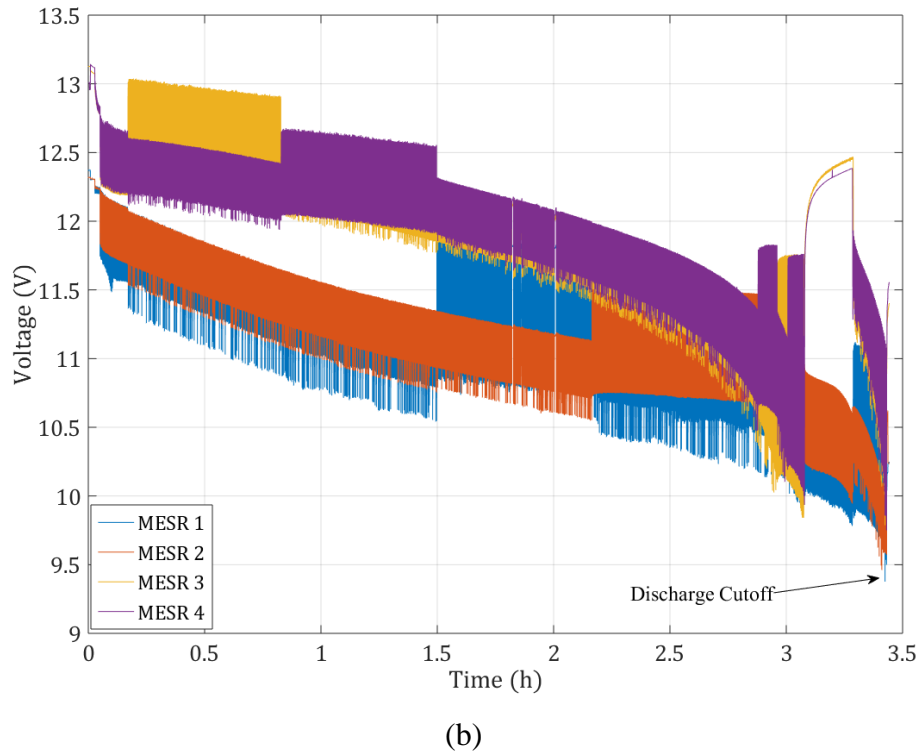
Figure 5.4 Test II: Endurance test.
(a) Without Rolling Charging and (b) With Rolling Charging.

5.4.3 Test III: 2 Lithium Ion, Lead Acid, & Supercapacitor (No rolling charging)

In the third test, one of the remaining lead acid batteries was replaced with a SC presenting further complications. To have accurate comparison, this test is used as the base case, where no rolling charging was applied. It can be seen from Figure 5.5 that the test was constrained to less than 10 minutes, explained by the vast difference in energy densities between the SC and the batteries. One of the disadvantages of the SC is its low energy density and high self-discharge rate. Very recent to the time of writing this dissertation, scientists at UCLA's California NanoSystems Institute have developed a new energy storing device that combines the high energy densities of batteries and the quick charge and discharge rates of supercapacitors. The hybrid supercapacitor is reportedly six times as energy-dense as a commercially available supercapacitor and

140

packs nearly as much energy per unit volume as a lead-acid battery [237]. However, this device is still within the domain of laboratory research and not available for public use or industrial utilization.
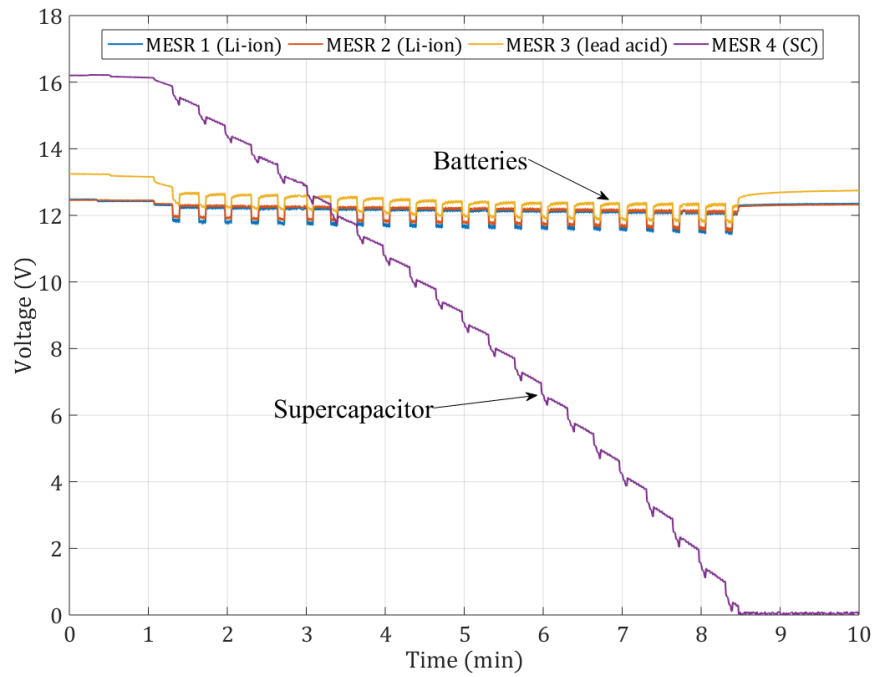
(a)
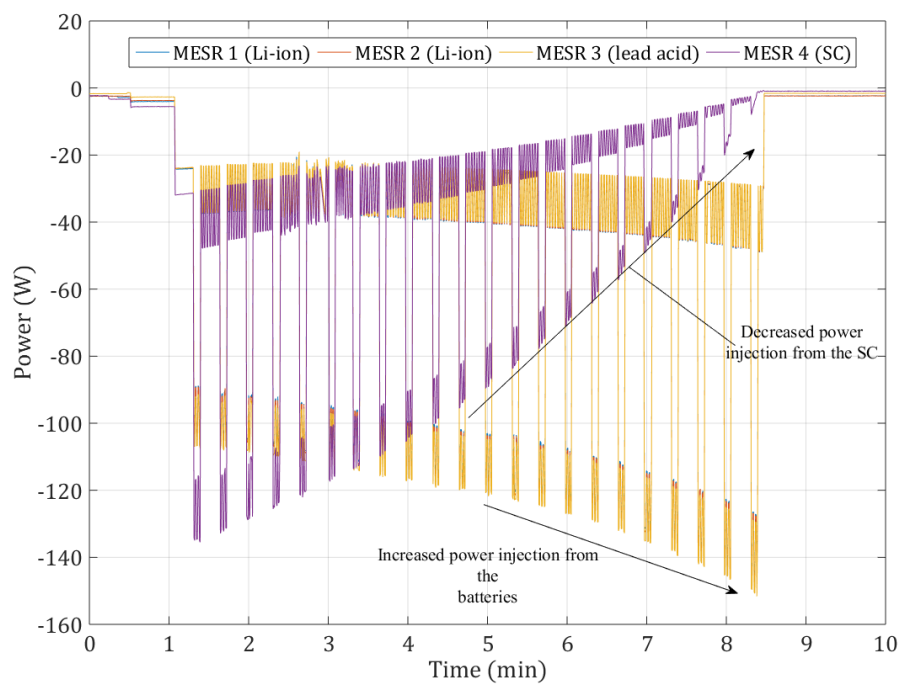
(b)

Figure 5.5 Test III: HESS performance without rolling charging.
(a) Voltage and (b) Power.

Figure 5.5(a) shows that the SC voltage decayed at a much higher rate than that of the batteries, reaching a very low value with which the HESS had to be disconnected. Figure 5.5(b) shows that the power absorbed from the SC gradually decreased which had to be compensated by a proportional increase in power injected by the batteries. Continued operation would cause a 33% increase in required current from remaining ES, further reducing runtime and impacting the long term SoH. Without the developed MESR, the solution of this problem would be increasing the size of the SC. This solution is not acceptable, especially when taking into account the fact that the prices of the SC are still considerably high.

5.4.4 Test IV: 2 Lithium Ion, Lead Acid, & Supercapacitor (SC Rolling)

Due to the significantly lower energy density of the SC, it represents the weakest link in the HESS; thus in this test it is elected to be rolling charged. In this scenario, a conservative approach is taken to maximize SoH of the batteries by only dynamically charging the SC. Shown in Figure 5.6, the total test duration was 3 hours where it can be seen that as the voltage of the capacitor decayed to a pre-specified level. Then, it was decoupled from the stack, charged, and placed back in after reaching full charge. 8 V (50% SoC) was preset in this scenario to avoid a major drop in the HESS array voltage, although this can be set by the operator to any desired value. This process was repeated until one of the remaining batteries reached its full discharge voltage cutoff. The switching operation performed seamlessly without noticeable impacts on the DC bus. Figure 5.6(b) shows a close-up of the SC depicting its wide voltage variation as well as how it saturates when approaching a full charge. The voltage spikes are because of the pulsed load, since during the pulse, the terminal voltage of the SC drops slightly. The impact of the saturation is noted in Figure 5.6(c) where the absorbed SC current

starts to decrease. An alternative solution to the energy mismatch problem is to increase the size of the SC. However, this would add weight and cost, two factors which are tightly constrained in the modern SPS. The MESR presents simple, yet effective solution.
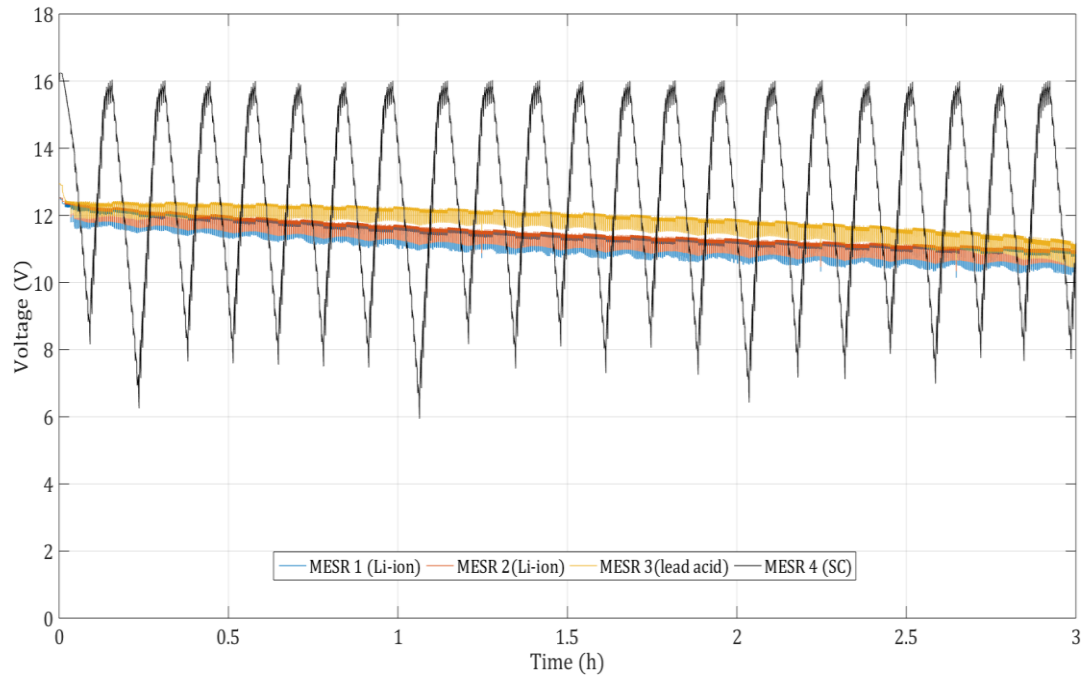
(a)
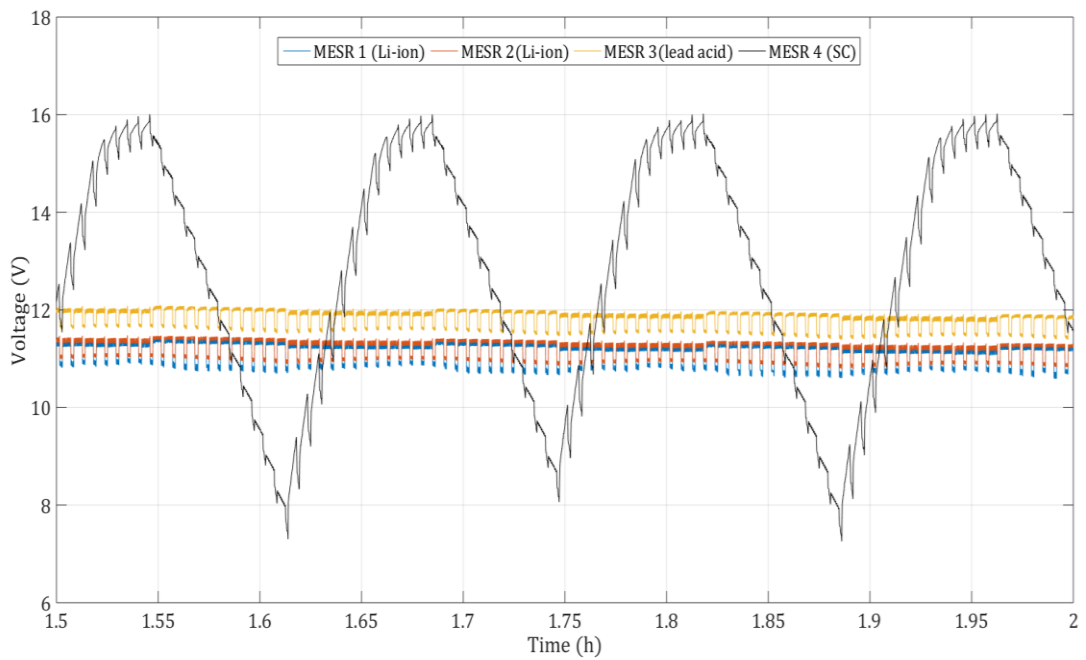
(b)
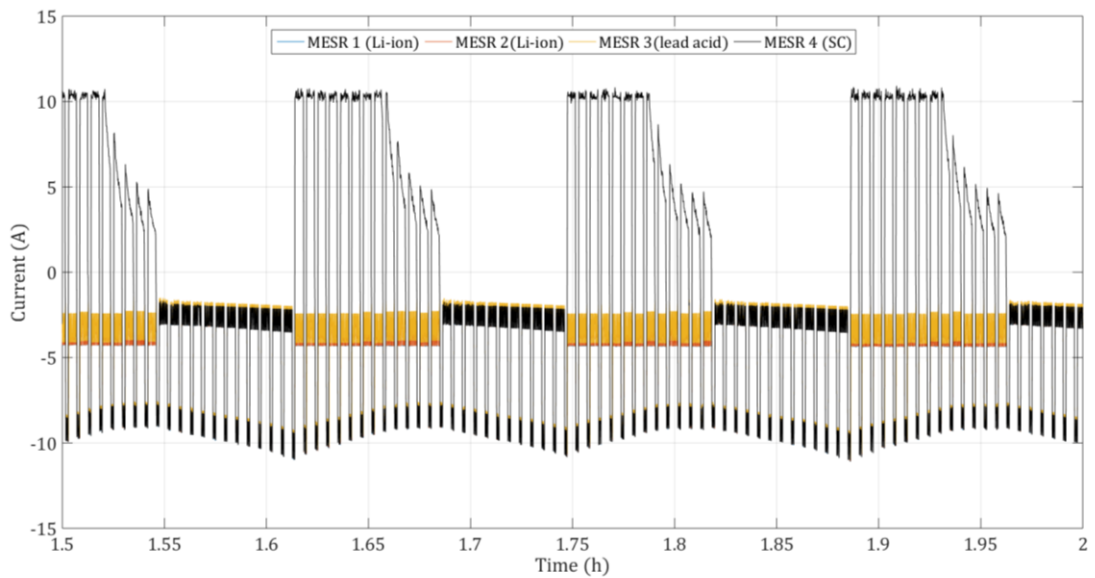
(c)
Figure 5.6 Test IV: Supercapacitor rolling charging.
(a) Voltage, (b) Voltage – 30 min zoom in, (c) Current over 30 min.

5.4.5 Test V: 2 Lithium Ion, Lead Acid, & Supercapacitor (charging all)

In the final test, the same configuration was utilized except, now, rolling charging is applied to all 4 ES elements to achieve a maximum runtime and SoC balance amongst ES modules. The test duration was 25 minutes (~0.42 h), divided into 7 intervals. The sequence of the 7 intervals are as follows: no charging of any ES module, charging the SC, charging the first lithium ion module, charging the SC again, charging the second lithium ion module, charging the SC again, and finally charging the lead acid battery. Figure 5.7(a) is showing the net energy which is the amount of energy withdrawn from/ injected to the ES module, the negative slope indicates discharging while positive one indicates charging. It can be seen that the energies of the four modules coincide with each other during the first interval. This is because the four modules are sharing the load equally and losing energy at the same rate. When the SC is extracted, sign of its energy slope changes representing receiving energy until the net energy goes back to

the zero level (if losses are omitted). In the next stage, the Li-ion battery is extracted; then slope of its net energy (represented by the blue line) changes to be positive. This can be further understood by referring to Figure 5.7(b) &(c), where one can see the current is pulsating because of the load nature. Please note that the same notation for the current is used; negative current indicates discharging while a positive one indicates charging. During the first interval, the current is negative, and the voltage of the SC (depicted in Figure 5.7(c)) is decreasing rapidly. Then, in the second interval, the current of the SC is positive during the off-pulse period, and the voltage is increasing. It should be highlighted that the voltage spikes on the SC voltage profile are because of the pulsed load. In the third interval, the SC is placed again; it can be seen that its voltage is decreasing. The current of the extracted Li-ion battery is positive indicating that it is charging and its voltage is higher than the others (indicated in light blue). This is the typical charging voltage for Li-ion batteries.

The arrows at the bottom of Figure 5.7(b) indicate a current envelope, as the current amplitude is either increasing or decreasing along each interval. This is explained by looking at Figure 5.7(c) and Figure 5.8(a). When charging the SC, its voltage quickly increases which was hereby reflected on the voltage of the entire stack as shown in Figure 5.8(a). Since constant power loads were used, increasing the stack voltage decreased the required current injection from each ES module. The reverse happens when discharging the SC; the voltage of the array decreases. Consequently, the injected current is increasing to maintain constant power supply to the load. From Figure 5.7(c), it can be seen that, over the entire test, the SC voltage was varied between 16.2 V and 8 V.

The comparison of the array voltage from the primary side of the boost converter and the output DC bus voltage depicted in Figure 5.8(a) reveal that the array voltage

experiences wide fluctuations due to coupling and decoupling of ES modules. However, these are not reflected on the DC bus voltage due to the converter. Only minor voltage fluctuations are detected on the DC bus and are well within standard limits. For further illustration, Figure 5.8(a) shows a close-up over a 36 second period, which is covering two cycles of the pulsed load. During the pulse, the stack voltage rises while it decreases during the inactive period of the pulse because of the extracted ES module. It should be noted that during all the performed tests, a simple boost converter with a conventional topology is used whose design is out of the scope of this dissertation. It can be seen from the presented figures that the varying charging characteristics for all 3 ES types are met and the operation is stable. The extraction and insertion of ES modules are done seamlessly without causing any interruptions. This test further highlights the importance of individual monitoring and control of each ES module in an HESS.
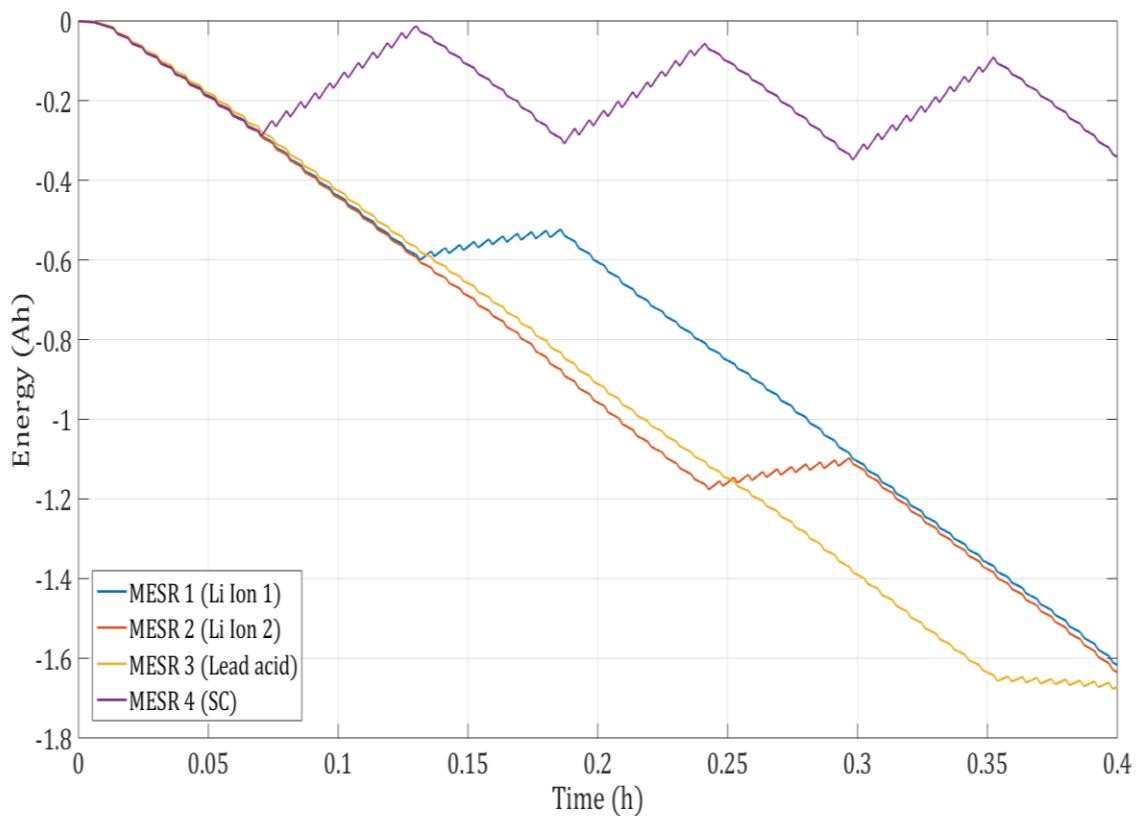
(a)
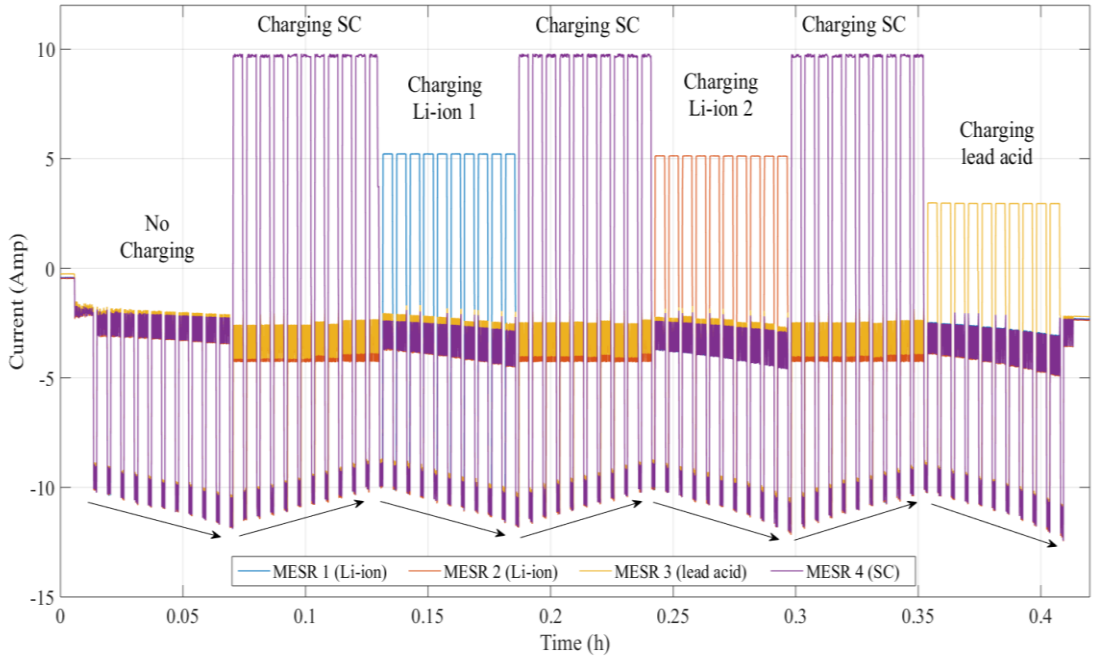
(b)
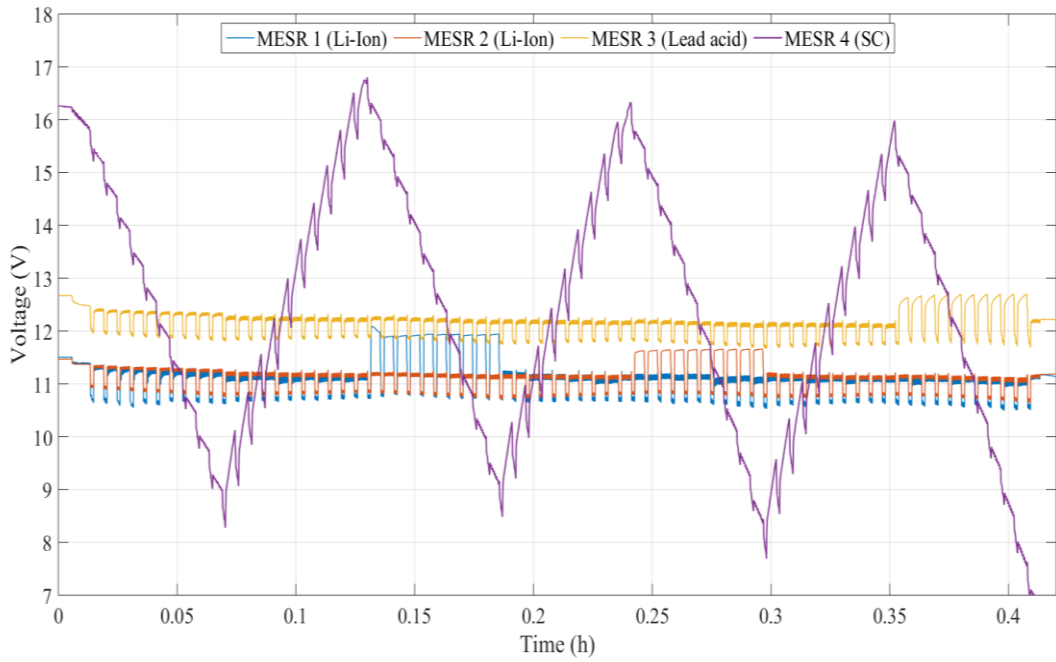
(c)

Figure 5.7 Test V: Rolling charging all ES modules.
(a) Net Energy (b) Current, (c) Voltage.
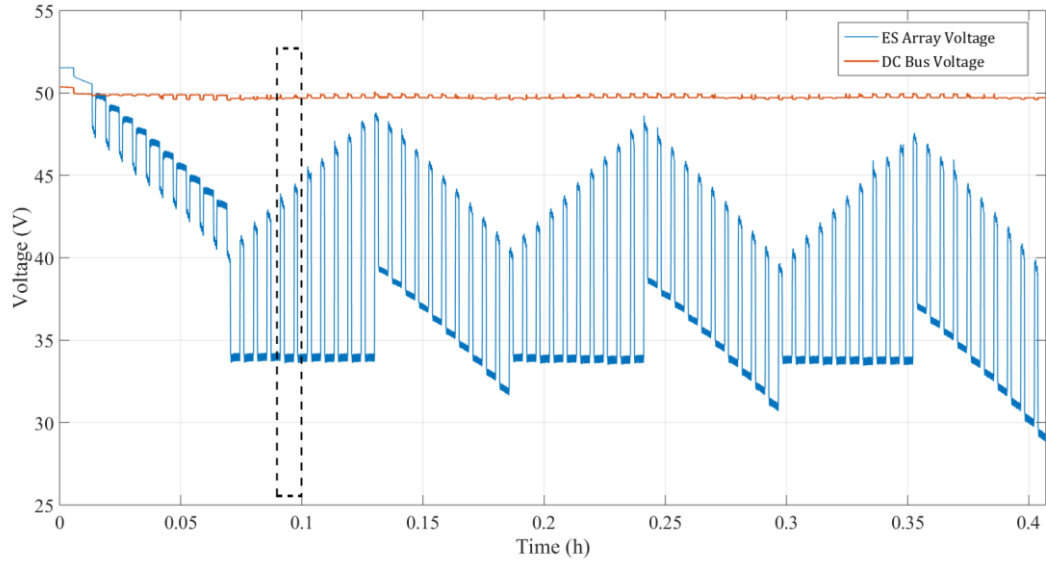
(a)
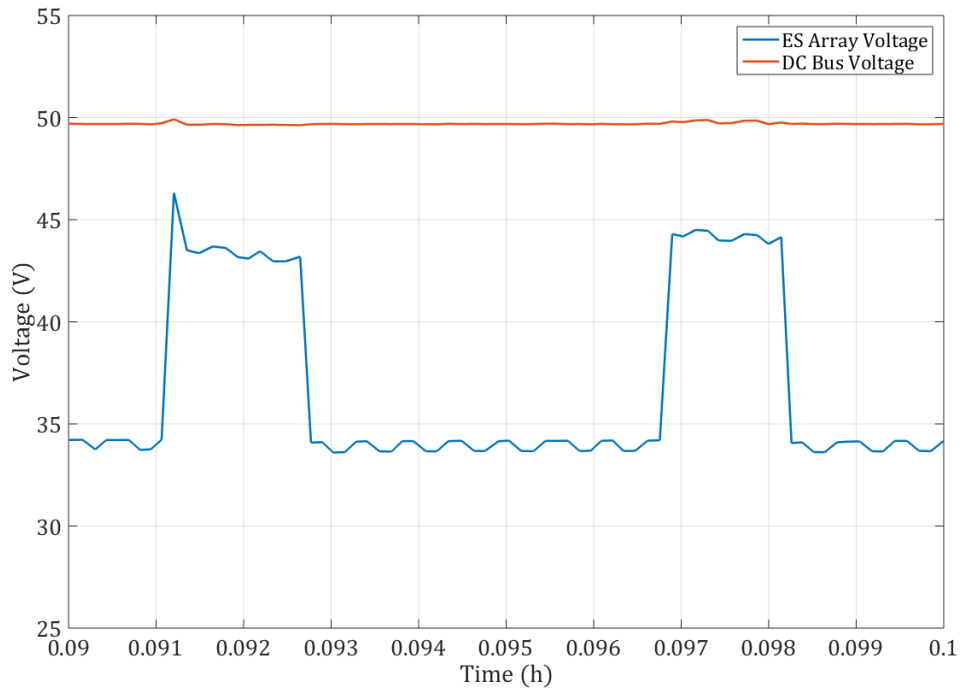
(b)

Figure 5.8 Test V: DC bus and ES array voltages
(a) Entire test period, (b) 36 seconds close up

5.5 Parallel Configuration of Lithium ion Battery and Supercapacitor

In the previous sections, the utilization of the developed MESR to control HESS

with series configuration was discussed in detail. In this section, the control of HESS

with parallel configuration is presented. This HESS is composed of a Lithium ion battery in parallel with a supercapacitor. Major modifications for the MESR had to be introduced. Mainly, the existence of the bypass relay in parallel configuration became unwanted, as it will not be operated in any operation mode. Unintentional activation of this relay may cause a short circuit across the modules' terminals. Therefore, this relay is eliminated from the topology. The control of the system is modified as well. A new management scheme is presented to be adequate for parallel configuration. The management scheme is detailed and validated in the following sections.

This system is discussed and presented in the context of Electric Vehicle (EV) applications. It is found that there's a serious need in the EV field to utilize such Li-ion-SC based HESS. Therefore, the developed MESR is modified and tested to be used in EV systems. Although EV studies are not within the scope of this dissertation, EV application is used as a practical validation case. Furthermore, this serves as a demonstration for the wide range of applications where MESR can be beneficial.

With both Plug-in Hybrid Electric Vehicles (PHEVs) and Battery Electric Vehicles (BEVs) placing a reliance on the battery bank, more research and engineering have been focused on the ES units. Legacy systems employed the usage of nickel metal hydride (Ni-MH) battery arrays. This has since shifted to utilize primarily lithium ion compounds as a result of their high volumetric energy density [238]. Further research showed that using supercapacitors in combination with batteries reduces the stresses of high-power pulses during regenerative braking [214], [239], [240]. In terms of dynamics, the SC also has a much higher power density and can respond much quicker than a lithium ion battery. These traits reveal that a SC is a good fit to reduce the burden of placing additional cycles on a battery when the energy requirement is not as high. This would leave the lithium ion battery to source the base power and the SC handling

of the high-frequency fluctuations. Another dimension of employing HESS importance is realized in cold conditions. In [241], it was found that at subzero temperature, Lithium-ion battery exhibits a significant capacity loss. The authors explained this as a result of internal resistance rise. Therefore, counting on Lithium-ion batteries only reduces the driving range, an HESS is recommended as a potential solution for this problem.
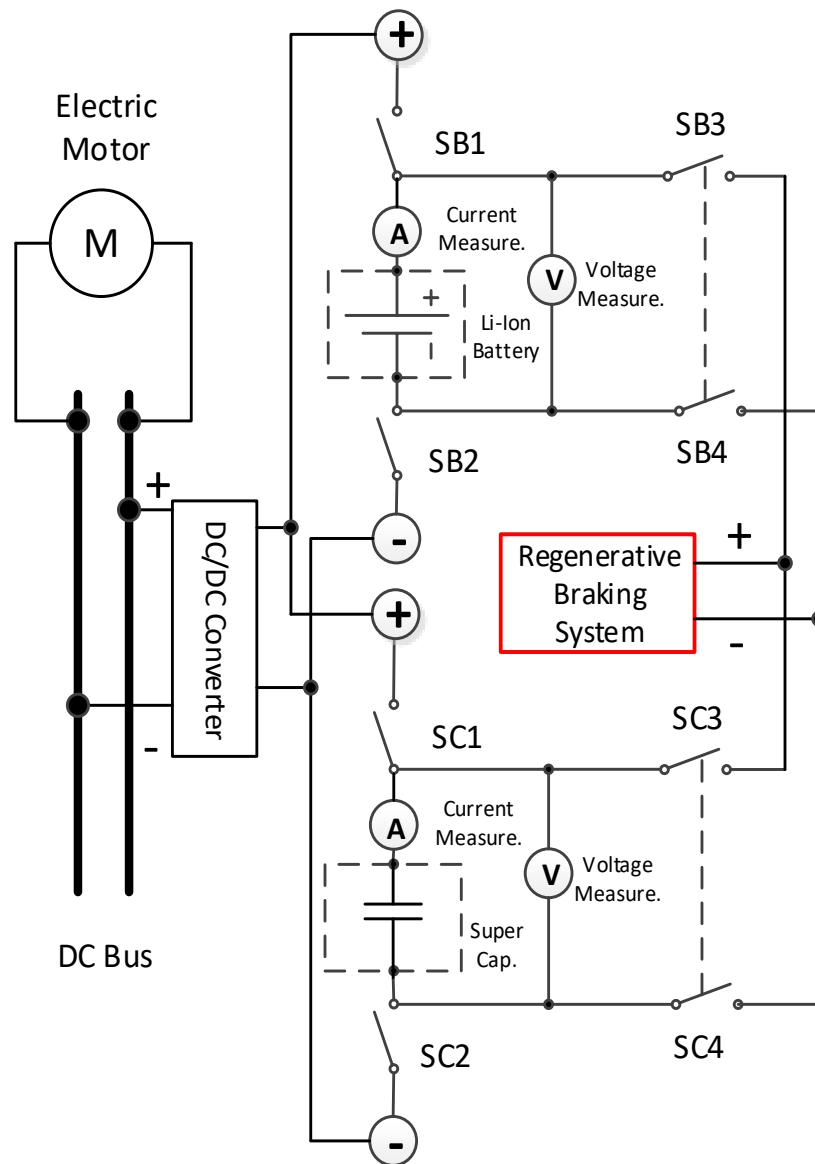
Figure 5.9 Schematic diagram for two MESR units connected in parallel for EV applications

5.6 Proposed HESS Management Scheme

The hybrid lithium ion and SC system utilized in this HESS will operate under multiple states. The main objective of the proposed management scheme is to reduce the cycling and stresses on the lithium ion battery, thus increasing its lifetime. Another objective is to reduce the wasted energy that cannot be absorbed by the battery when it is at a high SoC due to electrochemical limitations.

MESR was designed and implemented to gain control of individual ES elements for a series-connected system. A topology was proposed as a universal tool that could be deployed for a variety of applications. This regulator was modified to be used particularly to manage ES elements in a parallel-connected system. This tool provides individual control, monitoring, and protection of each ES module, as well as a number of unique control features. One of these features is complete decoupling between the charging and discharging circuits while maintaining the lightweight and small footprint to be adequate for an on-board application. The array is then interfaced through a DC/DC boost converter to maintain a constant bus voltage. A schematic diagram for two MESR units connected in parallel is shown in Figure 5.9.

The management scheme is broken into 3 different control states. However, since each ES type has a different discharge profile, switching between states is more complex. The states of the MESR switches for each operation state are shown in Table 5-1. The 3 states of the proposed scheme are outlined as follows:

1) State 1: The lithium ion battery is fully charged (for example, someone driving to work in the morning and the battery is charged overnight) and SC is fully discharged. In this state, the discharge pulse is handled by the battery while the charging pulse (regenerative braking) is handled by the SC. This only exposes the battery to a single cycle until the SC is fully charged, moving the system into State 2.

2) State 2: The SC reaches a full charge. In order to continue harvesting energy from the charge pulse, the SC and lithium ion battery are connected in parallel to absorb the discharging and charging pulses. In this stage, the SC helps to reduce battery current as it trickle charges near a full charge. However, in order to utilize the charging energy, the battery must be exposed to cycling. State 2 continues until near 50% SoC then progresses into State 3.

3) State 3: The lithium ion battery has discharged considerably where the SC is still near 100% SoC as a result of trickle charging in State 2. In this scheme, the charging pulse is applied only to the battery and discharge pulse is handled only by the SC. However, this state is limited in duration as a result of reduced energy density and the SoC-voltage relationship. Limited by the operation range of the boost converter, the SC can only operate until ~60% SoC as the output voltage through will drop below a usable range. Using a multistage boost converter can overcome this weakness. At this point, the system returns to State 1 and progresses through each state until the lithium ion battery bank has reached the full discharge cut-off voltage.

Table 5-1 States of MESR switches for each operation mode

State	Mode	Open switches	Close switches
1	Discharge Ideal Charge	SB3, SB4, SC1, SC2	SB1, SB2, SC3, SC4
2	Discharge Ideal Charge	SB3, SB4, SC3, SC4 SB3, SB4, SC3, SC4 SB1, SB2, SC1, SC2	SB1, SB2, SC1, SC2 SB1, SB2, SC1, SC2 SB3, SB4, SC3, SC4
3	Discharge	SB1, SB2, SC3, SC4	SB3, SB4, SC1, SC2

5.7   Test Procedure and Experimental Results

5.7.1   Hybrid Pulse Power Characterization (HPPC) Test

With the emergence of PHEV and BEV, a need arose for establishing a standard to quantify and assess ES performance. In 2010, the DOE Vehicle Technologies Program released an official "Battery Test Manual" based on technical targets to support the performance and life characterization of developed ES arrays [242], [243]. One of the tests listed in this manual is the Hybrid Pulse Power Characterization (HPPC) Test.

The HPPC test is as shown in Figure 5.10. One-minute cycles are conducted using a normalized current beginning with a 10-second discharge (drive) at full test current, followed by a 40-second rest and a 10-second charge (regenerative braking) pulse at 75% of the HPPC test current. The normalized HPPC current can be scaled based on a battery size factor (BSF) provided by the manufacturer. If a BSF is not provided, as in the case of this test, a C (coulombic) rate of 1C can be used, representing the 1-hour discharge current. For this test, 6.4 Ah lithium ion polymer batteries were used, thus the HPPC current is taken as 6.4 A. Hence, the discharge and charge pulses are set at -6.4 A and 4.8 A, respectively.
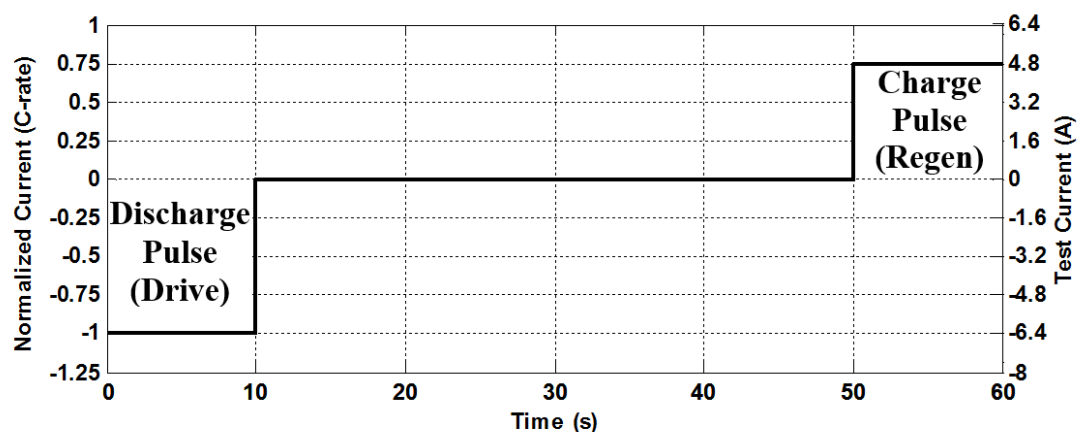
Figure 5.10 Hybrid pulse power characterization test profile

5.7.2 Experimental Results

In order to investigate the feasibility of the proposed management scheme, a hardware setup has been established according to the schematic shown in Figure 5.9. Two MESR units are connected in parallel, where each controller is comprised of four switches, and voltage and current measurements. Four 3.7 V, 6.4 Ah lithium ion cells were connected in series to form the battery module. The SC was comprised from three BMOD0058-E016-B02, 16.2 V modules connected in parallel. Each module is comprised of 6 cells with maximum stored capacity 0.35 Wh per cell. The SC capacitance is 58 F. The terminals of each ES element are connected to the controller to invoke the different controller functions. A unidirectional boost DC/DC converter is used to interface the HESS to a DC bus where the electric motor is coupled. The system is controlled in real time using a LabVIEW program implemented on a PC. However, since the scheme is simple, it can be embedded on a microcontroller or FPGA, which can be an open area for further work.

The experimental results for applying the DOE standard HPPC test for 225 min (~3.75 h) are depicted in Figure 5.11. To obtain the most reliable and realistic results, the test was performed to be lengthy enough to represent a long driving trip. Four minute close-ups around minutes 50 and 100, representing state 1 and 2, are provided in Figure 5.12(a) and (b), respectively. In state 1, by looking at the voltage depicted in Figure 5.11(a), one can see that the SC was charging from the regenerative braking and its voltage is increasing while the battery voltage is decreasing, since it is solely handling the load. Battery charging and SC discharging are indicated by negative and positive current injections, respectively, in Figure 5.11(b). In this state, the SC is absorbing the regenerative braking energy, thus no energy is wasted, which is increasing the overall efficiency of the system. Since the lithium ion battery bank was

at a high SoC, it would be unable to absorb all the regenerative braking energy. At a certain point when both voltages match, the system is switched to state 2, where both units are subjected to charging and discharging pulses. By looking at Figure 5.12(b) and analyzing the charging current injection for both elements, it can be seen that the SC injects more current than the battery. The reason for this is the faster response time for the SC than that of the battery (much lower time constant). Hence, it works as an electric shock absorber and reduces the stresses on the battery.
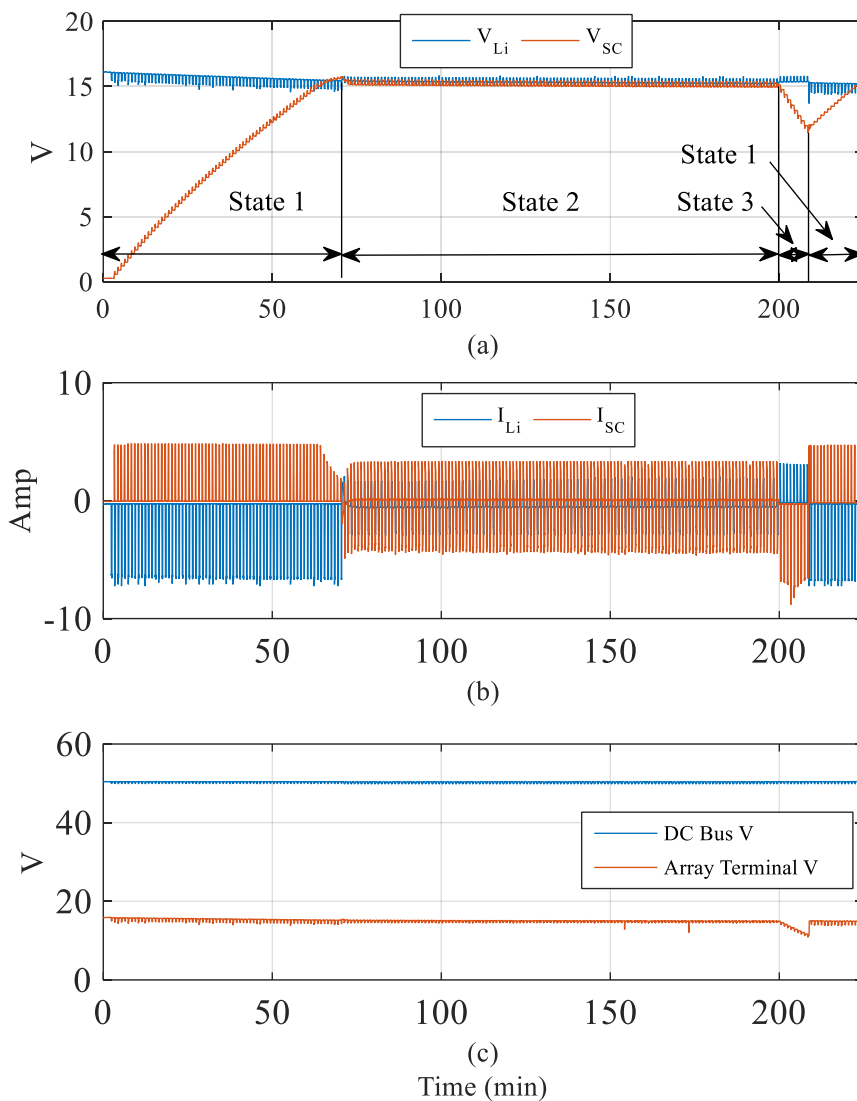
Figure 5.11 HESS in parallel configuration: experimental results
(a) ES Voltages (b) ES Currents (c) DC Bus and HESS Terminal Voltages.
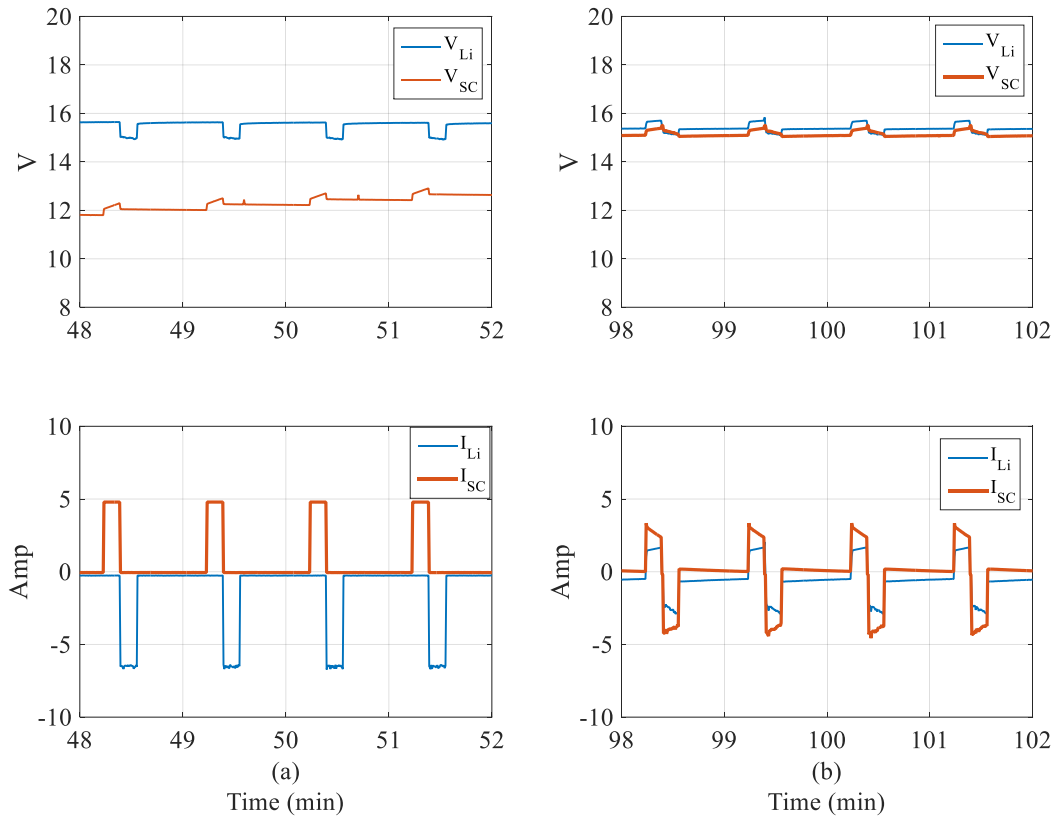
Figure 5.12 Operation states: detailed look (four cycles)
(a) State 1: Voltage (top) and Current (bottom), (b) State 2: Voltage (top) and Current (bottom).

After 200 minutes from starting the test, the system enters state 3, in which the battery is charging while the SC is supplying the electric motor. The current injections are reversed from state 1, as it can be seen that the SC current is negative while the battery current is positive (see Figure 5.11(b)). Despite all the switching activities, it can be seen from Figure 5.11(c) that the DC bus voltage is stable around the operating point (assumed to be 48 V in this test). A fter reaching a certain SoC of the SC, the system is switched back to state 1. The system remains in this state for around 10 minutes. Longer periods can be achieved by increasing the capacity of the SC. A voltage sag in the HESS terminal voltage is noticed in Figure 5.11(c) since the HESS terminal voltage is only regulated by the SC. However, this sag is compensated through the converter.

5.8 Summary

In this chapter, the Modular Energy Storage Regulator (MESR), which was developed earlier, is expanded to be utilized for the management of multi-chemistry energy storage systems. The developed MESR is validated through comprehensive testing procedures with serious and parallel connected Hybrid Energy Storage Systems (HESSs). HESS can be beneficial in a wide variety of applications. In this work, two major applications are tackled: Ship Power Systems (SPS) and Electric Vehicles (EV). A coordinated control technique was introduced to handle the charging of different ES types and extend the operating duration of the array under multiple pulsed loads, common in modern SPS. Using the developed management system, a single ES module could be extracted from the array and connected to a charging bus to restore some of the lost energy as a result of heavy loading periods or pulsed loads. This system provides an effective solution to manage multiple ES types to serve multiple pulsed loads on a SPS platform. The novelties of this work are as follows: 1) performance evaluation of multiple series-configured hybrid energy storage architectures, 2) testing of multiple overlapped pulsed loads with varying frequencies and magnitudes, and 3) the introduction of a specialized dispatch control scheme to coordinate charging and discharging of individual energy storage units while in operation to extend runtime while acknowledging SoH trade-offs. The effectiveness and seamless operation of the system has been verified through hardware testing.

Operation and management of parallel-configured HESS has been covered in this chapter as well. A management scheme for a HESS composed of a supercapacitor and lithium ion battery connected in parallel is proposed. This scheme is simple, yet effective and capable of seamlessly handling the charging and discharging of the HESS. The MESR is modified to be used in parallel configuration. The feasibility of the

developed scheme is experimentally investigated in the context of EV applications using a DOE standard testing profile. It is anticipated that this scheme will increase the lifetime of the battery and the available "in service" time for the ES system.

Chapter 6   Pareto Based Optimal Sizing and Energy Storage

Mix in Ship Power Systems

6.1   Introduction

Generally, the designers of transportation systems (Electric vehicles, aircrafts, space-crafts, trains and ships) face the same challenge, which is the tight constraints of space and weight. Among these systems, reducing the weight in naval platforms is indispensable, as it is twofold: either to reduce the signature of the platform, or to expand the platform capabilities by allowing more fuel and logistics on-board [153]. Another major challenge associated with these systems is they are confined without a strong external support to regulate the frequency or voltage. Thus any disturbance has to be mitigated locally, i.e. large transportation systems can be viewed and treated as islanded microgrids with their own generation and loads.

With reference to ship power systems, the loads can be classified into high and low power loads. High-power loads are supplied directly from the medium voltage level, while low power ones are supplied from the low-voltage side of a transformer through a power distribution module/unit (PDM/PDU) [152], [244]. Some of the high-power loads encounter a pulsed nature where the current sharply rises to high levels, causing undesirable consequences like voltage and frequency modulation. According to [172], a pulsed load is defined as an equipment, which demands frequent or repeated high-power input. A pulsed load is measured as the average power during the pulse interval minus the average power during the same interval immediately preceding the pulse. Therefore, the pulsed load profile exhibits a high peak for short duration and a low average over the entire cycle. This behavior made the utilization of a reliable energy storage system mandatory [245]. Recently, Energy Storage (ES) hybridization was

proposed in the literature. This means combining two or more ES technologies to overcome the shortcomings of a single technology. In this case, the produced Hybrid Energy Storage System (HESS) exhibits more enhanced characteristics (improved energy/power density or faster response) than the traditional single technology-based ES system [246], [247].

There's a strong trend in the marine systems industry to adopt DC distribution architectures with voltage higher than 1 kV giving a rise to the Medium Voltage DC (MVDC) architecture [152]. The utilization of DC offers a wide variety of merits, including the easy and efficient integration of ES systems, where the outputs of most of them are DC in nature [248]. Furthermore, the migration towards the DC-based architectures is supported by the stunning advancements in the power electronic converters, including Voltage Source Converters (VSC) and DC/DC converters. However, in the same context, advantages offered by AC synchronous generators cannot be neglected. Therefore, the power distribution systems of future shipboards are highly expected to be hybrid AC/DC. This adds another challenge to the optimization problem, as will be explained in the following sections.

Different methods and techniques have been introduced in the literature to address the optimal sizing of the ES. In [249], a Teaching-Learning-Based Optimization (TLBO) algorithm is utilized to determine the optimal size of the battery in Plug-in Electric Vehicle (PEV) to minimize the overall cost. Although the importance of optimizing the weight was highlighted in the paper, it wasn't included in the optimization problem. Sizing of ES in a microgrid with different renewable resources is address in [250]. The problem is formulated as a Mixed Linear Integer Problem (MILP) with a single objective to maximize the market benefit (MB). The sizing of a zinc-bromine flow battery system connected to a large wind farm was addressed

in [251]. Another cost-oriented optimization problem is presented in [252]. Genetic Algorithm (GA) optimization is used to maximize the Net Present Value (NPV). The optimization problem was solved considering one type of battery at each time. The Lead Acid Battery (LAB) and Vanadium Redox Battery (VRB) were the considered technologies. A near optimal, three-stage method for optimal allocation and sizing of ES systems was proposed in [253]. In this work, the authors utilized the DC representation for an AC transmission network. The method was applied on the IEEE Reliability Test System (RTS 96 bus) to prove its feasibility. In [185], the authors proposed a GA optimization to optimally size and allocate distributed energy storage in a radial AC distribution system. The objective was to enhance the system's reliability from an economic perspective. Four candidate ES technologies were considered: LAB, Compressed Air Systems (CAS), Sodium Sulfur battery and VRB.

This chapter is presenting a Multi-Objective Optimization (MOO) approach based on Pareto concept to select the optimal size and mix of different ES technologies. The objectives are to minimize the total weight of the ES system, including the converters, and minimize the voltage modulation upon the occurrence of a pulsed load. The optimization techniques and methodologies are abundant in the literature. Therefore, it is found to be important to perform a brief survey over the most used optimization techniques and their classifications.

6.2   Optimization Techniques: A Brief Survey

According to Merriam-Webster dictionary, the word "optimization" is defined as the act, process, or methodology of making something (as a design, system, or decision) as fully perfect, functional, or effective as possible. Optimization is essentially existing in everything, starting from simple daily life decisions to complicated engineering designs. For instance, planning a summer holiday or purchasing a car can be considered

as complex multi-objective optimization problems. Since financial resources and time are always limited, the decision maker will try to achieve the optimal utilization of these available resources and make the maximum benefits. A wide variety of optimization techniques are developed, discussed and utilized in the literature. Mainly, optimization techniques can be categorized according to their methodologies into deterministic and stochastic techniques.

6.2.1 Deterministic Optimization Techniques

Deterministic optimization, or sometimes referred to as mathematical programming, is the classical branch of optimization algorithms. The techniques involve algorithms, which solely rely on linear algebra, since they are commonly based on the computation of the gradient, and in some cases also of the Hessian matrices, of the response variables. Deterministic techniques are divided into two families depending on the problem, either unconstrained or constrained. The techniques for unconstrained optimization problems include:

6.2.1.1 Simplex Method

Sometimes referred to as the Polytope method, which was introduced in the early sixties by Spendley et al. This method involves starting from an initial polytope instead of one initial point. This initial polytope with n + 1 vertices (if n is the dimension of the parameter space) is set up. Hence, if n = 2, the polytope will take the shape of a triangle and Quadrilateral for n = 3. At each iteration, a new polytope will be generated by producing a new point to replace the "worst" point of the old polytope until the optimal point is reached [254].

6.2.1.2 Newton's Method

Newton's method is the most classic and known optimization algorithm. It is also known as the second derivative method since it involves calculating the first and second

derivatives of the objective function f(x) (e.g. the gradient g(x) and the Hessian matrix G(x)).

6.2.1.3 Quasi-Newton Method

The Quasi-Newton method is the simplified version of the Newton method, which only requires the first derivative of the objective function to be computed. The method is superior when the Hessian matrix is not available, thus the most obvious thing to do is to approximate it by finite differences in the gradient vector. In other words, it involves building up trend information as the iterations proceed, using the observed behavior of f(x) and the gradient matrix g(x) without explicitly forming the Hessian matrix [255].

Other methods like Gauss-Newton and Levenberg-Marquardt methods are utilized. The other family of deterministic techniques are used to solve constrained optimization problems. This family includes [255][256]:

6.2.1.4 Penalty and Barrier Function Method

When solving a general nonlinear optimization problem in which the constraints cannot be easily eliminated, it is necessary to balance the aims of reducing the objective function f(x) and staying inside or, at least, very close to the feasible region. Thus, this method transforms the generic minimization problem to a minimization problem of an unconstrained function whose value is penalized in case the constraints of the original problem are not respected.

6.2.1.5 Active Set Methods

Active set methods are methods for handling inequality constraints. The most common is the primal active set method. It is important to distinguish between constraints that hold exactly and those that do not. At a feasible point x, the constraint $a_i^T x \leq b_i$ is said to be active or binding if $a_i^T x = b_i$ and inactive if $a_i^T x < b_i$. In this

method, a correction $\delta^{(n)}$ is applied to a solution $x^{(n)}$ in iteration n. A line-search is performed along $\delta^{(n)}$ to find the best feasible point. If the search terminates at a point where an inactive constraint becomes active, the constraint is added to the active set. This process continues until the solution of the equality constraints problem yields $\delta^{(n)} = 0$, and no constraints are left to be removed from the active set, the optimization terminates and $x^{(n)}$ is flagged as the optimal solution.

6.2.1.6 Lagrangian Methods

There are different Lagrangian methods, some of them are coupled with active set methods or Newton and Quasi-Newton methods. The lagrangian methods involve extensive mathematical modeling. Since it will not be used further in this dissertation, the mathematical modeling of this method is not covered. However, the interested reader can find more information on lagrangian methods in [255], [256].

6.2.1.7 Quadratic Programming (QP)

Quadratic programming is a more direct approach than penalty and barrier function methods to nonlinear programming. In this method, the main problem is broken down to subprobelms, which are solved iteratively. In these subproblems, the objective function is approximated to a quadratic function and the constraints' functions are linearized.

6.2.1.8 Mixed Integer Programming (MIP)

Mixed integer programming is the study of optimization in cases where some of the variables are required to take integer or discrete values. An example is the optimization of a certain manufacturing process, where a decision variable such as number of labors must be an integer. Whereas, in the same problem, another variable which is the number of working hours is not restricted to be an integer. These kind of

problems are solved by the branch and bound method. In this method, the set of candidate solutions is thought of as a rooted tree with the full set at the root. Then, a subset of solutions are obtained by manipulating the rooted set. These subsets are called branches and the algorithm explores the branches of this tree [254].

Initially, it seems that the aforementioned deterministic techniques are appealing for practical problems. The main reason for this is that their convergence to a solution is much faster than the stochastic algorithms, which involve random variables (please see the following sub-sections). Further, they involve a lower number of objective function evaluations. However, these methods are looking for stationary points in response for a certain variable, thus they are more susceptible to be trapped in local optimum points. Moreover, these methods are basically relying on the extensive mathematical modelling of the problem. When speaking about practical problems, finding an accurate mathematical model is not always affordable. Therefore, if there is no or very little knowledge about the behavior of the objective function in the multi-dimensional search space, tackling the optimization problem with a stochastic method seems to be more practical. Hence, the deterministic techniques will not be discussed any further in this dissertation. Instead, more focus will be dedicated to the stochastic techniques.

6.2.2 Stochastic Optimization Techniques

Stochastic optimization methods include the optimization methods in which randomness is present in the search procedure. As a matter of fact, stochastic methods choose their path through the parameter space from randomly selected initial configurations to the optimal solution using a "random factor". Unlike the case in deterministic methods, this random nature causes different computation runs solving the same problem with the same conditions to lead to quite different results. Despite

this fact, this random nature can be viewed from another angle as an advantage, since stochastic methods feature high robustness when dealing with noisy measurement data. Moreover, including random factors enables the stochastic methods to accept deterioration in the objective function (temporarily worse solutions) during the iteration process. This fact enables them to escape local solutions and find the region of the global optimum with a high probability. This process is guaranteed with a high probability regardless of the starting point location [257].

Another point of criticism for the stochastic optimization methods is fueled by the fact that they require a high number of objective function evaluations. With enough confidence, it can be said that this was a serious concern 2-3 decades ago, before the stunning advancements in the computation power. With the high availability of parallel computing systems, Graphical Processing Units (GPUs) and powerful processors, several evaluations of complicated objective functions can be done in a reasonable time. This led to the high popularity of stochastic methods in solving real-world problems.

In the past, stochastic algorithms were often referred to as heuristic. Originally, the word "heuristic" is an ancient Greek word which means "to discover". Roughly speaking, heuristic means to discover by trial and error. Firstly, heuristic was introduced as a psychological concept by Nobel-Laureate Herbert A. Simon. Then, it was exploited in different science realms. As time progressed, and with the introduction of more developed techniques, the word "meta" was attached to the word "heuristic" to form the now term meta-heuristic. Here "meta" means "beyond" so "meta –heuristic" refers to higher-level algorithms.

When designing any metaheuristic algorithms, the designer should achieve a balance between two major concepts, namely intensification and diversification. Diversification means to generate diverse solutions so as to explore the entire search

space on a wide scale (which consequently increases the algorithm robustness), while intensification means to focus the search on a local region knowing that a current good solution is found in this region. Designing an algorithm with more intensification will be more susceptible to be trapped in a local minima. In contrast, an algorithm with more diversification will not converge in a reasonable time [256]. Hence, a tradeoff has to be made between the two concepts depending on the problem.

Many metaheuristic algorithms are discussed in the literature. Most of them are based on concepts from biology, metallurgy and observations of nature or animal behaviors. In this section, a brief overview on the existing metaheuristic techniques will be provided.

6.2.2.1 Simulated Annealing

Simulated Annealing (SA) is based on one of the metallurgy concepts, which is the metal annealing. This technique was introduced by Kirkpatrick et al. in 1983. The annealing is a techniques which involves heating the metal to a high temperature and slowly cooling it, to re-arrange its crystals in a configuration where the minimum energy is reached. If the cooling is sufficiently slow, the system has time to explore many configurations and settles in the minimum energy one. The main purpose of this process is to increase the material machinability. The contrast of this process is the metal quenching or hardening.

In simulated annealing, the actual search moves along a piecewise path. With each move, an acceptance probability is evaluated. The acceptance probability p is based on Boltzmann probability distribution, which is given by:

$$P = e^{-\frac{\Delta E}{K_B.T}}$$ (6-1)

where k_B is the Boltzmann's constant, T is the temperature for controlling the annealing

process and ΔE is the change in energy. This acceptance probability not only accepts changes that improve the objective function (a lower value in a minimization problem), but also keeps some changes that do not improve the objective (a larger objective value). This feature plays a significant role in helping the SA to achieve the global minimum. This transition probability is based on the Boltzmann distribution in statistical mechanics.

In SA optimization, a law defining how the temperature parameter decreases over successive iterations must be given. There are many ways to control the cooling rate or the temperature decrease. Two commonly used annealing schedules (or cooling schedules) are linear and geometric. The geometric cooling is the most widely used one, in which T is replaced by αT, where α is the cooling rate in range [0,1]. The advantage of the geometric cooling is that it doesn't need to specify maximum number of iterations. In order to make the cooling process slow enough to allow the system to explore more states and stabilize, α is selected in range of [0.7,0.99]. However, more conservative researchers limit the practical range of α to be within [0.7, 0.85]. The results of a comprehensive study to assess the influence of the key parameters of simulated annealing used for Maximum Power Point Tracking (MPPT) are presented in [258]. In this study, it is shown that the acceptance probability and the cooling schedule are affecting the convergence of the algorithm significantly. Further, it is found that Lundy and Simulated Quenching (SQ) cooling schedules are suitable for this application.

The objective function f(x) to be minimized can be considered the energy of the system while the different combinations/values of the decision variables of the optimization are its atomic configurations. The probability that a particular configuration, even a worse one, is accepted is ruled by a Boltzmann probability, which

was explained earlier. This particular acceptance criterion, which is the backbone of the method, allows some probability of accepting worse configurations. The probability of accepting worse solutions is dictated by the current temperature $T(n)$. As long as the temperature is very high, SA accepts every new solution, thus yielding a random jumps through the search space. On the other hand, with a lower temperature, only improvements are accepted.

6.2.2.2 Particle Swarm Optimization

Particle swarm optimization (PSO) is based on swarm behavior observed in nature, such as in bird flock or fish schooling. PSO was developed by J. Kennedy and R.C. Eberhart in 1995. Since then, PSO has attracted a lot of attention, and now forms one of the most exciting, ever-expanding stochastic techniques. It was found that when a flock of birds is looking for food, the individuals are following a leader who is the closest one to the food location. Then, each bird changes his location with a certain velocity in the direction of the leader. Thus, by imitating this concept, the food location will be the optimum solution in the search space and the flock leader is the fittest individual (the solution of the current iteration that achieves the minimum value of the objective function in a minimization problem).

PSO searches the space of an objective function by adjusting the trajectories of individual agents, called particles. When a particle finds a location that is better than any previously found locations, then it updates this location as the new current best for particle i. There is a current best for all particles at any time t at each iteration. The aim is to find the global best among all the current best solutions until the stopping criterion becomes true or after a certain number of iterations.

There are many algorithms that are derived from PSO, as well as hybrid algorithms obtained by combining PSO with other existing algorithms. One of the most noticeable

169

improvements is probably introducing an inertia function θ (t) so that velocity of a particle i, v_i is replaced by $\theta(t).v_i$ where θ takes a value between 0 and 1. In the simplest case, the inertia function can be taken as a constant, typically in the range of [0.5, 0.9]. This is equivalent to introducing a virtual mass to stabilize the motion of the particles, and thus the algorithm is expected to converge more quickly. Another improved PSO technique involves using chaotic inertia weights and a crossover operator to solve the economic dispatch problem [259].

6.2.2.3 Differential Evolution

Differential evolution (DE) was developed by R. Storn and K. Price. It is a vector-based evolutionary algorithm, and can be considered as a further development of genetic algorithms. Both algorithms aim at simulating the evolution of a population through successive generations of better performing individuals. Unlike genetic algorithms, differential evolution carries out operations over each component (or each dimension of the solution). Almost everything is done in terms of vectors, so a mutant individual is represented by a vector. DE can be viewed as a self-organizing search, directed towards the optimum solution. Similar to genetic algorithms, DE consists of three main steps: mutation, crossover and selection.

6.2.2.4 Ant Colony Optimization

Ant colony optimization was pioneered by M. Dorigo in 1992 and is based on the co-operative behavior of social ants when looking for food. Ants are social insects and live together in well-organized colonies consisting of approximately 2 to 25 million individuals. When searching for food, a swarm of ants interact or communicate in their local environment. Each ant lays scent chemicals or pheromone to communicate with others. Each ant is also able to follow the route marked by the chemicals laid by other ants. When an ant finds a food source, it will mark it with this chemicals and also mark

the path to and from it.

The process starts with an initial random route, where the individuals are dispersed over the search space. Since, the pheromone (laid chemicals) concentration varies, the ants follow the route with higher pheromone concentration. In turn, the pheromone is enhanced by the increasing number of ants (more laid chemicals). As more and more ants follow the same route, it becomes the favored path. Thus, some favorite routes emerge, often the shortest or more efficient ones leading to the optimal solution. In electrical engineering, ant colony was used in different subjects including: generation planning [260], [261][262] loss reductions of distribution systems [263] and scheduling of electric vehicle (EV) charging [264].

6.2.2.5 Bee Algorithms

Bee algorithms are another class of metaheuristic algorithms, inspired by the foraging behavior of bees. A few derivatives of the classical algorithm exist in the literature, including honeybee algorithm (HBA), artificial bee colony (ABC), and virtual bee algorithm (VBA). These algorithms are pioneered by D.T. Pham, C. A. Tovey and Xin-She Yang. It was initially introduced in 2004-2005.

Honey bees construct colonies, where they live and store honey. The communication mean among colony members is pheromone and `waggle dance'. When discovery bees find a good food source (flowers rich with nectar), they will communicate the location of the food source by performing what's called waggle dance as a signaling system. Such signaling dances vary from species to species, and it depends on the available amount of food. However, they are aimed at recruiting more bees by using directional dancing with varying strength so as to communicate the direction and distance of the food source. The same idea is utilized to develop the optimization algorithm where the optimal solution is referred to as the food source.

6.2.2.6 Cuckoo Search

Cuckoo search (CS) is one of the most recent nature-inspired metaheuristic algorithms, developed by Xin-She Yang and Suash Deb in 2009 [265]. Later on, in 2010, the same developers of this algorithm enhanced it by incorporating Lévy flights [266]. Recent studies show that CS is potentially more efficient than Particle Swarm Optimization (PSO) and simulated annealing. Cuckoos are fascinating birds as they make adorable sounds, however they have an aggressive parasitism strategy for their production. They remove other birds' eggs and lay theirs among the hosts' eggs to increase the hatching probability of their own eggs. The main steps of the algorithm are as the following:

- Each cuckoo lays one egg at a time, and dumps it in a randomly chosen hosting nest.

- The best nests with high-quality eggs are carried over to the next generations.

- The number of available host nests is fixed, and the egg laid by a cuckoo is discovered by the host bird with a probability $p \in [0,1]$, depending on the similarity of a cuckoo egg to its host eggs. In this case, the host bird can either get rid of the egg, or simply abandon the nest and build a completely new nest.

The CS is one of the promising optimization techniques to be used in Multi-Objective optimization problems. It was shown that it has higher accuracy and good convergence capabilities [267].

6.2.2.7 Grey Wolf Optimization (GWO)

GWO is proposed by Mirjaliliet al. [268]. The mathematical model of GWO is inspired by the hunting technique and the social hierarchy of grey wolves' herds. On top of this hierarchy, is the leader who is called alpha and the group follows his or her instructions. The second level of the hierarchy is called beta wolves and they assist the

alpha in making decisions. Omegas are the lowest ranking grey wolves of the hierarchy and they have to submit to all other dominant wolves. Delta wolves come in the hierarchy next to the alphas and betas but they lead the omega. The mathematical model of the optimization technique is analogous to the social hierarchy of grey wolves. First, the fitness solutions are determined and the best fitness solution is regarded as alpha (α) individual, the second and third best solutions are considered as beta (β) and delta (δ) individuals, while the rests of the fitness solutions are regarded as omega (ω) [269]. The effectiveness of the GWO technique has attracted the attention to it to be used in different applications [270]-[272].

6.2.2.8 Other Metaheuristic Algorithms

Some widely used techniques were selected to be briefly discussed in this chapter, however there are many other successful metaheuristic techniques that cannot be covered in a single chapter or article. The interested reader is highly encouraged to read about the other optimization methods. For example, Tabu search is one of the optimization techniques that explicitly uses memory and search history. Through the appropriate use of search history revisiting the same solutions can be avoided. The algorithm records recently tried solutions in tabu lists. The algorithm is prevented from going over these lists again. Over a large number of iterations, these tabu lists could save a significant amount of computing time, leading to improvements in search efficiency. Another technique is the Firefly algorithm which is based on the flashing (glowing) patterns of fireflies. Harmony search is a technique that is inspired by the improvisation process of a musician. Further, there's a technique called artificial immune system which is inspired by the actions of the immune system. This algorithm uses memory and learning which adds adaptive capabilities to its performance.

6.2.2.9 Genetic Algorithms

Genetic algorithms (GAs) are probably the most popular and successful evolutionary based algorithm. Its success can be widely seen in its applicability, where it has been utilized in a diverse range of applications. Further, a considerable number of well-known and complicated optimization problems have been solved by genetic algorithms. These problems include: graph coloring, pattern recognition, travelling-salesman problem, aerospace engineering, financial markets and economic dispatch. In addition, genetic algorithms are population-based and many modern evolutionary algorithms are directly based on, or have strong similarities to genetic algorithms.

From historical point of view, GAs were developed more than half a century ago in the 1960s by J. Holland. The core of the GA is the abstraction of biological evolution based on Charles Darwin's theory of natural selection. The first step of a GA is the initialization of a population of m individuals $x_1^{(1)}, x_2^{(1)}, ..., x_m^{(1)}$ on the discretized design space and evaluate the fitness function for each individual in the population. Each individual represents a solution and each solution is encoded as arrays of bits or character strings (chromosomes). Each iteration produces a generation, which is a set of new individuals. For each generation n, these steps are done:

-   Randomly select a pair of solutions. This process is called selection which is the first one to take place. Although, the selection of the parents is random but the probability of being selected is not the same for each individual as in other Evolutionary Algorithms. Different rules have been used for the selection mechanism; the most common are the roulette-wheel selection and the tournament selection. The mechanism that will be used in this study is the tournament selection, so it will be briefly explained. In tournament selection, a few individuals

are selected in a random manner to take part in a tournament. The individual with best fitness (achieves the minimum value of an objective function in a minimization problem) will be the winner of that tournament which will be selected. The individuals are ranked according to their fitness, the best individual is selected with probability p_t, the second best with probability $p_t \cdot (1 - p_t)$, the third best with probability $p_t \cdot (1 - p_t)^2$, and so on. Typically, $p_t \in [0.5, 1.0]$. Allowing suboptimal solutions to be selected helps in maintaining diversity in the population and prevent premature convergence. As mentioned earlier, in this section the designer should achieve a trade-off between diversification and intensification.

- Apply the cross-over operator with probability P_c, giving birth to two children. If no cross-over takes place, the two off-springs are exact copies of their parents. The cross-over probability is generally quite high in the range of [0.7, 0.99]. Some researchers reported successful using of values around 0.9. Simply, as implied from the process name, cross-over involves interchanging portions from the parents and combining them together to produce children. The most common crossover techniques are the one-point cross-over, two-points crossover, and uniform cross-over. In one-point cross-over, a single point along the parents' chromosomes is selected randomly and the genetic information beyond that point are swapped between the two parents in order to create the two children. While, in two-points cross-over two points along the parents chromosomes are selected randomly and the genetic information in between the two points is swapped between the two parents. In this research work, the single point crossover is used.

- Apply the mutation operator to each one of the reproduced two off-spring with probability P_m. The mutation probability is generally quite low ($P_m \in [0.005, 0.05]$). Thus, cross-over has more contribution than mutation in the evolution

process. Mutation operator acts simply swapping, from 0 to 1 and the other way round.

After finishing the above mentioned process for all the individual members, the new generation replaces the previous one, and the fitness of their individuals is evaluated. If the number of individuals per generation is odd, then one child is discarded randomly. Generally, the efficiency of GAs depends mainly on the accuracy of the fitness function and on the choice of the controlling parameters, such as pc, pm, and pt. In addition, the choice of the right population size is also very important. If the population size is too small, there will not be enough evolution, and there is a risk for the whole population to converge prematurely. On the other hand, if the population is too large, more evaluations of the objective function are needed which will require extensive computing time and effort.

6.2.3   Multi-objective Optimization (MOO)

Solving a multi-objective problem requires the determination of a set of points that all fit a pre-determined definition of an optimum solution. Since more than an objective function is involved in the optimization process, there's no single ultimate solution. Actually the multi-objective problems produce a set of solutions. This set of solutions is called Pareto Front (PF). This concept of defining optimal solutions is called Pareto Optimality. In Multi-objective Genetic Algorithm (MOGA), a redefinition of the selection rules is needed. For instance, the probability of winning the tournament in tournament selection will be higher for the individuals belonging to the Pareto frontier. Then, less probability is assigned to the individuals at farther distance from the front. More complex selection operators, which aim at achieving a more uniform distribution of the solutions on the Pareto frontier can also be defined. In this research work, it is proposed to use Non-dominated Sorting Genetic Algorithm II (NSGA II) to generate

non dominated Pareto Front.

NSGA was a popular non-domination based genetic algorithm for multi-objective optimization. However, it is criticized for its computational complexity. Then, a modified version, NSGAII was developed, which has a better sorting algorithm and less computational complexity. First, let us breakdown the name: N stands for non-dominated because it finds the non-dominated solution. Non-dominated solution is the one achieving the minimum objectives in a minimization problem. To relate it to our specific problem, the non-dominated solution is the one that is achieving the minimum voltage and frequency fluctuations. S stands for sorting because it sorts the population based on a fitness function. It puts the non-dominated individual in the front to form what is called Pareto front or Pareto efficient solution. Furthermore, NSGA-II utilizes an elitism operator which makes the most performing individual in the population to survive through the generations without mutation [273].

The first step is the initialization of the population similar to the regular GA. Once the population in initialized the population is sorted based on non-domination into each front. The first front is a completely non-dominant set in the current population and the second front is dominated by the individuals in the first front only, and the front ordering goes on. Each individual in each front is assigned rank (fitness) values based on the front which they belong to. Individuals in first front are given a fitness value of one, and individuals in second are assigned fitness value as two, and so on. Some examples in literature showed that it is successful in avoiding the local minima/maxima or local traps [273].

6.3 Optimization Methodology

In this section, the proposed optimization methodology to select the optimal energy storage mix and size in shipboard power systems is explained in detail.

6.3.1　Pareto optimality

The problem presented in this chapter is a multi-objective optimization problem (MOOP) with two objective functions. In many studies, the aggregate weighted function method is used to solve the MOOP. In this method, all the objective functions are aggregated in only one function by assigning a weight for each one as follows:

$$O.F = \sum_{x=1}^{Nobj} W_x \cdot f_x \qquad (6\text{-}2)$$

where W_x is the weight assigned to objective function x and N_{obj} is the number of objective functions in the problem. Then, after relaxing the multi-objective optimization problem into a single objective one, the problem is solved using any of the single objective techniques [274]. This method is simple, which is the reason it is preferred by many researches. However, this method suffers from major drawbacks, including the difficulty of the appropriate assignment of the weights and its failure to generate feasible solutions on the non-convex portions of the optimum solution front [275]. Furthermore, it generates only one solution, which significantly limits the options in the decision making process [276]. Whereas in the Pareto optimality (PO) a set of points that all fulfill the definition of an optimal solution and meet the problem constraints is defined. Thus, all the generated solutions in this set are considered optimal and satisfy the objective functions with varying degrees. This set of optimal solutions is known as the Pareto Front (PF), named after the economist Vilfredo Pareto [277].

Different methods were proposed in the literature to generate the PF. As an example, a combination of artificial immune system and ant colony optimization (AIS-ACO) was used in [278]. Reference [279] presents a Multi-objective Evolutionary Algorithm (MOEA) to generate the PF in the economic dispatch problem. In [280], a Niched Pareto Genetic Algorithm (NPGA) is proposed. However, among these

methods, Non-dominated Sorting Genetic Algorithm II (NSGA-II) has been one of the most successful techniques. The NSGA-II is an extension of the GA and uses an elitism approach and sorting mechanism to determine the PF. The PO method provides a set of optimal solutions that satisfy the objective functions but with varying degrees. In other words, it provides tradeoffs between the objectives to be optimized, even if they are explicitly contradicting. This feature can be of great help for the decision maker. However, at the end of the optimization process, only a single solution from the generated front should be selected. Therefore, a posteriori step is needed to select a single solution to be implemented. This is a point of criticism for the Pareto based methods.

6.3.2   Power Flow in Hybrid AC/DC distribution Systems

In order to determine the minimum size of ES units and evaluate the impacts of their installation on the distribution system, the power flow has to be solved. As mentioned earlier, the distribution architectures in modern marine platforms is hybrid AC/DC systems. Mainly, two approaches have been proposed in the literature to solve the power flow in AC/DC systems, namely unified and sequential. In the first, the AC and DC system equations are solved simultaneously (i.e. formulate a single Jacobian matrix for the entire system [281]). A disadvantage of this method is that the entire Jacobian matrix has to be updated in each iteration. Whereas in the later approach, the AC system equations are solved and then their output parameters are passed to the DC system equations to be solved [282]. Consider the simplified network depicted in Figure 6.1. In the first iteration, the AC network is solved using the traditional Newton Raphson method and initial values for its parameters (voltage magnitude, angle, active and reactive power) are calculated. Then these parameters are used to solve the DC system of equations. A single DC bus is designated as the slack for the DC network. At

each iteration, a power mismatch vector is calculated. The second iteration uses the values calculated previously. The process continues until a pre-specified value for the mismatch vector is reached. This method was initially developed for HVDC systems, major manipulations had to be introduced to the approach to be adequately used in MVDC distribution systems.
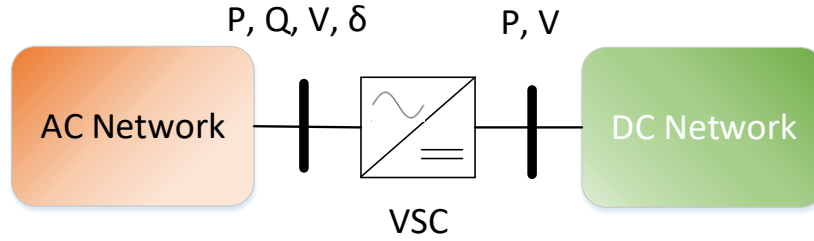
Figure 6.1 A simplified diagram for a hybrid AC/DC network.
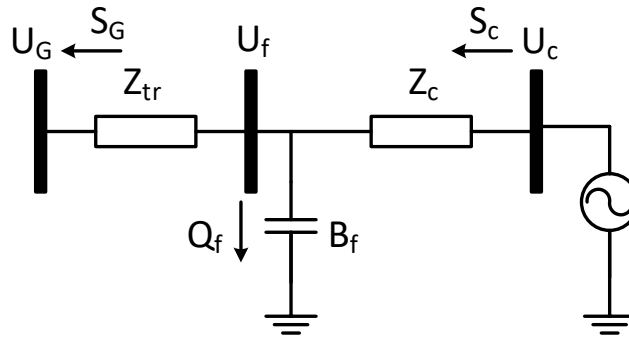
Figure 6.2 Equivalent one line diagram of a Voltage Source Converter (VSC).

The VSC can be modeled as an AC voltage source behind a phase reactance, as shown in Figure 6.2 [283]. Where the output of the voltage source is $U_c \angle \theta_c$, Z_c is the phase reactor impedance, Z_{tr} is the transformer impedance and B_f is the susceptance of the shunt filter. Consider that the AC network is divided into Z zones, then the injected active and reactive power from the VSC in to this zone is given by [282];

$$P_G^z = -U_G^2 . G_{tr} + U_G . U_f . \left[G_{tr} \cos(\theta_G - \theta_f) + B_{tr} \sin(\theta_G - \theta_f) \right] \qquad (6\text{-}3)$$

$$Q_G^z = U_G^2 . B_{tr} + U_G . U_f . \left[G_{tr} \sin(\theta_G - \theta_f) - B_{tr} \cos(\theta_G - \theta_f) \right] \qquad (6\text{-}4)$$

where G_{tr} and B_{tr} are the equivalent conductance and susceptance of the transformer, respectively, obtained from the Y_{Bus} matrix.

6.4 Optimization Problem Formulation

As mentioned earlier, the optimal sizing, mix and allocation of ES units in ship power system are determined through solving a MOO problem with two objectives. A meta-heuristic technique (NSGA-II) will be used to solve the problem and determine the set of Pareto efficient solutions. The problem is formulated as follows:

6.4.1 Objective Functions

The two objectives in the problem are to minimize the voltage deviation on all the buses either in the AC or DC sides and to minimize the total weight of the installed ES while considering the weight of the converters. The first objective function (O.F) is given as:

$$O.F_1 = \sum_{i=1}^{n} (V_i - \bar{V})^2 \qquad \forall i \in \{N_{AC} \cup N_{DC}\} \qquad (6\text{-}5)$$

Where V_i is the voltage magnitude at bus i. N_{AC}, N_{DC} are the sets of AC and DC buses, respectively, n is the total number of the busses in the system (n equals the length of $\{N_{AC} \cup N_{DC}\}$). $\bar{V}$ is the nominal voltage which is 1 p.u. The second objective function ($O.F_2$) calculates the weight of the energy storage systems.

$$O.F_2 = W_T = \sum_{K} d_K \cdot \left[\sum_{i} E_{i,K} \right] + \sum_{m \in ES\_Conv} f_{Cw}(P_m) \qquad (6\text{-}6)$$

where K is an subscript denoting the type of the energy storage, $K \in \{1,2,3,\ldots,n_K\}$, n_K is the number of energy storage technologies involved in the optimization problem. $E_{i,k}$ is the energy capacity of the energy storage unit of technology K installed at bus i, d_K is the energy density of energy storage of technology K. ES_{Conv} is the set of converters interfacing the energy storage units, P_m is the maximum output power of

converter m. f_{Cw} (•) is a function calculating the approximate weight of the converter as a function of its maximum output power. In (6-6), the total weight W_T of the installed ES system for a given solution is evaluated as the sum of the ES unit weight and the weight of the converter. The weight of the ES unit is a function of its energy storing capacity, while the weight of the power electronic converter depends on its maximum power capacity. The higher the converter power the larger cooling system has to be, which significantly contributes to the total weight of the converter [284]. A detailed procedure can be performed to derive the function f_{Cw} (•); however, in this research work, a linearized model is used to estimate the weight of the converter based on power-to-weight ratio. In order to calculate the power-to-weight ratio and for the sake of methodology integrity, a simplified topology is assumed in Figure 6.3. The topology comprises a five level flying capacitor multilevel inverter (FC-MLI), a medium frequency transformer, and a single phase inverter. This converter can be used to transfer the power bi-directionally between the medium voltage DC bus (at 7.2KV) to the low voltage at which the energy storage units are connected (assumed to be 600V). As shown in [285], the power density of the medium frequency transformer for transportation applications ranges from 2.5 kVA/kg to 5 kVA/kg. In this study, the lowest power density is used. The IXYS IGBT module [286] is assumed to be the switching element in the converter. This IGBT module has a maximum collector to emitter voltage of 2500V and a maximum collector current of 1200A. By considering the total number of switches and the heat sink calculations [287], a power to weight ratio is estimated as 1.25 kW/kg, which is reasonable with considering medium switching frequency if compared to low switching frequency power converters [288].

6.4.2 Decision Variables

Similar to the traditional GA, in NSGA-II, the generations are evolving, each
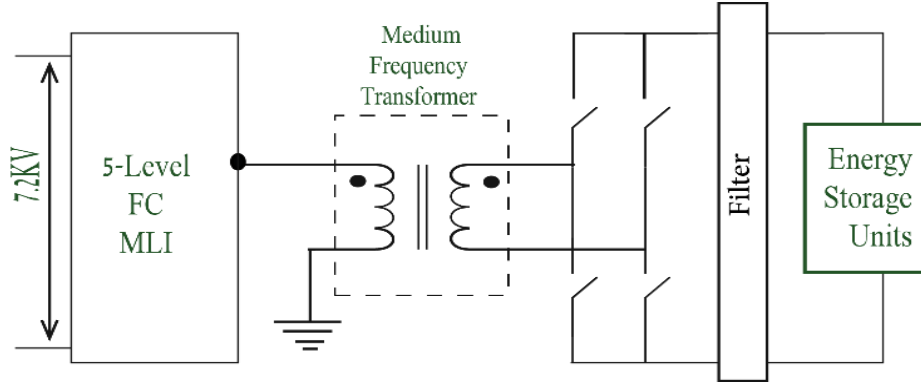
Figure 6.3 A simplified schematic diagram for the ES interfacing converter
(illustrated for weight calculation purposes).

generation consisting of a pre-determined number of individuals where each one
represents a solution to the problem. Each individual has chromosomes and each
chromosome controls a parameter. A decision variables vector X is assigned as follows:

1) Pulsed load location: An integer decision variable x_{pl} is assigned to control the
   location of the pulsed load, where $x_{pl} \in \{N_{pl}\}$. N_{pl} is the set of candidate buses
   for pulsed load connection.

2) Energy Storage location: An integer decision variable x_k is assigned to control
   the location of the energy storage from technology K, where $x_k \in \{N_K^{ES}\}$. N_K^{ES}
   is the set of candidate buses for installing energy storage from technology K.

3) Energy Storage Power Sizing: An integer decision variable $x_{i,K}$ is assigned to
   control the maximum power of the energy storage unit installed at bus i from
   technology K.

$$P_{i,K}^{ES} = x_{i,K}^{P} \times Sizing\ Step \qquad (6\text{-}7)$$

where $P_{i,K}^{ES}$ is the active power injected from the energy storage unit installed at bus i.
In this study, it is assumed that the ES units will be installed on the DC side only. Thus,
there is no Q injection. The sizing step is a constant referring to the size increment by

183

which the ES can be installed. The sizing step is assigned by the designer based on the commercially available systems and the physical requirements if any. It is worth mentioning that the length of the decision variable vector X equals to $2 \times n_{K+1}$, so, in case of having two energy storage technologies, length of $X = 5$.

6.4.3 Constraints

While solving the problem, it is essential to avoid violating any power system limits that may cause an undesirable operation scenario or disconnection of sensitive loads. Further, it should be assured that the optimal solution is feasible from the power system point of view. Thus, the problem is subject to the following constraints.

1) Voltage Limits:

$$V_{min} \leq V_i \leq V_{max}$$

(6-8)

where V_{min}, V_{max} are the minimum and maximum allowable voltage limits at each bus. In this study, V_{min}, V_{max} are taken as 0.95 p.u. and 1.05 p.u, respectively.

2) VSC limits: According to [282], [283], the working point must be situated within the P-Q capability chart of the converter. However, the most important limitation is the one imposed by the maximum current through the IGBT.

$$|I_{Conv.}| \leq I_{Conv}^{max}$$

(6-9)

where I_{Conv}^{max} is the maximum converter current, which is determined mainly based on the thermal characteristics of the used IGBT. The converter current I_{Conv} is determined by [282]:

$$I_{Conv.} = \frac{\sqrt{P_{Conv.}^2 + Q_{Conv.}^2}}{\sqrt{3} \cdot U_{Conv.}}$$

(6-10)

where $U_{Conv}, P_{Conv}, Q_{Conv}$ are the converter terminal voltage, active and reactive power, respectively.

3) Distribution Line Thermal limits:

$$|I_j| \leq I_j^{max} \qquad\qquad j \in \{N_{L_{AC}} \cup N_{L_{DC}}\} \qquad (\,6\text{-}11)$$

where $N_{L_{AC}}, N_{L_{DC}}$ are the sets of AC, DC distribution lines (cables), respectively. I_j is the current passing through line j.

4) Energy Storage Placement Constraints: In order to avoid installing very large units, the capacity of the installed ES units should be limited.

$$E_i \leq E_i^{max} \qquad\qquad (\,6\text{-}12)$$

where E_i^{max} is the maximum energy storage capacity that can be installed on bus i. Further, to avoid dispersing small energy storage units all over the system, a binary variable U_i is initiated where $U_i = 1$ if there's energy storage installed on bus i and 0 otherwise. Then:

$$\left[\sum_{i=1}^{n} U_i\right] \leq U_{max} \qquad\qquad i \in \{N_{AC} \cup N_{DC}\} \quad (\,6\text{-}13)$$

where U_{max} is the maximum number of buses on which the optimization algorithm is allowed to install energy storage.

5) Energy Storage Discharging Constraints: charging and discharging of energy storage, especially chemical based technologies, should be done according to the manufacturer's recommendation. Violating the recommended discharging rate causes significant degradation in the ES capacity and life time [289].

$$P_{i,K}^{ES} \leq P_K^{ES,max} \qquad\qquad (\,6\text{-}14)$$

where $P_{i,K}^{ES,max}$ is the maximum power that can be withdrawn from an energy storage unit of technology K.

6) Maximum allowed weight: The total weight of the ESS including the converters should be within the specified boundaries by the shipboard designer.

$$W_T \leq W_T^{max} \qquad (6\text{-}15)$$

where W_T is the total weigh calculated by (4). It should be noted here that the constraints listed in (6) and (12) can be explicitly contradicting for some values (i.e. certain sizes of energy storage cannot completely mitigate the pulsed load effects causing voltage drop on some buses). Thus, a tradeoff should be carried out when specifying the constraints. This tradeoff is assisted by the Pareto concept where a set of different solutions is provided to facilitate the decision making process.
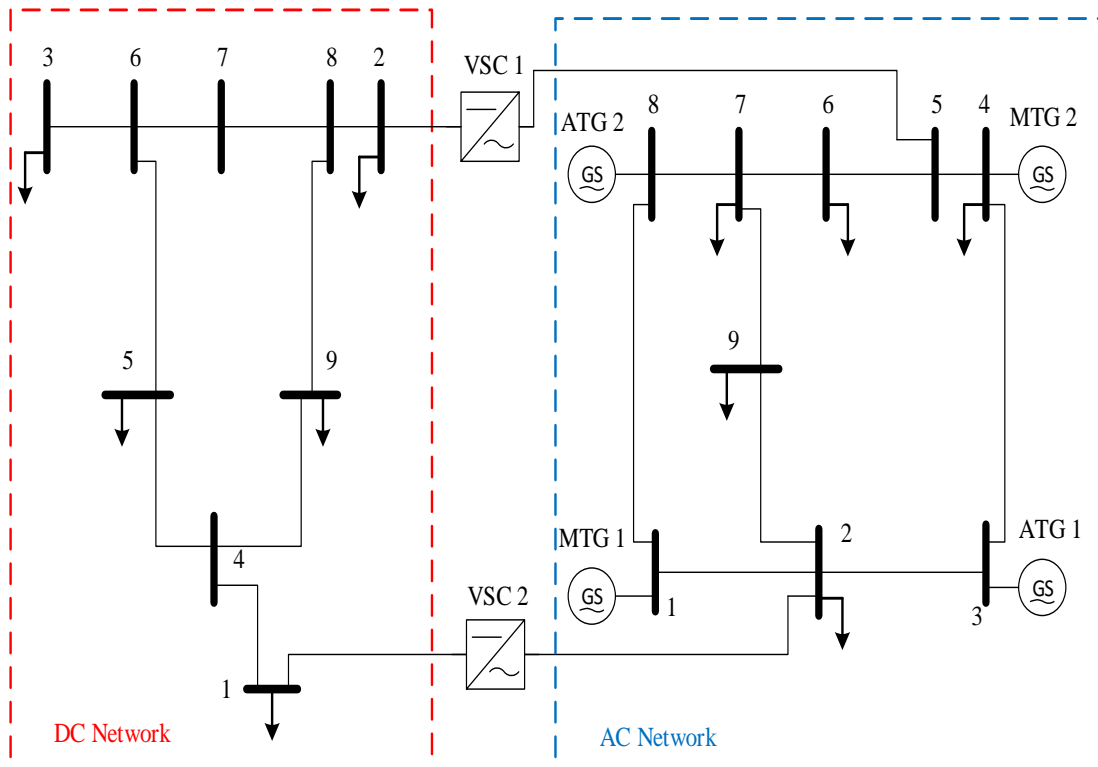
Figure 6.4 A notional AC/DC distribution architecture for ship power systems.

6.5 Case Studies and Results

In this section, two case studies are conducted to evaluate the proposed methodology. As depicted in Figure 6.4, a notional AC/DC distribution architecture is

utilized. Nevertheless, the proposed methodology is expandable to larger and different distribution architectures. Typically in ship power systems, four turbine generators are used [290], two of them are mains (MTG) while the others are auxiliaries (ATG). The propulsion system is represented as two aggregated loads on buses 4 and 7. The AC side consists of 9 buses, with distribution voltage of 4.16 kV and is interfaced to the DC side through two bi-directional VSCs. The DC side consists of 9 buses, with distribution voltage of 7.2 kV. The voltage levels are selected based on the study presented in [291]. The pulsed load amplitude is 20 MW with 5 seconds duration. Initially, the impedances of distribution lines are assumed similar to the IEEE 9 bus system. Then, major manipulations have to be done to the impedances to be close to ship power systems characteristics. These characteristics are small X/R ratios and lower impedance Z as the lines are shorter [290].

Table 6-1 Energy storage parameters

	Lead acid	Lithium ion	Super-capacitor
Energy density (Wh/Kg)	40	120	3.3
Maximum discharge rate (% of stored energy E)	20%	100%	1200%
Minimum discharge time (min)	300	60	5

The distribution system is built into MatACDC, which is an open source simulation package coded in MATLAB [292]. It is based on the original power flow package MATPOWER [293]. Since the proposed methodology is utilizing analytical power flow solution, it is computationally efficient. This significantly reduces the run time for the optimization.

In these case studies, three candidate energy storage technologies are involved:

Lead acid, Lithium ion batteries and Super-capacitors. The parameters of these energy storage technologies are shown in Table 6-1, these parameters are taken from data sheets of commercially available equipment [236], [294]. The maximum discharge rate is the maximum power allowed to be withdrawn from the ES as a function of its total stored energy, the reader should relate with the minimum discharge time. The maximum number of generations of NSGA-II is set to 100 and the number of individuals in each generation is 50.

6.5.1 Case I: Lead acid and Lithium ion Batteries

In the first case study, combining Lead acid and Lithium ion batteries is investigated. The optimization is run to determine the optimal size and mix of these two battery types. The Pareto front is depicted in Figure 6.5. This front is the last generation out of 100 generations and it has 50 individuals representing 50 optimal solutions. Five individuals are selected to be shown in Table 6-2. Since the Lead acid batteries are characterized by lower power and energy density, it can be seen that the optimization tends to form the Pareto front from mixtures where the Lithium ion is dominant. For example, individual 2 achieves the lowest energy storage weight; however, it has the highest voltage deviation. The mix in this individual is purely from Lithium ion battery. It can be noticed from the lower part on the figure that increasing the energy storage size achieves noticeable improvements in the voltage deviations without a drastic increase in the weight. In individual 19, the maximum limit of the Lithium ion battery weight is reached; thus, the algorithm starts to include more energy storage from the Lead acid. This results in a significant increase in the weight. In this case, where Lead acid and Lithium ion are combined, the lithium ion is dominating to achieve the minimum weight objective.

188

x 10^5

total Weight (kg)

14 ⎯

12 — Individual 7

10 ⎯

8 ⎯

6 ⎯

Individual 6

4 ⎯

Individual 19   Individual 2

2 ⎯   Individual 10

0 ⎯

0.004   0.006   0.008   0.01   0.012   0.014   0.016

Voltage Deviation
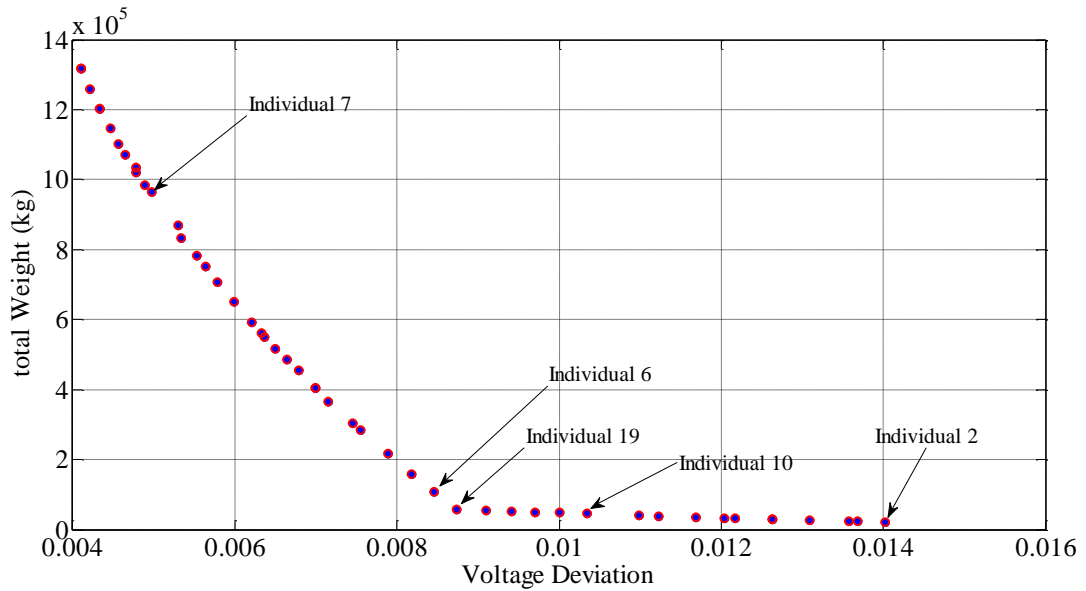
Figure 6.5 Pareto front for case I.

Table 6-2 Selected Individuals from the Pareto Front: Case I.

	Lead acid p_o (MW)	Lithium ion p_o (MW)	Location of Lead acid	Location of Lithium ion	Location of pulsed load	Obj. 1 (ΔV)	Obj. 2 (Weight, kg)	No of Violated Cons.
Individual 2	0	3.6	7	8	4	0.01402	21061.8	0
Individual 6	0.4	10	6	8	4	0.00845	108825	0
Individual 7	7.2	10	6	8	4	0.00497	964265	0
Individual 10	0	7.75	7	8	4	0.01035	45341.4	0
Individual 19	0	10	6	8	4	0.00873	58505.1	0

6.5.2 Case II: Lithium ion Battery and Super-capacitor

In this case, the Lead acid battery is replaced by a Super-Capacitor (SC). The Pareto front is shown in Figure 6.6 and 5 individuals are shown in Table 6-3. In individuals 4 and 19, the algorithm starts getting more power from the SC because of its higher power density. It should be noted that when the output of the lithium ion is zero, the optimization located it differently. This takes place because its output did not make any improvement/degradation to the objective functions, so it was located randomly. This

189

confirms that the algorithm is not trapped in a local minima. In individual 34, lithium ion is included in the mix. It can be seen, that this front provides more homogenous solutions with significant reduction of the total weight if compared to that of case I.
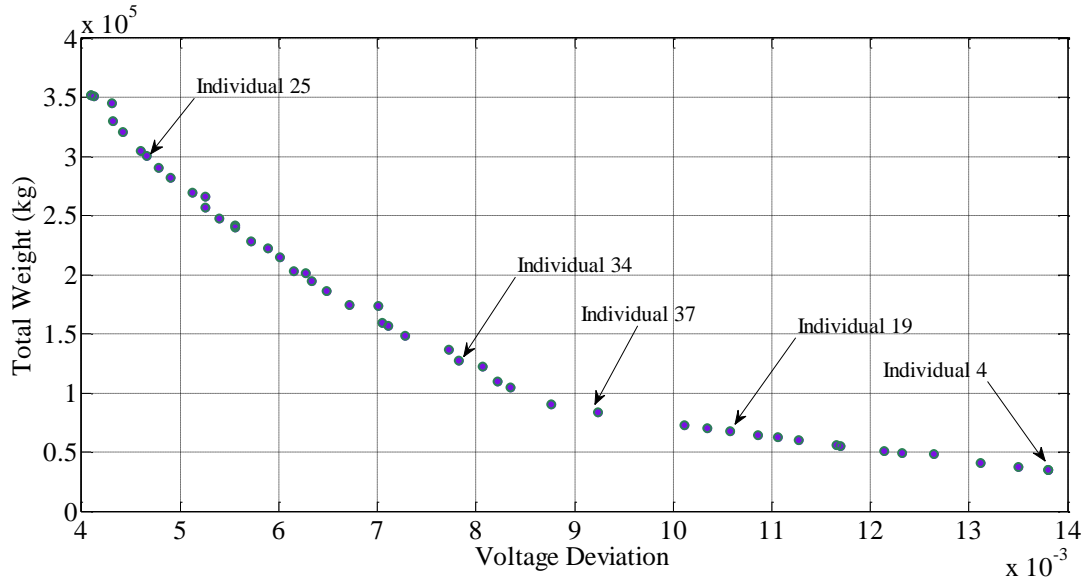
Figure 6.6 Pareto front for case II.

Table 6-3 Selected Individuals from the Pareto Front: Case II.

	Li p_o (MW)	SC p_o (MW)	Location of Li	Location of SC	Location of pulsed load	Obj. 1 (ΔV)	Obj. 2 (Weight, kg)	No of Violated Cons.
Individual 4	0	3.8	8	7	4	0.01379	34706	0
Individual 19	0	7.4	9	7	4	0.01058	67586.7	0
Individual 25	8.05	9.95	8	7	4	0.00466	300599	0
Individual 34	1.4	9.9	8	7	4	0.00783	126894	0
Individual 37	0	9.2	8	7	4	0.00923	84026.7	0

6.6 Summary

A computationally efficient multi-objective optimization algorithm using Pareto concept and NSGA-II is presented. The voltage corresponding to each ES size is determined through solving the AC/DC power flow using the sequential power flow

method. The algorithm provides the ship power system designer with an efficient tool to select the most optimal combination of the energy storage to minimize the weight and voltage deviation on the distribution system buses. Different ES combinations are explored to achieve a balance between the two objectives. In this work, three ES technologies were considered: Lead-acid batteries, Lithium-ion batteries and Super-Capacitors. However, the methodology can be expanded to include other ES types. As will be shown in the following chapter in detail, adding new variables to the problem impacts its complexity. Furthermore, considering more decision variables and objectives is associated with the involvement of more constraints. It should be kept in mind that the problem to be solved in this work, is AC/DC Optimal Power Flow (OPF) problem which involves non-linear constraints on both networks. Thus, increasing the complexity of the problem requires an optimization technique with a reliable convergence.

Chapter 7 Optimal Design of AC-DC Distribution Network Architectures with High Demand Loading Conditions Using a Multi-objective Approach

7.1 Introduction

Recent studies [60], [295], have shown that the existence of high demand loads in distribution systems can cause several power quality issues. A large electric vehicle park with several cars charging at the same time or an industrial facility are good examples of the high demand or pulsed loads. As a result of the strict requirements of reliability, supply continuity and power quality, the distribution networks are designed in a meshed configuration. Although radial configuration is superior in terms of cost, their reliability is less [296], [297]. Due to these recent changes and technological advancements, the designer/planner of these systems will face a variety of questions that need to be addressed [298].

In this chapter, the multi-objective optimization problem developed in Chapter 6 is expanded to form a complete optimization framework for designing hybrid AC/DC distribution system architectures. This framework can be used to design either off-shore distribution systems (microgrids) or ship power systems. In this expansion, more objectives and decision variables are included. Four objectives are considered to be minimized in the optimization problem: the voltage deviation from the nominal value, the frequency deviation, active power losses and the weight of the energy storage to be installed. These parameters are to be minimized in the existence of high demand loads, also known as Pulsed Power Loads (PPL). For example, the frequency drops when the PPL is energized and rises when it is de-energized. It is desired to use this framework to design an architecture where these deviations are minimal. Designing the distribution system architecture entails determining the following: 1) the optimal size and location

of energy storage (ES), 2) optimal location of the high demanding loads 3) optimal point of common coupling (PCC), and 4) optimal network connectivity (i.e. statuses of the reconfiguration switches).

Different formulations of the problem are considered. First, the problem is solved using two objectives: minimization of voltage deviation (ΔV) and active power losses (P_{Loss}). Then, the third objective, which is the minimization of frequency deviation (Δf), is included in the problem. Finally, the multi-objective optimization problem is solved while also considering the fourth objective, which is the weight of energy storage. The last case is of a particular importance to ship power systems, where weight and volume are tightly constrained. Thus, minimizing the weight of the equipment to be installed is considered as a main target. However, in other systems in which the weight is not a concern, such as the off-shore microgrids, other objectives can be considered in the problem. One of the objective functions that can be considered instead of the weight is the cost. This can done by replacing the physical weight models with the financial models of the energy storage. The cost objective function is included in several studies in the literature and will not be covered in this work.

Several algorithms and approaches have been proposed in the literature. However, each study has focused on a single aspect of the problem [185], [252], [253][269]. Most of the discussed studies focused on either economic benefits or reliability. The overarching approach to designing a hybrid AC/DC distribution system involving energy storage and high demand loads requires multiple aspects.

A plethora of methods have been applied in the literature to solve the multi-objective optimization problems. Mostafa et al proposed minimizing the current unbalance in the main distribution feeder and the energy losses in the system through the determination of the optimal states of the switched capacitors, voltage regulators

193

and reconfiguration switches [299]. The study was expanded in [300] and a third objective, which is the minimization of CO_2 emission, was included. A problem to optimally locate the switching devices in a medium voltage radial distribution feeder to minimize the reliability indices was formulated and presented in [301]. Li et al [302] proposed a piecewise normalized normal constraint (PNNC) method to obtain an evenly distributed set of optimal solutions. The method entails breaking the multi-objective problem into four sets of single objective optimization problems. The method is applied to solve the reactive power flow problem in a real AC/DC transmission network in China. The objectives are minimization of power losses and voltage deviation.

7.2 The Proposed Methodology

This chapter focuses on the design/planning problem of AC/DC distribution systems. The proposed methodology aims at providing a set of optimal solutions (architectures) to the distribution system planner. The goal is to reach the optimal design of a hybrid AC-DC distribution system that supplies the Pulsed Power Loads (PPLs) with minimal disturbances and without violating the limits imposed by standards or disconnecting other loads in the system. The problem is complex, combinatorial and involves non-linear constraints. The complexity of the problem is due to the nonlinearity of the power flow constraints. From the complexity point of view, this problem is classified as NP-hard [303], [304]. NP stands for Non-deterministic Polynomial-time. NP-hardness means that there's no deterministic techniques to solve this problem in polynomial time domain [305]. As mentioned in the previous section, the problem presented in this chapter is an expansion of the one presented earlier in Chapter 6. Therefore, some formulations and parts of the methodology are not re-explained here.

7.2.1 Pareto optimality

Pareto concept is used to solve the optimization problem and generate a set of optimal solutions. Please refer to section 6.3.1 for more information on Pareto optimality.

7.2.2 Power flow in hybrid AC/DC distribution systems

Sequential power flow method is used to solve the power flow in AC/DC distribution systems and obtain the voltage deviations from the nominal values and the total active power losses in the system. Please refer to section 6.3.2 for more information on the sequential power flow method.

7.2.3 Transient analysis in hybrid AC/DC distribution systems

One of the negative impacts of the PPL is the frequency fluctuations. The reason for these fluctuations is the slow time constant of the synchronous generators. The PPL is characterized by the high dP/dt, which requires high power supply in a very short time. However, the synchronous generator cannot supply this power as rapid as it should be. There is a delay associated with the governor action which opens the fuel valves. Then, because of the rotor mass and inertia, the prime mover can't accelerate instantaneously. This situation creates a torsion on the shaft tying the prime mover and the alternator. This may cause a mechanical failure to the system. A common solution for this problem is installing energy storage devices that are capable of handling these fast transients [306]. Sizing and siting of energy storage should be carried out while considering these transients to reach the most optimized design. Therefore, it is important to study the impacts of the PPL on the transient stability of the system. One of the major contributions of this dissertation is the integration of the transient analysis of AC/DC distribution systems to the optimization problem.

A variety of software packages that are capable of performing transient simulations is commercially available. Examples are DIgSILENT PowerFactory and MATLAB/SIMULINK. In these packages, the implementation aspects, such as integration algorithms, power flow solvers, and the implementation of models, remain hidden from the user and cannot be modified. This is done for commercial reasons. Therefore, this significantly limits the flexibility of the software. Furthermore, there are many graphical and advanced features added to the software. These added features extend the simulation time and consume much more computational resources. Since the presented problem in this work is NP-hard, which cannot be solved using deterministic techniques, the meta-heuristic techniques stand as the only reasonable candidate to solve the problem. The meta-heuristic techniques are criticized for the high number of objective function evaluations. Then, if each objective function evaluation takes long time when performed using one of the commercial packages, the entire optimization process will take an unreasonable amount of time. Thus, to address these two issues (the limited flexibility and long solution time), the Open Source Software (OSS) is considered as an alternative. Examples of OSSs are Power System Analysis Toolbox (PSAT) [307] and MatDyn [308]. MatDyn is coded using MATLAB, well organized and easy to access. Therefore, it is used in this study and integrated to the multi-objective optimization problem. The transient analysis under PPL operation is carried out as follows:

➢ The AC/DC power flow problem of the network is solved.

➢ The required power injection from each generator is determined.

➢ The exact generator, exciter and governor models are prepared in form of sets of Differential Algebraic Equations (DAEs) and Ordinary Differential Equations (ODEs).

196

➢ Each PPL cycle is divided into T time steps.

➢ For each time step t , the sets of DAEs and ODEs are solved.

➢ The frequency response upon the occurrence of the PPL is obtained.

In order to perform the transient analysis and investigate the system's response upon the occurrence of a heavy PPL, accurate models for all the systems components should be available.

7.2.3.1 Generator Model

According to [309], a synchronous generator can be represented by one of the following models: 1) four winding model (6th order), 2) two axis model (4th order), 3) one axis model (3rd order), 4) classical model (2nd order). The 6th order model is the most complex model of the synchronous generator [310]. By considering the fact that the generator model will be called and solved in each objective function evaluation during the optimization process, the number of differential equations to be solved needs to be reduced. On the other hand, in the classical model, the voltage behind the transient reactance is assumed to be constant. For such a representation, only the swing equation is needed to describe the dynamics of a synchronous machine. This is considered an oversimplification and may not produce the required accuracy. A study presented in [311], shows that the 4th order model is sufficient to represent synchronous generators in transient analysis studies. The 4th order model achieves the best trade-off between the complexity and accuracy. Thus, it is used in this work. The 4th order model is described by the following equations.

Stator magnetic equations:

$$\dot{E}'_q = \frac{1}{T'_{d0}}\left[V_{fd} - (X_d - X'_d)I_d - E'_q\right] \tag{7-1}$$

$$\dot{E}'_d = \frac{1}{T'_{q0}} \left[(X_q - X'_q) I_d - E'_q \right] \tag{7-2}$$

$$E'_q - V_q = R_a I_q + X'_d I_d \tag{7-3}$$

$$E'_d - V_d = R_a I_d - X'_q I_q \tag{7-4}$$

$$\psi_d = E'_q - X'_d I_d \tag{7-5}$$

$$\psi_q = -E'_d - X'_q I_q \tag{7-6}$$

Stator electrical equations:

$$V_d = -\omega \psi_q - R_a I_d \tag{7-7}$$

$$V_q = \omega \psi_d - R_a I_q \tag{7-8}$$

Motion equations:

$$\dot{\omega} = \frac{1}{2H} \left[P_m - P_e - D(\omega - \omega_s) \right] \tag{7-9}$$

$$\dot{\delta} = (\omega - \omega_s) \tag{7-10}$$

$$\dot{x} = \begin{bmatrix} \dot{\delta} & \dot{\omega} & \dot{E}'_q & \dot{E}'_d \end{bmatrix}^T \tag{7-11}$$

where:

H	Inertia constant
D	Damping constant
x_d	d-axis reactance
x_q	q-axis reactance
x'_d	d-axis transient reactance
x'_q	q-axis transient reactance
T'_d	d-axis time constant
T'_q	q-axis time constant
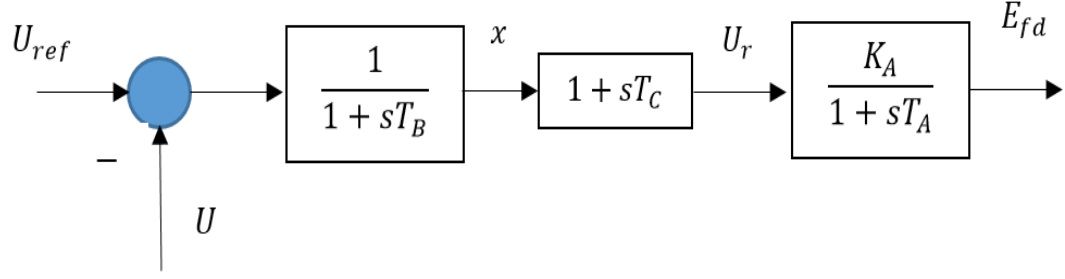
Figure 7.1 IEEE type AC4A excitation system.

7.2.3.2 Excitation system model

According to IEEE std 421.5 (2005), the synchronous generators excitation systems can be classified into:

- Type DC - Direct Current Commutator Exciters: types DC1A, DC2A, DC3A

- Type AC - Alternator Supplied Rectifier Excitation Systems: types AC1A, AC2A, AC3A, AC4A, AC5A, AC6A.

- Type ST-Static Excitation Systems: types ST1A, ST2A, ST3A.

In this work, the excitation system used is type AC4A. The block diagram of this system is depicted in Figure 7.1. From this figure, it can be seen that the model has two state variables E_{fd}, x, and five parameters to be adjusted $K_A, T_A, T_B, T_C, U_{ref}$. The state space equations can be written as follows:

$$\dot{x} = \frac{1}{T_B}\left(U_{ref} - U - x\right) \tag{7-12}$$

$$U_r = x + \dot{x}T_C \tag{7-13}$$

$$\dot{E}_{fd} = \frac{1}{T_A}\left(K_A U_r - E_{fd}\right) \tag{7-14}$$

By substituting from (7-12) in (7-13) and the result in (7-14), yields:

$$\dot{E}_{fd} = \frac{1}{T_A}\left(K_A(x + \frac{T_C}{T_B}(U_{ref} - U - x)) - E_{fd}\right) \tag{7-15}$$

199

7.2.3.3 Governor model

The IEEE model of a general speed-governing system is used. A simplified block diagram of the system is depicted in Figure 7.2. It can represent a mechanical-hydraulic or electro-hydraulic system by the appropriate selection of parameters [312]. The state space representation of the system is obtained as follows:

$$\dot{x} = k \left[-\frac{1}{T_1} x + \left(1 - \frac{T_2}{T_1} \right) . \left(\omega - \omega_{ref} \right) \right] \tag{7-16}$$

$$\dot{P} = \frac{1}{T_1} x + \left(\frac{T_2}{T_1} \right) . \left(\omega - \omega_{ref} \right) \tag{7-17}$$

$$y = \frac{1}{T_3} \left(P_0 - P - P_m \right) \tag{7-18}$$

$$\dot{P_m} = y \tag{7-19}$$

The proposed methodology is composed of a main optimization function, which is NSGA-II. This function is performing the sorting, selection, crossover and mutation. This function calls other functions to evaluate the individuals. These functions are AC/DC power flow (implemented using MatACDC toolbox), transient analysis (implemented using MatDYN toolbox) and energy storage weight estimator. The flow chart of the proposed optimization methodology is shown in Figure 7.3.

Figure 7.2 IEEE general speed governing system

Main calling function

Start

Set objectives

Run multi-objective optimization algorithm

Decision making criterion through Aggregated Penalty Function (APF)

End

NSGA-II multi-objective optimization

Initialize the first population

Set counter: nGen=1

Evaluate the fitness of each individual using the objective functions

Sort the population using non domination algorithm and crowding distance

Create mating pool and select the parents

Perform crossover

Perform mutation

Create a new population (off spring/children)

Evaluate the fitness of each individual using the objective functions

Combine the parents and children to form an intermediate population

Sort the population using non domination algorithm and crowding distance

Extract the next population and reject the low fitness individuals

Is the stopping criterion met?   No   nGen=nGen+1

YES

Generate the final Pareto Front

AC/DC sequential power flow

Initiate iteration counter i=1

Apply Newton Raphson to the AC network to determine all the quantites

The quantities P,Q,V, δ at the point of connection are known

Given the converter modulation index and losses, the quantities of the corresponding DC bus are determined (P,V).

Apply Newton Raphson to the DC network to determine all the quantities.

i=i+1   No   Converged ?

YES

Calculate ΔV & ΔP

Calculate ΔF using Excitation system transfer function

Evaluate Energy Storage weight OR volumetric size based on the physical data.

Return the fitness values to the optimization algorithm

Frequency estimation

Obtain power flow results

Set initial conditions X0

Solve Differential Equation X=F(X,Y,P) for Xt

Solve Differential Equation 0=G(X,Y,P) for Yt

Event occurred (pulsed load)?   Re-calculate Y_{bus}

Advance time t=t+h   Calculate Yt' by solving G

t≥ tmax

Output (frequency oscillations)

Figure 7.3 Flow chart of the proposed optimization methodology.

201

Table 7-1 Nomenclature used for multi-objective optimization
problem formulation.

Indicies:	
i, i'	AC bus indices.
j, j'	DC bus indices.
m, n	AC and DC lines indices.
k	Converter index.
g	Generator index.
l	Energy storage system index.
d	Load index.
a	Objective function index
y	Individual index.
ref	Script referring to reference values.
min	Script referring to minimum values.
max	Script referring to maximum values.

Variables and Parameters :	
$V_{ac,i}$	Voltage magnitude of AC bus i
$V_{dc,j}$	Voltage magnitude of DC bus j
$P_{ac,m}^{loss}$, $P_{dc,n}^{loss}$	Power losses in AC line m and dc line n.
$P_{conv,k}^{loss}$	Power losses in converter k.
$I_{conv,k}$	Current of converter k.
a_k, b_k, c_k	Loss coefficients of converter k.
$P_{conv,k}$	Active power at converter k AC bus.
$Q_{conv,k}$	Reactive power at converter k AC bus.
$V_{conv,k}$	Voltage magnitude at converter k AC bus .
$S_{x_{ES},l}$	Power capacity of energy storage l installed on bus x_{ES}.
Δx_{ES}	Sizing step of energy storage.
S_m	Apparent power flowing through AC line .
P_n	Active power flowing through DC line .
P_g, Q_g	Active and reactive power output of generator g.
U_{ES}	Maximum number of ES systems to be installed in the system.
$SoC_l^{initial}$	Initial state of charge of ES system l at the beginning of the load cycle.
t_{load}	Load duration.
$E_{x_{ES},l}$	Energy capacity of ES system l installed on bus x_{ES}.

η_l	Discharging efficiency of energy storage l.
U_l	Maximum number of distribution lines to be connected.
$\mathcal{T}(\cdot)$	Penalty function.
$f_{a,y}$	Normalized fitness value for objective function a for individual.
Sets:	
N_{ac}, N_{dc}	Sets of AC and DC buses.
N_{acl}, N_{dcl}	Sets of connected AC and DC lines.
N_{conv}	Set of connected converters.
N_k^{pcc}	Set of candidate AC buses for connecting PCC of converter k.
N_{load}	Set of candidate buses for load connection.
N_{SWacl}	Set of AC lines allowed to be switched
N_{SWdcl}	Set of DC lines allowed to be switched
N_{ES}	Set of candidate buses for ES installation.
N_G	Set of connected generators.
N_D	Set of loads including high demand.
N_{obj}	Set of objective functions.

7.3 Optimization Problem Formulation

In this section, the mathematical formulation of the MOOP is detailed. The decision making criterion applied to select a single architecture among the set of optimal solutions is presented as well. In the following formulation, the nomenclature shown in Table 7-1 is used.

7.3.1 Objective Functions

1) First objective function: Connecting the high demand loads can cause severe voltage drop not only on the bus where it is connected, but also on other busses, depending on the load flow. Therefore, it is required to optimize the system to minimize this voltage deviation upon energizing the loads. The reference values for the AC and DC voltages were taken as 1 p.u.

$$Minimize \sum_{i=1}^{N_{ac}} \left(V_{ac,i} - V_{ac,i}^{ref}\right)^2 + \sum_{j=1}^{N_{dc}} \left(V_{dc,j} - V_{dc,j}^{ref}\right)^2 \qquad (7\text{-}20)$$

2) Second objective function: In the second objective function, it is required to minimize the total active power losses in the systems, including the converters' losses.

$$Minimize \sum_{m=1}^{N_{acl}} \left(P_{ac,m}^{loss}\right) + \sum_{n=1}^{N_{dcl}} \left(P_{dc,n}^{loss}\right) + \sum_{k=1}^{N_{conv}} \left(P_{conv,k}^{loss}\right) \qquad (7\text{-}21)$$

Here, the DC system can be configured either in a monopolar or bipolar manner. The bipolar - symmetrically grounded configuration was considered in this research, where the DC line losses can be calculated as:

$$P_{dc,n}^{loss} = 2.I_{dc,n}^2.R_{dc,n} \qquad \forall\, n \in N_{dcl} \qquad (7\text{-}22)$$

The losses in a VSC can be divided into four main components: 1) valve losses, which are taking place in the switching device itself, and divided further into conduction and switching losses, 2) transformer losses, which are divided into no-load and load losses, 3) filter losses, and 4) phase reactor losses. To account for all these losses, an equivalent loss model was proposed in [313]. The model calculates the losses as a quadratic function of the converter current and is used here as:

$$P_{conv,k}^{loss} = a_k + b_k.I_{conv,k} + c_k.I_{conv,k}^2 \qquad \forall\, k \in N_{conv} \qquad (7\text{-}23)$$

with all quantities in p.u., the current of converter k is calculated as :

$$I_{conv,k} = \frac{\sqrt{P_{conv,k}^2 + Q_{conv,k}^2}}{V_{conv,k}} \qquad (7\text{-}24)$$

3) Third objective function: The third objective in the problem is to minimize the frequency departure from the nominal values.

$$Minimize\,(\Delta f) = max[(\max(f) - f_0), (f_0 - \min(f))] \qquad (7\text{-}25)$$

where f is the vector of frequency response of the system, f_0 is the nominal frequency, which is 60 Hz. In (7-25), the positive and negative deviations from the nominal frequency are calculated. Then, the maximum value of these two is selected to be minimized. The objective function is formulated in this way to assure its generality and improve its effectiveness.

4) Fourth objective function: this function is to minimize the weight of the energy storage. The objective function is considered in the context of designing ship power systems. This function is similar to the one used earlier in Chapter 6, please refer to section 6.4.1- equation (6-6).

7.3.2 Decision Variables

1) Location of the PCC on the AC network: A decision variable x_k^{pcc} is assigned to control the location of the PCC of converter k, where $x_k^{pcc} \in \{N_k^{pcc}\} \; \forall k \in N_{conv}$. It is considered in this work that the VSCs can be connected to different asynchronous AC networks. Also, it is assumed that each converter can be connected to only one AC bus.

2) High demand load location: A decision variable x_{load} is assigned to control the location of the load, where $x_{load} \in N_{load}$.

3) Distribution line status: Assuming that each distribution line is controlled through a switch, the binary decision variables x_{acl} and x_{dcl} are assigned to control the configuration switches controlling the AC and DC lines, respectively as:

$$x_{acl,m}, x_{dcl,n} = \begin{cases} 0 & if \; line \; m/n \; is \; disconnected \\ 1 & if \; line \; m/n \; is \; connected \end{cases}$$

$$\forall \, m \in N_{SWacl} \; \& \; n \in N_{SWdcl}$$

(7-26)

4) Energy Storage (ES) location: A decision variable x_{ES} was assigned to indicate

the bus number where the energy storage l is installed, where $x_{ES,l} \in N_{ES}$. To guarantee generality and flexibility of the proposed methodology, it is allowed to install ES on both AC and DC sides. As will be shown later, the optimal location of the ES is mostly determined based on the location of the high demand load.

5) Energy Storage Sizing: A decision variable $x_{x_{ES,l}}^{ESsize}$ is assigned to control the size of energy storage l to be installed on the bus determined earlier by $x_{ES,l}$, where:

$$S_{x_{ES,l}} = x_{x_{ES,l}}^{ESsize} . \Delta x_{ES} \tag{7-27}$$

where the sizing step is determined by the decision maker based on the availability of energy storage sizes in the market.

7.3.3 Constraints

1) AC network power flow constraints: where P_{gi}, P_{ki}, P_{di} and $\boldsymbol{P_{li}^{ES}}$ are the injected active power into bus i from generator g, converter k, load d and energy storage l, respectively. The same notation holds for the reactive power constraints in (7-29).

$$
\sum_{g=1}^{N_G} P_{gi} + \sum_{k=1}^{N_{conv}} P_{ki} - \sum_{d=1}^{N_D} P_{di} - \sum_{k=1}^{N_{conv}} \left(P_{conv,k}^{loss}\right) + \sum_{l=1}^{U_{ES}} P_{li}^{ES} =
$$
$$
V_{ac,i} \sum_{i'=1}^{N_{ac}} V_{ac,i'} . [G_{ii'} \cos(\Theta_i - \Theta_{i'}) + B_{ii'} \sin(\Theta_i - \Theta_{i'})] \tag{7-28}
$$
$$
\forall\ i, i' \in N_{ac}
$$

$$
\sum_{g=1}^{N_G} Q_{gi} + \sum_{k=1}^{N_{conv}} Q_{ki} - \sum_{d=1}^{N_D} Q_{di} + \sum_{l=1}^{U_{ES}} Q_{li}^{ES} =
$$
$$
V_{ac,i} \sum_{i'=1}^{N_{ac}} V_{ac,i'} . [G_{ii'} \sin(\Theta_i - \Theta_{i'}) - B_{ii'} \cos(\Theta_i - \Theta_{i'})] \tag{7-29}
$$
$$
\forall\ i, i' \in N_{ac}
$$

2) *DC network power flow constraints:*

$$-\sum_{k=1}^{N_{conv}} P_{kj} - \sum_{d=1}^{N_D} P_{dj} + \sum_{l=1}^{U_{ES}} P_{lj}^{ES} = 2V_{dc,j} \sum_{j'=1}^{N_{dc}} V_{dc,i'}.\,G_{jj'} \qquad \forall\, j,j' \in N_{dc} \qquad \text{(7-30)}$$

The factor of 2 is added because the topology is considered to be bipolar.

3) *VSC capability constraints:* It should be guaranteed for every solution that the VSC operating point is located within its safe operation range. The safe operation range of the VSC is mainly outlined by two limits:

- The first limit is the maximum current of the IGBT, which constitutes the apparent power capability of the VSC as follows:

$$P_{conv}^2 + Q_{conv}^2 \leq (V_{conv}.\,I_{conv}^{max})^2 \qquad \text{(7-31)}$$

In the $P - Q$ plane, this equation is plotted as a complete circle, as depicted in Figure 7.4.

- The second limit is the maximum DC voltage level, which determines the reactive power limits. This limit is plotted as an arc (dashed line) as shown in Figure 7.4. To simplify the calculations and constraint check, this limit can be simplified to be a straight line, set at the minimum values of the arc inside the
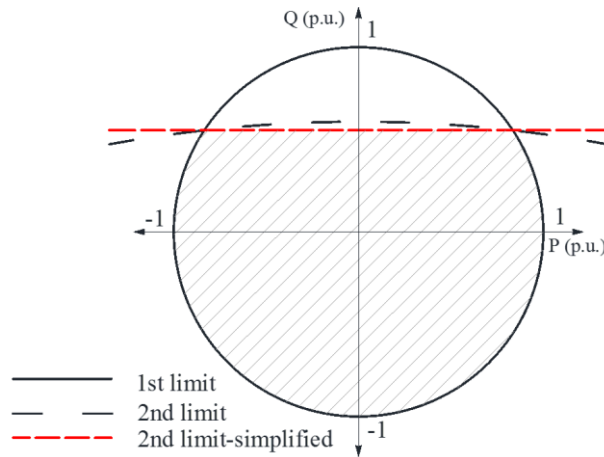
Figure 7.4 VSC safe operating range.

circle. This assumption is valid and can be justified because the reactive power variation over the entire operating range is small and can be neglected [314]. For the minimum reactive power limit, it is constrained by the converter current in the lagging region and can be omitted [282]. Overall, the operating point should be located within the safe operating area (shadowed).

4) *Bus voltage limits:*

$$V_{min} \le V_{ac,i} \le V_{max} \qquad \forall i \in N_{ac} \qquad (7\text{-}32)$$

$$V_{min} \le V_{dc,j} \le V_{max} \qquad \forall j \in N_{dc} \qquad (7\text{-}33)$$

The allowed voltage variations for AC and DC busses are set from 0.95 p.u. to 1.05 p.u.

5) *Frequency limits:* The frequency of the system should be maintained within the limits permitted by the standards. In this dissertation, the limits specified by MIL-Std-1399 [132], [172] are used. The allowed frequency range is $\pm 0.5\%$, which is 0.3 Hz in 60 Hz systems (i.e. f_{min} =57.7 and f_{max} = 60.3 Hz).

$$f_{min} \le f \le f_{max} \qquad (7\text{-}34)$$

6) *Distribution line capacity limits:*

$$|S_m| \le S_m^{max} \qquad \forall m \in N_{acl} \qquad (7\text{-}35)$$

$$|P_n| \le P_n^{max} \qquad \forall n \in N_{dcl} \qquad (7\text{-}36)$$

7) *Generator limits:*

$$P_g^{min} \le P_g \le P_g^{max} \qquad \forall g \in N_G \qquad (7\text{-}37)$$

$$Q_g^{min} \le Q_g \le Q_g^{max} \qquad \forall g \in N_G \qquad (7\text{-}38)$$

8) *Energy Storage Allocation Constraints:* In order to avoid over distributing the energy storage all over the system, a binary variable u^{ES} is assigned for each bus, where:

$$u_i^{ES}, u_j^{ES} = \begin{cases} 0 & No\ ES\ installed\ on\ bus\ i/j \\ 1 & ES\ installed\ on\ bus\ i/j \end{cases} \tag{7-39}$$
$$\forall i \in N_{ac}, j \in N_{dc}$$

$$\sum_{i=1}^{N_{ac}} u_i^{ES} + \sum_{j=1}^{N_{dc}} u_j^{ES} \leq U_{ES} \tag{7-40}$$

The constraint in (7-40) implies that the total number of installed ES in the entire distribution system should be less than a certain number determined by the decision maker [185].

9) *Energy Storage Operation Constraints:* Although the problem at hand is a planning one and not meant to be an operation or scheduling problem, the operation limits of the ES should be considered in the design phase. Under-sizing the energy storage may cause its State of Charge (SoC) to go below a certain limit, which is found to cause permanent damage to the ES, especially in case of batteries. This constraint can be omitted or modified in case of other energy storage technologies where the high depth of discharge (DoD) is acceptable (e.g. flywheel).

$$SoC_l^{initial} - S_l \cdot t_{load}/(E_l \cdot \eta_l) \geq SoC_l^{min} \qquad \forall l \in \{1,2,\dots,U_{ES}\} \tag{7-41}$$

The constraint in (7-41) means that after taking the required energy from each ES system to support the high demand load, the final SoC should be above a certain minimum level. It is assumed in this study that the ES is fully charged at the beginning of each load cycle (i.e $SoC_l^{initial} = 1$). If the inequality is changed to equality, then the minimum energy capacity E_l^{min} of the energy storage l required to fulfill this constraint

can be determined.

10) *Energy Storage Sizing Constraints:* The ES installation constraints are defined as follows:

$$S_{x_{ES}}^{min} \leq S_{x_{ES},l} \leq S_{x_{ES}}^{max} \qquad \forall l \in \{1,2,\dots,U_{ES}\} \qquad (7\text{-}42)$$

$$E_{x_{ES}}^{min} \leq E_{x_{ES},l} \leq E_{x_{ES}}^{max} \qquad \forall l \in \{1,2,\dots,U_{ES}\} \qquad (7\text{-}43)$$

$$\sum_{l}^{U_{ES}} S_{x_{ES},l} \leq S_{ES,T}^{max} \qquad (7\text{-}44)$$

$$\sum_{l}^{U_{ES}} E_{x_{ES},l} \leq E_{ES,T}^{max} \qquad (7\text{-}45)$$

The constraints (7-42) and (7-43) limit the power and energy capacity of the ES to be installed on a bus determined by the decision variable x_{ES} to be within the allowed installation limits of this bus. This is to avoid congestion in the network or violate the operation limits of the buses. Constraints (7-44) and (7-45) limit the total capacities of the ES installed in the entire system, keeping them below certain levels.

11) *Distribution Line Connectivity Constraints:* In some cases, the optimization algorithm will connect all the possible lines to allow more parallel paths; however, over connecting the distribution lines may not be acceptable from an infrastructure point of view. Therefore, the total number of connected AC and DC distribution lines in any given architecture should be constrained as:

$$\sum_{m=1}^{N_{acl}} x_{acl,m} + \sum_{n=1}^{N_{dcl}} x_{dcl,n} \leq U_l \qquad (7\text{-}46)$$

7.3.4 Decision Making Criterion

As mentioned earlier, the Pareto Front is the set containing the optimal solutions. In this set, it cannot be said that one solution is better than another. However, at the end of the process, a single solution should be selected for implementation. Accordingly,

introducing a decision making criterion is important. In this research work, a decision making criterion based on the Aggregated Penalty Function (APF) is proposed. The steps of the criterion are as follows:

- Following the determination of the PF, the fitness values for all the individuals for each objective function are normalized.

- Each individual y is penalized for each objective function a according to the linear penalty function shown in Figure 7.5. For example, if a given individual has a fitness value of one (considering a minimization problem) for a certain objective function, then this individual is assigned a penalty value of one.

- The APF for each individual in the front is calculated according to (7-47) for each objective functions.

- The PF is then re-sorted and the individual with the lowest APF is selected.

$$APF_y = \sum_{a=1}^{N_{obj}} f_{a,y}.\mathcal{T}(f_{a,y}) \tag{7-47}$$
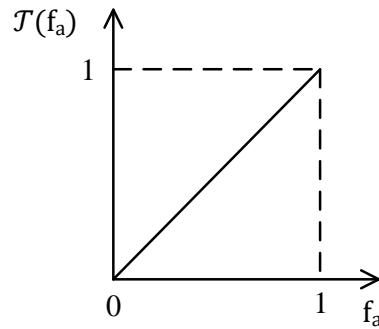
Figure 7.5 Penalty function.

7.4   Case Studies and Discussion

7.4.1   Two objectives problem

A case study is shown to evaluate the effectiveness of the proposed optimization

methodology. A model for a hybrid AC/DC distribution system was constructed. A modified version of the IEEE 30 bus system was used as the AC side of the distribution network. The modifications refer to using a nominal voltage of 13.8 kV, which is common for distribution systems, while the base MVA was assumed to be 20 MVA. The set of controlled AC lines N_{SWacl} is composed of a partial set of the existing lines in the original IEEE 30 bus system in addition to new added lines. The 3 machine, 9 bus system of the Western System Coordinating Council (WSCC) was used to resemble the DC side of the distribution network. The system was modified by omitting the reactance terms of the distribution lines. The 3 machines were replaced by 3 VSCs to move power bi-directionally between AC and DC sides. Converter 1 is designated as the slack converter for the DC network. A base DC distribution voltage of 7.2 kV is used. The data of both IEEE 30 bus system and the WSCC 9 bus system can be found in references [315], [316].

The distribution system being studied here is built into MatACDC, which is a free open source simulation package coded in MATLAB [292]. It is based on the efficient power flow package MATPOWER [293] and shares the same coding procedure. Originally, MatACDC package implements the sequential power flow method to solve the power flow problems for interconnected VSC based HVDC transmission networks. Therefore, major manipulations were introduced for the adequate utilization in distribution networks.

For NSGA-II, the maximum number of generations is 100 and the number of individuals in each generation is 50. The system's parameters and constraints are set as the follows: the maximum number of lines to be connected, U_l, is 12, the number of ES systems to be installed, U_{ES}, is taken as 1 for simplification, the maximum allowed power capacity for $E_{ES,T}^{max}$, is 18 MVA. The used energy storage is Lead acid batteries.

The power of the high demand load is 30 MW and it is assumed to be DC i.e. the set of candidate buses for installing the load is the set of DC busses ($N_{load}=N_{dc}$). The number of decision variables is 27.
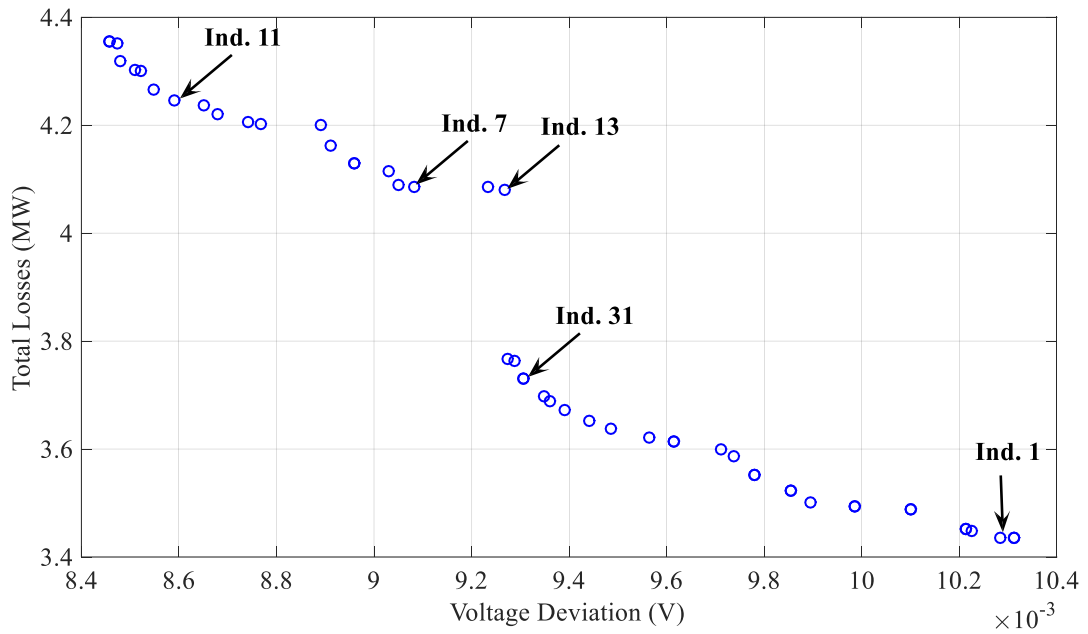
Figure 7.6 Pareto front.
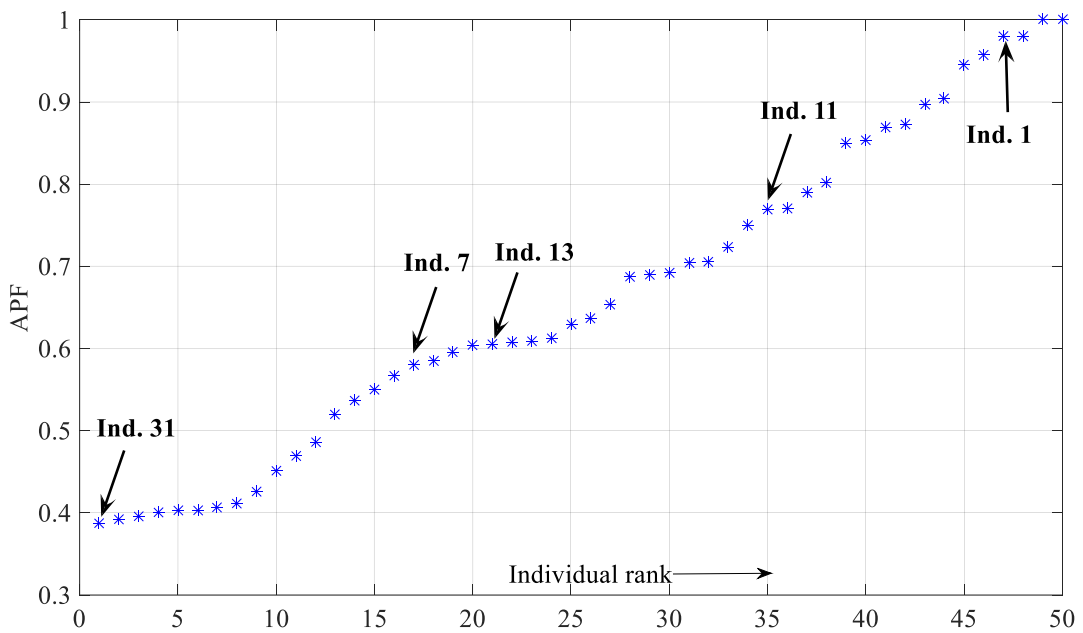
Figure 7.7 Redistributed Pareto front based on the APF.

The optimization problem is solved and the Pareto front was obtained as shown in Figure 7.6. Each point of the front represents an optimal architecture with its own resulting values for both objective functions. This PF assists the decision maker to explore the different options and achieve the optimal trade-off between the objectives. However, the number of the available options is high, as shown in Figure 7.6. Thus, the proposed decision making criterion based on APF was applied. The individuals in the PF is sorted according to the APF. The redistributed PF is shown in Figure 7.7 where the individuals were ranked in ascending order. It can be seen that the individual with the lowest penalty is individual 31. It can be said that this individual is the most appropriate and achieves the optimal trade-off between the two objectives. As the ranking continues, the individual 31 is followed by individuals 46 and 49 while the individuals with the lowest rank are 3 and 4. The last two individuals are with the highest penalty (1) because they are the extreme solutions on the PF. The extreme solutions are the ones achieving the minimum value for one objective, while its value for the other objective is the maximum among the front individuals. According to (7-47), the APF for these individuals are (APF=1×1+0×0). Figure 7.8 depicts the optimized distribution architecture based on the values of the decision variables obtained from individual 31. The red-dashed lines are the distribution lines connected by the optimization algorithm, the black solid lines were not included in the optimization and the lines to be disconnected are not shown in the figure.

For clear presentation of the results, four individuals were selected for display in addition to individual 31, which was selected by the decision making criterion. The five solutions (1, 7, 11, 31 and 13) are listed in Table 7-2 for comparison. The last row of the table indicates the number of violated constraints. In order to achieve solid validation and clear comparison, a base case was used. In the base case, the statuses of

214

the distribution lines were the same as the original IEEE 30 bus and WSCC 9 bus systems. The load, ES and PCC locations were selected based on the best practices. The size of the ES was selected to be half the load power (15 MW), which is larger than most of the optimal solutions. It can be seen that the base case yielded significantly higher voltage deviation and losses than all the PF individuals. The selected individual by the APF based decision making criterion achieved significant improvement of 36.7% and 33% on the first and second objective functions, respectively. Moreover, in the base case, some violations of the bus voltage limits were noticed. For example, the voltage on bus 30 dropped to 0.94 pu.

Figure 7.8 Optimized AC/DC distribution architecture (individual 31).

In order to assure that the global optimal point is reached, another comparison is conducted. The same problem is re-solved using the weighted sum (WS) approach with different weights (λ). In this approach, a single objective function is obtained, then the

215

Table 7-2 Values of Decision Variables and Objective Functions.

	Ind. 1	Ind. 7	Ind. 11	Ind. 31	Ind. 13	No Optimization
PCC1	4	5	7	7	5	3
PCC2	27	23	23	23	23	13
PCC3	19	19	19	19	18	30
load location	4	4	5	5	4	9
AC line 3- 4	1	1	1	1	1	1
AC line 2-6	1	1	1	1	1	1
AC line 4-6	0	0	1	0	1	1
AC line 6-8	1	1	1	1	1	1
AC line 18-19	0	1	1	0	1	1
AC line 13-30	1	1	1	1	1	0
AC line 16-17	1	1	0	0	1	0
AC line 11-16	0	0	0	0	0	0
AC line 4-11	0	0	0	0	0	0
AC line 23-26	0	0	0	0	0	0
AC line 12-15	1	1	1	1	1	1
AC line 23-13	0	0	0	0	0	0
AC line 23-27	1	0	0	1	0	0
DC line 5-6	1	1	1	1	1	1
DC line 8-9	1	1	0	1	1	1
DC line 5-9	1	0	1	1	0	1
DC line 7-9	0	0	1	0	1	0
DC line 6-9	1	1	0	0	0	0
DC line 4-7	1	1	1	0	1	0
DC line 5-8	0	0	1	1	0	0
DC line 3-5	0	0	0	0	0	0
ES location	9	9	9	9	9	7
ES power	12.0	12.1	15.1	16.2	12.8	15.0
f_1 (ΔV)	0.0103	0.0091	0.0086	0.0093	0.0092	0.0147
f2 (P_L)	3.4346	4.0858	4.2463	3.7313	4.0855	5.5728
No. of violated constraints	0	0	0	0	0	N/A

problem is solved using GA. The obtained solution, using the Pareto based method and the proposed APF decision criterion, is compared with two solutions obtained using WS approach at (λ=0.4 and λ=0.6). Figure 7.9 depicts the values of the objective functions: voltage deviation (ΔV) in percentage and power losses (P_{Loss}) in MW, both of which are on the same Y-axis. It can be seen that the developed method yields a better solution with less objective functions' values. Given the high number of decision variables, the proposed approach is computationally efficient. The solution time was around 265 seconds on a regular PC.
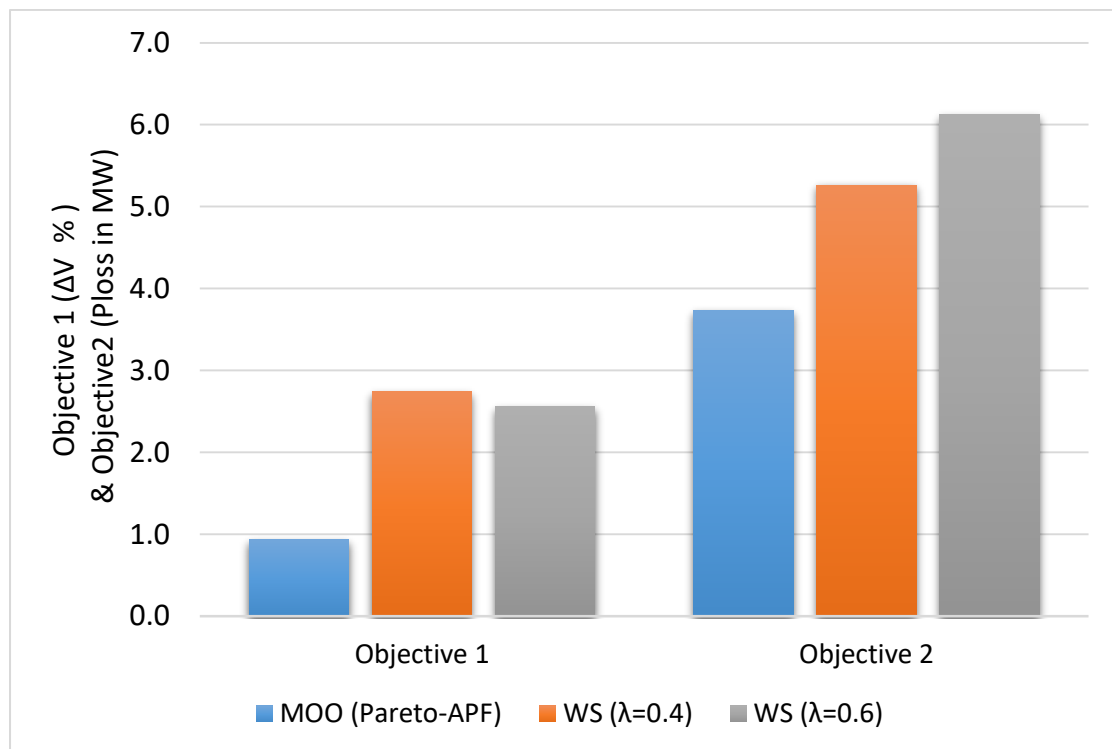
Figure 7.9 Values of objective functions obtained by weighted sum method (with different λ values) and the Pareto based approach.

7.4.2 Three objectives problem

The problem is resolved while adding a third objective, which is the frequency deviation from the nominal value (60 Hz). In this case, as was shown earlier in Chapter 6, the Pareto front is not following the same line trajectory, rather, it represents a

surface. In other words, the set of points representing the optimal solutions (architectures in this problem) are representing a surface if connected together. This differs from the case of 2D Pareto front, where two objectives are considered, in which the set of optimal solutions are forming a line if connected together. The 3D Pareto front is depicted in Figure 7.10. The first and second objective functions (total power losses and voltage deviation) are plotted on the horizontal axes, while the third objective function (frequency deviation) is plotted on the vertical axis.

For further clarification, two side views of the front are shown on Figure 7.11 and Figure 7.12. Figure 7.11 shows the relation between the power losses (P_{Loss}) and the frequency deviation (Δf). It can be seen that at lower frequency deviations, the power losses increase. This is justified by considering the fact that Δf is lowered by installing more ES in the system. Increasing the ES size incur more power losses, this is mainly due to the losses in the converter. View 2 is shown in Figure 7.12, where Δf and ΔV are plotted against each other. From the figure, one can tell that at lower frequency deviations, the voltage deviation is higher. This is because the installed ES is not capable of compensating the voltage profile at all the busses. By referring to equation (7-40), it can be found that the value of U_{ES}, which is the maximum number of ES arrays to be installed in the system, is set to one. In case of more voltage compensation is required, wider dispersion of ES arrays should be done, and then, higher values of U_{ES} should be used. However, it should be kept in mind, that the adopted Pareto based approach is presenting the different trade-offs among the solutions. Solutions from the middle of the front can be selected to achieve a balance between the objectives considered in the problem. The extreme solutions on the front should be avoided.

In order to select the most adequate solution, the same decision criterion is applied. The re-mapped Pareto front is depicted in Figure 7.13. It can be seen that the least

penalized individual is individual 30 followed by individuals 39 and 23, respectively. At the end of the list, with the highest penalty values, we can see the extreme solutions; individuals 18 and 2. The objectives' values of individual 30 are listed in Table 7-3.
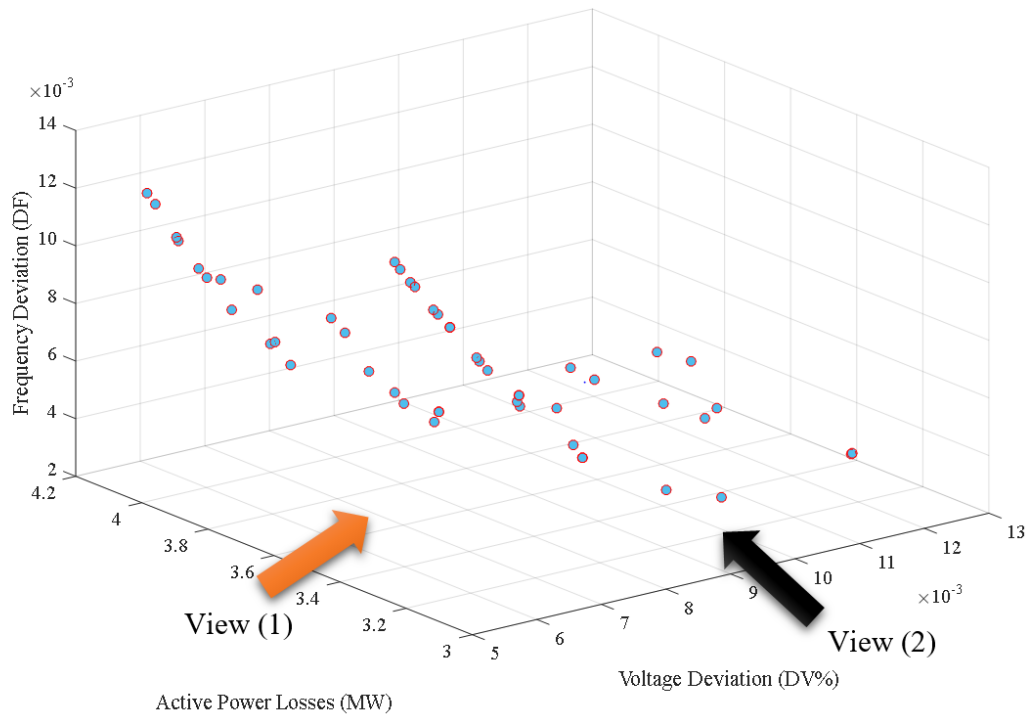
Figure 7.10 3D Pareto front for 3 objective problem

The Pareto front obtained from the three objectives problem is subject to further analysis. It is assumed that the problem is in the context of a weight sensitive application (e.g. large naval platform). The weight of the energy storage in all the front solutions is evaluated. Although, the weight wasn't included in the problem as an objective, an estimation of the weight is important for various design aspects. The energy storage parameters listed in Table 6-1 are used for the evaluation. The Pareto front with the weight evaluation is shown in Figure 7.14. The figure on the right hand is showing the relation between the weight of the installed ES and the frequency deviation. It can be seen that with installing more ES, the frequency deviation is reduced. The figure on the left hand is showing the relation between the power losses and the voltage deviation.

The weight of the ES required to be installed by individual 30, which is selected by the proposed decision making criterion, is 3.864×10^5 Kg.
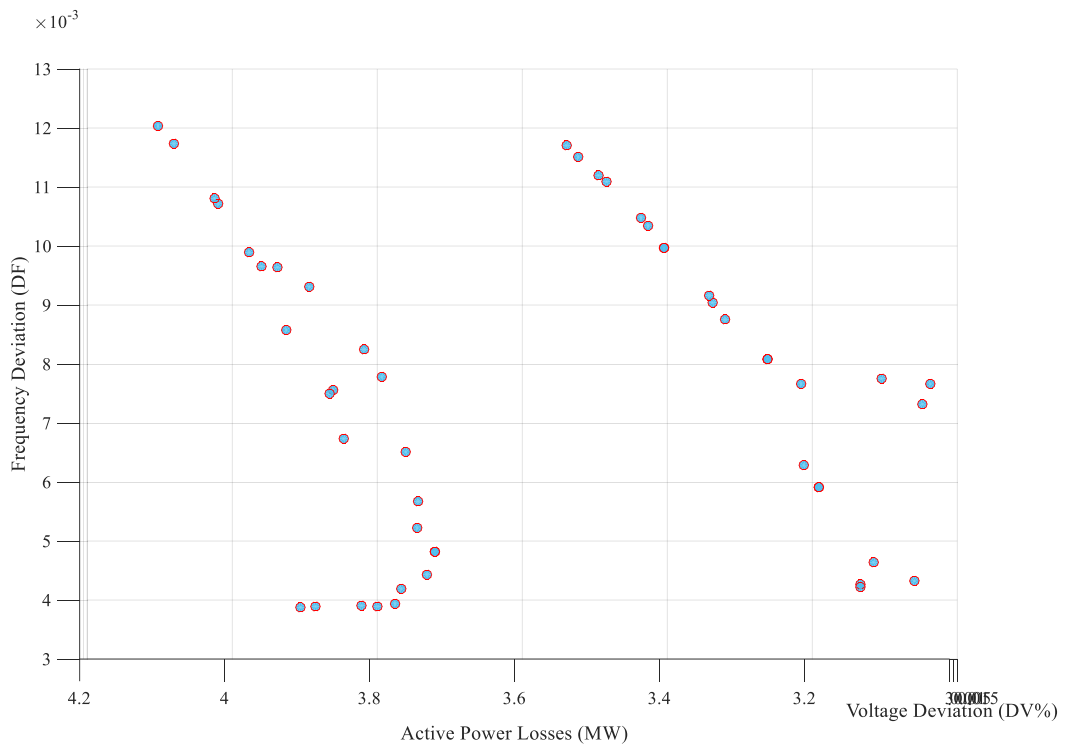
Figure 7.11 Side view of 3D Pareto front (View 1).
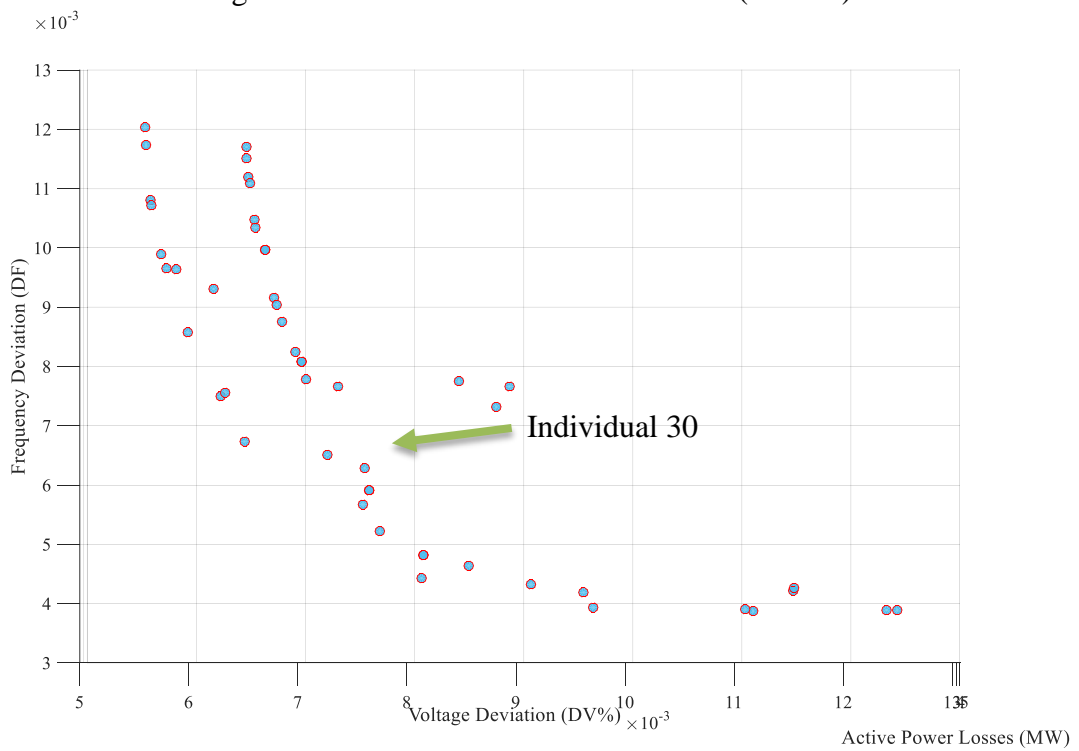
Figure 7.12 Side view of 3D Pareto front (View 2).
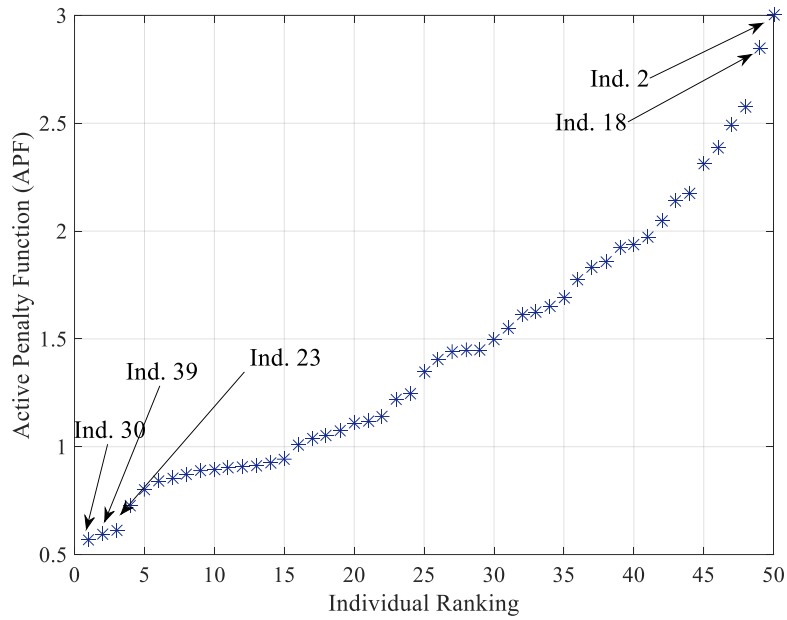
Figure 7.13 Re-mapping the Pareto front using the Aggregated Penalty Function.

Table 7-3 Individual 30 objectives' values.

Voltage Deviation	Power Losses	Frequency Deviation
0.765%	3.184 MW	0.59%
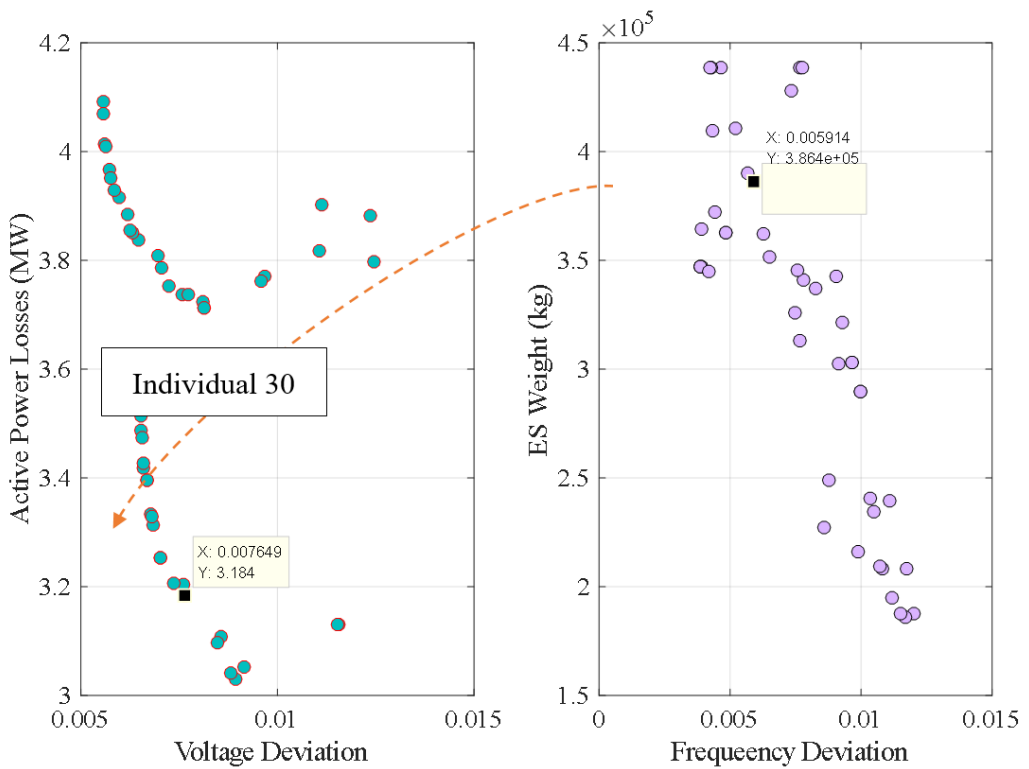
Figure 7.14 Three objectives Pareto front against ES weight.

7.4.3 Four objectives problem

In the previous section, the problem was solved while considering three objectives (minimizing the voltage deviation, minimizing the total power losses and minimizing the frequency deviation). In this part of the dissertation, in addition to the aforementioned three objectives, the problem is resolved while adding the ES weight as the fourth objective. The problem is of NP-hard complexity, mixed integer, combinatorial (e.g. involves continuous and discrete variables) and involves high number of non-linear constraints. The problem has four objectives, twenty-eight decision variables and twelve constraints. Furthermore, there are 2.0447×10^{16} possible solutions for the problem. The latter number is calculated by calculating the permutations of all the possible values for the decision variables.
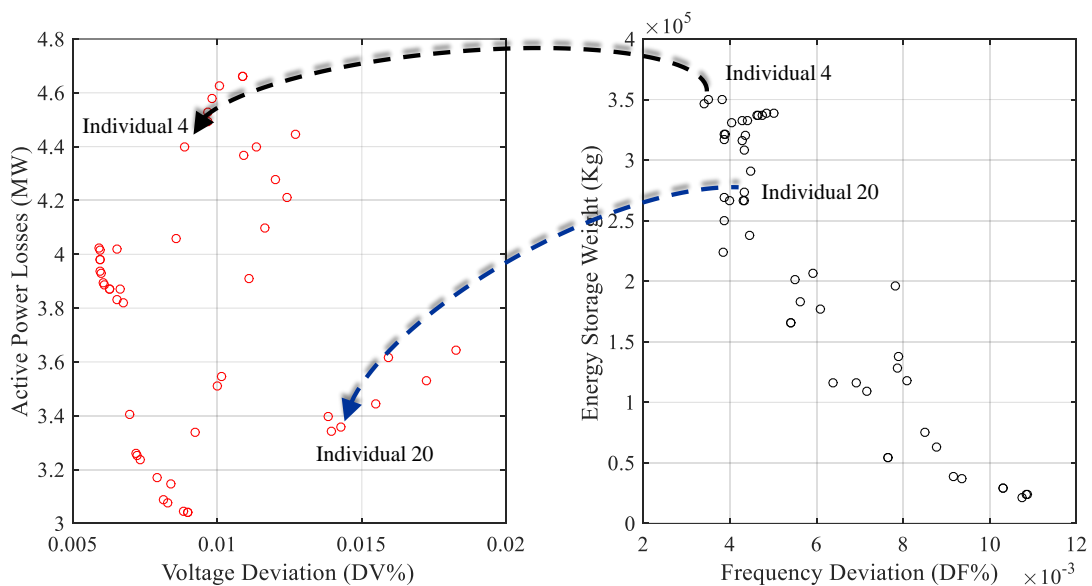
Figure 7.15 Pareto front for four objectives problem.

The problem is formulated, solved and the Pareto front is obtained as shown in Figure 7.15. In two objectives problem, the PF took the shape of a line, while in the three objectives problem, it took the shape of a surface. In the case of four objectives problem, the PF cannot be represented in a single figure as it needs a 4D representation,

which is not possible. Therefore, the PF is plotted on two figures (2×2D). The right figure shows the relation between the ES weight and the frequency deviation while the figure on the left side of the page shows the relation between the total active power losses and the voltage deviation. Each individual has two images, one on each figure. For example, by referring to Figure 7.15, individual 4 is represented on the right side figure, while the black-dashed arrow points at its image (projection) on the left hand side figure. The same is done for individual 20. It can be said that each individual is represented by a pair of points.
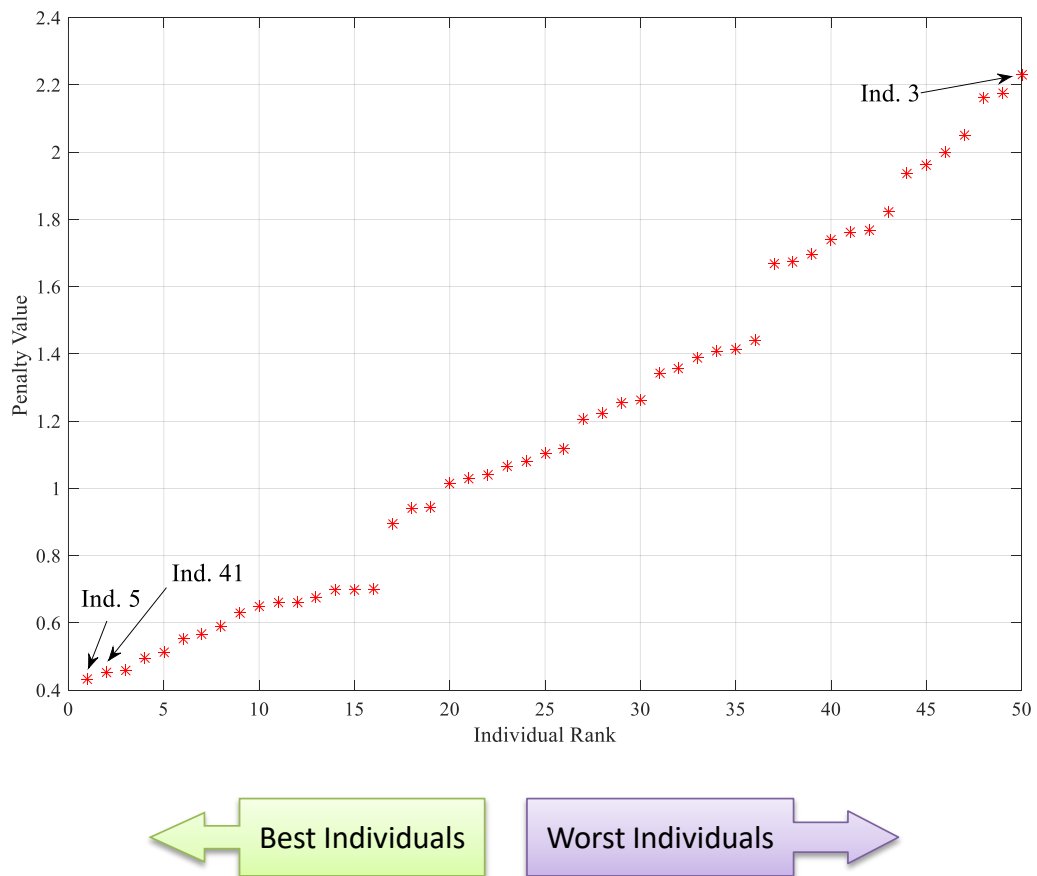
Figure 7.16 Four objectives Pareto front after applying decision making criterion.

The same decision making criterion is applied on the four objectives to select a single individual for implementation. The APF is applied using equation (7-47), where N_{obj} is four in this case. The results are depicted in Figure 7.16. It is found that the

223

individual with the lowest penalty is individual five. As shown in the figure, as the rank is getting higher, the penalty is getting higher as well, which means that the individual is less favored. The individual with the highest penalty is individual three.
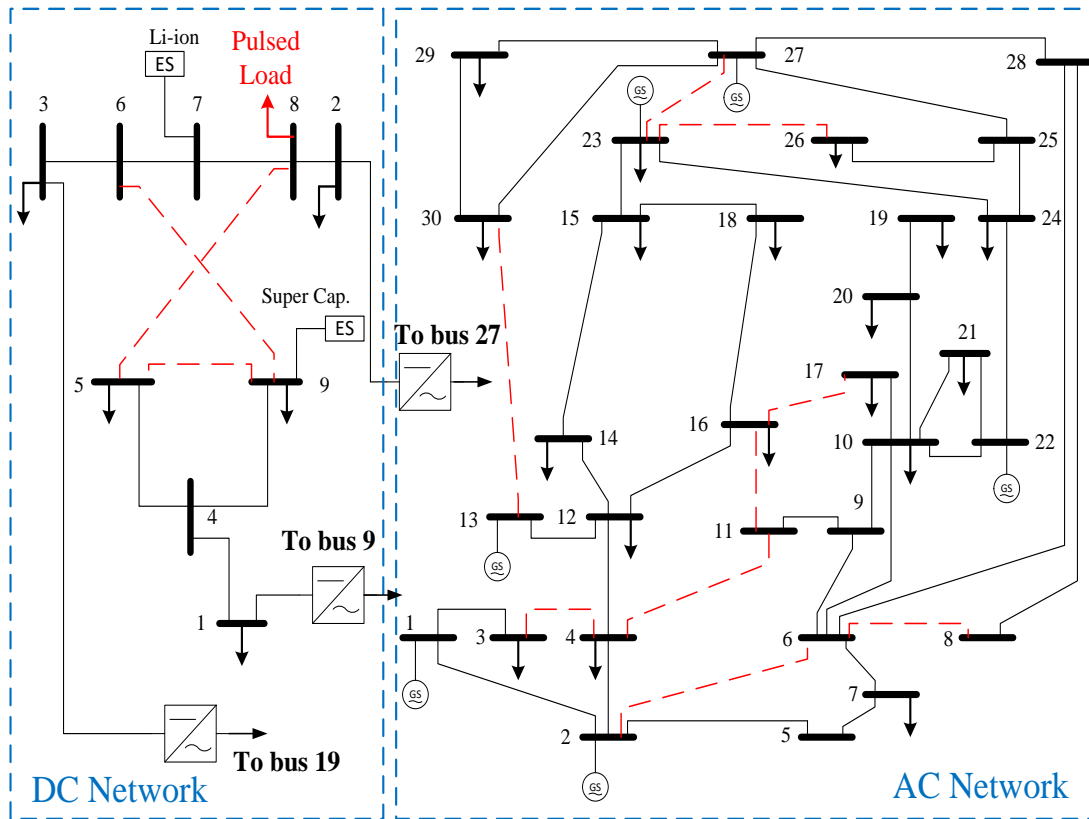
Figure 7.17 Design of the architecture of individual five.

The end result of the developed optimization framework is to determine the specifications of the optimized architecture. As each individual carries in its genes the characteristics of the architecture. The design of the architecture of individual five is shown in Figure 7.17. From the figure, the following optimal architecture design specifications are determined:

- The distribution lines to be connected/disconnected are specified. The lines to be connected are shown on the figure with red-dashed lines.

- A Li-ion array of power capacity of 2.635 MW should be connected at bus 7.

- A SC bank of power capacity of 5.135 MW should be connected at bus 9.

- The first VSC should be connected between DC bus 1 and AC bus 9.

- The second VSC should be connected between DC bus 2 and AC bus 27.

- The third VSC should be connected between DC bus 3 and AC bus 19.

There's an inevitable question that rises here, what if the decision maker/planner cares more about a certain objective over the others? Since in some systems or implantations, it is wanted to minimize a certain objective or a certain objectives is more effective than the others. According to Pareto concept, there's no improvement can be gained for a single individual without make the other individuals worst. In the previous cases, the APF decision making criterion was applied with equal penalty (i.e. all the objectives are penalized equally). In order to select a certain individual that performs in a particular objectives better than the others, a modified APF criterion should be adopted. In the modified criterion, the objectives are penalized differently; the objective of more interest to the designer is given a higher penalty. For instance, if the designer is interested in selecting an architecture that outperforms the other architectures in the frequency deviation objective (i.e. achieves further minimization of the frequency deviation). Then, the individuals who are not performing well in this objective are given higher penalty. This requires a modification in equation (7-47), the function $\mathcal{T}(f_{a,y})$ should be as shown in Figure 7.18. The modified $\mathcal{T}(f_{a,y})$ implies applying a penalty function with higher slope to the favored objective $(\mathcal{T}_2(f_{a,y}))$ while the penalty function $(\mathcal{T}_1(f_{a,y}))$ is applied to the other objectives. In this case, the slope of $(\mathcal{T}_2(f_{a,y}))$ is selected to be double that of $(\mathcal{T}_1(f_{a,y}))$. However, higher penalties can be applied. It should be highlighted, that the penalty values should be selected carefully because high differences in penalty values applied to the objectives can shift the

problem to be a single objective one. In other words, the obtained architecture will be performing very well in the favored objective, while significantly underperforming in the other objectives.
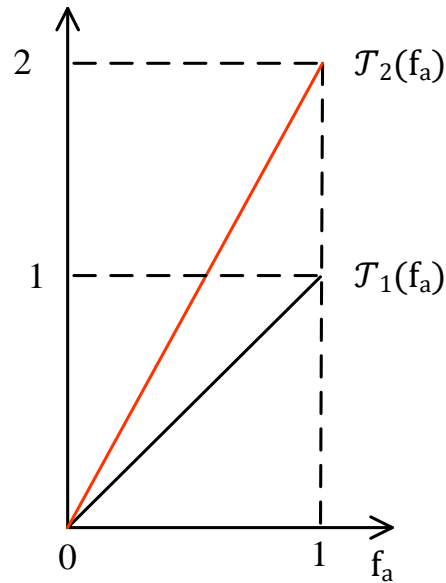
Figure 7.18 Modified Aggregated Penalty Function (APF).

A sensitivity analysis is performed to investigate the effect of changing the penalty value on the selected individual and the decision making process. The results of this sensitivity analysis are listed in Table 7-4. It is shown that in case of equal penalty (no particular objective is favored), individual five is the one to be selected. The same individual is used in case of penalizing the weight objective as it is still achieving the lowest penalty. The ES eight objective is assigned higher penalty than the other objectives $(\mathcal{T}_{ESweight}(f_{a,y}) = 2 \times \mathcal{T}_1(f_{a,y}))$. However, in case of penalizing the voltage and the frequency, individual twelve outperforms individual five. Therefore, if a particular interest is given to minimize the frequency deviation, individual twelve should be the one to be selected not individual five.

Table 7-4 Sensitivity analysis for penalty values
in the four objectives problem.

Equal Penalty	Penalizing Weight	Penalizing Voltage	Penalizing frequency
5	5	12	12
41	24	5	5
12	41	35	41
35	9	41	35
24	12	9	27
16	45	16	16
9	14	24	18
27	50	14	9
43	43	43	24
14	35	45	25
31	31	31	14
11	11	11	45
45	16	50	50
18	25	25	43
50	19	27	49
25	27	18	11
19	21	19	31
21	22	21	7
7	8	22	19
22	10	8	36
⋮	⋮	⋮	⋮
⋮	⋮	⋮	⋮
33	28	38	48
47	47	47	39
37	37	33	32
38	38	39	6
13	13	32	1
4	15	29	15
15	2	34	34
2	4	15	29
32	32	40	40
34	34	3	3
29	40	13	13
40	29	23	23
3	3	2	2

The results obtained from the three objectives problem and four objectives one are compared. This comparison is as shown in Table 7-6 and Figure 7.19. It can be concluded from this comparison, that including the energy storage weight as an

objectives, achieves significant reduction of the weight. In the three objectives problem, the ES weight is not seen or targeted by the optimization algorithm. However, when it is included in the problem, a more balanced objective values are obtained. This emphasizes the effectiveness and plausibility of the developed optimization framework.

Table 7-6 Results validation.

	Weighted Sum Approach (Traditional)	Developed Pareto Based Method
Voltage Deviation (DV%)	1.84 %	0.9%
Power Losses (MW)	4.1459	3.0411
Frequency Deviation (DF%)	0.72%	0.79%
ES Weight (kg)	3.22928e5	1.84515e5

(a)

(b)

(c)
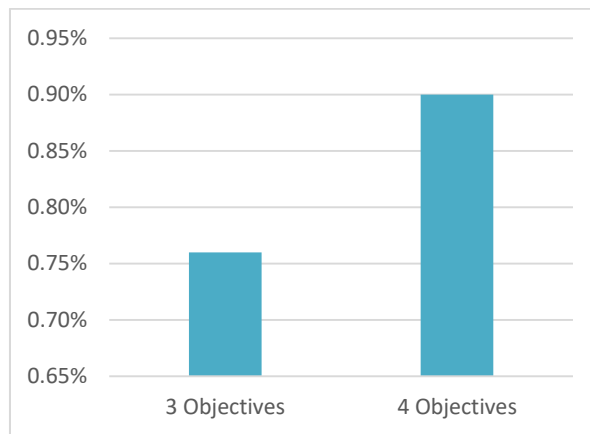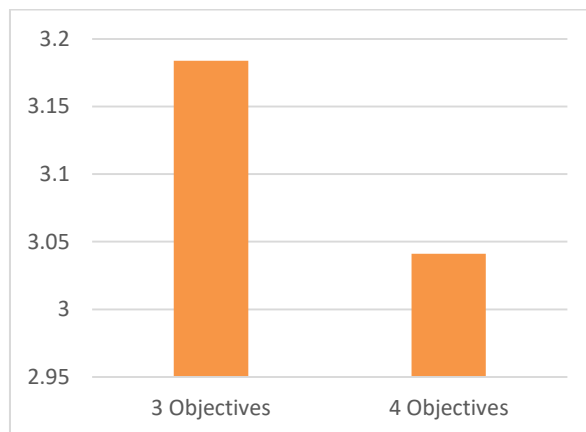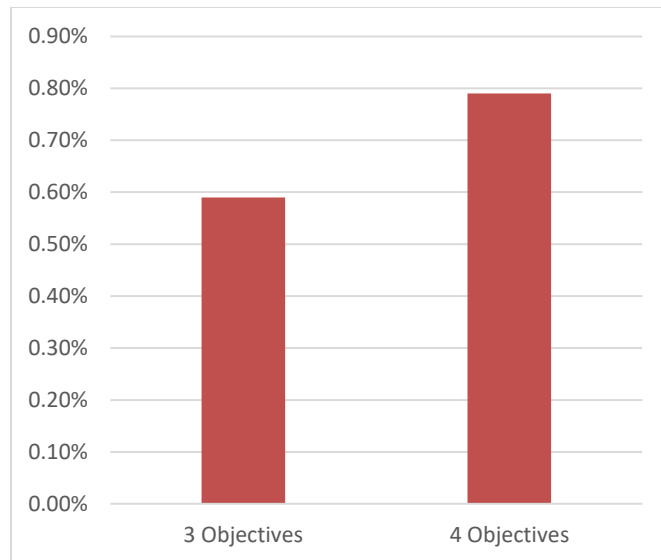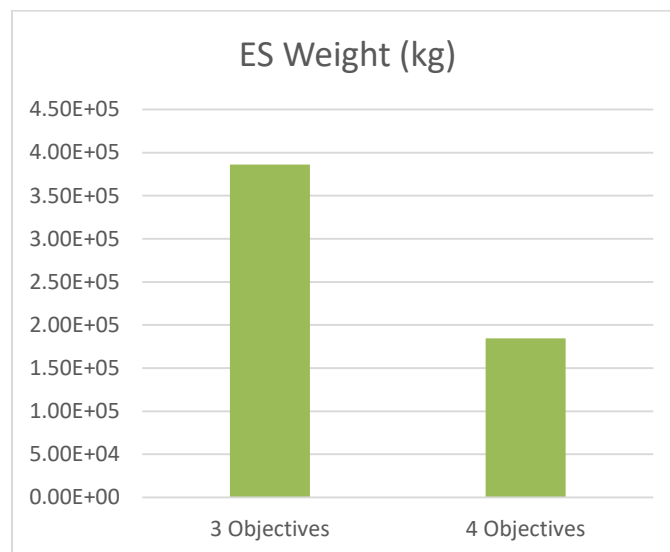
ES Weight (kg)

(d)

Figure 7.19 Comparing the results of three and four objectives problems.
(a) Voltage deviation, (b) Power losses, (c) Frequency deviation, (d) ES weight.

In order to validate the effectiveness of the developed methodology, a further investigation is performed. The same problem with the same conditions is re-solved using the weighted sum approach. In other words, the problem is relaxed to be a single objective then solved using the regular GA. This is done to test if the global optimal

point is obtained. The results are compared in the table below, it can be seen that the developed Pareto based method is achieving better results for three objectives out of the four.

7.5 Summary

In this chapter, a multi-objective optimization framework was proposed for the optimal design of AC/DC distribution systems. In the presented problem, it was required to find the best architecture to accommodate the high power demand loads while avoiding major disturbances in the system. The problem is solved using different formulations. First, two objective functions were considered: minimize the voltage deviation on all the buses and the total active power losses in the system including the losses in the converters. Then, a third objective is added to the problem, which is the minimization of frequency deviation. Finally, the problem is solved for four objectives, where the weight of ES to be installed is considered to be minimized. The decision (controlled) variables were the locations of load, ES and point of common coupling (PCC) and the connectivity of the distribution lines.

The considered distribution system is AC/DC being assumed for wider use and utilization in future smart energy systems and naval platforms. The sequential power flow method was applied to solve the power flow and evaluate each individual. The generator, exciter and governor are modeled to estimate the frequency response of the generator upon the occurrence of the pulsed load.

The proposed approach is based on Pareto Optimality. The efficient Non-dominated Sorting Algorithm NSGA-II was utilized to obtain the Pareto front which is the set of optimal solutions. A decision making criterion was applied to obtain only one solution among the frontier individuals. An aggregated Penalty Function (APF) was proposed and used as a decision making criterion. The APF was used to re-map the Pareto front

and rank the individuals based on their penalties. The obtained solution was compared to a base case and other solutions obtained using the traditional Weighted Sum (WS) approach. Major reductions in the objectives were achieved while keeping the voltage profile within the allowed limits and operation points of all the VSCs within the safe operating area. This validates that the global optimal point is reached.

Furthermore, a sensitivity analysis on the impact of selecting the penalty of the objectives on the obtained optimal architecture design is conducted. It was shown that if a certain objective (e.g. the frequency deviation) is favored, then a different architecture would be selected. A higher penalty is applied to the individuals who are underperforming in this objective to eliminate them from the decision making process. From a different point a view, the presented approach can be applied to microgrid planning as the distribution systems can be clustered into microgrids. The DC side of the distribution system can be viewed as a microgrid and it is desired to optimally connect it to a larger AC network.

Chapter 8 Modeling and Control of a Low Speed Flywheel Energy Storage System

8.1 Introduction

Driven by the latest developments in different engineering realms, such as superconducting and frictionless bearings, vacuum encased machinery and power electronic switching, flywheels gained much interest as a reliable energy storage element. Flywheel energy Storage System (FESS), or sometimes known as electromechanical batteries [176], have been used lately in several applications such as data centers [171], aerospace [20]-[317], shipboard power systems [168],[169], UPS [318], electrification of rural areas [178], fast charging of electric vehicles [319] and improving renewable energy integration [320]. Flywheel Energy Storage Systems (FESS) operate in three modes: charge, stand-by and discharge. Since flywheels are classified as short term energy storage [321][322], the transition among these three modes should be performed rapidly, unlike other types of energy storage elements. In order for this process to be done seamlessly, a fast acting, flexible and reliable driving system is required. Moreover, the control loop should be designed accurately to avoid either slow action, high overshoot or steady state errors.

Generally, flywheels can be classified according to their speed into low speed and high speed. High speed systems feature much lower weight and smaller size. However, they entail sophisticated technologies to reduce friction and their power output is limited by cost and difficulty of cooling [323]. A variety of machines have been discussed in the literature for use in low speed flywheel applications including induction machines (IM) [319], [324]-[326] and Doubly Fed Induction Machines (DFIM) [323], [327]-[331]. In [332], the control and performance of a large DFIM

based flywheel was investigated. In this system, the stator was connected to the grid through a step up transformer while the machine secondary (rotor) was connected to a cyclo-converter via slip rings. Thus, the existence of slip rings is acceptable in low speed flywheels while it is not in high speed ones. Consequently, brushless DC [333], homopolar inductor [334], Permanent Magnet Synchronous Machine (PMSM) [175], [335], Axial Flux Permanent Magnet (AFPM) [179] and synchronous reluctance machines [336] are preferred in high speed flywheels.

Different DC-DC converters topologies are utilized in the control of low speed flywheel driving systems. However, these converters are utilized as a secondary intermediate stage, not as the primary driver. In [180], a boost DC-DC converter with a parallel bypassing switch is used for FESS in UPS applications. The boost converter is operated in the flywheel discharging mode to increase the operating voltage range while it is bypassed during the charging mode. Since the boost converter is uni-directional, a Dual Active Bridge (DAB) DC-DC converter is utilized to interface a low speed FESS to an HVDC link [337]. This system is used to smooth the output power profile from a wind farm. Hedlund et al proposed a sliding mode four quadrant DC-DC converter to be utilized in controlling the power flow to a flywheel power buffer in an all-electric EV driveline [338].

In this chapter, the control and performance of a DC machine based flywheel in DC distribution networks is addressed. DC machines feature a rugged construction and reliable operation. Further, they can be interfaced to the DC distribution network through DC-DC converters, which are simpler and more efficient than their AC/DC counterparts. The detailed modeling of a DC-DC converter based driving system for a FESS including the parasitic resistances for all elements was carried out. In this work, the author integrates the machine model with the converter model. Then, a combined

state space model is obtained for the entire system for each mode of operation. In order to validate the derived model, it is compared to another model estimated using the MATLAB/Simulink environment. Two control loops are designed independently for each mode of operation. Improved voltage/current controllers are introduced to achieve steady operation during the charging and discharging modes.

8.2 System Modelling

The flywheel driving system is based on a DC-DC bi-directional buck-boost converter. Figure 8.1 shows a schematic diagram for the system. As shown in the figure, the utilized topology features two IGBT switches; during each mode of operation, one switch is operated while the other one is disabled. Given that the DC bus voltage is higher than the machine terminal voltage over the entire operation range, the converter acts as a buck converter in the charging mode while acts as a boost during discharging. Each mode was modeled separately with its two switching states, then an averaged state space model was obtained [339].
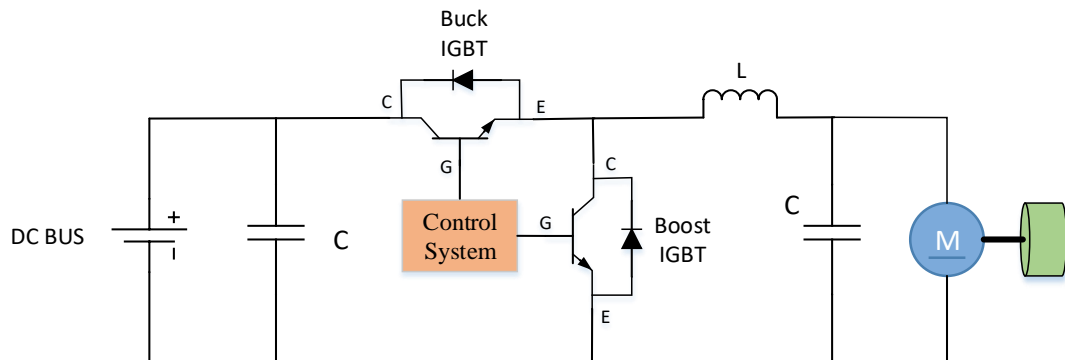
Figure 8.1 Schematic diagram for flywheel driving system.

8.2.1 Discharging state (Boost mode):

In the boost mode, the source will be the machine (i.e. the machine will be operated as a generator). The capacity of the DC network is much greater than the FESS and the voltage of the DC bus is controlled through a large stable source (e.g. large VSC or DC

generator). Thus, the DC network can be represented by a DC voltage source with a small internal resistance. This small impedance in the converter's output can lead to an impedance mismatch and, consequently, this mismatch can cause instability of the whole system due to the violation of Nyquist stability criterion [340]. In the boost mode, the control system controls the boost IGBT with a duty cycle (D) based on a reference current sent from the main distribution network controller while it disables the buck IGBT.

(a)

(b)
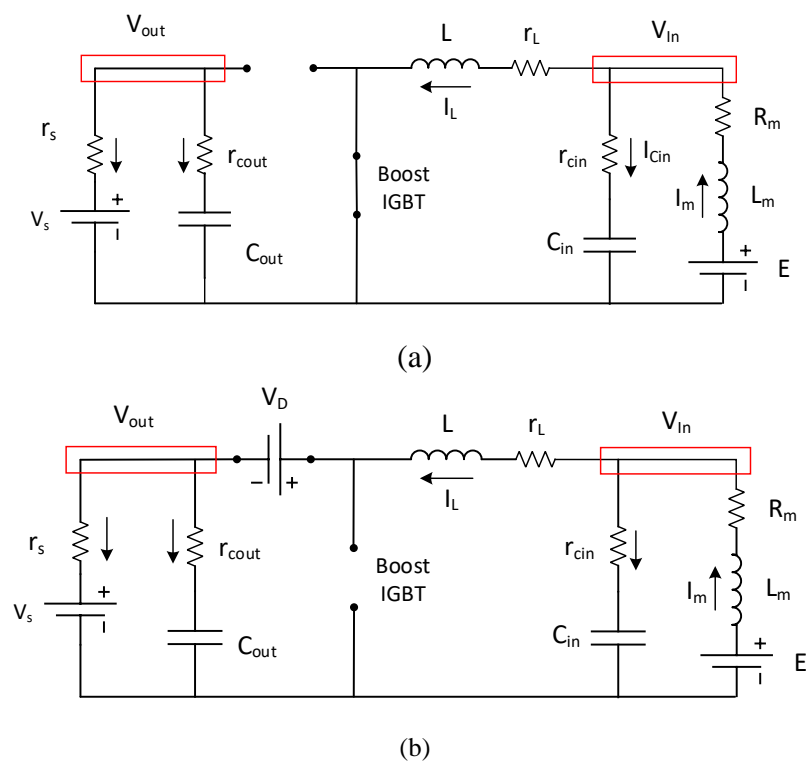
Figure 8.2 Equivalent circuit for the converter in boost mode during (a) ON state (b) OFF state.

8.2.1.1 ON state

When the IGBT is in its ON state, the converter equivalent circuit tends to be as shown in Figure 8.2 (a). In order to obtain the most accurate model, a model of the DC machine represented by R-L-E branch is added to the converter model. The state variables are the inductor current i_L, the machine current i_m, the input capacitor voltage

v_{cin} and the output capacitor voltage v_{cout}. By applying KVL and KCL, the dynamic equations of the system are derived as the following:

$$\frac{di_L(t)}{dt} = \frac{V_{In}(t) - i_L(t).r_L}{L} \tag{8-1}$$

where V_{in} is the input voltage, i_L, r_L and L are the inductor current, resistance and inductance, respectively. Then KCL is applied at the input node $\left(i_{cin}(t) = i_m(t) - i_L(t)\right)$ to find V_{in} as a function of the state variables.

$$V_{In}(t) = v_{cin}(t) + i_m(t).r_{cin} - i_L(t).r_{cin} \tag{8-2}$$

where r_{cin} is the input capacitor resistance. By substituting (8-2) into (8-1) yields:

$$\frac{di_L(t)}{dt} = -\frac{1}{L}.[r_{cin} + r_L].i_L(t) + \frac{r_{cin}}{L}i_m(t) + \frac{1}{L}.V_{cin}(t) \tag{8-3}$$

The derivative of the machine current i_m can be evaluated as:

$$L_m\frac{di_m(t)}{dt} = E - V_{In}(t) - r_m.i_m(t) \tag{8-4}$$

where L_m and r_m are the machine equivalent inductance and resistance, respectively. Similarly, by substituting from (8-2) into (8-4) and rearranging the equation terms yields:

$$\frac{di_m(t)}{dt} = \frac{r_{cin}}{L_m}.i_L(t) - \frac{1}{L_m}.(r_{cin} + r_m).i_m(t) - \frac{1}{L_m}V_{cin}(t) + \frac{1}{L_m}E \tag{8-5}$$

The derivative of the input capacitor voltage can be expressed as:

$$\frac{dv_{cin}(t)}{dt} = -\frac{1}{C_{in}}.i_L(t) + \frac{1}{C_{in}}.i_m(t) \tag{8-6}$$

where the capacitance of the input capacitor is C_{in}. In order to get V_{out} as a function of the state variables, KCL is applied at V_{out} node:

$$V_{out} = V_{cout}.\frac{r_s}{(r_s + r_{cout})} + V_s.\frac{r_{cout}}{(r_s + r_{cout})} \tag{8-7}$$

where V_s and r_s are the voltage and equivalent resistance of the voltage source representing the DC bus and r_{cout} is the resistance of the output capacitor. The derivative of the output capacitor voltage can be given by:

$$\frac{dv_{cout}(t)}{dt} = -\frac{1}{C_{out}\cdot(r_s+r_{cout})}\cdot V_{cout} + \frac{1}{C_{out}\cdot(r_s+r_{cout})}\cdot V_s \tag{8-8}$$

where C_{out} is the capacitance of the output capacitor. By using (8-3), (8-5), (8-6) and (8-8) to formulate the state space model as in (8-9) and writing it in the matrix form, results in (8-10). It should be noted here that the output equation is not used because the controlled variables are state variables [341].

$$\frac{dx(t)}{dt} = A_{on}x(t) + B_{on}\cdot u(t) \tag{ 8-9}$$

$$\frac{d}{dt}\begin{bmatrix} i_L(t) \\ i_m(t) \\ v_{cin}(t) \\ v_{cout}(t) \end{bmatrix} = \begin{bmatrix} -\frac{1}{L}\cdot[r_{cin}+r_L] & \frac{r_{cin}}{L} & \frac{1}{L} & 0 \\ \frac{r_{cin}}{L_m} & -\frac{1}{L_m}\cdot(r_{cin}+r_m) & -\frac{1}{L_m} & 0 \\ -\frac{1}{C_{in}} & \frac{1}{C_{in}} & 0 & 0 \\ 0 & 0 & 0 & -\frac{1}{C_{out}\cdot(r_s+r_{cout})} \end{bmatrix} \times$$

$$\begin{bmatrix} i_L(t) \\ i_m(t) \\ v_{cin}(t) \\ v_{cout}(t) \end{bmatrix} + \begin{bmatrix} 0 & 0 & 0 \\ 0 & \frac{1}{L_m} & 0 \\ 0 & 0 & 0 \\ \frac{1}{C_{out}\cdot(r_s+r_{cout})} & 0 & 0 \end{bmatrix} \times \begin{bmatrix} V_S \\ E \\ V_D \end{bmatrix} \tag{8-10}$$

8.2.1.2   OFF state

Figure 8.2(b) shows the equivalent circuit of the converter during the OFF state. In this case, the anti-parallel diode with the buck IGBT will be forward biased. In this case, the derivative of the inductor current is calculated as follows:

$$\frac{di_L(t)}{dt} = \frac{V_{In}(t) - i_L(t)\cdot r_L - V_{out}(t) - V_D}{L} \tag{8-11}$$

by applying KCL to the output node to express V_{out} as a function of the state variables, yields:

$$V_{out} = i_L\cdot\frac{(r_s\cdot r_{cout})}{(r_s+r_{cout})} + V_{cout}\cdot\frac{r_s}{(r_s+r_{cout})} + V_s\cdot\frac{r_{cout}}{(r_s+r_{cout})} \tag{ 8-12}$$

by substituting from both (8-2) and (8-12) into (8-11), the derivative of the inductor current is re-written in (8-13).

$$\frac{di_L}{dt} = -\frac{1}{L} \cdot \left[r_{cin} + r_L + \frac{(r_s \cdot r_{cout})}{(r_s + r_{cout})} \right] \cdot i_L + \frac{r_{cin}}{L} i_m + \frac{1}{L} \cdot V_{cin} -$$

$$\frac{r_s}{L \cdot (r_s + r_{cout})} \cdot V_{cout} - \frac{r_{cout}}{L \cdot (r_s + r_{cout})} \cdot V_s \qquad (8\text{-}13)$$

Using a similar approach, the state space model for the converter in the OFF state is written as shown in (8-14).

$$\frac{d}{dt} \begin{bmatrix} i_L(t) \\ i_m(t) \\ v_{cin}(t) \\ v_{cout}(t) \end{bmatrix}$$

$$= \begin{bmatrix} -\frac{1}{L} \cdot \left[r_{cin} + r_L + \frac{(r_s \cdot r_{cout})}{(r_s + r_{cout})} \right] & \frac{r_{cin}}{L} & \frac{1}{L} & -\frac{r_s}{L \cdot (r_s + r_{cout})} \\ \frac{r_{cin}}{L_m} & -\frac{1}{L_m} \cdot (r_{cin} + r_m) & -\frac{1}{L_m} & 0 \\ -\frac{1}{C_{in}} & \frac{1}{C_{in}} & 0 & 0 \\ \frac{r_s}{C_{out} \cdot (r_s + r_{cout})} & 0 & 0 & -\frac{1}{C_{out} \cdot (r_s + r_{cout})} \end{bmatrix} \qquad (8\text{-}14)$$

$$\times \begin{bmatrix} i_L(t) \\ i_m(t) \\ v_{cin}(t) \\ v_{cout}(t) \end{bmatrix} + \begin{bmatrix} -\frac{r_{cout}}{L \cdot (r_s + r_{cout})} & 0 & -\frac{1}{L} \\ 0 & \frac{1}{L_m} & 0 \\ 0 & 0 & 0 \\ \frac{1}{C_{out} \cdot (r_s + r_{cout})} & 0 & 0 \end{bmatrix} \times \begin{bmatrix} V_s \\ E \\ V_D \end{bmatrix}$$

An averaged state space model is obtained by multiplying each state by its corresponding duty cycle.

$$A = A_{on} \cdot D + A_{off} \cdot (1 - D) \qquad (8\text{-}15)$$

$$B = B_{on} \cdot D + B_{off} \cdot (1 - D) \qquad (8\text{-}16)$$

After obtaining the averaged model, the system is perturbed around a steady state operation point, then linearized by neglecting second order terms. By applying Laplace transformation, the steady-state operating point can be obtained by (8-17).

$$X = -A^{-1} \cdot B \cdot U \qquad (8\text{-}17)$$

Given that U is the input vector, the solutions of the state variables are given by

(8-18), then the transfer function of the duty cycle to each state variable can be obtained. In this case, the control loop of the boost converter mode will be controlling the injected current to the DC bus to fulfill the pulsed load required energy. Therefore, the important transfer function is the duty cycle-inductor current. This transfer function will be used for the accurate design and tuning of the PI controller.

$$\hat{x} = (SI - A)^{-1}.\left[(A_{on} - A_{off}).X - (B_{on} - B_{off}).U\right].\hat{d} \qquad (\text{ 8-18})$$

(a)

(b)
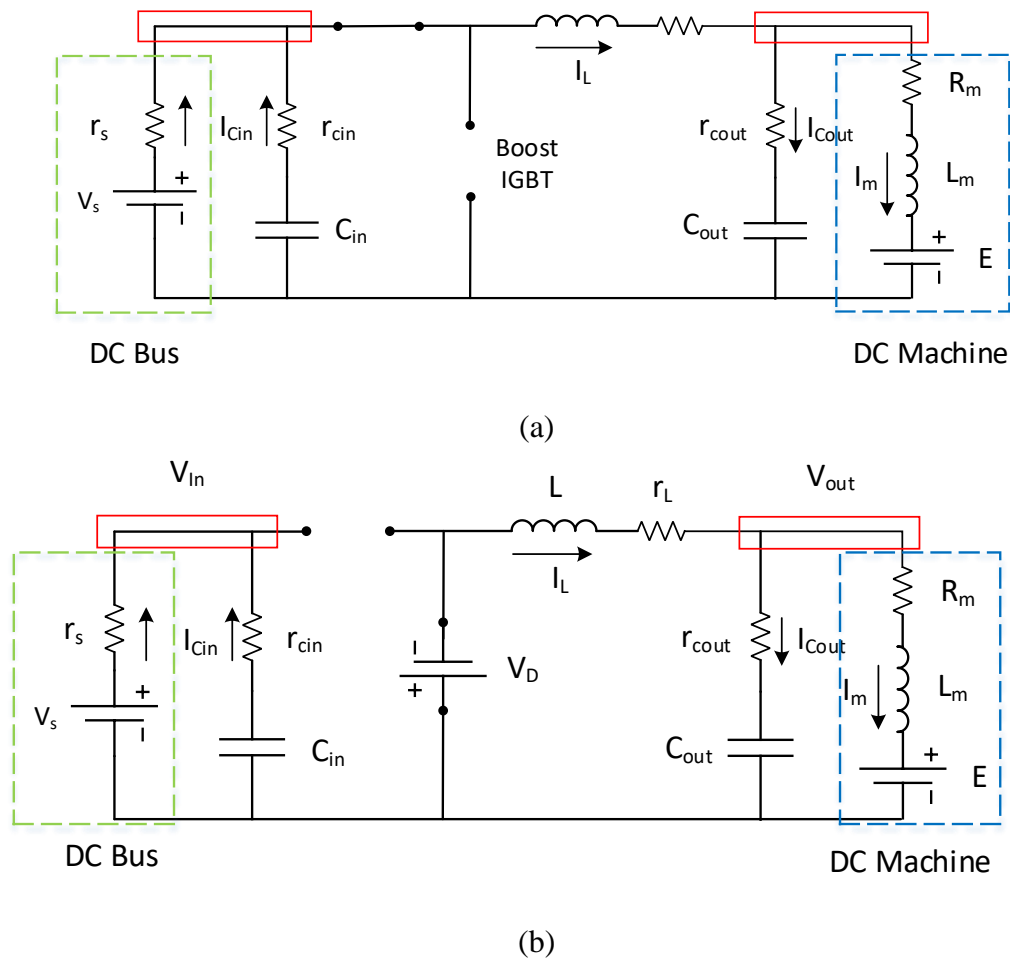
Figure 8.3 Equivalent circuit for the converter in buck mode during (a) ON state (b) OFF state.

8.2.2 Charging state (Buck mode)

The converter will be operated in this mode during off the pulse (the pulsed load is

not energized), so there's excess energy in the system to charge the flywheel. The power flow direction will be reversed to be from the DC network to the FESS. In this mode, the DC machine is working as a motor, in contrast to the boost mode where the machine was working as a generator. Figure 8.3 shows the converter equivalent circuits in both IGBT states. By using a similar procedure to the one used for the boost mode, the dynamic equations of the buck converter are determined during ON and OFF states and given in (8-19) and (8-20), respectively.

$$
\frac{d}{dt}\begin{bmatrix} i_L(t) \\ i_m(t) \\ v_{cin}(t) \\ v_{cout}(t) \end{bmatrix}
$$

$$
= \begin{bmatrix}
-\frac{1}{L} \cdot \left[\frac{(r_s \cdot r_{cin})}{(r_s + r_{cin})} + r_{cout} + r_L \right] & \frac{r_{cout}}{L} & \frac{r_s}{L \cdot (r_s + r_{cin})} & -\frac{1}{L} \\
\frac{r_{cout}}{L_m} & -\frac{1}{L_m} \cdot (r_{cout} + r_m) & 0 & \frac{1}{L_m} \\
\frac{r_s}{C_{in} \cdot (r_s + r_{cin})} & 0 & -\frac{1}{C_{in} \cdot (r_s + r_{cin})} & 0 \\
\frac{1}{C_{out}} & -\frac{1}{C_{out}} & 0 & 0
\end{bmatrix}
$$ (8-19)

$$
\times \begin{bmatrix} i_L(t) \\ i_m(t) \\ v_{cin}(t) \\ v_{cout}(t) \end{bmatrix} + \begin{bmatrix}
\frac{r_{cin}}{L \cdot (r_s + r_{cin})} & 0 & 0 \\
0 & -\frac{1}{L_m} & 0 \\
-\frac{1}{C_{in} \cdot (r_s + r_{cin})} & 0 & 0
\end{bmatrix} \times \begin{bmatrix} V_s \\ E \\ V_D \end{bmatrix}
$$

$$
\frac{d}{dt}\begin{bmatrix} i_L(t) \\ i_m(t) \\ v_{cin}(t) \\ v_{cout}(t) \end{bmatrix} = \begin{bmatrix}
-\frac{1}{L} \cdot [r_{cout} + r_L] & \frac{r_{cout}}{L} & 0 & -\frac{1}{L} \\
\frac{r_{cout}}{L_m} & -\frac{1}{L_m} \cdot (r_{cout} + r_m) & 0 & \frac{1}{L_m} \\
0 & 0 & \frac{1}{C_{in} \cdot (r_s + r_{cin})} & 0 \\
\frac{1}{C_{out}} & -\frac{1}{C_{out}} & 0 & 0
\end{bmatrix}
$$ (8-20)

$$
\times \begin{bmatrix} i_L(t) \\ i_m(t) \\ v_{cin}(t) \\ v_{cout}(t) \end{bmatrix} + \begin{bmatrix}
0 & 0 & -\frac{1}{L} \\
0 & -\frac{1}{L_m} & 0 \\
\frac{1}{C_{in} \cdot (r_s + r_{cin})} & 0 & 0
\end{bmatrix} \times \begin{bmatrix} V_s \\ E \\ V_D \end{bmatrix}
$$

The transfer functions of the duty cycle to each state variable are determined; however, the controller in the buck mode will be controlling the machine terminal voltage to control the charging rate. Thus, the transfer function of the duty cycle to the output capacitor voltage is used to design the PI control loop for the buck mode.

Table 8-1 Machine Parameters

Arm. Voltage	100 V
Arm. Current	19 A
Field Voltage	100 V
Field Current	0.6 A
r_m	0.44 Ω
L_m	12.9 mH
r_f	207 Ω
L_f	115 H
Rated Speed	1750 rpm

8.2.3 Model Validation

Before proceeding to the controller design based on the obtained transfer functions, it is important to validate those functions. The frequency response of the determined converter model is plotted using Matlab and compared to an estimated transfer function using the approach introduced in [342]. This approach is based on building an accurate converter model in Matlab/Simulink environment. The duty cycle is then perturbed with sinusoids of different frequencies and the resulting output is saved. From these, the designer can find how the system modifies the magnitude and phase of the injected sinusoids, giving discrete points on the frequency response. For more details please refer to [342]. The calculations were carried out using machine and converter parameters listed in Table 8-1 and Table 8-2, respectively. The frequency responses for the determined (analytical) and estimated (simulation) transfer functions are shown in Figure 8.4. It can be seen that there is a remarkable coincidence between both responses

241

over a wide range of frequencies. However, there's a slight deviation at higher frequencies, which are beyond the usable operation range in our application.

Table 8-2 Converter Parameters

DC Bus Voltage	325
r_s	0.01 Ω
C_{out}	1200 μF
r_{cout}	0.008 Ω
L	12.7mH
r_L	0.125 Ω
C_{in}	1200 μF
r_{cin}	0.008 Ω
V_D	1.75 V
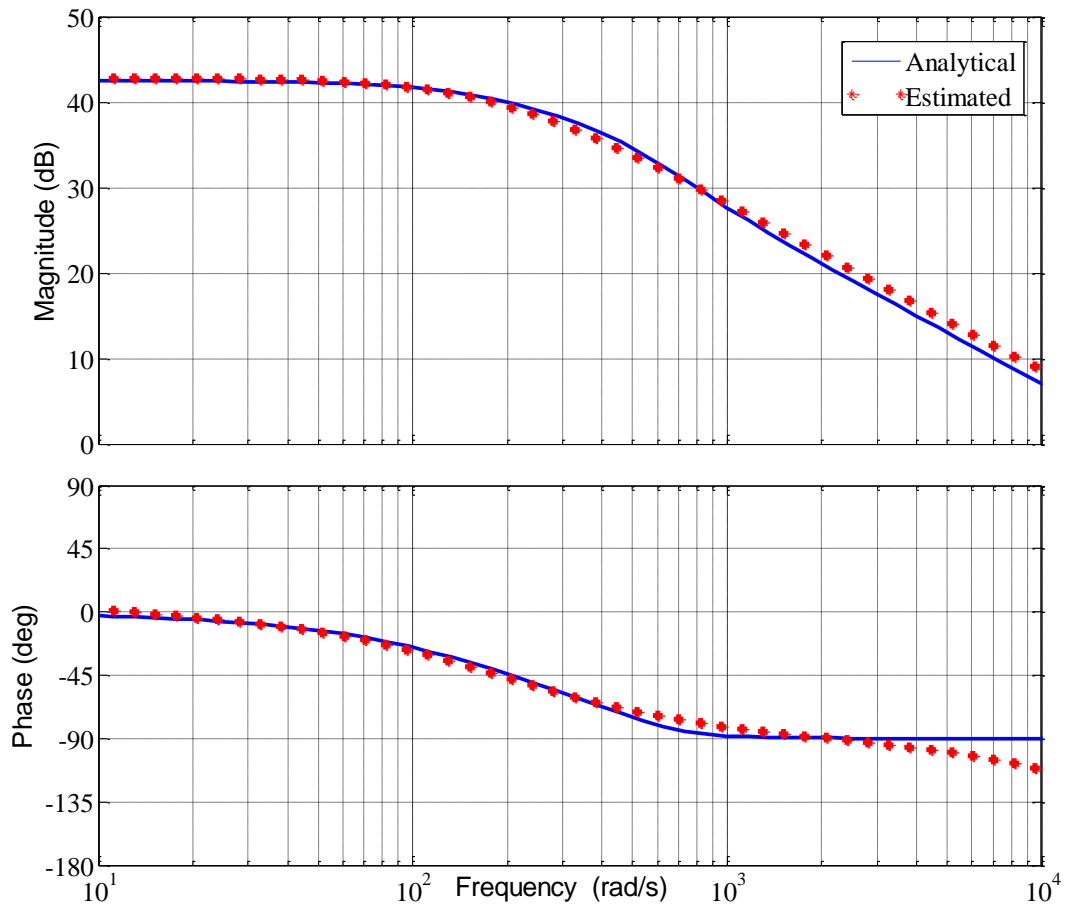
Figure 8.4 Frequency response of the duty cycle to inductor current transfer function for the boost converter.

8.3 Controller Design

Two PI control loops were designed, one for each operation mode. Switching between both controllers is performed through the main supervisory controller of the distribution network based on its needs. The main purpose is to utilize the available energy in the FESS to fill the energy gap caused by the pulsed load and prevent any voltage fluctuations. The controller of the buck mode is designed to control the charging rate through the control of the machine voltage. It is known that the DC machine can withdraw high current during the starting until the motor rotation can build up the counter emf. For this reason, a constant voltage reference can't be used; rather, a soft starting approach was utilized. The controller generates an internal ramping up voltage reference. One should keep in mind that the duration of the pulsed load is unknown; consequently, the State of Charge (SoC) of the FESS at the end of a given discharging cycle is unknown. Since, the SoC is directly dependent on the machine speed, the machine speed and voltage are not known at the end of the pulsed load period either. To assure a stable operation over a wide range of pulses, it is mandatory that the controller picks the last voltage value before switching to the buck mode (charging). Then the controller generates the ramping voltage reference starting from this value and ending at the full speed of the machine (full SoC). This approach allows the utilization of a very wide speed range of the machine, which can be an advantage over the DFIMs since the operation speed range of the DFIM is limited by the allowed slip typically within ±15% [332] to ±30% [323].

A block diagram showing the controller design is given in Figure 8.5. There are two independent Proportional Integral loops for the buck/boost modes controlling the charging and discharging of the flywheel, respectively. The transfer function for the buck mode controller is C_{buck} and C_{boost} for the boost mode controller. The gains of the

two PI controllers are listed in Table 8-3. It should be emphasized here that when the FESS is operating in a certain mode, the other IGBT should be turned off. For example, if the machine is charging, the buck mode controller is activated and the buck IGBT is working (please refer to Figure 8.1). Hence, the boost IGBT should be kept off and vice versa. An interlocking logic circuit is provided for this function. Moreover, this design is prepared to be suitable for hardware and practical implementation. An input is provided to disable the converter and turn off both switches in case of an emergency or fault. One of the merits of this controller is its simplicity with avoiding heavy computations so it can be easily implemented on any microcontroller or FPGA chip.
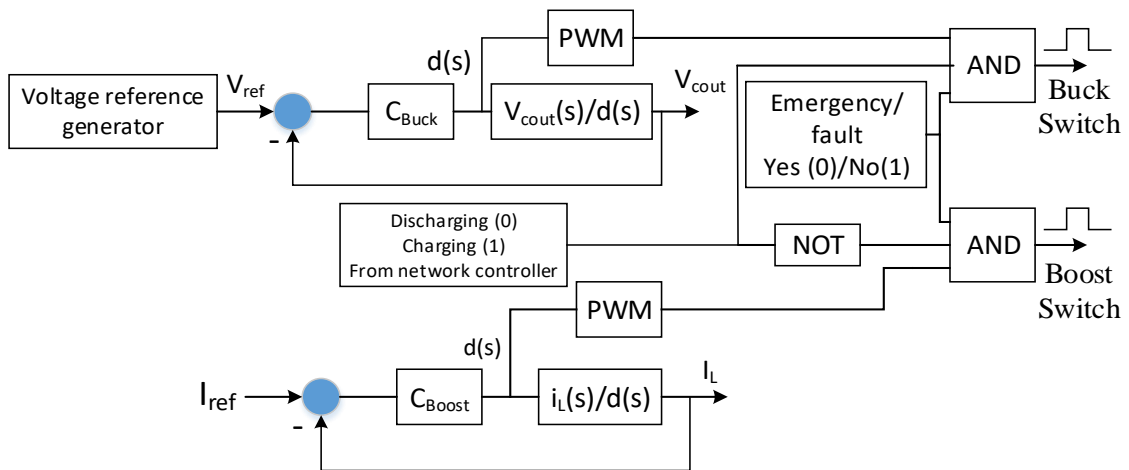
Figure 8.5 Block diagram for the developed FESS controller.

Table 8-3 PI Controllers' Parameters

	K_p	K_i
Buck Converter	9.75	29
Boost Converter	0.75	30.45

As mentioned previously, the converter in boost mode works in current control to control the injected current into the DC bus. The reference current (I_{ref}) is

calculated and passed from an outer control loop, which is typically resolved by a slower controller [319], [343]. This research work focusses on the design of the inner control loops, while the details of the outer control ones are beyond the scope of this work.
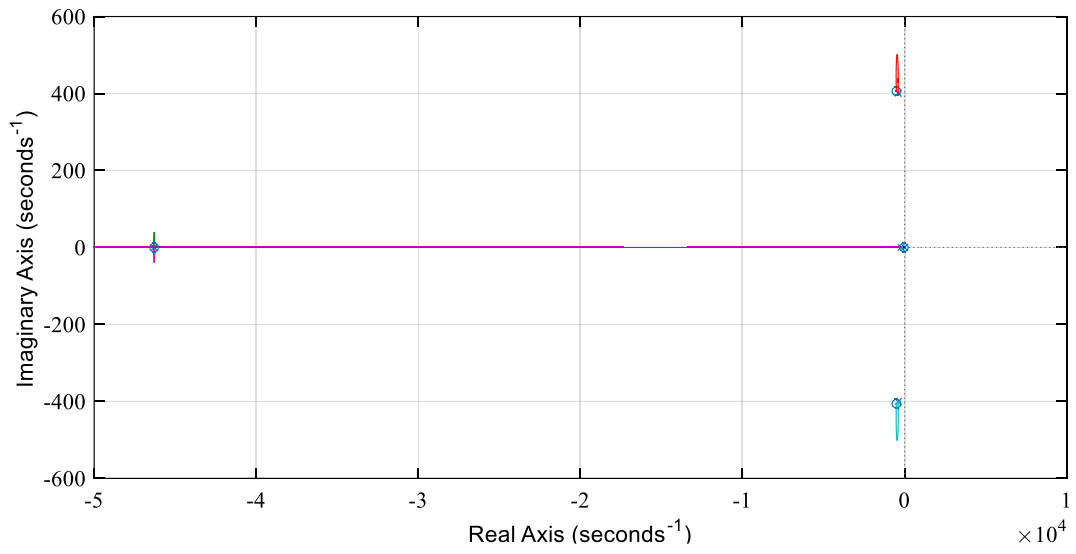
(a)
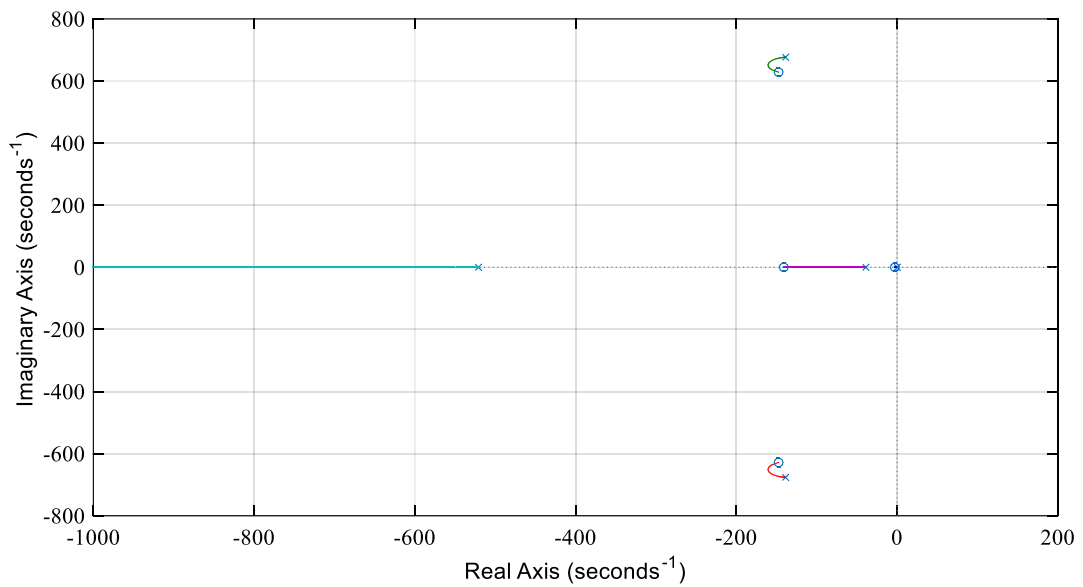
(b)

Figure 8.6 Root locus for the systems in (a) Boost mode (b) Buck mode.

At this point, the stability of the system after adding the controller is still a concern. In order to guarantee safe operation, the stability of the system in both operation modes shall be investigated. The root locii for the system in the boost and buck modes are traced as depicted in Figure 8.6 (a) and (b), respectively. It can be seen that the poles are in the left hand side plane, which implies the stable operation of the system.
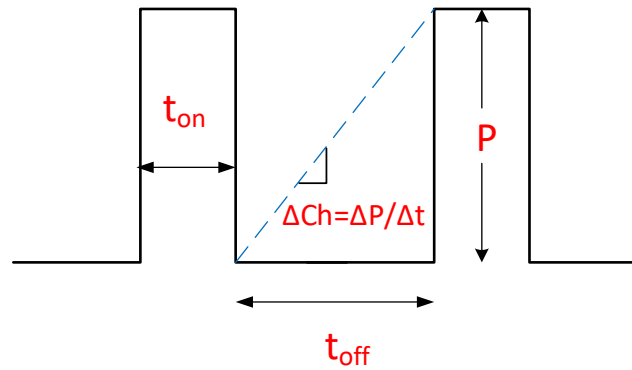
Figure 8.7 Generic pulsed load profile.

8.4 FESS Parameters Selection

The previous sections covered the modelling, design and control of the FESS. This section discusses the selection of the FESS speed and rate of charge to meet the requirements of a certain pulsed load. In this work, the author is presenting a simple formula to select the optimum speed for the flywheel based on the pulsed load parameters. Flywheel speed selection is very crucial since overestimating the speed may involve unnecessary expenses and design complications. On the other hand, underestimating the speed may cause premature discharging of the flywheel and energy insufficiency to mitigate the pulsed load.

Given the generic pulsed load profile shown in Figure 8.7, the amplitude of the power pulse is P, the period of the pulse is t_{on} and the span between any two consecutive pulses is t_{off}. It is required to calculate the minimum safe speed of the

flywheel to mitigate such a load. The stored energy in the flywheel is:

$$E_{fw} = \frac{1}{2}.J.\omega_{fw}^2 \tag{8-21}$$

Where ω_{fw} and J are the flywheel speed and moment of inertia, respectively. The amount of energy needed to mitigate a pulsed load (area under the curve) as shown in Figure 8.7 is:

$$E_{Pul} = (1/\eta_{dis}).P.t_{on} \tag{8-22}$$

Where η_{dis} is the discharging efficiency. One of the disadvantages of the flywheel is the high self-discharging rate (σ), so it will be considered in any calculations. It is worth mentioning that the self-discharge rate is dependent on the mechanical friction and type of the used bearings. This is the reason why magnetic bearing is preferred with high speed machines. Equating both energies yields:

$$(1-\sigma).\frac{1}{2}.J.\omega_{fw}^2 = (1/\eta_{dis}).P.t_{on} \tag{8-23}$$

Then the minimum flywheel speed can be calculated as:

$$\omega_{fw} = \sqrt{\frac{2.P.t_{on}}{\eta_{dis}.J.(1-\sigma)}} \tag{8-24}$$

At the instance of the coming pulse, the flywheel has to be fully charged (i.e. when the pulse starts the flywheel is at 100% SoC). In order to achieve this a rate of charging, acceleration (Δ_{ch}) should be selected and embedded in the controller design. The amount of energy injected to the flywheel during t_{off} is given as:

$$E_{fw} = \frac{1}{2}.J.(\omega_{fw}^2 - \omega_0^2).\eta_{ch} \tag{8-25}$$

where ω_0 is the flywheel speed before the acceleration (at the end of the previous pulse) and η_{ch} is the charging efficiency. Thus, the machine should be accelerated with this rate:

$$\Delta_{ch} = \frac{\omega_{fw}}{t_{off}} = \left(\frac{1}{t_{off}}\right) \cdot \sqrt{\frac{2.P.t_{on}}{\eta_{ch}.J} + \omega_0^2} \tag{8-26}$$

In the case of random (non-uniform) pulsed loads, it is possible to change the charging rate dynamically based on the changed parameters and characteristics of the pulsed load profile. It is important to select the adequate charging rate for the flywheel to avoid premature occurrence of the pulse at an early point where the flywheel is not completely charged, while, charging the flywheel with high rate (quickly) can cause unnecessary high currents, which can cause fluctuations.
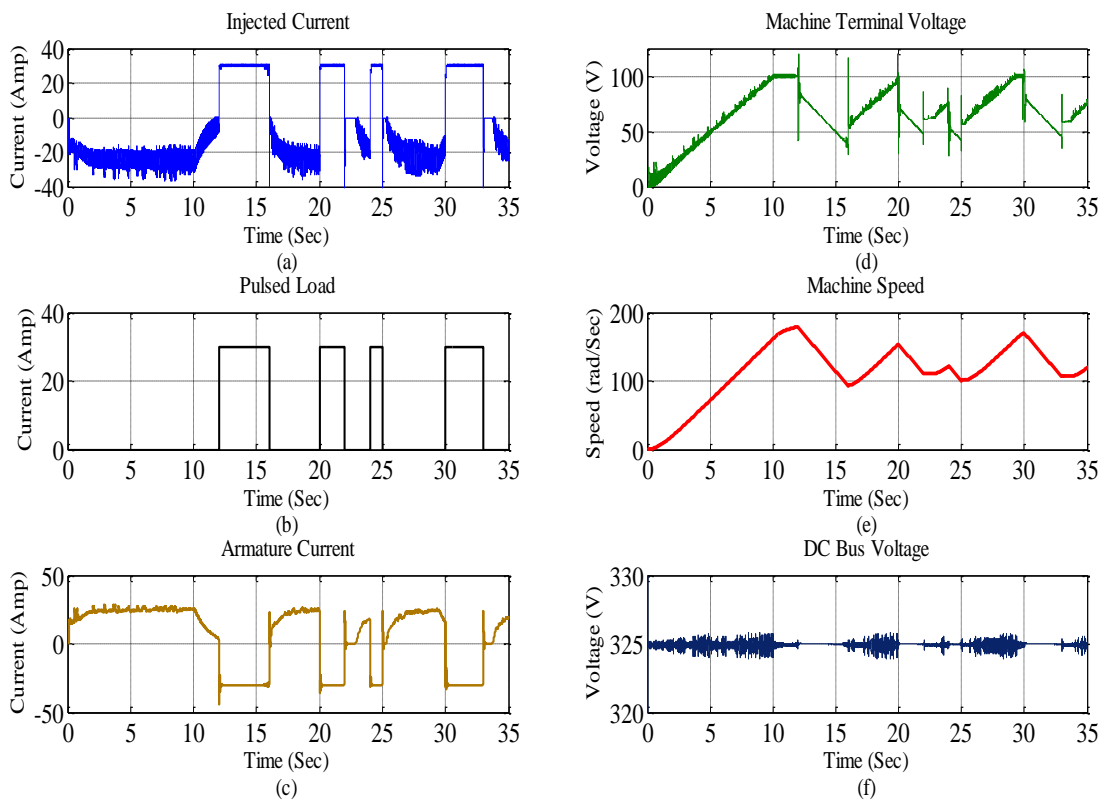
Figure 8.8 FESS operation under pulsed load.

8.5 Case Studies and Discussion

A model for a DC distribution network with a pulsed load and the proposed FESS is built in Matlab/Simulink environment. The flywheel inertia (J) is taken as 0.75 kg.m^2. For more realistic testing, the performance of the FESS is investigated through two

case studies. In the first, a purely square wave pulsed load is used, while in the second case a distorted one is applied.

8.5.1   Case I: Purely Square Wave Pulsed Load

The simulation results are shown in Figure 8.8. The pulsed load profile is as shown in Figure 8.8 (b). In this case, the duty cycle of the pulsed load varies (i.e. non-uniform pulsed load profile) and its amplitude is 30 A. The injected current to/from the DC bus is shown in Figure 8.8 (a). It can be seen that during the pulse, the injected current perfectly follows the pulsed shape to fulfill the energy gap and meet the pulse load requirements. This is due to the fast yet stable response of the controller. The injected current is steady around the 30 A level, which is the amplitude of the pulse.

When the pulsed load is off the machine charges, which is denoted by a negative current in Figure 8.8 (a). The machine terminal voltage and speed are shown in Figure 8.8 (d) and (f), respectively. It can be seen that the machine is accelerating smoothly during charging and then decelerates during the load, indicating losing charge. Because of the non-uniformity of the pulse load profile, at some points, the span between any two consequent pulses is very short. Thus, the next pulse occurs while the FESS is not completely charged. The FESS can flexibly react to this situation and switch seamlessly from charging to discharging without any interruptions. Minor spikes are detected in the machine voltage during charging. This is because a high current is withdrawn during the build-up of the counter emf. This is reflected as fluctuations in the DC bus voltage. However, these fluctuations are less than 0.5 %, which is acceptable by the standards [127]. On the other hand, there's no fluctuations during the pulse, which indicates complete mitigation of the pulsed load. The armature current is shown in Figure 8.8 (c), which is the reverse of the current shown in Figure 8.8 (a).
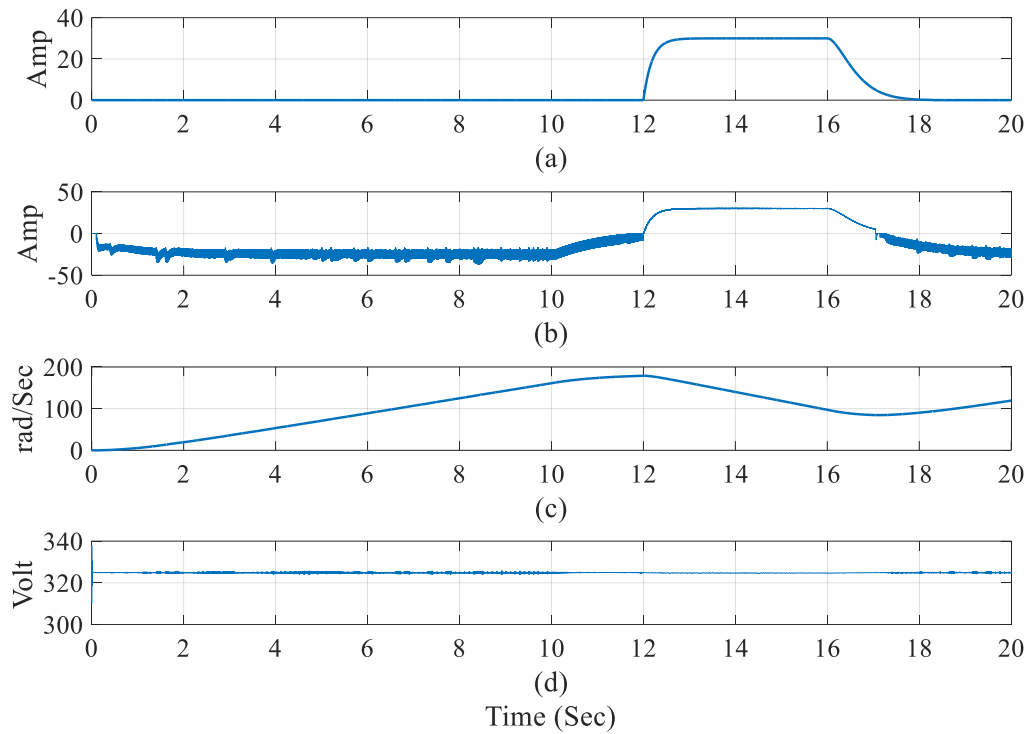
Figure 8.9 FESS performance under distorted pulsed load (a) Load current (b) Machine current (c) Machine speed (d) Bus voltage.

8.5.2   Case II: Distorted Pulsed Load

Although most of the pulsed loads have a nearly pure square waveform [245], [344], in some real world scenarios they may exhibit a distorted shape. In order to achieve a broader investigation for the FESS performance, a pulsed load with a distorted waveform is simulated and applied to the system. The results are depicted in Figure 8.9 and the load profile is shown in Figure 8.9 (a). The machine current and speed are shown in Figure 8.9 (b) and (c), respectively. From Figure 8.9 (d), it can be seen that the FESS is still compensating the load efficiently while preventing any fluctuations on the DC bus voltage.

8.6   Hardware Implementation and Experimental Results

The developed design for the FESS was implemented as shown in Figure 8.10. The current flowing in the system is measured at four points I1, I2, I3 and I4. The DC bus

and machine voltages are measured. The machine is coupled to a 12 in. diameter steel disc as the rotating mass. The weight of the steel disc is 63 Kg Approximately. Figure 8.11 shows a block diagram for the implemented hardware setup implemented in Energy Systems Research Laboratory (ESRL). It can be seen that the flywheel is interfaced to the DC bus though the developed converter. The pulsed load is implemented using a large resistive load bank which is switched using a 40 Amp contactor manufactured by GE. Figure 8.12 depicts the flywheel. The used DC machine is separately excited.
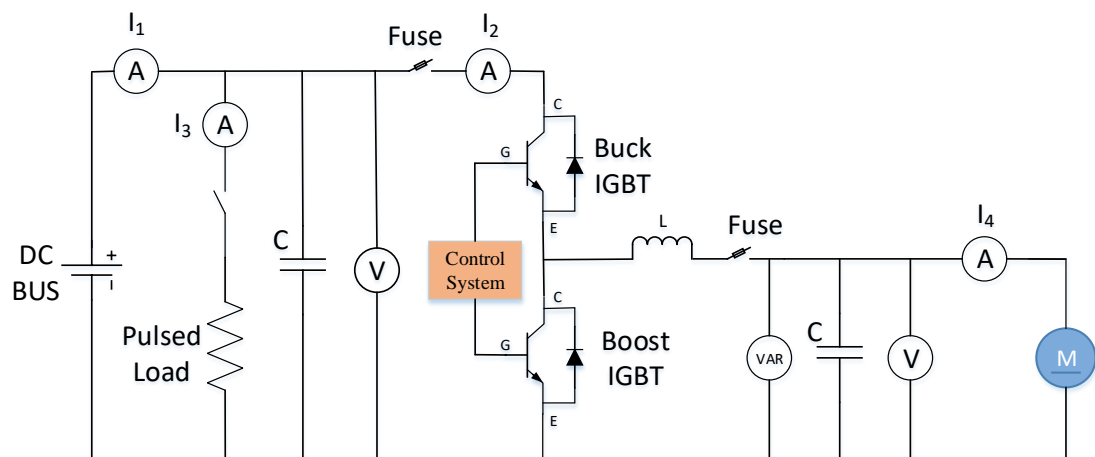
Figure 8.10 Hardware implementation of the FESS.

The converter was designed and implemented in a modular manner for ease of assembly, diagnostics and maintenance. The details of the implemented converter are shown in Figure 8.13. Two fast IGBT modules with anti-parallel diodes were used, the module part number is HGTG30N60C3D. The converter was implemented in two main separable parts as shown in Figure 8.13 (c). The first one is the main board to carry the power components. The second comprises the control, protection and the driving circuits. Different protection functions were provided to disable the IGBT gate signals and protect the system. These functions are loss of field, over voltage, over current and IGBT driver error. Four LEDS are used to indicate the type of fault as shown in

Figure 8.13 (d). A varistor was connected at the converter side connected to the machine terminals to protect the machine against over-voltages. The system control was implemented using dSPACE 1104. The switching frequency was 10 kHz.
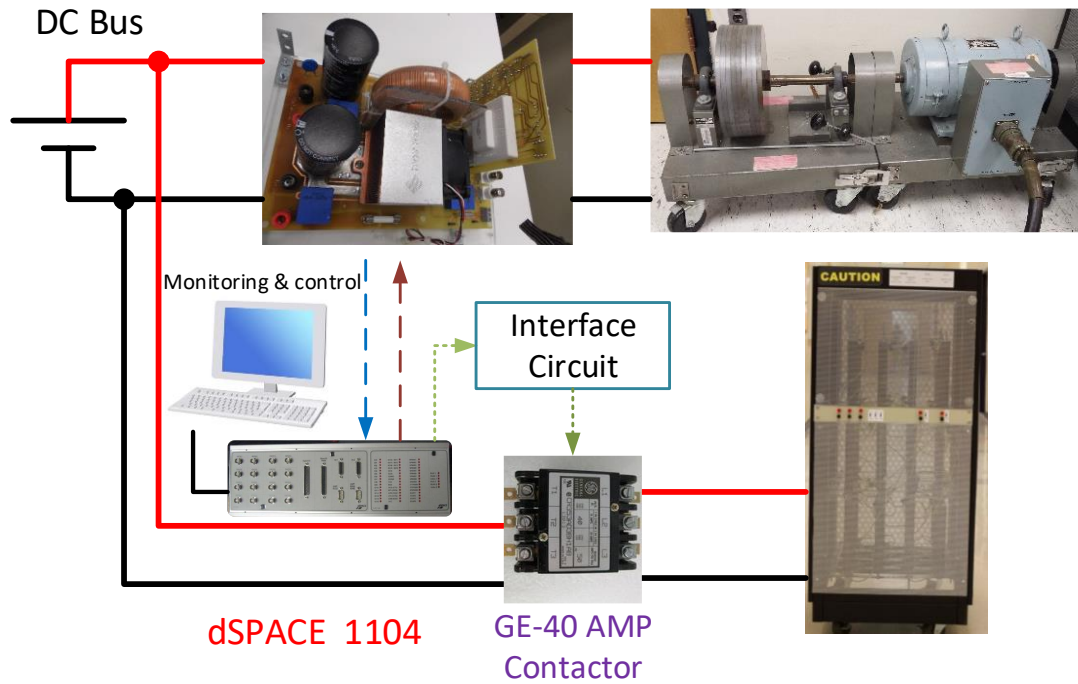
Figure 8.11 Experimental setup.
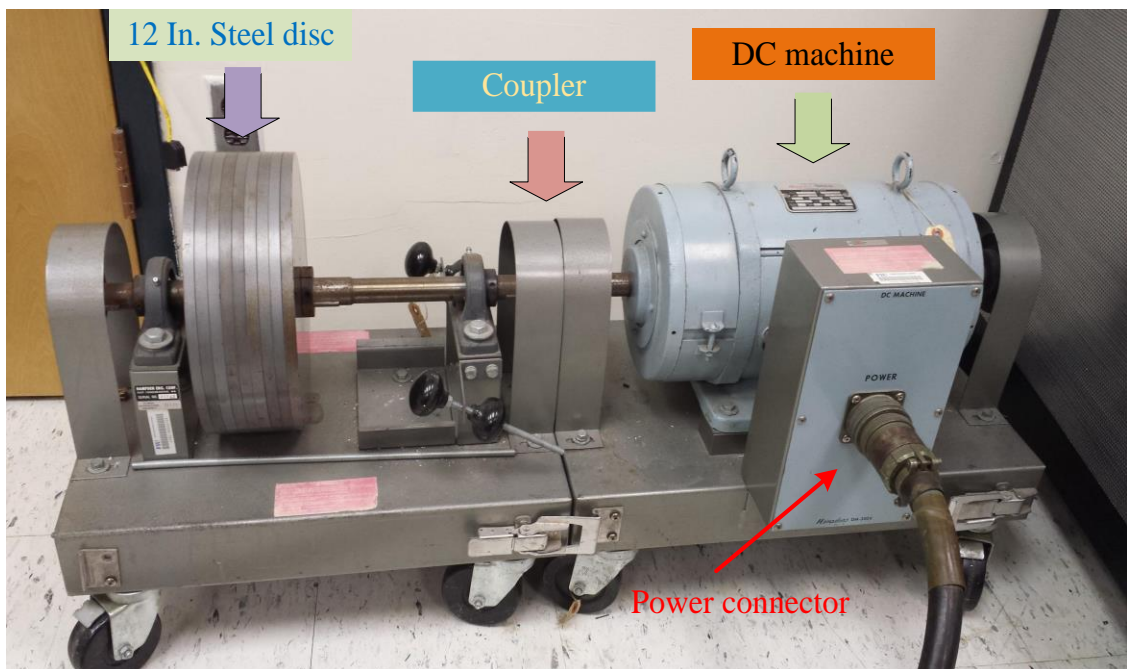
Figure 8.12 DC machine based flywheel.
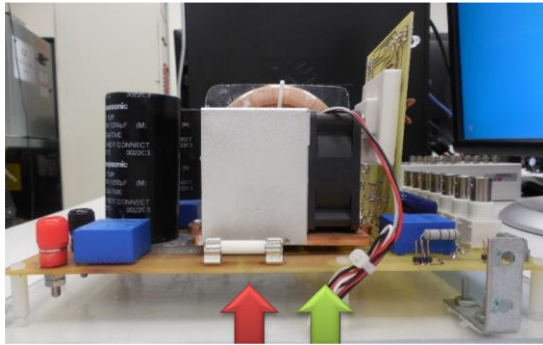
Two IGBTs under a heat sink for thermal stability.

(a)

12.7 mH inductor
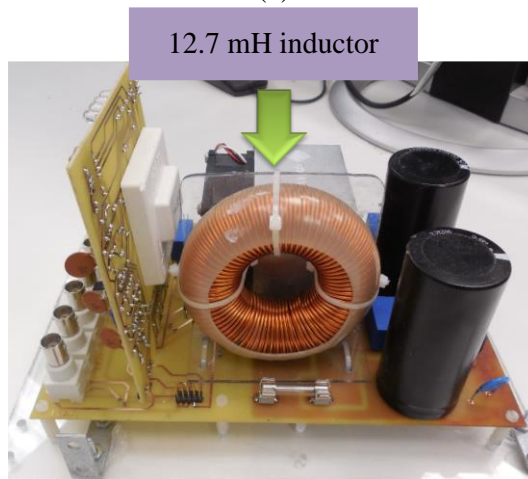
(b)

Input and output capacitors to minimize DC voltage ripples.
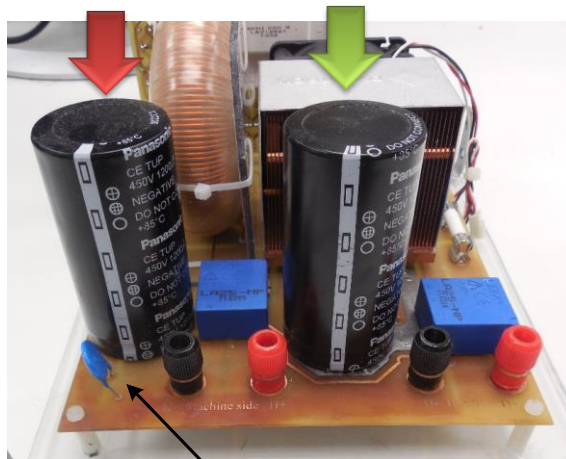
125 Volt rated Varistor to protect the machine against over voltage.

(c)
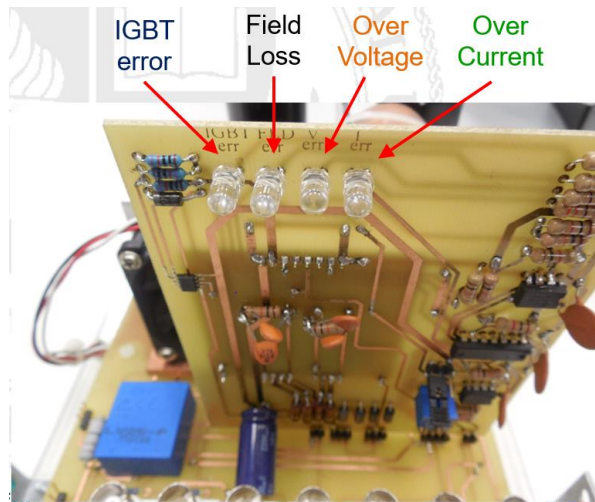
(d)

Figure 8.13 Details of the implemented driving converter.

The used driver is SKHI 22AR manufactured by SEMIKRON. This driver is capable of driving to IGBTs. Therefore, only one module is used, the circuit diagram of the driver is shown in figure 8.14.

In order to examine the effectiveness of the developed system, the system will be tested under a heavy pulsed load (11.5 Amps at 318 DCV). Figure 8.14 depicts the system results without the flywheel. It can be seen that under the pulsed load, the bus voltage drops to around 297.5 V (93.5%), violating the limits specified by the standards (indicated by red dashed lines). It should be noted that the allowed range for voltage variation is ±5%. This can result in disconnection of critical loads or underperformance of some other loads in the system.

The FESS is connected to mitigate the effect of the pulsed load and share the load with the supply to fill the energy deficit. The experiment was performed under the same load conditions. The experimental results are depicted in Figure 8.15. It can be seen that the pulsed load current is shared between the DC bus and the FESS. Thus, the FESS clipped the pulsed load current to limit the loading on the DC bus and maintain the voltage. Also, the machine charging current is shown on the bus current, but with a

reversed sign as the current direction is reversed. The pulsed load current (I_3) is the algebraic sum of the DC bus current (I_1) and the machine current (I_2). Since the voltage at the machine side is less than the DC bus side (one third of the DC bus voltage), the current in the machine side of the converter is around three times that of the DC bus side (i.e. $I_4 \approx 3*I_2$).
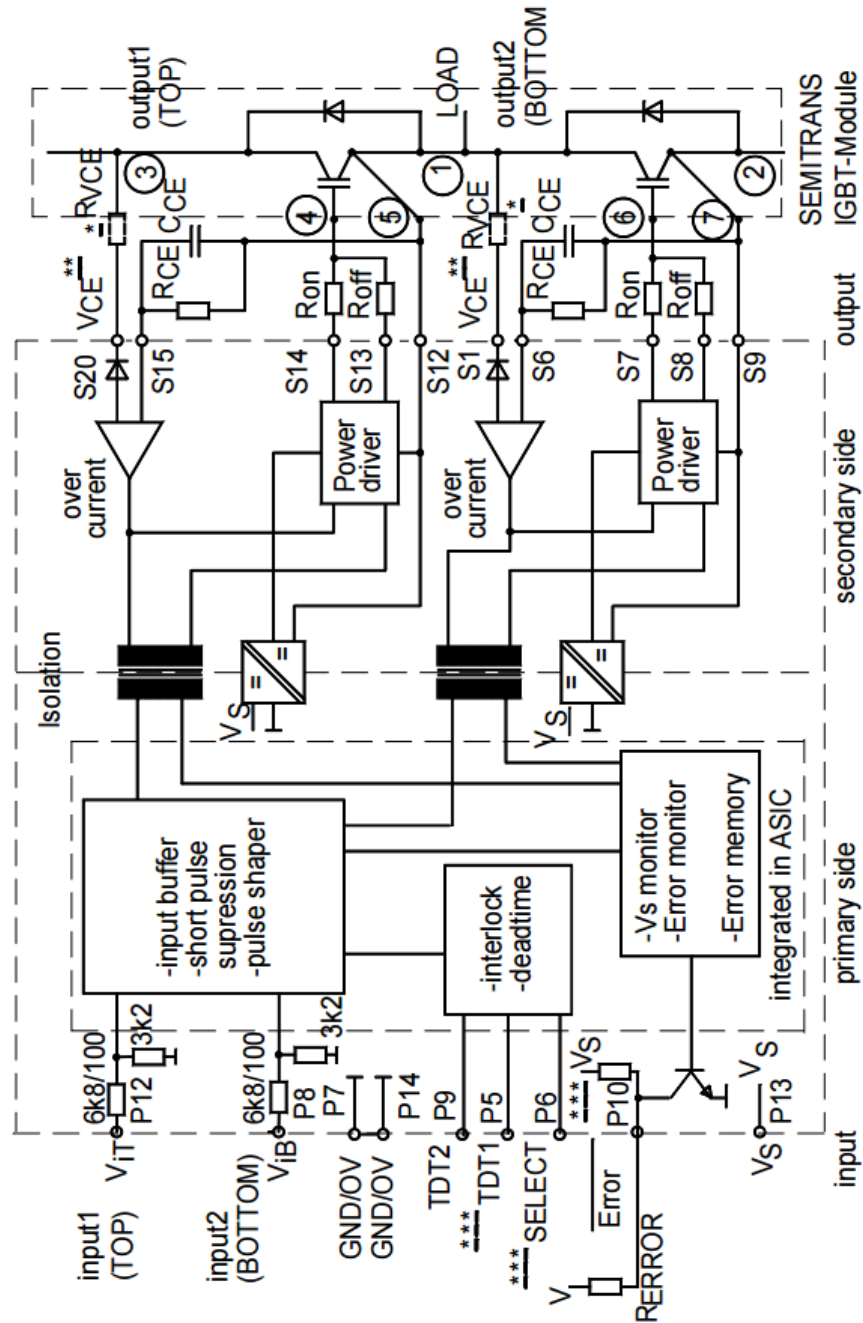
Figure 8.14 Dual IGBT driver circuit.
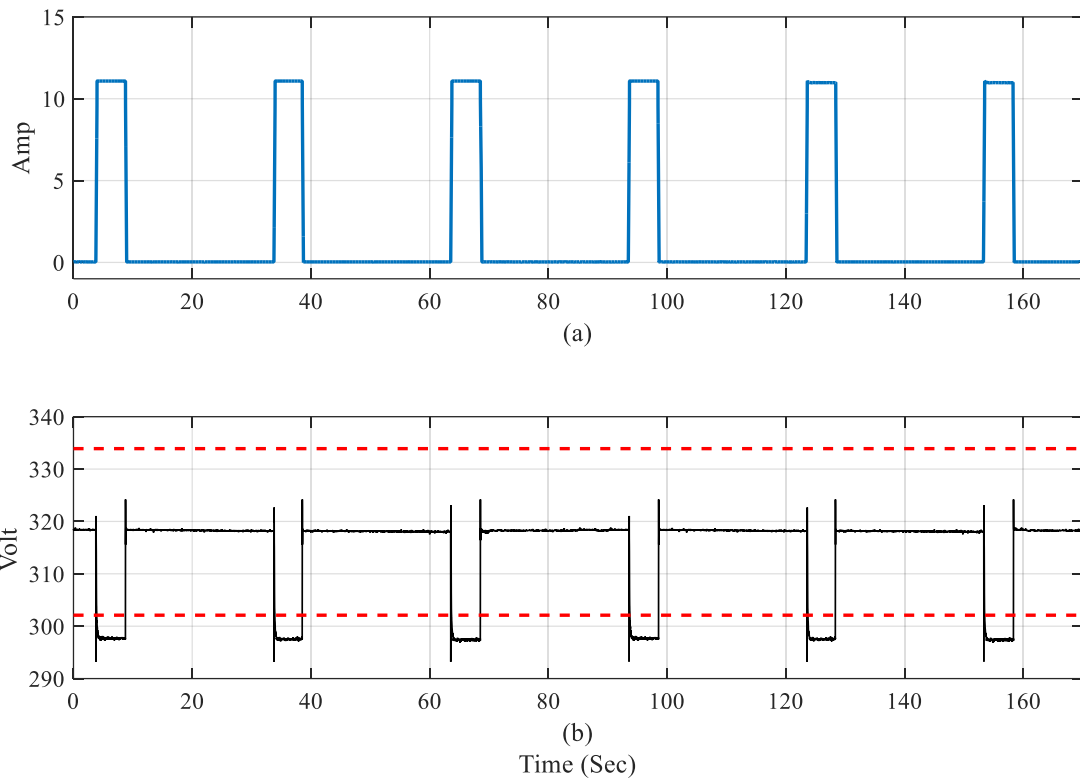
Figure 8.15 System performance without FESS (a) pulsed load profile (b) DC bus voltage.

It is shown that the machine voltage is increasing gradually, indicating smooth charging of the flywheel. The charging current of the machine is increasing smoothly as well, without large spikes. Then, the voltage is constant around the reference value, which is 85 Volts. Finally, the DC bus voltage is shown in Figure 8.15 (f). Some high frequency fluctuations are detected due to the charging and discharging of the machine and switching actions. However, the magnitude of these voltage spikes are well below allowed limits by the standards (the limits are shown with the red dashed lines). Thus, the effectiveness of the developed system is proven. The effect of the pulsed load didn't propagate to the DC bus, which allows adding more critical loads to the DC bus without being concerned with the impacts of the pulsed load.
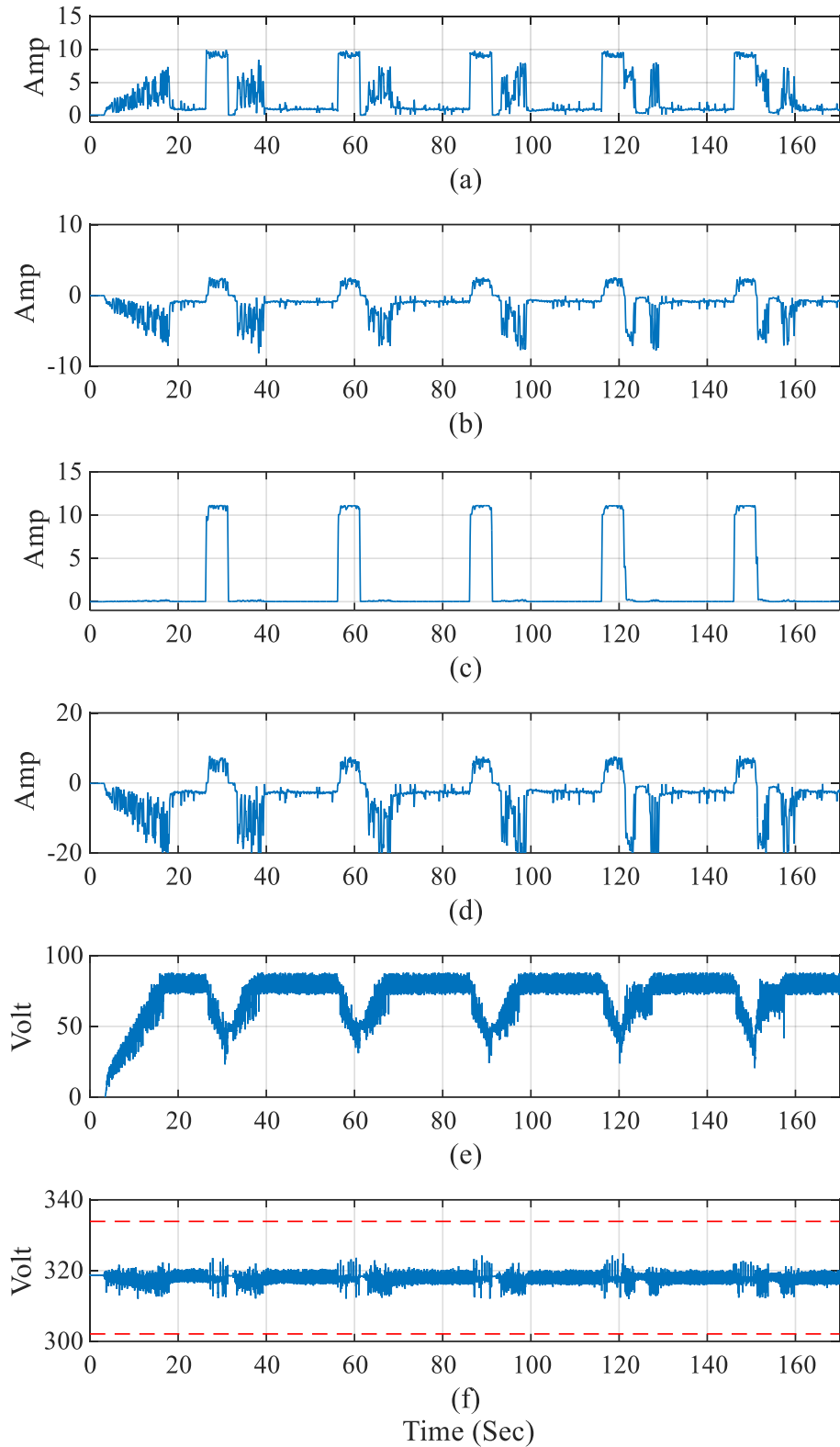
Figure 8.16 Experimental results showing FESS performance under pulsed load.

(a) Bus current (I1). (b) Converter current-bus side (I2). (c) Pulsed load current (I3). (d) Converter current-machine side (I4). (e) Machine voltage. (f) DC bus voltage.

8.7 Summary

Flywheel is providing a suitable and feasible solution for short term energy storage. It has been used widely in industry. There's a large flywheel that is installed in Cisco data center in Texas. There's another one that is installed in a large electronic manufacturing facility in Germany. Moreover, it is used in spaceships, ship power systems, data centers, grid frequency regulation, electrification of rural areas, electric vehicles and electric buses. In low speed flywheels, DFI and DC machines can be used. Both are using mechanical contacts for rotor connection, which is acceptable in such applications. This chapter presented an improved modeling and control method for a DC machine based low speed FESS. The DC machine can offer more advantages including lower cost, simplicity and wider speed range. This wide operation range allows more utilization of the stored kinetic energy. The machine model was integrated to the converter model. A state space model was obtained for the entire system as a single entity. The model was validated through a comparison with another estimated model. Based on the obtained model, accurate tuning of the PI controllers was achieved. An efficient performance was shown through simulation results under heavy pulsed load with non-uniform profile. The proposed design was validated through hardware setup and the experimental results aligned with the simulation. It was shown through laboratory hardware setup that the FESS is effectively mitigating the pulsed load.

Chapter 9   Hierarchical Control of a Cluster of DC Microgrids

9.1   Introduction

The performance of power grids have long been evaluated based on their reliability, which is measured by analyzing the frequency and duration of power outages [345], [346]. Power system planners/operators have succeeded over the years to shorten the restoration time, and minimize the impacts of relatively high-probability low-impact outages, leading to a high reliability index. However, the recent spate of severe storms has clearly shown that reliable distribution grids are not necessarily resilient against high-impact low probability catastrophic events. Grid resilience, in the context of this paper, refers to the ability of the grid to withstand and recover from incidents/accidents that can lead to a widespread blackout. A resilient distribution grid shall be able to supply, at least, its critical loads during blackouts.

Microgrids are the key solution to achieve increased grid resilience [347]. According to the U.S. Department of Energy, a microgrid is "a group of interconnected loads and distributed energy resources (DERs) with clearly defined electrical boundaries that acts as a single controllable entity with respect to the electric utility grid." A microgrid can be connected to the grid, in a grid-connected mode, or independent from the grid, in an islanded mode. Operation and control of microgrids have lately received genuine attention in the literature.

In the previous chapters, the design and planning of the distribution architecture are investigated. The control of the different energy storage components, which is done on the local level, is studied. This chapter is presenting a higher level control strategy for a cluster of microgids. This comes as an integration to the previously presented planning and local control studies to realize this dissertation as a comprehensive work.

In this chapter, a real-time tertiary control algorithm for DC microgrids will be developed and implemented. Tertiary control, in the context of this work, refers to the control layer that transcends the boundaries of a single microgrid, and hence supervises a group of microgrid central controllers (MGCC). Each of the individual microgrid resources, and controllable loads, needs a controller. These localized controllers are referred to as local or resource controllers (LC), and collectively represent a primary control layer. In addition, an MGCC is needed to act as a coordinator/supervisor to the LCs forming the secondary control layer. The speed and bandwidth requirements significantly vary between the primary and secondary layers [348]. For instance, a controlled unidirectional DC-DC converter that interfaces a photovoltaic (PV) system to the dc bus of a microgrid would require an LC that receives current and voltage feedback signals, and runs algorithms to track the maximum power point (MPP) of the PV system. This tracking process typically repeats several thousand times per second. Likewise, a battery bidirectional DC-DC converter (charger) needs a fast controller to read its terminal voltage and current in order to control its charging/discharging level.

An MGCC needs only to communicate more abstract parameters with LCs and convey power/voltage set points, e.g. receives the output power of the PV system, the battery state of charge (SoC), the amount of power shared with the grid, etc., and yields higher-level commands (set points) for the battery charger and inverter. The MGCC control actions are slower than those of the LCs, and are typically in the "seconds" to "minutes" time range. While LCs and MGCCs operate within a single microgrid, coordination of multiple microgrids within a close electrical proximity may be required, especially at high penetration levels of DERs and Electric Vehicles (EVs). This mandates forming a tertiary control that supervises the MGCCs [349]. The tertiary controller could possibly by a third party private entity, or the utility distribution

company. Most of the research on microgrid control has been centered around primary and control layers, with minimal focus, if any, on the design and implementation of tertiary control.

In this work, a tertiary control algorithm for hybrid power systems involving distributed microgrids is introduced. The main aim of this control algorithm is to make best use of the available energy assets in the DC microgrids to improve the power quality and/or solve operational issues on the main AC network, without compromising the performance of the individual microgrids. This is done by efficiently managing the power flow in the network, and continuously monitoring its parameters. For instance, if one of the buses of the distribution feeder encounters an under-voltage condition and requires reactive power compensation, one or more of the microgrids can supply the needed reactive power if they happen to have surplus energy. Furthermore, the developed control algorithm enables microgrids to virtually exchange power through the utility grid infrastructure. The proposed algorithm was examined experimentally under some operational scenarios.

Therefore, the main contributions of the work presented in this chapter can be summarized as follows: 1) a tertiary DC microgrid control algorithm will be developed; 2) detailed hardware based testing will be used to verify the proposed algorithm; 3) the paper will investigate the usage of microgrids for ancillary service provision to the utility grid.

9.2 Real-time control and operation

The proposed real-time control framework is structured in a decentralized hierarchical architecture; each microgrid has its own MGCC. The various microgrids are supervised by the proposed regional tertiary controller. Hence, the energy within each microgrid as well as the energy transfer with the main AC grid is controlled via

the MGCC, which continuously communicates with the microgrid LCs as well as the main SCADA system of the main AC grid. This structure can achieve economic benefits especially in the de-regulated markets. A detailed flow chart of the proposed control algorithm is shown in Figure 9.1.

The controller is designed to operate in real time aiming at addressing reliability and resilience issues. Specifically, the tertiary controller maintains continuity of power supply during emergencies to increase the power system survivability. As an example, a distribution system including two microgrids connected to the main grid, will be used as a case study. An overview of the proposed controller design and implementation, including some of the ancillary services that the microgrids can provide to the main grid, are described herein.

9.2.1 Reactive power compensation service

The tertiary controller continuously monitors the state of the system. It measures the voltage magnitude and –possibly- angle i.e. if micro synchrophasor measurements are available at the distribution level, at each bus and detect any voltage violation. If any of the voltages goes below or exceeds pre-specified limits, chosen in this work as 0.9 p.u. and 1.1 p.u., respectively, the controller will seek reactive power compensation from the connected microgrids. This process has to be done without violating the voltage limits at other buses or the P-Q limits of the inverter [282]. Thus, the required Q values are calculated by solving an optimization problem using genetic algorithm (GA). The objective of this optimization problem is to yield the amount of reactive power required from each of the microgrids such that the total amount of Q received collectively from all microgrids is minimized. Therefore, each individual of the population represents a trial solution to the problem of minimizing the value of the fitness function.
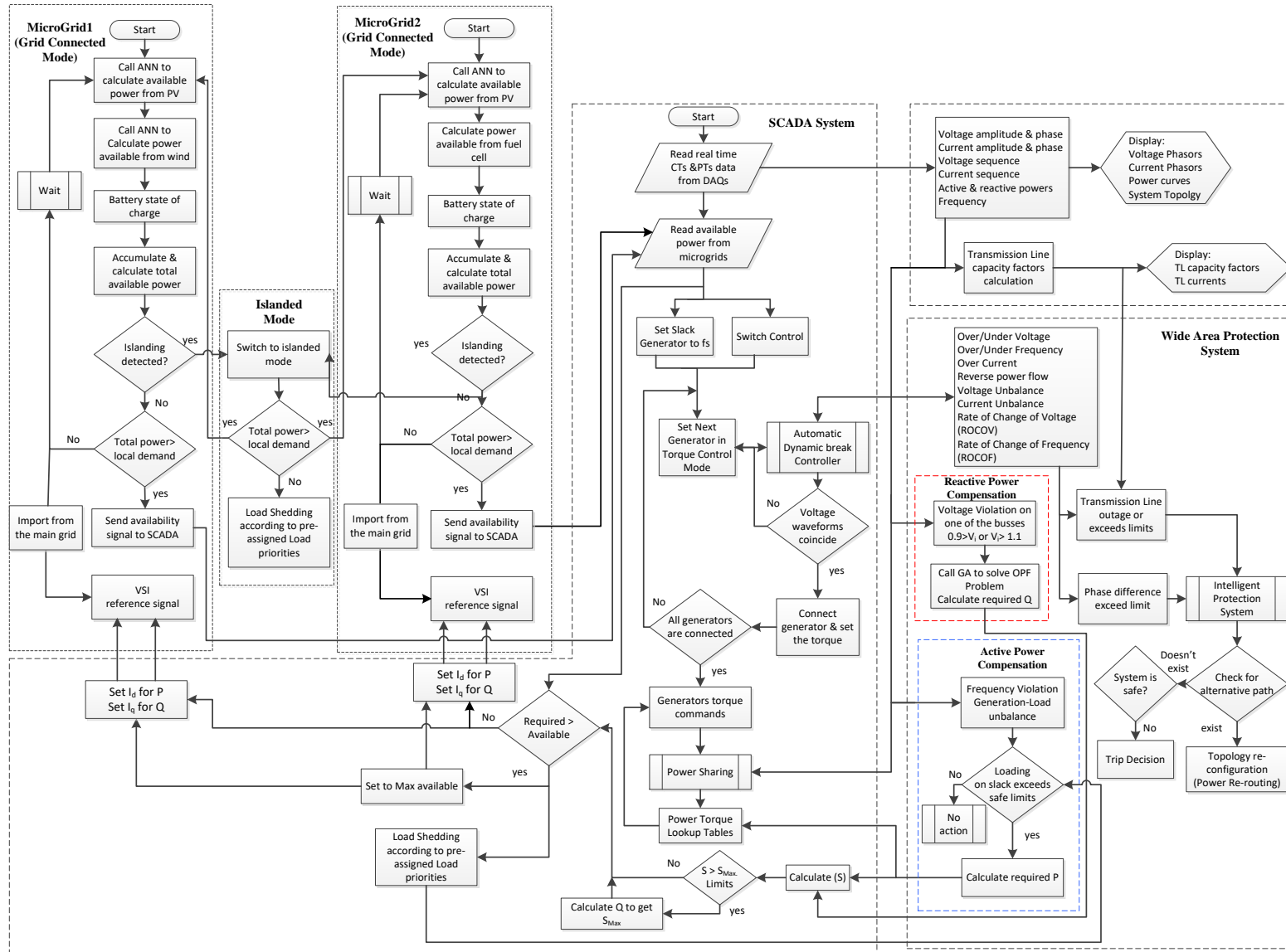
Figure 9.1 Flow chart of the proposed tertiary control algorithm.

The formulation of the optimization problem for an example system with n microgrids is given as the following.

$$F(Q_1,...,Q_n) = \min\left(\sum_{x=1}^{n}Q_x\right)^2 \tag{9-1}$$

where n is the total number of microgrids and Q_x is the amount of reactive power injected by microgrid x.

S. t.

$$\begin{cases} 0.9 < V_i \pounds 1.1 \\ I_{ij} \pounds I_{ij\_th} \\ Q_x < Q_{x,max} \end{cases} \tag{9-2}$$

Where V_i is the voltage at bus i, I_{ij} is the current of the transmission line tying busses i and j, I_{ij_th} is the thermal capacity of transmission line ij, $Q_{x,max}$ is the maximum instantaneous reactive that can be injected from microgrid x. This upper limit is mainly determined by the fixed apparent power capacity of each inverter and the instantaneous real power generation P. This limit is calculated every 6 minutes according to the following equation.

$$Q_{x,max} \leq \sqrt{S_{x\_max}^2 - P_x^2} \tag{9-3}$$

9.2.2 Active power Compensation

At high penetration levels of DERs and microgrids, e.g. if DERs represent as high as 50 % of the total generation, there will be less apparent total headroom available from conventional generation for primary or governor response, and for automated generation control or secondary response. This lack of inertia can cause frequency variations, and may disturb the stability of the system during sudden load or generation fluctuations. In order to overcome the lack of inertia problem, microgrids distributed

over geographically-dispersed areas may be virtually aggregated to form a virtual power plant (VPP) under the control of the developed tertiary controller and offer ancillary and spinning reserve-like services to the utility grid. In the developed control system, the controller continuously monitors the frequency of the system and the percentage loading of the slack generator. If the frequency oscillation persists or exceeds specified limits by IEEE-Std 1547 [126] and the loading of the slack generator exceeds the pre-defined safe limits, the SCADA systems calculates the minimum required active power to re-balance the system. Then, as shown in the flow chart (Figure 9.1), the main controller communicates with the microgrids' controllers to get information about the available active power in each one. After getting the information, the main controller decides the amount required from each microgrid based on the available amount in each microgrid. In this work, the controller simply divides the total needed amount among the microgrids with a ratio proportional to the ratio of their available power. An illustrative numerical example is put in order here. If the available active power from two microgrids MG1 and MG2 are 100W and 200W, respectively and the total required amount is 150 W, then, 50W and 100W will be requested from MG1 and MG2, respectively. Based on the relation between the total required amount and the available amount from the microgrids, "If…else" cases are defined to handle irregular situations. In some cases, if the aforementioned ratio does not meet the required power by the system or the requested power is close to the total available power in both microgrids, then the output power of (MG2) is set to the maximum available amount. If the required amount is still not met yet, the controller requests to set the output power of (MG2) to its maximum. If both microgrids reach their maximum available and the power balance is not achieved, then load shedding is inevitable. The loads are shed according to a pre-assigned priority indexes according to their

importance. The controller will start shedding the loads with lower priority indexes first.

The local controller of each microgrid calculates the available power that can be transferred to the AC system based on the weather conditions and the forecasted local loads. An Adaptive Artificial Neural Network (AANN) is called by the controller to forecast the next hour values for the wind speed, solar irradiance and load, based on the historical data. Then by projecting the forecasted wind speed and the solar irradiance to the characteristics of the used PV module and wind turbine the available power can be estimated.

9.2.3 Islanded mode

The control algorithm is designed to enable the DC microgrid to operate cooperatively with the grid while it is in the grid connected mode. In addition, the SCADA has the capability to detect islanding and enable the microgrid to continue operation while supplying its local loads. During normal operation, the microgrid inverter is synchronized with the utility voltage using Phase Locked Loop (PLL). During the islanding mode, the PLL loop loses the frequency reference signal and the PLL internal oscillator frequency starts to drift from the fundamental frequency. By implementing a frequency drift detection mechanism and defining an appropriate threshold, the islanding mode can be detected from the frequency drift. The detection mechanism can trigger the control to switch to internal stable frequency reference, at the same time, it switches the control of the DC bus voltage to be handled by the DC-DC converter interfacing the PV. Moreover the trigger signal is used to reconfigure the controller to switch from power control mode to voltage control mode to regulate the AC bus voltage. In this operation mode, the microgrid operates as a slack generator to regulate the voltage and frequency [350].

9.3 Experimental platform

The proposed tertiary controller presented in this dissertation was tested on a 72 kW laboratory-based testbed setup as shown in Figure 9.2 [161], [162]. This testbed represents an intelligently-operated hybrid AC/DC power system involving distributed architectures, and computation and communication infrastructure. The architecture of the network emulates a real power system with microgrids connected to it. These microgrids can be buildings or small residential communities. The system is scaled down in terms of power and voltage.

9.3.1 Main Grid

The main AC grid consists of four self-excited AC synchronous generators, two of which are rated 13.8 kVA, while the other two generators are rated 10.4 kVA. These generators are driven by different types of motors acting as prime movers. The generators are rated 208 V, 60 Hz and 1800 rpm. Each generator is connected through an automatic synchronizer to its corresponding switching and measurement bus. The connectivity on the AC network is realized using various π-section transmission line/cable emulators. A total of 18 transmission line/cable emulators and 14 bus emulators were used. The bus and line modules can be flexibly used to vary the system's network architectures.

9.3.2 DC Microgrids

Two DC microgrids, namely MG1 and MG2, were connected to the main AC grid. The first DC microgrid (MG1) includes a PV source, a wind energy conversion system (WECS) and battery storage. The PV source is connected to the DC bus through a DC-DC converter. The WECS is cascaded by an uncontrolled rectifier followed by a controlled DC-DC converter. The DC bus voltage is 380 VDC [351] ,[352]. The second DC microgrid (MG2) involves a 6 kW photovoltaic (PV) and a 6 kW fuel cell (FC)

emulators. The system includes a 12 kWh backup Lead-Acid battery array that can support load deficiencies. A 325 VDC bus is used to integrate the PV, FC and battery energy to the system. Controlled DC-DC boost converters are used as power conditioning units between each of these sources and the DC bus. A 4 kW PWM fully controlled bi-directional AC-DC/DC-AC converter (i.e. smart voltage source inverter (VSI)) was used to tie each DC network to the AC grid. Each converter has the ability of controlling the amount of active/reactive power flowing between the AC and DC grid in both directions. Further, it is responsible for voltage regulation on the DC side in grid connected mode, while in islanded mode, the local controller switches the voltage regulation to one of the DC-DC converters interfacing the PV system. This VSI has the capability of receiving reference values for active as well as reactive power and hence will play a major role in the active/reactive power compensation processes [353].

9.4 Measurement and communication infrastructure

9.4.1 Measurement inside the main AC grid

Several calibration, measurement and data acquisition units were utilized to capture real-time data of the AC system at a sampling rate of 12 kHz from about 200 measurement devices, including current transducers (CTs) and potential transducers (PTs). Four different types of national instrument data acquisition modules (DAQ) with wired and wireless communication capability were used.

9.4.2 Measurement within the Microgrids

The measurements within the DC microgrids were mainly collected using current and voltage transducers (LA55-P, LA25-NP, LV-25P). These measured voltages and currents were used to enable proper closed-loop control of converters' output currents/voltages, or used as inputs to the maximum power point tracking (MPPT) algorithms.
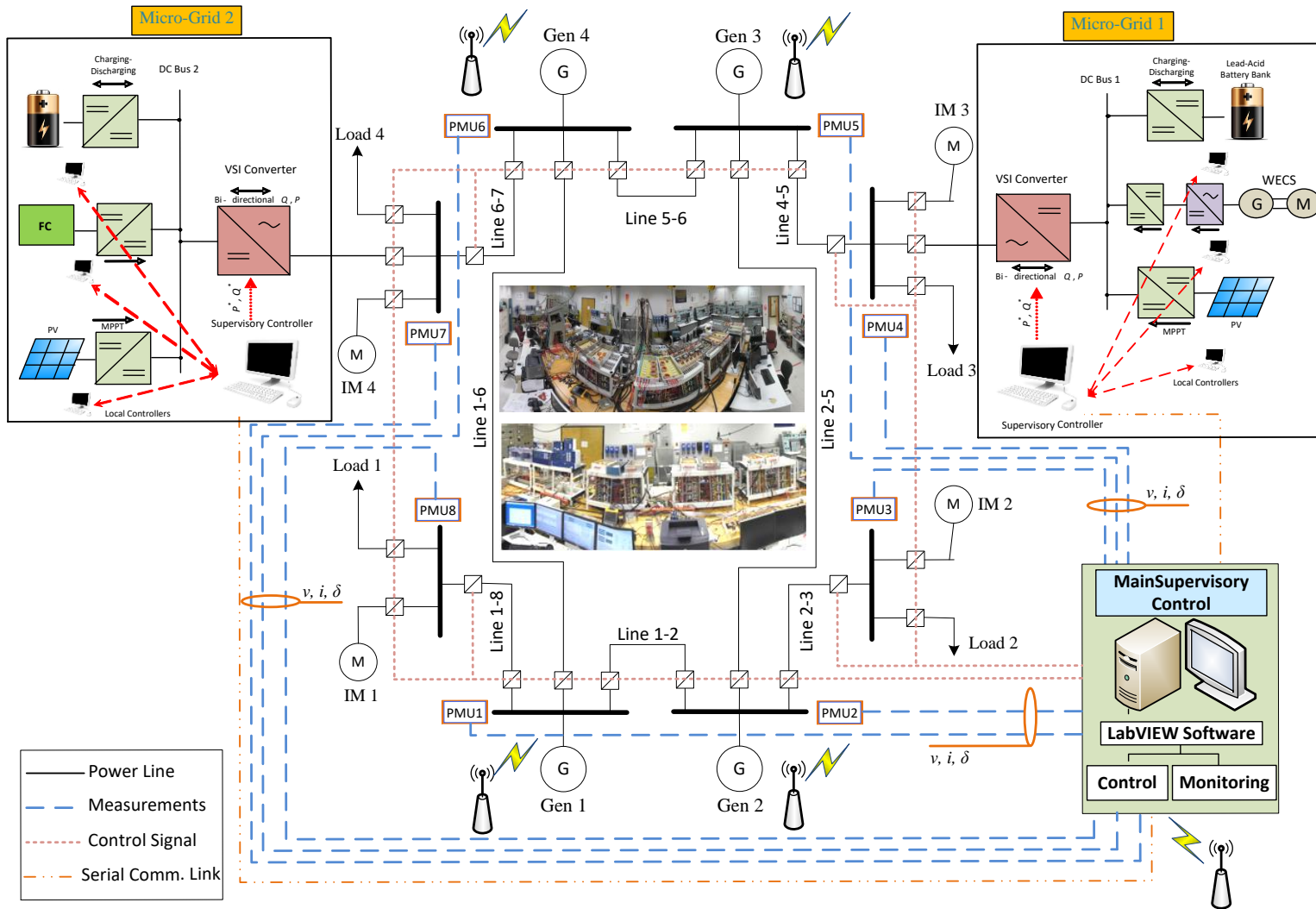
Figure 9.2 Schematic diagram for the experimental platform.

In addition, some AC measurements were collected for the voltages of the grid at the point of common coupling (PCC) for synchronization of the VSI converter and islanding detection. The grid current is measured for power flow control.

9.4.3 Communication within the Main Grid

The communication infrastructure consists of several types of communication mediums, the SCADA system collects the data from data acquisition units using Ethernet and secured Wi-Fi communication. The control commands are sent to generators and load emulators by wireless link (ZigBee). The supervisory controller exchanges the data and control command with microgrids through two serial links (RS-232).

9.4.4 Communication with the Microgrids

A local communication infrastructure was established within each DC microgrid to enable two way communications between local supervisory controller and microgrid entities. The communication infrastructure for the microgrid consists of serial links to control load and renewable energy emulators, fiber optics link to exchange the information with embedded controllers.

9.5 Results and discussion

In order to verify the validity of the proposed tertiary controller, two case studies were experimented. These case studies have been performed with realistic scenarios that are similar to actual situations and problems of real power system. The purposes of these experiments are: 1) to prove the effectiveness of the developed control algorithm and hardware infrastructure under realistic conditions, 2) to investigate the effectiveness of DC microgrids in solving power system's problems and preventing black/brown outs, and 3) to study how DC microgrids respond to certain AC system's power quality issues. In this work, the control system is tested on a system with two

microgrids, however, the control system is expandable to systems with a larger number
of microgrids.
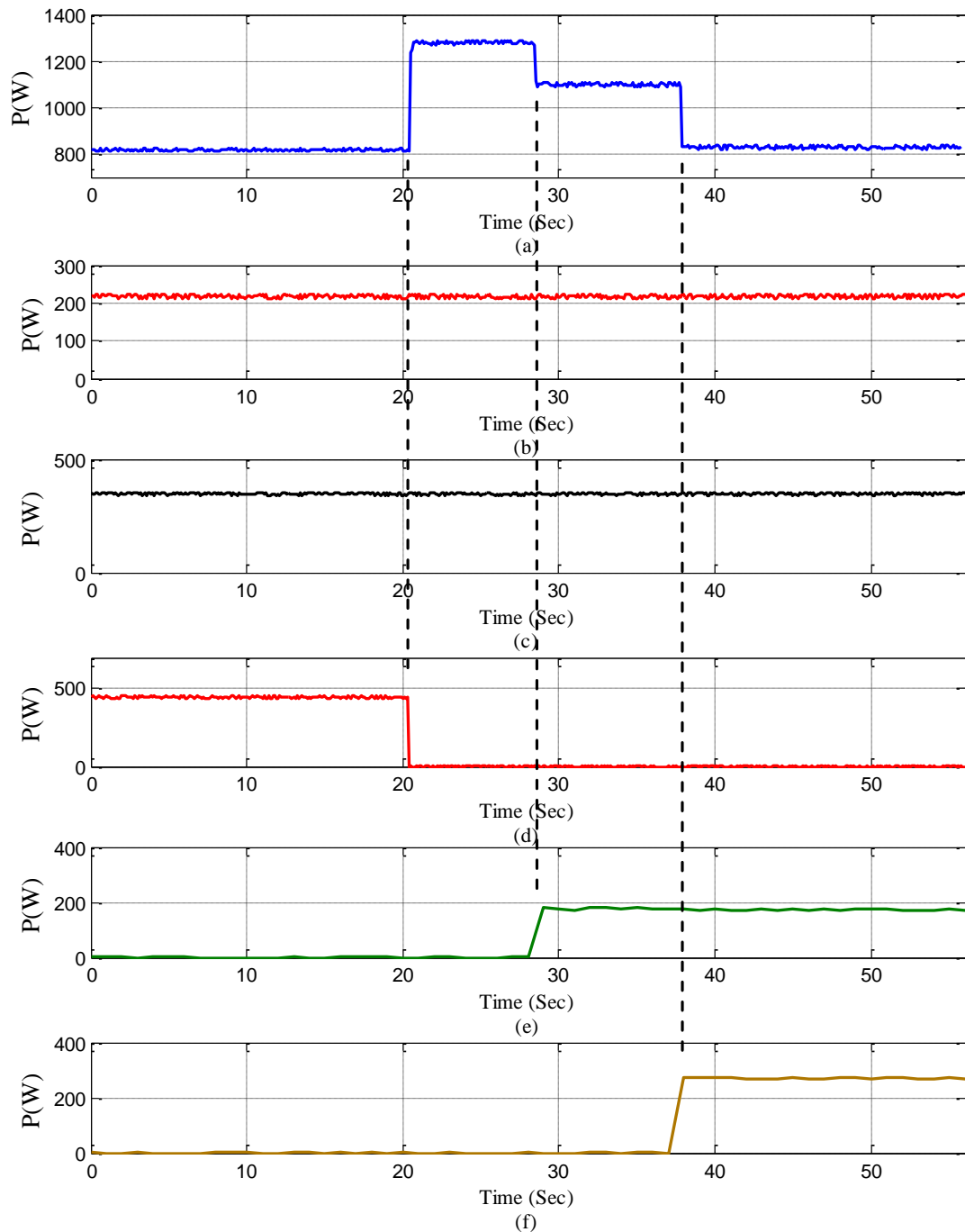
Figure 9.3 The proposed controller behavior in case of a generator outage.
(a) Output power of the slack bus. (b) Output power of generator 2. (c) Output power
of generator 3. (d) Output power of generator 2. (e) Output power of microgrid1. (f)
Output power of microgrid2.

9.5.1 Case Study 1

This case involves a scenario in which a sequence of events (failures) occur, which may eventually lead to a blackout. This study shows the response of the tertiary controller and how it acts to mitigate the effects of these failures by utilizing the available energy in the DC microgrids. In the first case study, three events are created to investigate the proposed controller behavior and how it is dealing with these conditions.

9.5.1.1 Event 1: Generator outage

As explained earlier, the system consists of four synchronous generators and two microgrids. The control of generator 1 is speed control to fix the frequency of the system at 60 Hz, and hence it acts as a slack bus, while the control of the other three generators is torque control. This means that the output power of each one of these three generators can be changed by changing the reference torque signal sent to the prime mover. Figure 9.3 depicts the active power generation of the AC generators and both microgrids during the experiment; Figure 9.3(a) through (d) are showing the output power of the four generators, Figure 9.3(e) and (f) are showing the output of microgrid 1 and microgrid 2, respectively. At the beginning, the four synchronous generators were sharing the loads; generators 1 through 4 are generating 820, 225, 400 and 440 W, respectively. The system has four AC resistive loads, namely load 1, load 2, load 3 and load 4 (as shown in Figure 9.2) with power of 600, 300, 300 and 600W, respectively. The difference between the total generated power (1885) and loads (1800) is the losses in the system, which represents 4.5% of the total generated power.

The two microgrids were supplying local loads but there is no transmitted power to the AC side. At the second 21, an outage of generator 4 occurred resulting in unbalance between the generation and load. This difference between generation and load has to

be supplied by the slack bus to regulate the frequency. Consequently, generator 1 increases its output power to settle around 1270 W. At this value, Gen 1 was overloaded. The controller sent commands to MG1&MG2 to supply the lost amount of active power due to losing generator 4 in order to help the slack generator. This amount is compared with the available amount sent by the local controller (refer to the flow chart shown in Figure 1). At this moment, the available amount was 190 W in MG1 and no excess available power to be transferred from MG2. The main controller accepts to transfer the whole amount from MG1 as shown in Figure 9.3(e), this is done by setting the value of i_d to a suitable value. However, the controller is still detecting an overload on Gen 1. After 10 seconds, MG2 sends availability signal declaring that it has available power of around 300 W. Hence, the main controller requests 250W to restore the state of the slack generator. It is worthy to mention that the time span for sending availability signals is defined as 10 seconds for experimental purposes. It can be seen that both microgrids have high flexibility and capability to supply the required active power in short time to reduce the stresses on the AC system. This seamless power flow is enhanced by the high controllability of the developed control algorithm.

9.5.1.2 Event 2: Voltage sag

Due to increase in local load or decrease in the available power from renewable energy sources, MG1 was not capable of supplying power to the AC side anymore. The lost amount of power (190 W Approx.) is being supplied by the slack bus again. Hence, the situation of the system as follows: three generators (Gen1, Gen2 and Gen3) and MG2 are sharing the loads (total of 1800W). Since, Gen 4 is still out of service, a significant portion of load 4 connected to bus 7 is met through two parallel paths; the first one is directly through line 1-6 and the other one is through line 1-2, line 2-5, line 5-6 and line 6-7.
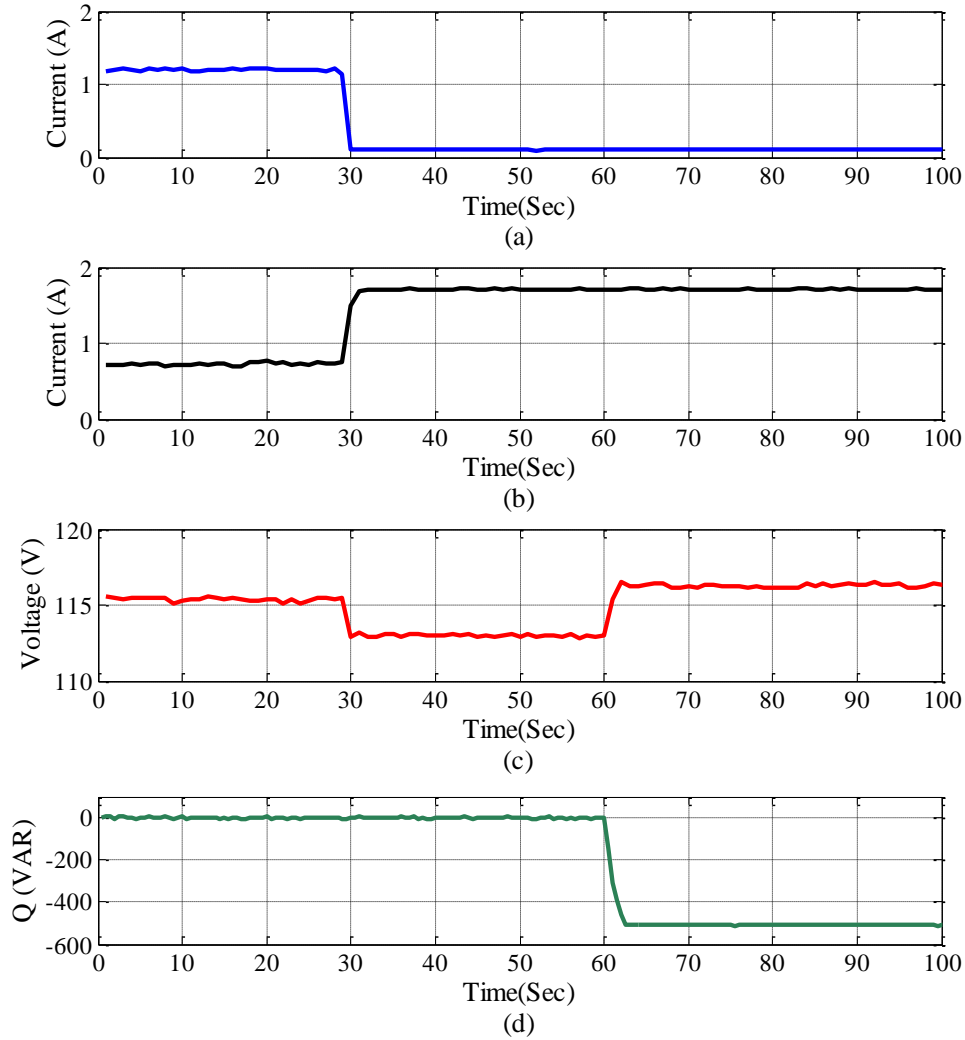
Figure 9.4 Voltage sag correction.
(a) Current of transmission line 1-6. (b) Current of transmission line 5-6. (c) Voltage of bus 7. (d) Injected reactive power by microgrid2.

In this event, an outage of transmission line 1-6 is created. The outage is shown in Figure 9.4(a), the current passing in transmission line 1-6 drops at the second 29 to almost zero. As expected, the current rises in the alternative path from 0.7 A to 1.7A as shown in Figure 9.4(b), which is very close to its thermal capacity (assumed to be 1.75A). In this case, the power is fed to bus 7 through only one path, this path models a physically longer transmission system and encounters higher voltage drop. Therefore, the phase voltage at the electrically far bus (bus 7) drops from 115.4V to 113.2V as

274

shown in Figure 9.4(c). Since this drop is not significant and within pre-specified limits, the controller is set to wait for 30 seconds to verify that the voltage drop is not temporary before injecting reactive power. The delay time can be adjusted by the operator according to the level of voltage drop and the sensitivity of the loads connected to this bus. Shorter delay (5 seconds) is set for higher voltage drop and down to 108V which corresponds to 90% of 120V. For any further voltage drop, a protection action would be required by the protection device.

During the delay time, the SCADA system calls the GA to calculate the required amount of Q, through solving the load flow problem for the whole system as mentioned previously. The solution of the load flow problem yields that it is required to inject 508 VAR from MG2 to the AC side. The GA solution did not yield any reactive power injection from MG1 because that would violate the second constraint in (9-2) as the line 2-5 is already close to its thermal limit. After the delay time is elapsed and since the bus voltage is not restored, the controller starts resetting the *iq* of the inverter to the suitable value to inject the required amount of Q to restore the voltage. It is shown in Figure 9.4(c) that the voltage increased from 113.2V to 116.1V approximately as second 60. The reactive power injected by MG2 is shown in Figure 9.4(d).

9.5.1.3 Event 3: Islanding Condition

Up to this stage of the experiment, the microgrid is operating in a grid-connected mode. In order to test the microgrid capability to support the loads and operate in standalone mode, the transmission line 6-7 is disconnected. The local controller in the microgrid detects the islanding situation. Consequently, it switches its control to the islanding mode. In the islanding mode, the microgrid generates an internal frequency reference signal. Depending on the generated signal, the microgrid is fixing the frequency at 60 Hz and supplying the load connected to the same AC bus. In addition,

the microgrid is responsible for fixing the bus voltage, the voltage of bus 7 is shown in Figure 9.5(a). From the figure, the voltage drops to 98 volts during transient before the microgrid injects active power to support the connected load and stabilize both voltage and frequency. Figure 9.5(b) shows the active power injected by the microgrid. At this moment, the available power from renewable energy sources in the microgrid is around 700W, which is enough to supply the load. In case of energy shortage (the available power is less than the required to support the load due to variations in the renewable energy sources), the controller will start shedding the loads with lower priorities according to a pre-assigned priority index.
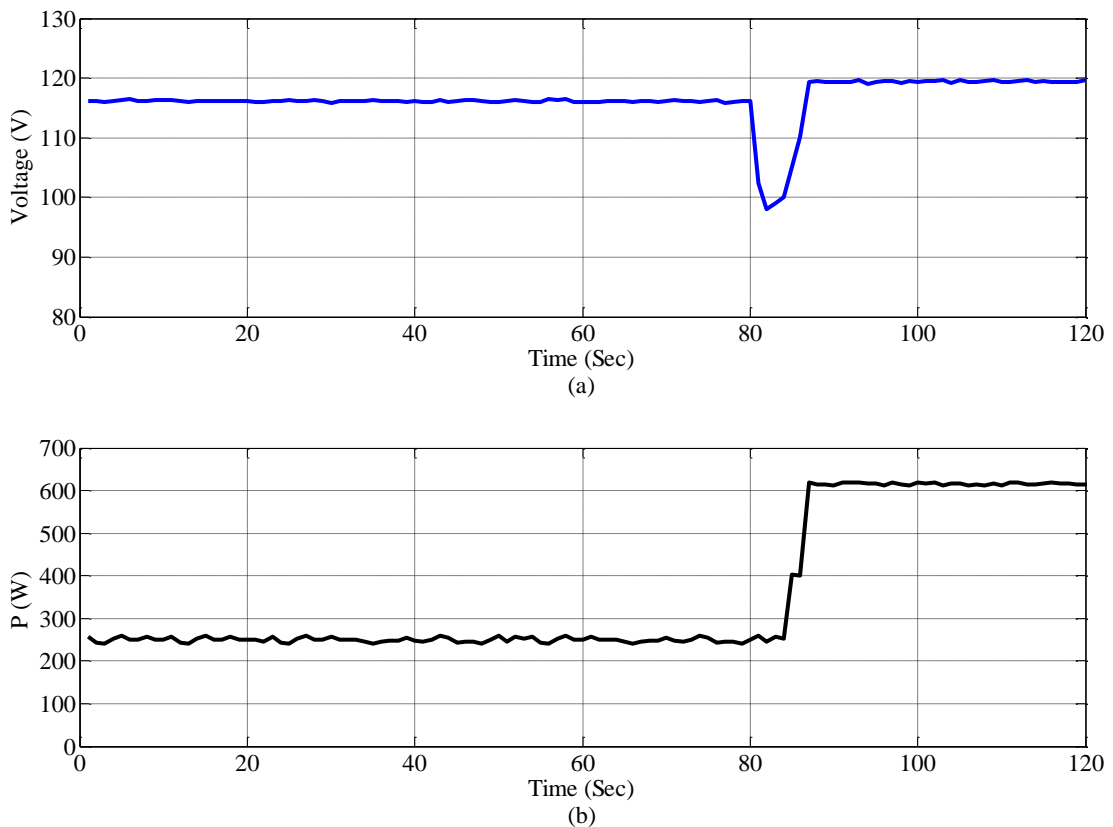
Figure 9.5 Microgrid operation in the islanded mode.
(a) Voltage of bus 7. (b) Injected active power by microgrid2.
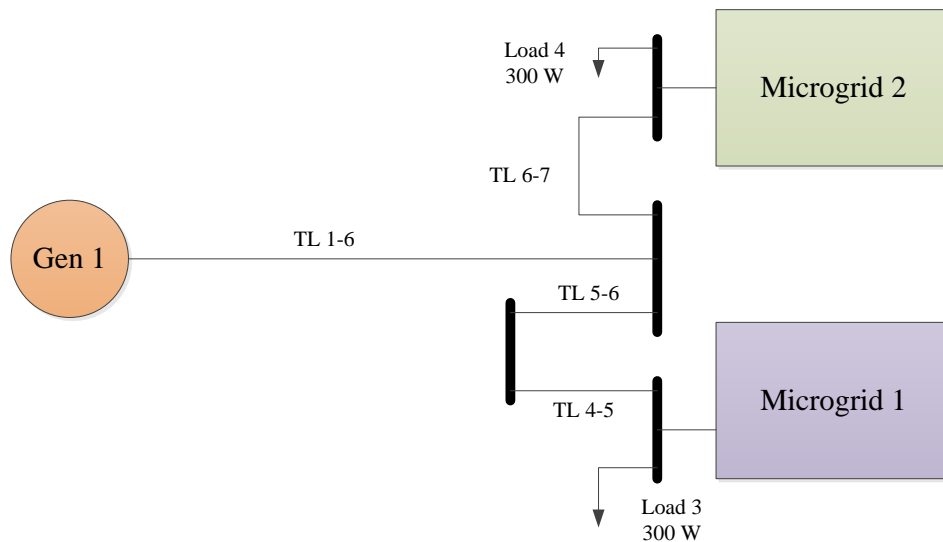
Figure 9.6 System configuration used in case II.

9.5.2 Case Study 2

In the previous case, it was shown that the microgrid can solve different issues on the AC side while maintaining support for its own local loads. Moreover, a microgrid can solve issues and support loads within another microgrid. This case presents another scenario where the renewable energy sources in one microgrid are not capable of supplying the local loads and renewable energy assets available in another microgrid will be used to virtually supply this energy deficiency. This situation is inevitable in practice in order to overcome the intermittency of DER based microgrids. The tertiary controller should consider transferring energy seamlessly from one microgrid to another one regardless of their size and type, i.e. AC or DC. This requires efficient power electronic enabling devices. In addition, the performance of both microgrids when they are linked together as an island is investigated. The system configuration at the beginning is shown in Figure 9.6; only Gen 1 is running and connected to the two microgrids through TL 1-6. Each microgrid has a local AC load of 300 W connected to the same bus.
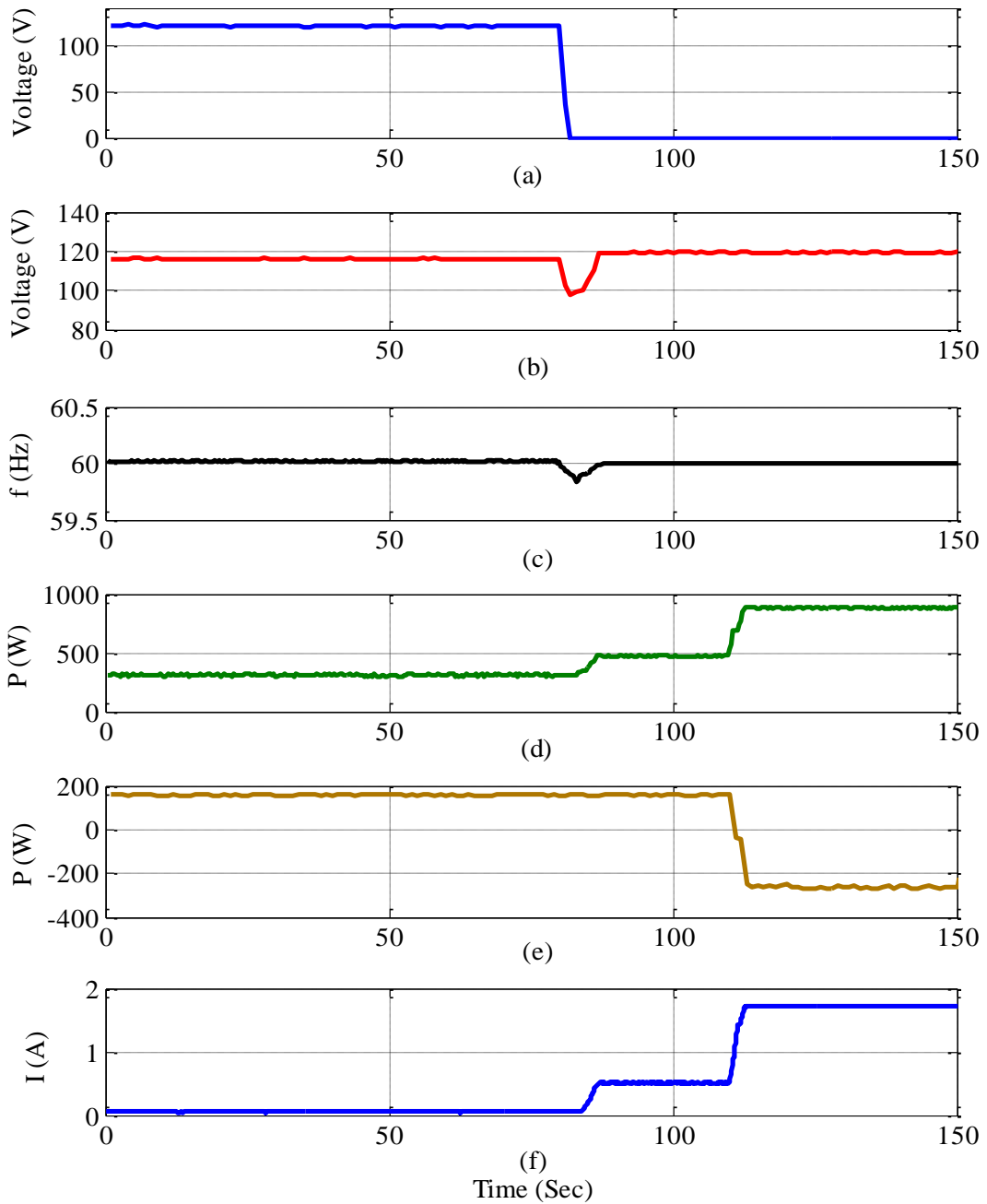
Figure 9.7 Case II: supporting Microgrid loads by assets of another.

(a) Voltage of Gen 1 (b) Voltage of the PCC of microgrid 1 (c) Frequency measured at the PCC of microgrid 1 (d) Active power injected by microgrid 2 (e) Active power flow at the PCC of microgrid 1 (f) Current in TL6-7.

Initially, MG1&MG2 are supplying around 160W and 310w, respectively as shown in Figure 9.7(e) & (d). The remaining power is supplied by Gen 1. At second 80, Gen 1 is disconnected and the voltage drops to zero as shown in Figure 9.7(a). Consequently,

the voltage and frequency starts to drop as shown in Figure 9.7(b) and (c). At the moment the voltage reaches a pre-specified value, the controller sends a signal to MG2 to switch to islanded mode and generates its own internal frequency reference. Once the microgrid switched to the standalone mode, no active power reference is followed. The microgrid is supplying the necessary active power to maintain the voltage and frequency at the specified reference values (depending on the availability). Hence, the injected active power by MG2 increased to 500 W to restore the voltage and frequency at 120V and 60 Hz, respectively. In the current situation, both microgrids are acting together as one island, where MG2 is playing the role of the slack bus.

The second event in this scenario occurs at the second 110, when MG1 starts to suffer from energy deficit due to absence of some of the renewable energy sources (due to low wind speed or cloud cover) and depletion of the stored energy in the battery bank. As explained earlier, the microgrid sends availability signal every 10 seconds. MG1 was supplying 160W to the local AC load and there is 400W load connected to the DC bus. Based on the forecasted solar irradiance and wind speed, the anticipated generation will be around 200 W only. This energy shortage causes the voltage of the DC bus to fluctuate; consequently, the VSI starts to stabilize the voltage by transferring power from the AC side (reverse the power flow direction). MG2 supplies the required amount as long as it is within the available amount and without violating the voltage of its DC bus or inverter loading limits. It is shown in Figure 9.7(d) that the injected power from the microgrid increased to approximately 900 W. The direction of power flow measured at the PCC of MG1 is reversed as shown in Figure 9.7(e). The current passing through transmission line 6-7 tying the two microgrids is shown in Figure 9.7(f). It can be noticed from Figure 9.7(b) and (c) that the microgrid is regulating the voltage and frequency without noticeable drops.

It was noticed during the experiment that the voltage of the DC bus dropped from 325V to 319V (1.85%) after the supplied power increased. The reason for this drop is that the microgrid was operating close to its maximum available power limit. It should be noticed that the local controller is observing the voltage of the DC bus and percentage loading of the inverter all the time. If the voltage continues to drop or the percentage loading on the inverter continues to increase, the local controller would take the necessary action either by load shedding or opening the Solid State Relay (SSR) to protect the microgrid.

9.6 Summary

In this chapter, an algorithm for automated tertiary control of distributed microgrids with high penetration levels of renewable energy sources has been presented. This control algorithm is rule based and it is designed to operate in real time and to autonomously respond to various contingencies. Different scenarios have been presented; each scenario is a sequence of cascaded events or outages that can happen in a real power system. These scenarios were implemented in realistic conditions in the Smart Grid test-bed to investigate the performance of the controller. It has been shown how microgrids can be utilized to prevent previously inevitable blackouts.

Furthermore, it has been shown that renewable energy assets available on the DC microgrids can reduce the stresses on the AC system or the slack bus and reduce the overloading on transmission lines. It was experimentally proven that with simple modification in the PLL and local control of the inverter, the microgrid can regulate the voltage and frequency of the AC system. In another case it has been shown experimentally that one microgrid can solve a problem or compensate energy deficit in another "weak" microgrid. The performance of the microgrids in connected and islanded modes was investigated and explained.

Chapter 10   Conclusions and Future Work

10.1 Conclusions

Different aspects related to the control, design, implementation and optimization of hybrid AC/DC power systems and DC distributed architectures involving energy storage and pulsed loads were presented throughout this dissertation. The dissertation started with a survey of the efforts conducted on DC distribution systems and DC microgrids. In light of this survey, it can be concluded that the feasibility of adopting DC systems became evident, especially with the high penetration of DC-supplied loads, and the presence of advanced power electronics technologies. Voltage selection, modeling, control, stability, protection and grounding of DC systems have been investigated. The latest standardization efforts have been discussed.

A comparative study to determine the optimal combination for a hybrid energy storage system to mitigate the negative effects of pulsed power loads on a ship power system was presented. This study showed that the battery and flywheel combination deserves merit and can achieve better performance over the other combinations. It is shown that a combination comprised of a flywheel, and an ultra-capacitor can cause frequency oscillations. Further studies were performed to investigate the performance of the flywheel and ultra-capacitor combination.

The idea of allocating small flywheels in a distributed manner was proposed to reduce the frequency oscillations. Three different cases were conducted to investigate the effectiveness of the proposed idea. The results of each case were analyzed and discussed. It was proven that flywheels can play an effective role in maintaining the system's stability and reduce the frequency oscillations. Furthermore, a comparison between the distributed and centralized FESS was conducted. It was shown that three

small flywheels can provide better results than one large flywheel. The distributed flywheel solution reduced the frequency oscillations significantly.

The design and implementation of an advanced Battery Management Systems (BMS) is presented. A laboratory prototype is built in Energy Systems Research Laboratory (ESRL) and tested under different loading conditions. The developed BMS is capable of monitoring the voltage, current, power, energy and SoC of each battery in the array. Furthermore, it can independently control individual batteries. By isolating individual batteries, the operator can charge one or more batteries in a series stack while the system continues to supply the load. This reduces the impacts associated with heavy pulsed loads. This topology significantly increases the reliability of the system. It was proven that the load can be supplied normally even when a four battery stack has been significantly reduced to only one or two batteries (depending on load current). In addition, this system is lower in cost as no bi-directional converter is needed. The converter is eliminated because the batteries are charged from another low voltage DC source. Accordingly, the system is suitable for wide range of applications. It can be used in utility scale energy storage systems, as the large battery array can be divided into sub-sections or stacks and each stack is monitored and controlled using a BMS unit.

The BMS developed in chapter three was expanded in chapter four and equipped with new functionalities to be utilized for the management of multi-chemistry energy storage systems. In order for the name to represent the new scope of the system, the name is changed from BMS to Modular Energy Storage Regulator (MESR). The performance of the developed MESR is investigated through extensive experimental testing. The testing procedures were carried out under single and multiple overlapped pulsed loads with serious and parallel connected Hybrid Energy Storage Systems (HESSs). HESS

can be beneficial in a wide variety of applications. Two applications were tackled: Ship Power Systems (SPS) and Electric Vehicles (EV). A coordinated control technique was introduced to handle the charging of different ES types and extend the operating duration of the array under multiple pulsed loads, which are common in modern SPS. The developed management system provides an effective solution to manage multiple ES types to serve multiple pulsed loads on a SPS platform. A specialized dispatch control scheme was introduced to coordinate charging and discharging of individual energy storage units. With this scheme, the system is capable of coordinating charging/discharging of the units during operation to extend runtime while acknowledging SoH trade-offs. This scheme is coined as "rolling charging". The effectiveness and seamless operation of the system has been verified through hardware testing.

Operation and management of parallel-configured HESS has been investigated in this dissertation. A management scheme for a HESS composed of a supercapacitor and lithium ion battery connected in parallel is developed and tested. This scheme is simple, yet effective and capable of seamlessly handling the charging and discharging of the HESS. The MESR is modified to be used in parallel configuration. It is anticipated that this scheme will increase the lifetime of the battery and the available "in service" time for the ES system.

A multi-objective optimization problem was developed for the optimal design of AC/DC distribution systems. In this problem, it was required to find the best architecture to accommodate the high power demand loads while avoiding major disturbances. The AC/DC power flow and transient analysis were solved to evaluate the individuals. Considering the transient analysis in the optimization problem emphasizes its integrity. This is one of the major contributions of this dissertation that

has not been previously considered in the literature. Four objective functions were considered: minimize the voltage deviation on all the buses, the total active power losses, the frequency deviations and the weight of the installed energy storage. Different formulations of the problem were investigated through considering different sets of objectives. The decision (controlled) variables were: the locations of high demand load (bus connection), ES and PCC) and the connectivity of the distribution lines. A decision making criterion was applied to obtain only one solution among the frontier individuals. The obtained solution was validated through comparison to a base case and other solutions that were obtained using the traditional weighted sum approach. Major reductions in the voltage deviation and power losses were achieved as a result of implementing the proposed technique.

The modeling, design, control and hardware implementation of a DC machine based low speed Flywheel Energy Storage System (FESS) was presented. The DC machine can offer more advantages including lower cost, simplicity and wider speed range. This wide operation range allows more utilization of the stored kinetic energy. Following the design final steps, the system's performance was investigated through simulation. The simulation results proved the capability of the system to mitigate the pulsed load and maintain the bus voltage at the required levels. Then, a FESS prototype was implemented. It was shown through the laboratory hardware setup that the FESS is effectively mitigating the pulsed load.

10.2 Future Work

The research area of DC distribution systems and microgrids is still needs further development. More detailed studies need to be conducted on the equipment that were originally designed for AC operation to be reused in DC systems. The stability of DC microgrids is another area that is worth investigating. The stability of AC systems is

well studied and extensively investigated, while the stability of the DC systems is still demanding more studies. More focus should be dedicated to the transient stability in DC microgrids and when multiple power electronic converters are tightly regulating the voltage. More work and effort should be directed towards creating standards for DC systems. The cooperation between industry and academia should be elevated to propel the global standardization efforts. For example, up to the time of finalizing this dissertation, there's no standard voltage level for DC systems and no unified framework for designing those systems. These standards are highly required to encourage entrepreneurs to invest in DC systems.

The experimentally-verified studies presented in this dissertation showed that the flywheel can provide a reliable energy storage mean. More studies will be conducted on increasing the round-trip efficiency of the flywheel. Design and implementation of a high speed flywheel (>10,000 rpm) will be performed. Some sophistications are associated with the design of the driver of the high speed flywheel. For example, high speed switching devices will be needed, which require utilizing Gallium Nitride (GaN) switches. In general, an accurate design with new ideas is needed to address the arising sophistications.

A complete DC distribution architecture design needs to be comprehensively investigated with its practical aspects and impacts. Recent optimization techniques can be investigated and used to develop a multi-objective framework to optimally design the system. Grey Wolf Optimization (GWO) and Random Drift Particle Swarm Optimization (RDPSO) are proven to be successful techniques with reliable convergence. Therefore, they can be investigated to be used in future optimal AC/DC power flow studies.

Since, the microgrid are utilized more in a distributed manner, this geographical

dispersion requires more utilization of reliable communication links. The security of these links is very critical as any attack can cause not only outages to the power system, but also damage for costly physical equipment. Therefore, the security of the communication links tying microgrids should be studied as an integrated Cyber-Physical System (CPS). Where, the characteristics and requirements of the physical components are considered.

LIST OF REFERENCES

[1] P. Fairley, DC Versus AC: The Second War of Currents Has Already Begun [In My View], IEEE Power and Energy Mag., 10 (2012) 104-103.

[2] Seung-Hee Ryu, Jung-Hoon Ahn, Byoung-Kuk Lee, Kwang-Seung Cho, Single-switch ZVZCS quasi-resonant CLL isolated DC-DC converter for low-power 32″ LCD TV, IEEE Energy Convers. Congr. and Expo. (ECCE), (2013) 4887-4893.

[3] Cheng-Hung Tsai, Ying-Wen Bai, Ming-Bo Lin, RJR Jhang, Chih-Yu Chung, Reduce the standby power consumption of a microwave oven, IEEE Trans. Consum. Electron., 59 (2013) 54-61.

[4] D. Salomonsson, A. Sannino, Load modelling for steady-state and transient analysis of low-voltage DC systems, IET Electr. Power Appl., 1 (2007) 690-696.

[5] M. Amin, Y. Arafat, S. Lundberg, S. Mangold, Low voltage DC distribution system compared with 230 V AC, IEEE Electr. Power and Energy Conf. (EPEC), (2011), pp. 340-345.

[6] K. Techakittiroj, V. Wongpaibool, Co-existence between AC-Distribution and DC-Distribution: in the view of appliances, 2nd Int. Conf. on Comput. and Electr. Engineering (ICCEE), (2009), pp. 421-425.

[7] M. Ryu, H. Kim, J. Kim, J. Baek, J. Jung, Test bed implementation of 380V DC distribution system using isolated bidirectional power converters, IEEE Energy Convers. Congr. and Expo. (ECCE), (2013), pp. 2948-2954.

[8] B. A. Thomas, Edison revisited: impact of DC distribution on the cost of LED lighting and distribution generation, 27th Annual IEEE Appl. Power Electron. Conf. and Expo. (APEC), (2010), pp. 588-593.

[9] Wensong Yu, Jih-Sheng Lai, Hongbo Ma, Cong Zheng, High-Efficiency DC–DC Converter With Twin Bus for Dimmable LED Lighting, IEEE Trans. Power Electron., 26 (2011), pp.2095-2100.

[10] G.C. Lazaroiu, D. Zaninelli, A control system for dc arc furnaces for power quality improvements, Electr. Power Syst. Res., 80 (2010), pp. 1498-1505.

[11] Peng Wang, L. Goel, Xiang Liu, Fook Hoong Choo, Harmonizing AC and DC: A hybrid AC/DC future grid solution, IEEE Power and Energy Mag., 11 (2013), pp. 76-83.

[12] P. S. Maniscalco, V. Scaini, W. E. Veerkamp, Specifying DC chopper systems for electrochemical applications, IEEE Trans. Ind. Appl., 37 (2011), pp. 941-948, May/Jun. 2001.

[13] G. F. Reed, DC technologies: solutions to electric power system advancements, IEEE Power and Energy Mag., 10 (2012), pp. 10-17.

[14] B. T. Patterson, DC, come home: DC microgrids and the birth of the Enernet, IEEE Power and Energy Mag., 10 (2012), pp. 60-69.

[15] T. Wu, C. Chang, L. Lin, G. Yu, Y. Chang, DC-bus voltage control with a three-phase bidirectional inverter for DC distribution systems, IEEE Trans. on Power

Electron., 28 (2013), pp. 1890-1899.

[16] C. Dierckxsens, K. Srivastava, M. Reza, S. Cole, J. Beerten, R. Belmans, A distributed DC voltage control method for VSC MTDC systems, Electr. Power Syst. Res., 82 (2012) pp. 54-58.

[17] M. Aragüés-Peñalba, A. Egea-Àlvarez, S. G. Arellano, O. Gomis-Bellmunt, Droop control for loss minimization in HVDC multi-terminal transmission systems for large offshore wind farms, Electr. Power Syst. Res., 112 (2014) PP. 48-55.

[18] M. Brenna, E. Tironi and G. Ubezio, "Proposal of a local DC distribution network with distributed energy resources," 11th International Conference on Harmonics and Quality of Power, 2004, pp. 397-402.

[19] A. Al-Diab, C. Sourkounis, Integration of flywheel energy storage system in production lines for voltage drop compensation, IEEE 37th Annual Conf. Ind. Electron. *(IECON)*, (2011), pp. 3882-3887.

[20] B. H. Kenny, R. Jansen, P. Kascak, T. Dever, W. Santiago, Integrated power and attitude control with two flywheels, IEEE Trans. Aerospace and Electron. Syst., 41 (2005), pp. 1431-1449.

[21] D. Becker, B. Sonnenberg, DC microgrids in buildings and data centers, IEEE 33rd Int. Telecommun. Energy Conf. (INTELEC), (2011), pp. 1-7.

[22] P. Gross, K. Godrich, Total DC Integrated Data Centers, IEEE 27th Int. Telecommun. Conf. (INTELEC), (2005) pp.125-130.

[23] S. Rajagopalan, B. Fortenbery D. Symanski, Power quality disturbances within DC data centers, IEEE 32nd Int. Telecommun. Energy Conf. (INTELEC), (2010), pp. 1-7.

[24] G. AILee, W. Tschudi, Edison redux: 380 Vdc brings reliability and efficiency to sustainable data centers, IEEE Power and Energy Mag., 10 (2012), pp. 50-59.

[25] D. Kim, T. Yu, H. Kim, H. Mok, K. Park, 300V DC feed system for Internet data center, IEEE 8th Int. Con. on Power Electron. and ECCE Asia (ICPE & ECCE), (2011), pp. 2352-2358.

[26] A. Pratt, P. Kumar, T. Aldridge, Evaluation of 400V DC distribution in telco and data centers to improve energy efficiency, IEEE 29th Int. Telecommun. Energy Conf. (INTELEC), (2007), pp. 32-39.

[27] N. Rasmussen, AC vs. DC power distribution for data centers, APC White paper # 63, (2006).

[28] DC power distribution cuts data center energy use, (2014) [Online]. Available: http://hightech.lbl.gov/documents/data_centers/CEC-TB-40.PDF

[29] High-performance data centers; a research roadmap, (2014) [Online]. Available: http://hightech.lbl.gov/documents/datacenters_roadmap_final.pdf

[30] L. Zhang, F. Jabbari, T. Brown, S. Samuelsen, Coordinating plug-in electric vehicle charging with electric grid: Valley filling and target load following, J. of Power Sources, 267 (2014), pp. 584-597.

[31] G. Mills, I. MacGill, Potential power system and fuel consumption impacts of plug in hybrid vehicle charging using Australian National Electricity Market load profiles and transportation survey data, Electr. Power Syst., Res., 116 (2014), pp. 1-11.

[32] C. Liu, K.T. Chau, Diyun Wu, Shuang Gao, Opportunities and Challenges of Vehicle-to-Home, Vehicle-to-Vehicle, and Vehicle-to-Grid Technologies, Proc. of the IEEE, 101 (2013) pp.2409-2427.

[33] Y. Ota, H. Taniguchi, J. Baba, A. Yokoyama, Implementation of autonomous distributed V2G to electric vehicle and DC charging system, Electr. Power Syst. Res., (2014), In Press.

[34] M.A. López, S. Martín, J.A. Aguado, S. de la Torre, V2G strategies for congestion management in microgrids with high penetration of electric vehicles, Electr. Power Syst. Res., 104 (2013), pp. 28-34.

[35] L. Drude, L. C. Pereira Junior, R. Rüther, Photovoltaics (PV) and electric vehicle-to-grid (V2G) strategies for peak demand reduction in urban regions in Brazil in a smart grid environment, Renew. Energy, 68 (2014), pp. 443-451.

[36] M. Tabari, A. Yazdani, A DC distribution system for power system integration of Plug-In Hybrid Electric Vehicles, IEEE Power and Energy Soc. General Meeting (PES), (2013), pp.1-5.

[37] A. Mohamed, V. Salehi, Tan Ma, O. Mohammed, Real-Time Energy Management Algorithm for Plug-In Hybrid Electric Vehicle Charging Parks Involving Sustainable Energy, IEEE Trans. Sustain. Energy, 5 (2014), pp.577-586.

[38] B.E. Noriega, R.T. Pinto, P. Bauer, Sustainable DC-microgrid control system for electric-vehicle charging stations, 15th European Conf. on Power Electron. and Appl. (EPE), (2013), pp.1-10.

[39] L. Roggia, C. Rech, L. Schuch, J.E. Baggio, H.L. Hey, J.R. Pinheiro, Design of a sustainable residential microgrid system including PHEV and energy storage device,14th European Conf. on Power Electron. and Appl. (EPE), (2011), pp.1-9.

[40] Dong Chen, Lie Xu, Autonomous DC voltage control of a DC microgrid with multiple slack terminals, IEEE Trans. Power Syst., 27 (2012), pp.1897-1905.

[41] M. Farhadi, O. Mohammed, Realtime operation and harmonic analysis of isolated and non-isolated hybrid DC microgrid," Accepted in IEEE Trans. Ind. Appl., (2014), In Press.

[42] Y. Gu, X. Xiang, W. Li, X. He, Mode-Adaptive decentralized control for renewable DC microgrid with enhanced reliability and flexibility," IEEE Trans. Power Electron., 29 (2014), 5072-5080.

[43] Lie Xu, Dong Chen, Control and operation of a DC microgrid with variable generation and energy storage," IEEE Trans. Power Deliv., 26 (2011), pp.2513-2522.

[44] Xunwei Yu, Xu She, Xiaohu Zhou, A.Q. Huang, Power management for DC microgrid enabled by solid-state transformer, IEEE Trans. Smart Grid, 5 (2014), pp.954-965.

[45] T. Dragicevic, J.M. Guerrero, J.C. Vasquez, D. Skrlec, Supervisory control of an adaptive-droop regulated DC microgrid with battery management capability, IEEE Trans. Power Electron., 29 (2014), pp.695-706.

[46] Xu She, A.Q. Huang, S. Lukic, M.E. Baran, On integration of solid-state transformer with zonal DC microgrid, IEEE Trans. Smart Grid, 3 (2012), pp.975-985.

[47] K. Strunz, E. Abbasi, Duc Nguyen Huu, DC microgrid for wind and solar power integration, IEEE J. of Emerging and Sel. Top. in Power Electron., 2 (2014), pp.115-126.

[48] Baochao Wang, M. Sechilariu, F. Locment, Intelligent DC microgrid with smart grid communications: control strategy consideration and design, IEEE Trans. Smart Grid, 3 (2012), pp.2148-2156.

[49] M. Simonov, Dynamic partitioning of DC microgrid in resilient clusters using event-driven approach, IEEE Trans. Smart Grid, (2014), In Press.

[50] Xiaonan Lu, Kai Sun, J.M. Guerrero, J.C. Vasquez, Lipei Huang, State-of-Charge balance using adaptive droop control for distributed energy storage systems in DC microgrid applications, IEEE Trans. Ind. Electron., 61 (2014), pp.2804-2815.

[51] Xiaonan Lu, J.M. Guerrero, Kai Sun, J.C. Vasquez, An improved droop control method for DC microgrids based on low bandwidth communication with DC bus voltage restoration and enhanced current sharing accuracy, IEEE Trans. Power Electron., 29 (2014), pp.1800-1812.

[52] Chi Jin, Peng Wang, Jianfang Xiao, Yi Tang, Fook Hoong Choo, Implementation of hierarchical control in DC microgrids, IEEE Trans. Ind. Electron., 61 (2014) pp.4032-4042.

[53] D. Chen, L. Xu, L. Yao, DC voltage variation based autonomous control of DC microgrids, IEEE Trans. Power Deliv., 28 (2013) pp.637-648.

[54] S. Anand, B.G. Fernandes, M. Guerrero, Distributed control to ensure proportional load sharing and improve voltage regulation in low-voltage DC microgrids, IEEE Trans. Power Electron., 28 (2013), pp.1900-1913.

[55] A. Kwasinski, Quantitative evaluation of DC microgrids availability: effects of system architecture and converter topology design choices, IEEE Trans. Power Electron, 26 (2011) pp.835-851.

[56] H. Kakigano, Y. Miura, T. Ise, Distribution voltage control for DC microgrids using fuzzy control and gain-scheduling technique, IEEE Trans. Power Electron., 28 (2013), pp.2246-2258.

[57] N. Eghtedarpour, E. Farjah, Distributed charge/discharge control of energy storages in a renewable-energy-based DC micro-grid, IET Renew. Power Generation, 8 (2014), pp.45-57.

[58] S.-M. Chen, T.-J. Liang, K.-R. Hu, Design, analysis, and implementation of solar power optimizer for DC distribution system, IEEE Trans. Power Electron.*, 28 (2013), pp.1764-1772.

[59] J. J. Justo, F. Mwasilu, J. Lee, J. Jung, AC-microgrids versus DC-microgrids with distributed energy sources: A review, Renew. and Sustain. Energy Reviews, 24 (2013), pp. 387-405.

[60] A. Mohamed, V. Salehi, O. Mohammed, Real-time energy management algorithm for mitigation of pulse loads in hybrid microgrids, IEEE Trans. Smart Grid, 3 (2012), pp. 1911-1922.

[61] A. Mohamed, A. Ghareeb, T. Youssef, O. A. Mohammed, Wide area monitoring and control for voltage assessment in smart grids with distributed generation, IEEE Innov. Smart Grid Technol. Conf. (ISGT), (2013), pp.1-6.

[62] D. J. Hammerstrom, AC versus DC distribution systems: Did we get it right?, IEEE Power & Energy Soc. General Meeting, (2007), pp. 1-5.

[63] G. Seo, J. Baek, K. Choi, H. Bae, B. Cho, Modeling and Analysis of DC Distribution Systems, IEEE 8th Int. Conf. on Power Electron. and ECCE Asia (ICPE & ECCE), (2011), pp. 223-227.

[64] M.R. Starke, L.M. Tolbert, B. Ozpineci, AC vs. DC distribution: A loss comparison, IEEE PES Transmission and Distribution Conf. and Expo. (T&D), (2008), pp. 1-7.

[65] K. Engelen, E. Leung Shun, P. Vermeyen, I. Pardon, R. D'hulst, J. Driesen, R. Belmans, The feasibility of small-scale residential DC distribution systems, IEEE 32nd Annual Conf. on Ind. Electron. (IECON), (2006), pp.2618-2623.

[66] J. Pellis, The dc low-voltage house, Master's thesis, TU Eindhoven, (1997).

[67] [online] Available on (2014): http://www.nexans.us/eservice/USen_US/ fileLibrary/Download_540190061/US/files/CORFLEX%20USA%202011%20 (2)_1.pdf

[68] [online] Available on (2014): http://www.nexans.co.nz/NewZealand/ 2013/Power%20Cable%20Catalogue%20Full%20version%202012.pdf

[69] [online] Available on (2014): http://www.elsewedyelectric.com/FE/Common/ ProductCategoryDetails.aspx?/13/2/Low%20Voltage%20Cables/

[70] A. W. Cirino, H. de Paula, R. C. Mesquita, E. Saraiva, Cable parameter determination focusing on proximity effect inclusion using finite element analysis, Brazilian Power Electron. Conf. (COBEP), (2009), pp. 402-409.

[71] F. Wang, Yunqing Pei, D. Boroyevich, R. Burgos, Khai Ngo, Ac vs. dc distribution for off-shore power delivery, IEEE 34th Annual Conf. of IEEE on Ind. Electron. (IECON), (2008), pp. 2113-2118.

[72] D. M. Larruskain, I. Zamora, O. Abarrategui, Z. Aginako, Conversion of AC distribution lines into DC lines to upgrade transmission capacity, Electr. Power Syst. Res., 81 (2011), pp. 1341-1348.

[73] D. Salomonsson, A. Sannino, Low voltage DC distribution systems for commercial power systems with sensitive electronic loads, IEEE Trans. Power Deliv., 22 (2007), pp. 1620–1627.

[74] A. Sannino, G. Postiglione, M. H. J. Bollen, Feasibility of a DC network for commercial facilities, IEEE Trans. Ind. Appl., 39 (2003) pp. 1499–1507.

[75] M. E. Baran, N. R. Mahajan, DC distribution for industrial systems: Opportunities and challenges, IEEE Trans. Ind. Appl., 39 (2003), pp. 1596–1601.

[76] R. Majumder, Aggregation of microgrids with DC system, Electr. Power Syst. Res., 108 (2014), pp. 134-143.

[77] D. Salomonsson, L. Söder, A. Sannino, An adaptive control system for a DC microgrid for data centers, IEEE Trans. Ind. Appl., 44 (2008), pp. 1910–1917.

[78] H. Kakigano, Y. Miura, T. Ise, R. Uchida, DC micro-grid for super high quality distribution- System configuration and control of distributed generations and energy storage devices, *Proc. IEEE PESC*, (2006), pp. 3148–3154.

[79] H. Kakigano, Y. Miura, T. Ise, Low-Voltage Bipolar-Type DC Microgrid for Super High Quality Distribution, IEEE Trans. Power Electron., 25 (2010), pp. 3066–3075.

[80] R. S. Balog, W. W. Weaver, P. T. Krein, The load as an energy asset in a distribution dc smart grid architecture, IEEE Trans. Smart Grid, 3 (2012), pp. 253–260.

[81] D. L. Logue, P. T. Krein, Preventing instability in DC distribution systems by using power buffering, in Rec. IEEE Power Electron. Specialists Conf., (2001), pp. 33–37.

[82] *FREEDM System*, [Online]. Available on (2014): http://www.freedm.ncsu.edu/

[83] X. She, X. Yu, F. Wang, A.Q. Huang, Design and demonstration of a 3.6KV-120V/10KVA solid state transformer for smart grid application, IEEE Trans. Power Electron. , 29 (2014), pp. 3982–3996.

[84] N. O. Sokal, System oscillations from negative input resistance at power input port of switching-mode regulator, amplifier, DC/DC converter, or DC/AC inverter, IEEE Power Electron. Specialists Conf. PESC, (1973), pp. 138-140.

[85] R. D. Middlebrook, Input filter considerations in design and application of switching regulators, IEEE Ind. Appl. Soc. Annu. Meet. , 1976.

[86] R. D. Middlebrook, Design techniques for preventing input-filter oscillations in switched-mode regulators, Proc. of the Fifth Natl. Solid State Power Convers. Conf., 1978.

[87] Xiaogang Feng, Jinjun Liu, F. C. Lee, Impedance specifications for stable DC distributed power systems, IEEE Trans. on Power Electron., 17 (2002), Mar 2002.

[88] Xiaogang Feng, Zhihong Ye, Kun Xing, F.C. Lee, D. Borojevic, Individual load impedance specification for a stable DC distributed power system, 14th Annu. Appl. Power Electron. Conf. and Expo., APEC '99, 2 (1999), pp.923-929.

[89] Jian Sun, Impedance-based stability criterion for grid-connected inverters, *IEEE Trans. on Power Electron.,* 26 (2011), pp.3075-3078.

[90] Xiaoyan Yu, M. Salato, An optimal minimum-component DC–DC converter input filter design and its stability analysis, IEEE Trans. on Power Electron., 29 (2014), pp.829-840.

[91] Amr A. A. Radwan, Yasser A.-R. I. Mohamed, Stabilization of medium-frequency modes in isolated microgrids supplying direct online induction motor loads, IEEE Trans. Smart Grid, 5 (2014), pp.358-370.

[92] Amr A. A. Radwan, Yasser A. I. Mohamed, Assessment and mitigation of interaction dynamics in hybrid AC/DC distribution generation systems, IEEE Trans. on Smart Grid, 3 (2012), pp.1382-1393.

[93] Amr A. A. Radwan, Yasser A. -R. I. Mohamed, Linear active stabilization of converter-dominated DC microgrids, IEEE Trans. on Smart Grid, 3 (2012), pp.203-216.

[94] A. Kahrobaeian, Yasser A.-R. I. Mohamed, Analysis and mitigation of low-frequency instabilities in autonomous medium-voltage converter-based microgrids with dynamic loads, IEEE Trans. Ind. Electron., 61 (2014), pp.1643-1658.

[95] A. A. A. Radwan, Y. A.-R. I. Mohamed, Analysis and active-impedance-based stabilization of voltage-source-rectifier loads in grid-connected and isolated microgrid applications, IEEE Trans. on Sustain. Energy, 4 (2013), pp.563-576.

[96] Yasser A. –R. I. Mohamed, A. A. A. Radwan, T. K. Lee, Decoupled reference-voltage-based active DC-link stabilization for PMSM drives with tight-speed regulation, IEEE Trans. on Ind. Electron., 59 (2012), pp.4523-4536.

[97] R. Maheshwari, S. Munk-Nielsen, Kaiyuan Lu, An active damping technique for small DC-link capacitor based drive system, IEEE Trans. on Ind. Inform., 9 (2013), pp.848-858.

[98] Wook-Jin Lee, Seung-Ki Sul, DC-link voltage stabilization for reduced DC-link capacitor inverter, IEEE Trans. on Ind. Appl., 50 (2014), pp.404-414.

[99] P. Magne, D. Marx, B. Nahid-Mobarakeh, S. Pierfederici, Large-signal stabilization of a DC-link supplying a constant power load using a virtual capacitor: impact on the domain of attraction, IEEE Trans. on Ind. Appl., 48 (2012), pp.878-887.

[100] Zhonghui Bing, Jian Sun, Line-frequency rectifier dc-bus voltage instability analysis and mitigation, (2010), IEEE 12th Workshop on Control and Modeling for Power Electron. (COMPEL).

[101] M. Davari, Y. Mohamed, Variable-structure-based nonlinear control for the master vsc in DC-energy-pool multiterminal grids, IEEE Trans. on Power Electron., 29 (2014), pp.6196-6213.

[102] S. Anand, B. G. Fernandes, Reduced-order model and stability analysis of low-voltage DC microgrid, IEEE Trans. on Ind. Electron., 60 (2013), pp.5040-5049.

[103] Y. A -R I. Mohamed, Mitigation of converter-grid resonance, grid-induced distortion, and parametric instabilities in converter-based distributed generation," IEEE Trans. on Power Electron., 26 (2011), pp.983-996.

[104] S.R. Rudraraju, A.K. Srivastava, S.C. Srivastava, N.N. Schulz, Small signal stability analysis of a shipboard MVDC power system, (2009), IEEE Electr. Ship Technol. Symp., ESTS 2009, pp.135-141.

[105] A. Griffo, J. Wang, Modeling and stability analysis of hybrid power systems for the more electric aircraft, Electric Power Systems Research, 82 (2012), pp. 59-67.

[106] M. Benidris, S. Elsaiah, S. Sulaeman, J. Mitra, Transient stability of distributed generators in the presence of energy storage devices, 2012, North American Power Symp. (NAPS).

[107] Qing-Chang Zhong, G. Weiss, Synchronverters: inverters that mimic synchronous generators, IEEE Trans. Ind. Electron., 58 (2011), pp.1259-1267.

[108] Qing-Chang Zhong, Phi-Long Nguyen, Zhenyu Ma, Wanxing Sheng, Self-synchronized synchronverters: inverters without a dedicated synchronization unit, IEEE Trans. on Power Electron., 29 (2014), pp.617-630.

[109] S. M. Ashabani, Yasser A. I. Mohamed, A flexible control strategy for grid-connected and islanded microgrids with enhanced stability using nonlinear microgrid stabilizer, IEEE Trans. Smart Grid, 3 (2012), pp.1291-1301.

[110] Juan P. Torreglosa, Pablo García-Triviño, Luis M. Fernández-Ramirez, Francisco Jurado, Control strategies for DC networks: A systematic literature review, Renewable and Sustainable Energy Reviews, Vol. 58, pp. 319-330, May 2016.

[111] M. Tucci; S. Riverso; J. C. Vasquez; J. M. Guerrero; G. Ferrari-Trecate, "A Decentralized Scalable Approach to Voltage Control of DC Islanded Microgrids," in *IEEE Transactions on Control Systems Technology* , pp.1-15, doi: 10.1109/TCST.2016.2525001.

[112] A. Berizzi, A. Silvestri, D. Zaninelli, Stefano Massucco, Short-circuit current calculations for DC systems, IEEE Trans. Ind. Appl., 32 (1996), pp. 990-997.

[113] D. Salomonsson, L. Söder, A. Sannino, Protection of low-voltage DC microgrids, IEEE Trans. Power Deliv., 24 (2009), pp. 1045–1053.

[114] Lianxiang Tang, Boon-Teck Ooi, Locating and isolating DC faults in multi-terminal DC systems, IEEE Trans. on Power Deliv., 22 (2007), pp.1877-1884.

[115] J.-D. Park, J. Candelaria, Fault detection and isolation in low-voltage DC-bus microgrid system, IEEE Trans. on Power Deliv., 28 (2013), pp.779-787.

[116] Huimin Li, Weilin Li, Min Luo, A. Monti, F. Ponci, Design of smart MVDC power grid protection, IEEE Trans. on Instrum. and Meas., 60 (2011), pp.3035-3046.

[117] J. Jeon, J. Kim, J. Hur, H. Jin, Design guideline of DC distribution systems for home appliances: issues and solution, (2011), IEEE Int. Electr. Mach. and Driv. Conf. (IEMDC), pp. 657-662.

[118] M. E. Baran, N. R. Mahajan, Overcurrent protection on Voltage-Source-Converter-based multiterminal DC distribution systems, IEEE Trans. on Power Deliv., 22 (2007), pp.406-412.

[119] S. D. A. Fletcher, P. J. Norman, S.J. Galloway, P. Crolla, G. M. Burt, Optimizing the roles of unit and non-unit protection methods within DC microgrids, IEEE Trans. on Smart Grid, 3 (2012), pp.2079-2087.

[120] R. Mehl, P. Meckler, Comparison of advantages and disadvantages of electronic and mechanical protection systems for higher voltage DC 400 V, Proc. of the 35th Int. Telecommun. Energy Conf. (INTELEC), pp.1-7.

[121] J.-M. Meyer, A. Rufer, A DC hybrid circuit breaker with ultra-fast contact opening and integrated gate-commutated thyristors (IGCTs), IEEE Trans. on Power Deliv., 21 (2006), pp.646-651.

[122] S. Parhizi, H. Lotfi, A. Khodaei and S. Bahramirad, "State of the Art in Research on Microgrids: A Review," in *IEEE Access*, vol. 3, no. , pp. 890-925, 2015.

[123] IEEE Recommended Practice for the Design of DC Auxiliary Power Systems for Generating Stations, IEEE Std. 946-2004, (2004).

[124] IEEE Recommended Practice for Emergency and Standby Power Systems for Industrial and Commercial Applications, IEEE Std. 446-1995, (1995).

[125] IEC 61660, Short-circuit currents in dc auxiliary installations in power plants and substations, (1997).

[126] IEEE Recommended practice for interconnecting distributed resources with electric power systems distribution secondary networks, IEEE Std 1547.6-2011, (2011).

[127] M. W. Earley, J. S. Sargent, C. D. Coache, R. J. Roux, National electrical code handbook, Twelfth edition, NFPA, (2011).

[128] NFPA 70®: National Electric Code®, 2014 Edition, (2014).

[129] [Online]. Available on (2014): http://www.emergealliance.org/

[130] Public overview of the Emerge Alliance occupied space standard version 1.1.

[131] Public overview of the Emerge Alliance data/telecom center standard version 1.0.

[132] MIL-STD-1399/390, military standard: interface standard for shipboard systems (section 390) electric power, direct current, (1987).

[133] D. Marquet, T. Tanaka, K. Murai, T. Toru, T. Babasaki, DC power wide spread in telecom/datacenter and in home/office with renewable energy and energy autonomy, Proc. of the 35th Int. Telecommun. Energy Conf. (INTELEC), 2013.

[134] F. Grassi, S. Pignari, J. Wolf, Channel characterization and EMC assessment of a PLC system for spacecraft DC differential power buses, IEEE Trans. on Electromagn. Compat., 53 (2011), pp. 664-675.

[135] S. Gerber, R. Patterson, B. Ray, C. Stell, Performance of a spacecraft DC-DC converter breadboard modified for low temperature operation, Proc. of the 31st Intersoc. Energy Convers. Eng. Conf., *IECEC 96.,* 1 (1996), pp. 592-598.

[136] R. Nelms, L. Grigsby, Simulation of DC spacecraft power systems, IEEE Trans. on Aerosp. and Electron. Syst., 25 (1989), pp. 90-95.

[137] O. Mourra, A. Fernandez, F. Tonicello, S. Landstroem, Multiple port DC-DC converter for spacecraft power conditioning unit, 27th Annu. IEEE Appl. Power Electron. Conf. and Expos. (APEC), (2012), pp. 1278-1285.

[138] D. Kintner, Duke energy - EPRI DC powered data center demonstration: executive summary, Electric Power Research Institute (EPRI), (2011).

[139] D. Thompson, DC voltage stabilization control in telecommunications DC distribution systems, 24th Int. Telecommun. Energy Conf. (INTELEC), (2002), pp. 74- 78.

[140] T. Gruzs, J. Hall, AC, DC or hybrid power solutions for today's telecommunications facilities, 22nd Int. Telecommun. Energy Conf. (INTELEC), (2000), pp. 361-368.

[141] C. Foster, M. Dickinson, High voltage DC power distribution for telecommunications facilities, IEEE 30th Int. Telecommun. Energy Conf. (INTELEC), (2008), pp. 1-4.

[142] I. Barbi, R. Gules, Isolated DC-DC converters with high-output voltage for TWTA telecommunication satellite applications, IEEE Trans. on Power Electron., 18 (2003), pp.975-984.

[143] Sangsun Kim, M. H. Todorovic, P. N. Enjeti, Three-phase active harmonic rectifier (AHR) to improve utility input current THD in telecommunication power distribution system, IEEE Trans. on Ind. Appl., 39 (2003), pp.1414-1421.

[144] Kongwei, Qinlijun, Yangqixun, Dingfuhua, DC side short circuit transient simulation of DC traction power supply system, Int. Conf. on Power Syst. Technol. (PowerCon), 1 (2004), pp. 182- 186.

[145] Y. Cai, M. Irving, S. Case, Iterative techniques for the solution of complex DC-rail-traction systems including regenerative braking, IEE Proc.-Gener., Transm. and Distrib., 142 (1995), pp. 445-452.

[146] S. Joshi, R. Pathak, A. Jain, Modeling and analysis of DC traction system in light of recent innovations from HPC and virtual reality, Int. Conf. on Adv. in Recent Technol. in Commun. and Computing (ARTCom '09), 2009, pp. 525-527.

[147] Z. Panfeng, L. Yongli, An adaptive protection scheme in subway DC traction supply system, Int. Conf. on Power Syst. Technol., 2 (2002), pp. 716- 719.

[148] H. Ouyang, K. Zhang, P. Zhang, Y. Kang, J. Xiong, Repetitive compensation of fluctuating DC link voltage for railway traction drives, IEEE Trans. on Power Electron., 26 (2011), pp. 2160-2171.

[149] W. Liu, Q. Li, Minwu Chen, Study of the simulation of DC traction power supply system based on AC/DC unified Newton-Raphson method, Int. Conf. on Sustain. Power Gener. and Supply (SUPERGEN '09), (2009), pp. 1-4.

[150] D. Paul, DC traction power system grounding, IEEE Trans. on Ind. Appl., 38 (2002), pp. 818-824.

[151] P. Arboleya, G. Diaz, M. Coto, Unified AC/DC power flow for traction systems:

a new concept, IEEE Trans. on Vehicular Technol., 61 (2012), pp. 2421-2430.

[152] M. Cupelli et al., "Power Flow Control and Network Stability in an All-Electric Ship," in Proceedings of the IEEE, vol. 103, no. 12, pp. 2355-2380, Dec. 2015.

[153] J. Ciezki, R. Ashton, Selection and stability issues associated with a navy shipboard DC zonal electric distribution system, IEEE Trans. on Power Deliv., 15 (2000), pp. 665-669.

[154] P. Kankanala, S. Srivastava, A. Srivastava, N. Schulz, Optimal control of voltage and power in a multi-zonal MVDC shipboard power system, IEEE Trans. on Power Syst., 27 (2012), pp. 642-650.

[155] Y. Pan, P. M. Silveira, M. Steurer, T. L. Baldwin, P.F. Ribeiro, A fault location approach for high-impedance grounded DC shipboard power distribution systems, IEEE Power and Energy Soc. General Meeting, (2008), pp. 1-6.

[156] G. Sulligoi, A. Tessarolo, V. Benucci, M. Baret, A. Rebora, A. Taffone, Modeling, simulation, and experimental validation of a generation system for medium-voltage dc integrated power systems, IEEE Trans. on Ind. Appl., 46 (2010), pp. 1304-1310.

[157] Il-Yop Chung, W. Liu, K. Schoder, D. A. Cartes, Integration of a bi-directional DC–DC converter model into a real-time system simulation of a shipboard medium voltage DC system, Electric Power Systems Research, 81 (2011), pp. 1051-1059.

[158] M. Albu, E. Kyriakides, G. Chicco, M. Popa, A. Nechifor, Online monitoring of the power transfer in a DC test grid, IEEE Trans. Instrum. and meas., 59 (2010), pp.1104-1118.

[159] S. D. Sudhoff, S. Pekarek, B. Kuhn, S. Glover, J. Sauer, D. Delisle, Naval combat survivability testbeds for investigation of issues in shipboard power electronics based power and propulsion systems, IEEE Power Eng. Soc. Summer Meeting, 2002, pp.347-350.

[160] B. Cassimere, C. R. Valdez, S. Sudhoff, S. Pekarek, B. Kuhn, D. Delisle, E. Zivi, System impact of pulsed power loads on a laboratory scale integrated fight through power (IFTP) system, IEEE Electr. Ship Technol. Symp., (2005), pp.176-183.

[161] V. Salehi, A. Mohamed, A. Mazloomzadeh, O. A. Mohammed, Laboratory-based smart power system, part I: design and system development, IEEE Trans. on Smart Grid, 3 (2012), pp.1394-1404.

[162] V. Salehi, A. Mohamed, A. Mazloomzadeh, O.A. Mohammed, Laboratory-based smart power system, part II: control, monitoring, and protection, IEEE Trans. on Smart Grid, 3 (2012), pp.1405-1417.

[163] J. P. Kelley, D. A. Wetz, J.A. Reed, I. J. Cohen, G. K. Turner, W. Lee, The impact of power quality when high power pulsed DC and continuous AC loads are simultaneously operated on a microGrid testbed, IEEE Electr. Ship Technol. Symp. (ESTS), (2013), pp.6-12.

[164] S. K. Chaudhary, J. M. Guerrero and R. Teodorescu, "Enhancing the Capacity of the AC Distribution System Using DC Interlinks—A Step Toward Future

DC Grid," IEEE Transactions on Smart Grid, vol. 6, no. 4, pp. 1722-1729, July 2015.

[165] X. Liu, P. Wang and P. C. Loh, "A Hybrid AC/DC Microgrid and Its Coordination Control," in IEEE Transactions on Smart Grid, vol. 2, no. 2, pp. 278-286, June 2011.

[166] N. Eghtedarpour and E. Farjah, "Power Control and Management in a Hybrid AC/DC Microgrid," in IEEE Transactions on Smart Grid, vol. 5, no. 3, pp. 1494-1505, May 2014.

[167] R. R. Bushway, "Electromagnetic aircraft launch system development considerations," in IEEE Transactions on Magnetics, vol. 37, no. 1, pp. 52-54, Jan 2001.

[168] H. A. Toliyat, S. Talebi, P. McMullen, Co Huynh and A. Filatov, "Advanced high-speed flywheel energy storage systems for pulsed power applications," IEEE Electric Ship Technologies Symposium, PP. 379-386, 2005.

[169] J. McGroarty, J. Schmeller, R. Hockney and M. Polimeno, "Flywheel energy storage systems for electric start and an all-electric ship," IEEE Electric Ship Technologies Symposium, PP. 400-406, 2005.

[170] C. S. Hearn, M. C. Lewis, and R. E. Hebner, "Sizing advanced flywheel energy storage," Center for Electromechanics (CEM), the University of Texas at Austin, Aug. 2012. "Available Online: http://www.utexas.edu/ research/cem/images/GCEP%20Program.pdf"

[171] S. McCluer and J.-F. Christin "Comparing Data Center Batteries, Flywheels, and Ultracapacitors," Schneider Electric-Data Center Science Center, white paper No. 65, Rev. 2, 2011.

[172] Department of Defense Interface Standard for shipboard systems: Electric Power, Alternating Current, MIL-STD-1399, Section 300B, Apr. 2008.

[173] A. S. Nagorny, N. V. Dravid, R. H. Jansen, and B. H. Kenny, "Design aspects of a high speed permanent magnet synchronous motor/generator for flywheel applications," in Proc. IEEE International Electric Machines and Drives Conference (IEMDC), 2005, pp. 635–641.

[174] M. Farhadi, and O. Mohammed, "Adaptive Energy Management in Redundant Hybrid DC Microgrid for Pulse Load Mitigation," IEEE Transactions on Smart Grid, vol. 6, no. 1, pp. 54–62, Jan. 2015.

[175] L. Zhou, and Z. ping Qi, "Modeling and control of a flywheel energy storage system for uninterruptable power supply," IEEE International Conference on Sustainable Power Generation and Supply (SUPERGEN '09), 2009.

[176] R. Hebner, J. Beno and A. Walls, "Flywheel batteries come around again," IEEE Spectrum, vol. 39, no. 4, pp. 46–51, 2002.

[177] Available Online: http://www.grc.nasa.gov/WWW/RT/2004/RS/RS10S-jansen.html

[178] R. Okou, A. Sebitosi, M. A. Khan, P. Barendsa, and P. Pillay "Design and analysis of an electromechanical battery for rural electrification in sub-Saharan

Africa," IEEE Transactions on Energy Conversion, vol. 26, no. 4, pp. 1198-1209, Dec. 2011.

[179] T. D. Nguyen, K. J. Tseng, S. Zhang, and H. T. Nguyen, "A novel axial flux permanent magnet machine for flywheel energy storage system: Design and analysis," IEEE Transactions on Industrial Electronics, vol. 58, no. 9, pp. 3784–3794, Sep. 2011.

[180] R. S. Weissbach, G. G. Karady and R. G. Farmer "A combined uninterruptible power supply and dynamic voltage compensator using a flywheel energy storage system," IEEE Transactions on Power Delivery, vol. 16, no. 2, pp. 265-270, April. 2001.

[181] James R. Hall, "Electronic Equipment Handbook on Methods for Meeting U.S. Navy Shipboard Electrical Power Interface Requirements," Dahlgren division naval surface warfare center, April, 2000.

[182] B. P. Roberts and C. Sandberg, "The Role of Energy Storage in Development of Smart Grids," Proceedings of the IEEE, vol. 99, no. 6, pp. 1139–1144, Jun. 2011.

[183] M. C. Such and C. Hill, "Battery energy storage and wind energy integrated into the Smart Grid," in Innovative Smart Grid Technologies (ISGT), 2012 IEEE PES, 2012, pp. 1–4.

[184] L. Xu, Z. Miao, and L. Fan, "Control of a battery system to improve operation of a microgrid," in 2012 IEEE Power and Energy Society General Meeting, 2012, pp. 1–8.

[185] Ahmed S. A. Awad, Tarek H. M. El-Fouly, and Magdy M. A. Salama, "Optimal ESS Allocation and Load Shedding for Improving Distribution System Reliability," IEEE Trans. on Smart Grid, vol.5, no.5, pp.2339-2349, Sept. 2014.

[186] K. W. Wee, S. S. Choi and D. M. Vilathgamuwa, "Design of a Least-Cost Battery-Supercapacitor Energy Storage System for Realizing Dispatchable Wind Power," in IEEE Transactions on Sustainable Energy, vol. 4, no. 3, pp. 786-796, July 2013.

[187] FACT SHEET: Obama Administration Announces Federal and Private Sector Actions on Scaling Renewable Energy and Storage with Smart Markets, Available Online: https://www.whitehouse.gov/the-press-office/2016/06/16/fact-sheet-obama-administration-announces-federal-and-private-sector. Retrieved 06/16/2016

[188] M. A. Roscher, J. Assfalg and O. S. Bohlen, "Detection of Utilizable Capacity Deterioration in Battery Systems," in IEEE Transactions on Vehicular Technology, vol. 60, no. 1, pp. 98-103, Jan. 2011.

[189] GTMResearch & Energy Storage Association (ESA) " U.S. Energy Storage Monitor: Q2 2016 Executive summary", June 2016.

[190] J. Kim, S. Lee, and B. Cho, "Discrimination of battery characteristics using discharging/charging voltage pattern recognition," in IEEE Energy Conversion Congress and Exposition, ECCE 2009, pp. 1799–1805.

[191] D. Zhu, S. Yue, Y. Wang, Y. Kim, N. Chang, and M. Pedram, "Designing a residential hybrid electrical energy storage system based on the energy buffering

strategy," in 2013 International Conference on Hardware/Software Codesign and System Synthesis (CODES+ISSS), 2013, pp. 1–9.

[192] H. Babazadeh, B. Asghari, and R. Sharma, "A new control scheme in a multi-battery management system for expanding microgrids," in Innovative Smart Grid Technologies Conference (ISGT), IEEE PES, 2014, pp. 1–5.

[193] R.S. Treptow, "The Lead-Acid Battery: Its Voltage in Theory and in Practice," J. Chemical Educ., vol. 79, no. 3, pp. 334-338, 2002.

[194] Z. Miao, L. Xu, V. R. Disfani, and L. Fan, "An SOC-Based Battery Management System for Microgrids," IEEE Transactions on Smart Grid, vol. 5, no. 2, pp. 966–973, Mar. 2014.

[195] H. Chaoui and P. Sicard, "Hierarchical energy management scheme for multiple battery-based smart grids," in 2014 IEEE 23rd International Symposium on Industrial Electronics (ISIE), 2014, pp. 2020–2023.

[196] S. W. Moore and P. J. Schneider, "A review of cell equalization methods for lithium ion and lithium polymer battery systems," presented at the SAE 2001 World Congr., Detroit, MI, Mar. 2001.

[197] H. Qian, J. Zhang, J.-S. Lai, and W. Yu, "A high-efficiency grid-tie battery energy storage system," IEEE Transactions on Power Electronics, vol. 26, no. 3, pp. 886–896, Mar. 2011.

[198] M. T. Lawder, B. Suthar, P. W. C. Northrop, S. De, C. M. Hoff, O. Leitermann, M. L. Crow, S. Santhanagopalan, and V. R. Subramanian, "Battery Energy Storage System (BESS) and Battery Management System (BMS) for Grid-Scale Applications," Proceedings of the IEEE, vol. 102, no. 6, pp. 1014–1030, Jun. 2014.

[199] Jiapeng Wen, and Jiuchun Jiang, "Battery management system for the charge mode of quickly exchanging battery package," IEEE Vehicle Power and Propulsion Conference, 2008. VPPC '08, pp.1-4, 3-5 Sept. 2008.

[200] Wangbiao Qiu, and Zhiyuan Qiu, "Design for symmetrical management of storage battery expert system based on single battery," Proceedings of the 2006 IEEE International Conference on Mechatronics and Automation, pp.1141-1146, 25-28 June 2006.

[201] D. Tran and A. M. Khambadkone, "Energy Management for Lifetime Extension of Energy Storage System in Micro-Grid Applications," IEEE Transactions on Smart Grid, vol. 4, no. 3, pp. 1289–1296, Sep. 2013.

[202] S. Grillo, M. Marinelli, S. Massucco, and F. Silvestro, "Optimal Management Strategy of a Battery-Based Storage System to Improve Renewable Energy Integration in Distribution Networks," IEEE Transactions on Smart Grid, vol. 3, no. 2, pp. 950–958, Jun. 2012.

[203] G. Yifeng and Z. Chengning, "Study on the fast charging method of lead-acid battery with negative pulse discharge," in 2011 4th International Conference on Power Electronics Systems and Applications (PESA), 2011, pp. 1–4.

[204] W.-S. Jwo and W.-L. Chien, "Design and Implementation of a Charge Equalization Using Positive/Negative Pulse Charger," in Conference Record of

the 2007 IEEE Industry Applications Conference, 2007. 42nd IAS Annual Meeting, 2007, pp. 1076–1081.

[205] M. Coleman, C. K. Lee, and W. G. Hurley, "State of Health Determination: Two Pulse Load Test for a VRLA Battery," in 37th IEEE Power Electronics Specialists Conference, 2006. PESC '06, 2006, pp. 1–6.

[206] Y. Shi, C. Ferone, C. Rao, and C. D. Rahn, "Nondestructive forensic pathology of Lead-Acid batteries," in American Control Conference (ACC), 2012, 2012, pp. 1350–1355.

[207] T. K. Cheung, K. W. E. Cheng, H. L. Chan, Y. L. Ho, H. S. Chung, and K. P. Tai, "Maintenance techniques for rechargeable battery using pulse charging," in 2nd International Conference on Power Electronics Systems and Applications, 2006. ICPESA '06, 2006, pp. 205–208.

[208] D. Linden, T. B. Reddy, "Lead Acid Batteries" in Handbook of Batteries, 3rd ed. New York, NY: McGraw-Hill, 2002, ch, 23.

[209] K. Onda, M. Nakayama, K. Fukuda, K. Wakahara, and T. Araki, "Cell Impedance Measurement by Laplace Transformation of Charge or Discharge Current–Voltage," J. Electrochem. Soc., vol. 153, no. 6, pp. A1012–A1018, Jun. 2006.

[210] NI 9206: 16-Channel Analog Input Module for Fuel Cells, National Instruments, Austin, TX, Feb. 2008.

[211] UPG, "UB121100 12V 110 Ah SLA Battery Spec Sheet," UPG No. 45824, Carrollton, TX. Available Online on: http://upgi.com/Themes/leanandgreen/images/UPG/ProductDownloads/45981.pdf

[212] Maxwell Technologies, "Application Note: BOOSTCAP Energy Storage Modules Life Duration Estimation", 2007, Available Online on: http://www.maxwell.com/images/documents/applicationnote_1012839_1.pdf

[213] T. Dragičević, X. Lu, J. C. Vasquez and J. M. Guerrero, "DC Microgrids—Part II: A Review of Power Architectures, Applications, and Standardization Issues," in IEEE Transactions on Power Electronics, vol. 31, no. 5, pp. 3528-3549, May 2016.

[214] Junyi Shen and A. Khaligh, "A Supervisory Energy Management Control Strategy in a Battery/Ultracapacitor Hybrid Energy Storage System," in IEEE Transactions on Transportation Electrification, vol. 1, no. 3, pp. 223-231, Oct. 2015.

[215] A. Esmaili, B. Novakovic, A. Nasiri and O. Abdel-Baqi, "A Hybrid System of Li-Ion Capacitors and Flow Battery for Dynamic Wind Energy Support," in

IEEE Transactions on Industry Applications, vol. 49, no. 4, pp. 1649-1657, July-Aug. 2013.

[216] Z. Miao, L. Xu, V. R. Disfani, L. Fan, An SOC-Based Battery Management System for Microgrids, IEEE Trans. on Smart Grid, vol. 5, no. 2, pp. 966–973, Mar. 2014.

[217] J.-Y. Kim, J.-H. Jeon, S.-K. Kim, C. Cho, J. H. Park, H.-M. Kim, K.-Y. Nam, Cooperative Control Strategy of Energy Storage System and Microsources for Stabilizing the Microgrid during Islanded Operation, IEEE Trans. on Power Electron., 25 (2010) 3037–3048.

[218] H. Karimi, H. Nikkhajoei, R. Iravani, Control of an Electronically-Coupled Distributed Resource Unit Subsequent to an Islanding Event, IEEE Trans. on Power Delivery, 23 (2008) 493–501.

[219] G. Diaz, C. Gonzalez-Moran, J. Gomez-Aleixandre, A. Diez, Scheduling of droop coefficients for frequency and voltage regulation in isolated microgrids, IEEE Trans. Power Syst., 25 (2010) 489–496.

[220] M. Guerrero, J. C. Vasquez, J. Matas, M. Castilla, L. G. de Vicuna, Control strategy for flexible microgrid based on parallel line-interactive UPS systems, IEEE Trans. Industrial Electronics, 56 (2009) 726–736.

[221] "AeroWeb | DDG 1000 Zumwalt Class Destroyer,AeroWeb. [Online]. Available: http://www.bga-aeroweb.com/Defense/DDG-1000-Zumwalt-Destroyer.html.

[222] T. Jaster, A. Rowe, Z. Dong, Modeling and simulation of a hybrid electric propulsion system of a green ship, 2014 IEEE/ASME 10th International Conference on Mechatronic and Embedded Systems and Applications (MESA), 2014, pp. 1–6.

[223] M. Steurer, M. Andrus, J. Langston, L. Qi, S. Suryanarayanan, S. Woodruff, P. F. Ribeiro, Investigating the Impact of Pulsed Power Charging Demands on Shipboard Power Quality, IEEE Electric Ship Technologies Symposium, 2007. ESTS '07, pp. 315–321.

[224] A. Neffati, M. Guemri, S. Caux, and M. Fadel, "Energy management strategies for multi source systems," Electric Power Systems Research, vol. 102, pp. 42–49, Sep. 2013.

[225] M. Falahi, K. L. Butler-Purry, M. Ehsani, Reactive Power Coordination of Shipboard Power Systems in Presence of Pulsed Loads, IEEE Trans. on Power Systems, 28 (2013) 3675–3682.

[226] E. A. Lewis, M. Butcher, Managing multiple and varying energy demands in naval combatants with integrated electric propulsion, Pulsed Power Symp., 2005, pp. 32/1–32/6.

[227] L. N. Domaschk, A. Ouroua, R. E. Hebner, O. E. Bowlin, W. B. Colson, Coordination of Large Pulsed Loads on Future Electric Ships, IEEE Trans. on Magnetics, 43 (2007) 450–455.

[228] B. Vural and C. S. Edrington, Ultra-capacitor based pulse power management in electrical ships, 2012 IEEE Transportation Electrification Conference and Expo (ITEC), 2012.

[229] B. M. Huhman, J. M. Neri, D. A. Wetz, Design of a battery intermediate storage system for rep-rated pulsed power loads, 2013 IEEE Electric Ship Technologies Symp. (ESTS), 2013.

[230] I. Lahbib, A. Lahyani, A. Sari, P. Venet, Performance analysis of a lead-acid battery/supercapacitors hybrid and a battery stand-alone under pulsed loads, 2014 Intl. Conf. on Green Energy, 2014, pp. 273–278.

[231] G. L. Kusic, J. M. Heinzel, D. J. Hoffman, Monitoring pulsed power on ship electrical systems, 2013 IEEE Electric Ship Technologies Symposium (ESTS), 2013, pp. 13–20.

[232] Y. Tang, A. Khaligh, Bidirectional hybrid Battery/Ultracapacitor Energy Storage Systems for next generation MVDC shipboard power systems, 2011 IEEE Vehicle Power and Propulsion Conference (VPPC), 2011.

[233] L. Gao, R. A. Dougal, S. Liu, Power enhancement of an actively controlled battery/ultracapacitor hybrid, IEEE Trans. on Power Electron., 20 (2005) 236–243.

[234] Batteryspace.com, Lithium Ion Polymer Rechargeable Battery, Model HA055275, Richmond, CA. Available Online at: http://www.batteryspace.com /Prod-specs/A055275-21Ah.pdf

[235] IEC 62576, "Electric double-layer capacitors for use in hybrid electric vehicles - Test methods for electrical characteristics", IEC, Edition 1.0, Aug., 2009.

[236] Maxwell, 16V small cell module, Model: BMOD0058 E016 B02 (16.2V-58 F), San Diego, CA. Available Online at: http://www.maxwell.com/images/

documents/datasheet_16v_small_cell_module.pdf

[237] Dexter Johnson, " "Holey" Graphene Boosts Energy Density of Supercapacitors", *IEEE Spectrum*, Aug., 2014. Available Online: http://spectrum.ieee.org/nanoclast/consumer-electronics/portable-devices/ holey -graphene-boosts-energy-density-of-supercapacitors

[238] M. S. Whittingham, "History, Evolution, and Future Status of Energy Storage," in *Proceedings of the IEEE*, vol. 100, no. Special Centennial Issue, pp. 1518-1534, May 13 2012.

[239] K. Mikkelsen, "Design and evaluation of hybrid energy storage systems for electric powertrains," M.S. thesis, University of Waterloo, Waterloo, ON, Canada, 2010.

[240] S. Lu, K. A. Corzine, and M. Ferdowsi, "A new battery/ultracapacitor energy storage system design and its motor drive integration for hybrid electric vehicles,"IEEE Trans. Veh. Technol. , vol. 56, no. 4, pp. 1516– 1523, Jul. 2007

[241] P. Keil, M. Englberger and A. Jossen, "Hybrid Energy Storage Systems for Electric Vehicles: An Experimental Analysis of Performance Improvements at Subzero Temperatures," in *IEEE Transactions on Vehicular Technology*, vol. 65, no. 3, pp. 998-1006, March 2016.

[242] U.S. Department of Energy Vehicle Technologies Program, "Battery Test Manual For Plug-In Hybrid Electric Vehicles, REVISION 0".

[243] Christopher R. Lashway, Ahmed Elsayed, and O. A. Mohammed, " Management Scheme for Parallel Connected Hybrid Energy Storage in Electric Vehicles," IEEE Power and Energy Society General Meeting, Boston, MI, Jul. 17-21, 2016.

[244] IEEE Recommended Practice for Electrical Installations on Shipboard," IEEE Std 45-2002, Oct. 2002.

[245] M. Farhadi and Osama A. Mohammed, "Performance Enhancement of Actively Controlled Hybrid DC Microgrid Incorporating Pulsed Load," in IEEE Transactions on Industry Applications, vol. 51, no. 5, pp. 3570-3578, Sept.-Oct. 2015.

[246] Junyi Shen and A. Khaligh, "A Supervisory Energy Management Control Strategy in a Battery/Ultracapacitor Hybrid Energy Storage System," in IEEE Transactions on Transportation Electrification, vol. 1, no. 3, pp. 223-231, Oct. 2015.

[247] A. Esmaili, B. Novakovic, A. Nasiri and O. Abdel-Baqi, "A Hybrid System of

Li-Ion Capacitors and Flow Battery for Dynamic Wind Energy Support," in IEEE Transactions on Industry Applications, vol. 49, no. 4, pp. 1649-1657, July-Aug. 2013.

[248] Ahmed T. Elsayed, Ahmed A. Mohamed and Osama A. Mohammed, "DC microgrids and distribution systems: An overview", Electric Power Systems Research Journal, 119, February 2015, 407-417.

[249] A. Ostadi and M. Kazerani, "Optimal Sizing of the Battery Unit in a Plug-in Electric Vehicle," in IEEE Transactions on Vehicular Technology, vol. 63, no. 7, pp. 3077-3084, Sept. 2014.

[250] S. X. Chen, H. B. Gooi and M. Q. Wang, "Sizing of Energy Storage for Microgrids," in IEEE Transactions on Smart Grid, vol. 3, no. 1, pp. 142-151, March 2012.

[251] T. K. A. Brekken, A. Yokochi, A. von Jouanne, Z. Z. Yen, H. M. Hapke and D. A. Halamay, "Optimal Energy Storage Sizing and Control for Wind Power Applications," in IEEE Transactions on Sustainable Energy, vol. 2, no. 1, pp. 69-77, Jan. 2011.

[252] Changsong Chen, Shanxu Duan, Tao Cai, Bangyin Liu and Guozhen Hu, "Optimal Allocation and Economic Analysis of Energy Storage System in Microgrids," in IEEE Transactions on Power Electronics, vol. 26, no. 10, pp. 2762-2773, Oct. 2011.

[253] H. Pandžić, Y. Wang, T. Qiu, Y. Dvorkin and D. S. Kirschen, "Near-Optimal Method for Siting and Sizing of Distributed Storage in a Transmission Network," in IEEE Transactions on Power Systems, vol. 30, no. 5, pp. 2288-2300, Sept. 2015.

[254] Frederick S. Hillier and Gerald J. Lieberman "Introduction to Operations Research", Seventh Edition, New York, McGraw-Hill, 2001.

[255] U. Baumgartner, T. Ebner, and C. Magele, "Optimization in Electrical Engineering," Technical University of Graz, Austria.

[256] Marco Cavazzuti, "Optimization Methods: From Theory to Design," Springer, 2013.

[257] Joshua A. Taylor "Convex Optimization of Power Systems", Cambridge University Press, 2015.

[258] S. Lyden, and M. E. Haque " A Comprehensive Study of the Key Parameters of the Simulated Annealing Method for Maximum Power Point Tracking in

Photovoltaic Systems," IEEE Power and Energy Society General Meeting, Boston, MA, Jul. 17-21, 2016.

[259] Jong-Bae Park; Yun-Won Jeong; Joong-Rin Shin; Lee, K.Y., "An Improved Particle Swarm Optimization for Nonconvex Economic Dispatch Problems," in Power Systems, IEEE Transactions on , vol.25, no.1, pp.156-166, Feb. 2010

[260] Saber, A.Y.; Senjyu, T., "Memory-Bounded Ant Colony Optimization With Dynamic Programming and A∗ Local Search for Generator Planning," in Power Systems, IEEE Transactions on , vol.22, no.4, pp.1965-1973, Nov. 2007.

[261] Vlachogiannis, J.G.; Hatziargyriou, N.D.; Lee, K.Y., "Ant Colony System-Based Algorithm for Constrained Load Flow Problem," in Power Systems, IEEE Transactions on , vol.20, no.3, pp.1241-1249, Aug. 2005.

[262] Favuzza, S.; Graditi, G.; Ippolito, M.G.; Sanseverino, E.R., "Optimal Electrical Distribution Systems Reinforcement Planning Using Gas Micro Turbines by Dynamic Ant Colony Search Algorithm," in Power Systems, IEEE Transactions on , vol.22, no.2, pp.580-587, May 2007.

[263] Chung-Fu Chang, "Reconfiguration and Capacitor Placement for Loss Reduction of Distribution Systems by Ant Colony Search Algorithm," in Power Systems, IEEE Transactions on , vol.23, no.4, pp.1747-1755, Nov. 2008.

[264] Shaobing Yang; Mingli Wu; Xiu Yao; Jiuchun Jiang, "Load Modeling and Identification Based on Ant Colony Algorithms for EV Charging Stations," in Power Systems, IEEE Transactions on , vol.30, no.4, pp.1997-2003, July 2015.

[265] Engineering Optimization by Cuckoo Search, Available Online: https://arxiv.org/pdf/1005.2908.pdf.

[266] Cuckoo Search via Levy Flights, Available Online: https://arxiv.org/pdf/1003.1594.pdf

[267] Yang, Xin-She and Deb, Suash, "Cuckoo search: recent advances and applications" Journal of Neural Computing and Applications, Springer, vol. 24, no. 1, pp. 169-174, Jan. 2014.

[268] Mirjalili, S., Mirjalili, S.M., Lewis, A.:'Grey Wolf Optimizer', Int. J. Adv. Eng. Softw., 2014,69, (1), pp. 46– 61.

[269] S. Sharma, S. Bhattacharjee and A. Bhattacharya, "Grey wolf optimisation for optimal sizing of battery energy storage device to minimise operation cost of microgrid," in IET Generation, Transmission & Distribution, vol. 10, no. 3, pp. 625-637, 2 18 2016.

[270] S. Mohanty, B. Subudhi and P. K. Ray, "A New MPPT Design Using Grey Wolf Optimization Technique for Photovoltaic System Under Partial Shading Conditions," in IEEE Transactions on Sustainable Energy, vol. 7, no. 1, pp. 181-188, Jan. 2016.

[271] J. Rameshkumar, S. Ganesan, M. Abirami and S. Subramanian, "Cost, emission and reserve pondered pre-dispatch of thermal power generating units coordinated with real coded grey wolf optimisation," in IET Generation, Transmission & Distribution, vol. 10, no. 4, pp. 972-985, 3 10 2016.

[272] H. Ghazzai, E. Yaacoub, M. S. Alouini, Z. Dawy and A. Abu-Dayya, "Optimized LTE Cell Planning With Varying Spatial and Temporal User Densities," in IEEE Transactions on Vehicular Technology, vol. 65, no. 3, pp. 1575-1589, March 2016.

[273] K. Deb, A. Pratap, S. Agarwal and T. Meyarivan, "A fast and elitist multiobjective genetic algorithm: NSGA-II," in IEEE Transactions on Evolutionary Computation, vol. 6, no. 2, pp. 182-197, Apr 2002.

[274] L. Chen; H. Li, "Optimized Reactive Power Supports Using Transformer Tap Stagger in Distribution Networks," in IEEE Transactions on Smart Grid , vol.PP, no.99, pp.1-10, 2016, doi: 10.1109/TSG.2016.2539824

[275] I. Das and J. E. Dennis, "A closer look at drawbacks of minimizing weighted sums of objectives for Pareto set generation in multicriteria optimization problems," Struct. Optim., vol. 14, pp. 63–69, 1997.

[276] R. Baños, F. Manzano-Agugliaro, F.G. Montoya, C. Gil, A. Alcayde and J. Gómez, "Optimization methods applied to renewable and sustainable energy: A review," Renewable and Sustainable Energy Reviews, vol. 15, no. 4, pp. 1753-1766, May 2011.

[277] V. Pareto, "Manual of Political Economy," New English Trans. edition, Publisher: Augustus M. Kelley, 1971.

[278] A. Ahuja, S. Das and A. Pahwa, "An AIS-ACO Hybrid Approach for Multi-Objective Distribution System Reconfiguration," in IEEE Transactions on Power Systems, vol. 22, no. 3, pp. 1101-1111, Aug. 2007.

[279] M. A. Abido, "Multiobjective evolutionary algorithms for electric power dispatch problem," in IEEE Transactions on Evolutionary Computation, vol. 10, no. 3, pp. 315-329, June 2006.

[280] M.A. Abido, A niched Pareto genetic algorithm for multiobjective

environmental/economic dispatch, International Journal of Electrical Power & Energy Systems, vol. 25, no. 2, pp. 97-105, February 2003.

[281] M. Baradar and M. Ghandhari, "A Multi-Option Unified Power Flow Approach for Hybrid AC/DC Grids Incorporating Multi-Terminal VSC-HVDC," in IEEE Transactions on Power Systems, vol. 28, no. 3, pp. 2376-2383, Aug. 2013.

[282] J. Beerten, S. Cole and R. Belmans, "Generalized Steady-State VSC MTDC Model for Sequential AC/DC Power Flow Algorithms," in IEEE Transactions on Power Systems, vol. 27, no. 2, pp. 821-829, May 2012.

[283] S. Cole, J. Beerten and R. Belmans, "Generalized Dynamic VSC MTDC Model for Power System Stability Studies," in IEEE Transactions on Power Systems, vol. 25, no. 3, pp. 1655-1662, Aug. 2010.

[284] C. Gammeter; F. Krismer; J. Kolar, "Comprehensive Conceptualization, Design, and Experimental Verification of a Weight-Optimized All-SiC 2kV/700V DAB for an Airborne Wind Turbine," in IEEE Journal of Emerging and Selected Topics in Power Electronics, vol. PP, no.99.

[285] D. Kampen, "Advanced compact medium frequency transformers," PCIM Europe 2015; International Exhibition and Conference for Power Electronics, Intelligent Motion, Renewable Energy and Energy Management; Proceedings of, Nuremberg, Germany, 2015, pp. 1-5.

[286] Available Online: http://media.digikey.com/pdf/Data%20Sheets/ IXYS%20PDFs/MIO1200-25E10.pdf)

[287] Available Online: http://www.wakefieldvette.com/ Portals/0/resources/datasheets/392.pdf

[288] M. Hajian, J. Robinson, D. Jovcic and B. Wu, "30 kW, 200 V/900 V, Thyristor LCL DC/DC Converter Laboratory Prototype Design and Testing," IEEE Transactions on Power Electronics, vol. 29, no. 3, pp. 1094-1102, March 2014.

[289] L. Tang, G. Rizzoni and S. Onori, "Energy Management Strategy for HEVs Including Battery Life Optimization," IEEE Transactions on Transportation Electrification, vol. 1, no. 3, pp. 211-222, Oct. 2015.

[290] T. L. Baldwin and S. A. Lewis, "Distribution load flow methods for shipboard power systems," IEEE Transactions on Industry Applications, vol. 40, no. 5, pp. 1183-1190, Sept.-Oct. 2004.

[291] M. E. Baran and N. R. Mahajan, "DC distribution for industrial systems: opportunities and challenges," IEEE Transactions on Industry Applications, vol.

39, no. 6, pp. 1596-1601, Nov.-Dec. 2003.

[292] J. Beerten, and R. Belmans, "Development of an Open Source Power Flow Software for HVDC Grids and Hybrid AC/DC Systems: MatACDC," IET Generation Transmission and Distribution, vol. 9, no. 10, Jun. 2015, pp. 966-974.

[293] R. D. Zimmerman, C. E. Murillo-Sánchez, and R. J. Thomas, "MATPOWER Steady-State Operations, Planning and Analysis Tools for Power Systems Research and Education,", IEEE Transactions on Power Systems, vol. 26, no. 1, pp. 12-19, Feb. 2011.

[294] Available Online: http://batteryuniversity.com/learn/article/the_high_power_lithium_ion.

[295] D. Temkin, T. Boehmer and A. Billups, "Adaptive Power System for Managing Large Dynamic Loads," in IEEE Transactions on Power Delivery, vol. 31, no. 2, pp. 630-639, April 2016.

[296] D. Sciano et al., "Evaluation of DC Links on Dense-Load Urban Distribution Networks," IEEE Transactions on Power Delivery, vol. 31, no. 3, pp. 1317-1326, June 2016.

[297] A. K. Basu, S. Chowdhury and S. P. Chowdhury, "Impact of Strategic Deployment of CHP-Based DERs on Microgrid Reliability," IEEE Trans. on Power Delivery, vol. 25, no. 3, pp. 1697-1705, Jul. 2010.

[298] G. T. Heydt, "The Next Generation of Power Distribution Systems," in IEEE Transactions on Smart Grid, vol. 1, no. 3, pp. 225-235, Dec. 2010.

[299] H. A. Mostafa, R. El-Shatshat and M. M. A. Salama, "Multi-Objective Optimization for the Operation of an Electric Distribution System With a Large Number of Single Phase Solar Generators," in IEEE Transactions on Smart Grid, vol. 4, no. 2, pp. 1038-1047, June 2013.

[300] H. A. Mostafa, R. El Shatshat and M. M. A. Salama, "Optimal Distribution Systems Operation Using Smart Matching Scheme (SMS) for Smart Grid Applications," in IEEE Transactions on Smart Grid, vol. 5, no. 4, pp. 1938-1948, July 2014.

[301] A. Vieira Pombo, João Murta-Pina, and V. Fernão Pires, "A multiobjective placement of switching devices in distribution networks incorporating distributed energy resources," Electric Power Systems Research, vol. 130, pp. 34-45, Jan. 2016.

[302] Q. Li, M. Liu and H. Liu, "Piecewise Normalized Normal Constraint Method Applied to Minimization of Voltage Deviation and Active Power Loss in an AC–DC Hybrid Power System," in IEEE Transactions on Power Systems, vol. 30, no. 3, pp. 1243-1251, May 2015.

[303] Dorit S. Hochbaum "Approximation Algorithms for NP-Hard Problems" Course technology, 1st edition, 1996.

[304] Feng-Tse Lin, Cheng-Yan Kao and Ching-Chi Hsu, "Applying the genetic approach to simulated annealing in solving some NP-hard problems," in IEEE Transactions on Systems, Man, and Cybernetics, vol. 23, no. 6, pp. 1752-1767, Nov/Dec 1993.

[305] K. Lehmann, A. Grastien and P. Van Hentenryck, "AC-Feasibility on Tree Networks is NP-Hard," in *IEEE Transactions on Power Systems*, vol. 31, no. 1, pp. 798-801, Jan. 2016.

[306] Z. Jin, G. Sulligoi, R. Cuzner, L. Meng, J. C. Vasquez and J. M. Guerrero, "Next-Generation Shipboard DC Power System: Introduction Smart Grid and dc Microgrid Technologies into Maritime Electrical Networks," in IEEE Electrification Magazine, vol. 4, no. 2, pp. 45-57, June 2016.

[307] F. Milano, "An open source power system analysis toolbox,"IEEETrans. Power Syst., vol. 20, no. 3, pp. 1199–1206, Aug. 2005.

[308] S. Cole and R. Belmans, "MatDyn, A New Matlab-Based Toolbox for Power System Dynamic Simulation," in *IEEE Transactions on Power Systems*, vol. 26, no. 3, pp. 1129-1136, Aug. 2011.

[309] P. Sauer and M. A. Pai, Power System Dynamics and Stability, Prentice Hall, 1998.

[310] Krause, P.C., Analysis of Electric Machinery, McGraw-Hill, 1986.

[311] T. Weckesser, H. Jóhannsson and J. Østergaard, "Impact of model detail of synchronous machines on real-time transient stability assessment," *Bulk Power System Dynamics and Control - IX Optimization, Security and Control of the Emerging Power Grid (IREP), 2013 IREP Symposium*, Rethymno, 2013, pp. 1-9.

[312] I. C. Report, "Dynamic Models for Steam and Hydro Turbines in Power System Studies," IEEE Transactions on Power Apparatus and Systems, vol. PAS-92, no. 6, pp. 1904-1915, Nov. 1973.

[313] G. Daelemans, "VSC HVDC in meshed networks," Master's thesis, Katholieke

Universiteit Leuven, Leuven, Belgium, 2008.

[314] W. Feng, L. A. Tuan, L. B. Tjernberg, A. Mannikoff and A. Bergman, "A New Approach for Benefit Evaluation of Multiterminal VSC–HVDC Using A Proposed Mixed AC/DC Optimal Power Flow," in IEEE Transactions on Power Delivery, vol. 29, no. 1, pp. 432-443, Feb. 2014.

[315] Power Systems Test Case Archive, University of Washington, Available Online: https://www.ee.washington.edu/research/pstca/

[316] P. M. Anderson and A. A. Fouad, "Power System Control and Stability" 2nd edition, New York, Wiley-IEEE Press, 2002.

[317] B.H. Kenny, P.E. Kascak, R. Jansen, T. Dever, and W. Santiago, "Control of a high-speed flywheel system for energy storage in space applications," IEEE Transactions on Industry Applications, vol.41, no.4, pp.1029,1038, July-Aug. 2005.

[318] R. G. Lawrence, K. L. Craven, and G. D. Nichols, "Flywheel UPS," IEEE Industry Applications Magazine, vol.9, no.3, pp.44-50, May-June 2003.

[319] T. Dragicevic, S. Sucic, J.C. Vasquez, and J.M. Guerrero, "Flywheel-Based Distributed Bus Signalling Strategy for the Public Fast Charging Station," IEEE Transactions on Smart Grid, vol.5, no.6, pp.2825,2835, Nov. 2014.

[320] G.O. Suvire, M.G. Molina, and P.E. Mercado, "Improving the Integration of Wind Power Generation Into AC Microgrids Using Flywheel Energy Storage," IEEE Transactions on Smart Grid, vol.3, no.4, pp.1945,1954, Dec. 2012

[321] Bingsen Wang, and G. Venkataramanan,"Dynamic Voltage Restorer Utilizing a Matrix Converter and Flywheel Energy Storage," IEEE Transactions on Industry Applications, vol.45, no.1, pp.222-231, Jan.-Feb. 2009.

[322] R. Arghandeh, M. Pipattanasomporn, and S. Rahman, "Flywheel Energy Storage Systems for Ride-through Applications in a Facility Microgrid," IEEE Transactions on Smart Grid, vol.3, no.4, pp.1955-1962, Dec. 2012.

[323] L. Ran, Dawei Xiang, J.L. Kirtley, "Analysis of Electromechanical Interactions in a Flywheel System With a Doubly Fed Induction Machine," IEEE Transactions on Industry Applications, vol.47, no.3, pp.1498-1506, May-June 2011.

[324] S. Samineni, B.K. Johnson, H.L. Hess, and J.D. Law, "Modeling and analysis of a flywheel energy storage system for Voltage sag correction," IEEE Transactions on Industry Applications, vol.42, no.1, pp.42-52, Jan.-Feb. 2006.

[325] M.I. Daoud, A. Massoud, S. Ahmed, A.S. Abdel-Khalik, and A. Elserougi, "Ride-through capability enhancement of VSC-HVDC based wind farms using low speed flywheel energy storage system," 2014 Twenty-Ninth Annual IEEE Applied Power Electronics Conference and Exposition (APEC), pp.2706-2712, 16-20 March 2014.

[326] M.I. Daoud, A.S. Abdel-Khalik, A. Elserougi, S. Ahmed, and A.M. Massoud, "DC bus control of an advanced flywheel energy storage kinetic traction system for electrified railway industry," 39th Annual Conference of the IEEE Industrial Electronics Society, IECON 2013, pp.6596-6601, 10-13 Nov., 2013.

[327] A.S. Abdel-Khalik, A.A. Elserougi, A.M. Massoud, and S. Ahmed, "Fault Current Contribution of Medium Voltage Inverter and Doubly-Fed Induction-Machine-Based Flywheel Energy Storage System," IEEE Transactions on Sustainable Energy, vol.4, no.1, pp.58-67, Jan. 2013.

[328] A. Abdel-Khalik, A. Elserougi, A. Massoud, and S. Ahmed, "A power control strategy for flywheel doubly-fed induction machine storage system using artificial neural network," Electric Power Systems Research, vol 96, pp. 267-276, March 2013.

[329] D. Kairous, and R. Wamkeue, "DFIG-based fuzzy sliding-mode control of WECS with a flywheel energy storage," Electric Power Systems Research, vol 93, pp. 16-23, December 2012.

[330] J. Goncalves de Oliveira, H. Schettino, V. Gama, R. Carvalho, and H. Bernhoff, "Study on a doubly-fed flywheel machine-based driveline with an AC/DC/AC converter," IET Electrical Systems in Transportation, vol.2, no.2, pp.51-57, June 2012.

[331] I.A. Gowaid, A.A. Elserougi, A.S. Abdel-Khalik, A.M. Massoud, and S. Ahmed, "A series flywheel architecture for power levelling and mitigation of DC voltage transients in multi-terminal HVDC grids," IET Generation, Transmission & Distribution, vol.8, no.12, pp.1951-1959, Dec. 2014.

[332] H. Akagi, and H. Sato, "Control and performance of a doubly-fed induction machine intended for a flywheel energy storage system," IEEE Transactions on Power Electronics, vol.17, no.1, pp.109-116, Jan 2002.

[333] S.R. Gurumurthy, V. Agarwal, and A. Sharma, "Optimal energy harvesting from a high-speed brushless DC generator-based flywheel energy storage system," IET Electric Power Applications, vol.7, no.9, pp.693-700, November 2013.

[334] P. Tsao, M. Senesky, and S.R. Sanders, "An integrated flywheel energy storage system with homopolar inductor motor/generator and high-frequency drive," IEEE Transactions on Industry Applications, vol.39, no.6, pp.1710,1725, Nov.-Dec. 2003

[335] M. M. Flynn, P. McMullen, and O. Solis, "Saving energy using flywheels," IEEE Industry Applications Magazine, vol.14, no.6, pp.69-76, November-December 2008.

[336] Jae-Do Park; C. Kalev, and H.F. Hofmann, "Control of High-Speed Solid-Rotor Synchronous Reluctance Motor/Generator for Flywheel-Based Uninterruptible Power Supplies," IEEE Transactions on Industrial Electronics, vol.55, no.8, pp.3038-3046, Aug. 2008.

[337] Raymond G. Gadelrab, Mostafa S. Hamad, Ayman S. Abdel-Khalik, Amr El Zawawi, "Wind farms-fed HVDC system power profile enhancement using solid state transformer based flywheel energy storage system," Journal of Energy Storage, vol. 4, pp. 145-155, Dec. 2015.

[338] Magnus Hedlund, Janaína G. Oliveira, Hans Bernhoff, "Sliding mode 4-quadrant DC-DC converter for a flywheel application," Control Engineering Practice, vol. 21, no. 4, pp. 473-482, Apr. 2013.

[339] R. D. Middlebrook and S. Cuk, "A general unified approach to modelling switching-converter power stages," IEEE Power Electronics Specialists Conference Record PESC, pp. 18-34, 1976.

[340] A.A.A. Radwan, and Y.A.-R.I. Mohamed, "Linear Active Stabilization of Converter-Dominated DC Microgrids," IEEE Transactions on Smart Grid, vol.3, no.1, pp.203-216, March 2012.

[341] M. C. Mira, A. Knott, O. C. Thomsen, and M. A. E. Andersen, "Boost converter with combined control loop for a stand-alone photovoltaic battery charge system," 2013 IEEE 14th Workshop on Control and Modeling for Power Electronics (COMPEL), pp.1-8, 23-26 June 2013.

[342] Available Online: http://www.mathworks.com/help/ident/examples/estimating-transfer-function-models-for-a-boost-converter.html

[343] M.A. Awadallah, and B. Venkatesh,"Energy Storage in Flywheels: An Overview," Canadian Journal of Electrical and Computer Engineering, vol.38, no.2, pp.183-193, Spring 2015.

[344] J. I. Garate, E. Ibarra, I. Martínez de Alegría, I. Kortabarria, and J.A. Araujo,

"Analysis of DC–DC power supply systems for pulsed loads from green electronics perspective," IET Power Electronics, vol.8, no.6, pp.957-966, 2015.

[345] Majed A. Alotaibi, M.M.A. Salama, An efficient probabilistic-chronological matching modeling for DG planning and reliability assessment in power distribution systems, Renewable Energy, Vol. 99, December 2016, pp. 158-169.

[346] Gianni Celli, Emilio Ghiani, Fabrizio Pilo, Gian Giuseppe Soma, Reliability assessment in smart distribution networks, Electric Power Systems Research, Vol. 104, November 2013, pp. 164-175.

[347] N. Hatziargyriou, H. Asano, R. Iravani and C. Marnay, "Microgrids," in IEEE Power and Energy Magazine, vol. 5, no. 4, pp. 78-94, July-Aug. 2007.

[348] M. Hosseinzadeh and F. R. Salmasi, "Robust Optimal Power Management System for a Hybrid AC/DC Micro-Grid," in IEEE Transactions on Sustainable Energy, vol. 6, no. 3, pp. 675-687, July 2015.

[349] D. E. Oflivares et al., "Trends in Microgrid Control," in IEEE Transactions on Smart Grid, vol. 5, no. 4, pp. 1905-1919, July 2014.

[350] Tarek Youssef, Osama A. Mohammed, Adaptive SRF-PLL with Reconfigurable Controller for Microgrid in Grid-Connected and Stand-Alone Modes, IEEE Power and Energy Society General Meeting, Vancouver, B.C., Canada, 21-25 Jul 2013.

[351] M. M. Amin and O. A. Mohammed, "Development of High-Performance Grid-Connected Wind Energy Conversion System for Optimum Utilization of Variable Speed Wind Turbines," in *IEEE Transactions on Sustainable Energy*, vol. 2, no. 3, pp. 235-245, July 2011.

[352] M. M. Amin, O. A. Mohammed, Vector oriented control of voltage source PWM inverter as a dynamic VAR compensator for wind energy conversion system connected to utility grid, Twenty-fifth Annual IEEE Applied Power Electronics Conference and Exposition (APEC), 1640-1650, 2010.

[353] A. Mohamed, O. A. Mohammed, Smart vector-decoupling control of three phase rectifiers for grid connectivity of sustainable energy sources, IEEE PES Conference on Innovative Smart Grid Technologies – Middle East (ISGT Middle East), 2011.

VITA

AHMED ELSAYED

July 15, 1984	Born, Qalyubia, Egypt
2001-2006	B.Sc. Benha University, Egypt
2008-2010	M.Sc. Benha University, Egypt
2007-2012	Research/Teaching Assistant, Benha University, Egypt
2012-2015	Graduate Assistant, Florida International University, USA
2016	Dissertation Year Fellowship (DYF), Florida International University, USA

SELECTED PUBLICATION AND PRESENTATIONS

- Ahmed T. Elsayed, Tarek Youssef, and O. A. Mohammed, " Modeling and Control of a Low Speed Flywheel Driving System for Pulsed Load Mitigation in DC Distribution Networks," IEEE Transactions on Industrial Applications, vol. 52, no. 4, pp. 3378-3387, Aug. 2016.

- Ahmed T. Elsayed, Christopher R. Lashway and Osama A. Mohammed, "Advanced Battery Management & Stabilization System for Smart Grid Infrastructure" IEEE Transactions On Smart Grid, vol. 7, no. 2, pp. 897-905, Mar. 2016. doi: 10.1109/TSG.2015.2418677.

- Ahmed T. Elsayed, Ahmed A. Mohamed and Osama A. Mohammed, "DC microgrids and distribution systems: An overview", Electric Power Systems Research Journal, 119, Febraury 2015, 407-417.

- Christopher R. Lashway, Ahmed T. Elsayed, and Osama A. Mohammed, "Modelling and Coordinated Control of Hybrid Energy Storage Systems for Extended Operation" Electric Power Systems Research Journal (ELSEVIER), vol. 141, pp. 50-62, Dec. 2016.

- Abla O. Hariri, Tarek Youssef, Ahmed T. Elsayed, Osama Mohammed, "A Computational Approach for a Wireless Power Transfer Link Design Optimization Considering Electromagnetic Compatibility", IEEE Transactions on Magnetics, vol. 52, no. 3, pp. 1-4, Mar. 2016.

- Tarek Youssef, Ahmed T. Elsayed, and O. A. Mohammed, "Data Distribution Service-Based Interoperability Framework for Smart Grid Testbed Infrastructure," MDPI- Energies (OA), 9, 150, Mar. 2016.

- Ahmed T. Elsayed, and Osama A. Mohammed, "Optimal Design of AC-DC Distribution Network Architectures with High Demand Loading Conditions Using a Multi-objective Approach" Submitted to International Journal of Electrical Power and Energy Systems, Nov. 2016.

- Tarek A. Youssef, Mohamad El Hariri, Ahmed T. Elsayed, Osama Mohammed, "Energy Management System Framework for Small Microgrids Utilizing DDS Middleware", submitted to IEEE Transactions on Industrial Informatics, Special Issue on "Smart Grid and Renewable Energy Resources: Information and Communication Technologies with Industry Perspective", Dec. 2016.

- Christopher R. Lashway, Ahmed Elsayed, and O. A. Mohammed, " Management Scheme for Parallel Connected Hybrid Energy Storage in Electric Vehicles," IEEE Power and Energy Society General Meeting, Boston, MA, Jul. 17-21, 2016. (Winner of Best paper Award).

- Ahmed Elsayed, Nour Elsayad, and O. A. Mohammed, " Pareto Based Optimal Sizing and Mix of Energy Storage in Ship Power Systems With Considering Weight," submitted to 2016 IEEE Industrial Application Society (IAS) Annual Meeting.

- Ahmed Elsayed, Tarek Youssef, and O. A. Mohammed, " Modeling and Control of a Low Speed Flywheel Driving System for Pulsed Load Mitigation in DC Distribution Networks," 2015 IEEE Industrial Application Society (IAS) Annual Meeting, Addison, TX., Oct., 18-22, 2015, pp.1-6.

- Christopher R. Lashway, Ahmed Elsayed, and O. A. Mohammed, " Ripple Voltage Analysis for a Flywheel-Battery Based Energy Storage System," The 31st Annual IEEE Applied Power Electronics Conference (APEC), Long Beach, CA, USA, 2016, pp. 1267-1272.

- Ahmed Elsayed, and O. A. Mohammed, " A Comparative Study on the Optimal Combination of Hybrid Energy Storage System for Ship Power Systems," 2015 IEEE Electric Ship Technology Symposium (ESTS), Alexandria, VA, 2015, pp. 140-144.

- Ahmed Elsayed, and O. A. Mohammed, "Distributed Flywheel Energy Storage Systems for Mitigating the Effects of Pulsed Loads," 2014 IEEE Power and Energy Society General Meeting, Washington D.C., USA, 27-31 Jul.2014.

- Ahmed Elsayed, A. Mohamed and O. A. Mohammed, " DC Microgrids and Distribution Systems: An Overview," 2013 IEEE Power and Energy Society General Meeting, Vancouver, B.C., Canada, 21-25 Jul 2013.

- Ahmed Elsayed and O. A. Mohammed, " Wavelet-Adaptive ANN Forecaster for Renewable Energy Sources for Continuous Supply in Microgrid Applications," 2013 IEEE Power and Energy Society General Meeting, Vancouver, B.C., Canada, 21-25 Jul 2013.